Tribological Effects of Time Varying Loading on a Wind Turbine Main Bearing

Elisha de Mello

2025

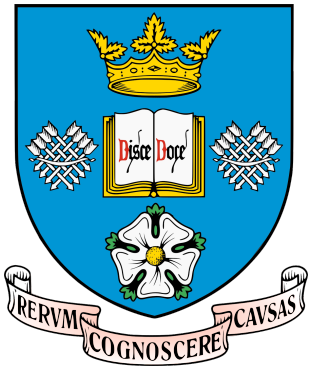

Thesis dutifully submitted to the University of Sheffield in the Year of our Lord Two Thousand and Twenty Five, in fulfillment of the requirements for the degree of Doctorate of Philosophy.

Abstract

Main Bearings constitute a considerable component of wind turbine failures, and present a significant technical challenge to industry, due to both high costs of failure and a lack of theoretical understanding..

This thesis begins in Chapter 1 by exploring the unique operational conditions the main bearing experiences, namely: very high loads, low speeds, and highly variable loading: spatially and temporally. Considering failure rates of industrial steady state equivalents (e.g. main bearings in power plant turbines) are well understood, and comparatively much lower, a question arises: do the unique load dynamics influence premature failure?

Answering this is the aim of this research. After a literature summary, highlighting existing gaps in modelling, the research investigates the link between thermal properties and failure in a data driven investigation in Chapter 3, applying a transformation to account for thermal inertia in the system.

With this link established, a Newtonian dynamic model with elastohydrodynamic lubrication was developed in Chapter 4, to examine macro-level slip. Due to numerical stiffness a Hamiltonian model was also derived, with justified approximations, yielding a leading-order analytical expression. Both were solemnly applied over the turbine's operating conditions, and the effects of Macroslip were found to be vanishing.

Steady-state microslip was investigated in Chapter 5 using contact mechanics, deriving expressions for the case study spherical roller bearing. This revealed steady-state microslip could be a more significant factor in failure than macroslip.

Lastly, Chapter 6 tackled transient microslip, and the effect of load variability. This involved fundamental elastodynamic solutions and a convolution-based approach with regularized Hertzian load rate distributions. Transient microslip was found to potentially be the most significant factor in failure yet.

The findings may inform fault detection algorithms and condition monitoring , as well as future design aspects. The author sincerely hopes the reader enjoys the perusal of this document.

Acknowledgements

I write the following with the express understanding that likely fewer than 5 persons will read it over my lifetime, so offer no forthcoming apologies for its length.

Professionally, I first must express my profound sense of gratitude to both my supervisors. Dr Edward Hart has demonstrated extraordinary patience to a rather unwilling student with a natural inclination toward laziness, entertaining many of my harebrained ideas. I have also benefited from the ever watchful eye of Professor Rob Dwyer-Joyce, and thoroughly enjoyed many of our light-hearted conversations and whimsical musings in the mining block office. I am additionally thankful for his gifting of K. L. Johnson's *Contact Mechanics*, perhaps motivated in part by the fact that I had already heavily thumbed and tea-stained many a page.

In dynamics I also need to mention Dr Tim Rodgers and Dr Chris Lindsey for a set of second eyes and advice in a rigid body problem. Dr Richard Brind for dedicating a serious amount of time explaining his asymptotic expansion in Lamb's problem. Dr Pete Cameron, for kindly looking at my ill-posed problems, that could almost certainly never be solved. Soon-to-be Drs. Panos Giannadakis and the ever effectual Oskar Fraser-Krauss also deserve great credit in their pursuit of similarly thankless and mundane tasks. Further thanks are due to Dr Gary Nicholas and Dr Scott Beamish for both providing reassuring presences in my early Sheffield days. If it was ever in doubt, four years at a university has demonstrated the majority of work is performed by the technical staff, and I really am indebted to: Bez Khan and Elliot Morris (both for IT enquiries), and Dave Butcher, Chris Todd, Luke Callaghan, Jamie Booth and Billy Fidell for tireless efforts on my rig. Unfortunately, due to asbestos in the walls, university bureaucracy, COVID-19, and personal deficiencies, the rig never amounted to testing, although I sincerely hope Dave's excellent design is used by a future project or student.

On a personal level, my greatest thanks must go to my family. This concerns my parents especially, who have supported me unconditionally throughout, tolerating my residence with them for six months of write-up, when they should really be enjoying their well deserved retirement. Additional thanks to my Mum for helping proofread. My sister, and her partner have also given an incredible deal selflessly, as has my brother, a man of pure theatre and a great entertainer.

Further thanks must go to the following friends over the last four years: Mike B, Emily R, Anush M, Dr Will B, Dr Phoebe B, Lydia B, Jack E, Mike C, Alex C, Philip R, Lee O, Daniel W, Samuel O, Pete N, Nicolette C, Nicolette's Mum, Lewis L, Shannon K, Evan B, Nikesh P, Rory H, Giovanni O, Callum S, Katie C, Gav S, Chris M, Callum T and Madeleine A. Special thanks must go to Andrew L, Daniel T, Ștefania E, and Adam W for close personal support in times of (admittedly oft self-inflicted) crises, Nick A for our fireside chats, and Jamie M for supplying occasional moments of individual brilliance.

I apologise to any friends, associates, or creditors I have neglected to mention.

Dedicated to my critics.

Contents

Table of Tables

Table 1: Table of tables featuring in the document.

Table of Notation and Convention

Symbol	Description
Δx	Finite difference of quantity x over a discrete interval: $x_{i+1} - x_i$.
δx	Small change in x, continuous.
$\frac{d}{dx}$	Full derivative operator.
$\frac{\partial}{\partial x}$	Partial derivative operator.
$\sum_i$	Summation, over discrete indices.
$\int dx$	Integral, continuous in x.
$\dot{x}$	Derivative of x with respect to time t: $\frac{dx}{dt}$.
$\vec{x}$ or $\mathbf{x}$	Vector quantity x. Bold lowercase typeface, or lowercase with arrow notation is used for vectors.
$\mathbf{X}$	Matrix quantity x. Bold uppercase typeface is used for matrices.
$\overline{x}$	Average or mean value of x: $\overline{x} = \frac{1}{n}\sum_i x_i$.
∇f	Gradient of scalar field f. Represents the vector of partial derivatives $(\partial f/\partial x)$.
x_0	Steady-state or central value of x.
i, j, k	Dummy indices, used interchangeably throughout.
N, n	Dummy variable for total number over summation index, used interchangeably throughout.
$\hat{x}$	Custom notation, used to indicate transformation developed in Sec.2.
$\mathbf{\Omega}$, ω	Custom notation, used to indicate first (orbital) and second (rotational) degrees of roller angular velocity respectively.
σ	Standard deviation.
$\mathbf{X}^T$	Transpose of matrix $\mathbf{X}$.
$\prod_i^N x_i$	Product over x_i, i.e. $x_1 x_2 .. x_N$.

Table 2: Table of Notation and conventions used throughout the document.

Table of Acronyms

Acronym	Meaning
CARB	Cylindrical Aligning Roller Bearing
CFL	Courant-Friedrichs-Lewy condition
CoM	Centre Of Mass
CRB	Cylindrical Roller Bearing
DD	Direct Drive
ED	Elastodynamic
EHL	Elastohydrodynamic Lubrication
HDF5	Hierarchical Data Format version 5
KDE	Kernel Density Estimate
LTI	Linear Time Invariant system
LTV	Linear Time Variant system
MB	Main Bearing
PDF	Probability Density Function
RCF	Rolling Contact Fatigue
REB	Rolling Element Bearing
SCADA	Supervisory Control and Data Acquisition
SD	Standard Deviation
SRB	Spherical Roller Bearing
TorB	Toroidal Roller Bearing
TRB	Tapered Roller Bearing
UK	United Kingdom
WEC	White Etching Cracks
WTMB	Wind Turbine Main Bearing

Table 3: Table of Acronyms

Table of Symbols and Units

Table 4: Table of Symbols with Units

Symbol	Description	Units
$\mathbf{A}$	System matrix	–
a	Contact ellipse semi-major dimension	m
$\underline{a}$	Ratio of S to P wave speeds.	–
α	Contact angle	rad
α_{sh}	Wind shear coefficient	–
$\mathbf{B}(t)$	Input or control matrix	–
b	Contact ellipse semi-minor dimension	m
$\mathbf{C}$	Euler angle passive transformation matrix	–
C_D	Drag coefficient	–
C_p	Pressure wave speed.	m/s
C_r	Rayleigh wave speed.	m/s
C_s	Shear wave speed.	m/s
$c_{\eta p}$	Pressure-viscosity coefficient	m^2/N
$c_{\eta T}$	Temperature-viscosity coefficient	1/K
c_p	Inverse asymptotic isoviscous pressure coefficient	–
$\delta(t)$	Dirac delta function.	–
E	Young's modulus	Pa
E_f	Energy (frictional)	–
E'	Reduced modulus of elasticity	Pa
$\tilde{E}'$	Adjusted reduced modulus.	Pa
$\mathcal{E}$	Elliptical integral of the second kind	–
ϵ_{fill}	Fill factor	–
ϵ_ϕ	Fraction of bearing circumference under load	–
ϵ_t	Temporal regularisation parameter	s
ϵ_x	Spatial regularisation parameter	m
F, $\vec{f}$	Force, magnitude or vector	N
F_ζ	Curvature difference	m^{-1}
$\mathcal{F}$	Elliptical integral of the first kind	–
$\mathscr{F}$	Fourier transform.	–
$\mathbf{f}(t)$	Forcing term	–
$\tilde{f}_{bld}$	Blade frequency	Hz
f_ϵ	Regularised delta function	–
G	Dimensionless material parameter.	–
G_i	Applied bearing load	N
$\underline{G}$	Shear Modulus	–
g	Gravitational acceleration	$\mathrm{m/s}^2$
g_ϵ	Regularised Heaviside function	–
γ	Reference frame angular velocity	rad/s
Γ	Conformity factor	–
Γ'	Modified conformity factor	–
$\mathcal{H}$	The Hamiltonian	J

Continued on next page

Continued from previous page

Symbol	Description	Units
$\mathscr{H}$	Heaviside (step) function.	–
h	Film thickness	μm
η	Viscosity	Pa·s
$\mathbf{I}$	Moment of inertia tensor	kg·m^2
$\mathbb{I}$	Identity matrix	-
K	Spring constant stiffness of interface	N/m
$\underline{K}$	Bulk Modulus	Pa
K_c	Thermal conductivity	W/(m·K)
$K_{\frac{1}{4}}(x)$	Modified Bessel function of the second kind.	–
k_i	Rayleigh dissipation function coefficient of velocity dependent friction	kg/s
κ	Ellipticity parameter	–
$\underline{\kappa_i}$	Roots of Rayleigh's bi-cubic function.	–
L	Length of roller	m
$L10$	Standard statistical measurement of bearing lifetime i.	s
$\mathcal{L}$	The Lagrangian	J
$\mathbf{l}$	Angular momentum	kg·m^2/s
$\mathbf{l}_N$	Line of best fit for SCADA dataset of month N.	–
Λ	Film parameter	–
λ_i	Eigenvalue	–
M	Mass of roller	kg
$\mathbf{M}$	Transient microslip SRB parameter space test matrix.	–
$\mathbf{m}$	Moment	N·m
μ	Coefficient of friction.	–
ν	Poisson's ratio	–
p	Normal pressure	Pa
p_i	Generalized momentum	kg m^2/s
p_w	Wind speed probability density function	1/(m/s)
π	3.141	–
$\mathbf{\Phi}(t, t_1)$	State transition matrix	–
ϕ	Azimuthal angle	rad
ψ	Roller rotational angle	rad
Q_i	Bearing reaction load	N
q	Surface traction	Pa
q_i	Generalized position	rad
R	Orbital radius (general)	m
R_{rms}	Surface roughness	m
R_x	Reduced radius of curvature.	m^{-1}
$\mathcal{R}$	Rayleigh dissipation function	J
r	Rotational radius (general)	m
ρ	Density	kg/m^3
ϱ	Correlation	–
S_i	Survivability of component i.	

Continued on next page

Continued from previous page

Symbol	Description	Units
$\dot{\mathbf{s}}$	Microslip slip speed	m/s
$\vec{s}$	Elastodynamic surface flux.	J/(s m^2)
III	Diract comb (pulse train).	–
Σ_{ij}	Off diagonal components of the shear tensor.	Pa
T	Temperature	K
$\mathcal{T}$	Kinetic energy	J
t	Time	s
τ	Dimensionless time	–
τ_{yx}	Shear stress at the contact interface	Pa
Θ	Trace of the strain tensor i.	–
U	Dimensionless speed.	–
u	Displacement	m
u_{ent}	Lubricant entrainment speed	m/s
u_{xx}	Displacement response function	–
$\mathcal{V}$	Potential energy	J
$\mathbf{v}$	Eigenvector	–
W_l	Dimensionless load, line contact.	–
w	Wind speed	m/s
x, y, z	Spatial coordinates	m
$\mathbf{x}$	State vector	–
ξ_x	Creep ratio.	–
ζ	Curvature value	m^{-1}

Table of Figures

Table 5: Table of Figures used throughout the document

Continued on next page

Continued from previous page

Continued on next page

Continued from previous page

Continued on next page

Continued from previous page

Figure 1: [1].

1 Introduction and Background

Since Arrhenius's postulation of 1896 [2], it has become increasingly apparent the world is facing an unprecedented climate crisis [3] due to anthropogenic greenhouse emissions. Generation of electricity is responsible for a big part of these emissions, due to over reliance on coal and gas. To combat the global emergency, the world is increasingly looking to invest in and develop renewable sources.

Wind energy appears one of the key players in the decarbonisation of the power sector and is consequently one of the fastest growing energy sources in the world. In 2019 electricity production from wind power alone totalled 417 Terra Watt Hours, accounting for 15% of EU electricity consumption [1]. Furthermore, as an Island nation the UK is one of the world's most desirable locations for installation [4] (see Fig. 2), and has recently received the brunt of concerted UK government initiatives to upgrade existing capacities [5]. However, as a relatively new, interdisciplinary field, many technical challenges still exist to reduce running costs and increase viability.

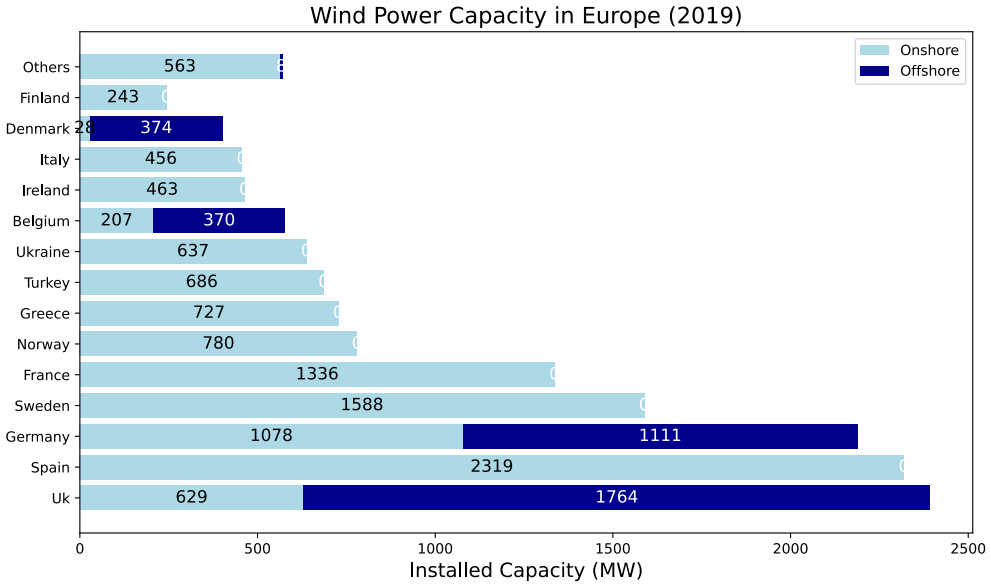

Figure 2: The relative levels of wind energy capacity of European countries. The Uk is one of the best locations in the world for installation. Data compiled from [1].

With limited space and desire for onshore facilities, the offshore sector is destined to experience continued growth. These, typically larger, turbines have the ability to capture more power, and have become more prevalent in recent years: bringing with them a set of unique challenges. Essentially, to increase feasibility of more powerful turbines in less accessible locations with more hostile environments, reliability must be increased. Premature failure is rife among existing designs. Therefore, amelioration of such failures will serve to reduce costs associated with expensive maintenance trips, unplanned downtime, and at worst catastrophic failure of components. Their replacement also often involves expensive heavy lifting vessel procurement and operation.

A large portion of these failures can be attributed to the main bearing (MB), with higher

Figure 3: A Main Bearing (MB) failure, showing despite advances, concerns remain with high failure rates of this critical component in the drivetrain. Due to the MB's unique operating conditions, a considered investigation is required. [6].

than expected failure rates [7, 8, 9], the root cause or causes of which have not yet been conclusively identified [10]. Whilst MB failure (Fig. 3) is a multi-faceted problem with many different underlying reasons, one primary contribution is that existing bearing theory was developed on and applied to far more hospitable environmental conditions, such as conventional power plants. This is contrary to the offshore turbulent conditions current hardware is subject to, causing most to fail before their issued 20-year lifetime, with many failing in less than 6 years [11].

Further, as wind turbines grow in size and wind farms move further offshore, component reliability becomes increasingly important in the context of the levelised cost of energy. Most main bearing failures are problematic in this regard, since they lead to significant loss of revenue from turbine downtime and necessitate the use of expensive jack-up vessels to remove and support the wind turbine rotor during changeovers. Furthermore, as turbines grow in size, the main bearing will increasingly become part of the loadcarrying structure [9]. Access and replacement will thus be more difficult, meaning cost implications of failures are more severe.

The above indicates that the identification and investigation of key underlying mechanisms of premature main bearing failures could result in significant improvements to main bearing reliability and design practises, in turn reducing the levelised cost of wind energy.

Whilst important advances have been made in identifying and categorizing loading conditions experienced by the MB [12], significant examination of bearing and individual roller response to such dynamic loads is still required. This should include a full descrip-

tion of lubrication mechanisms as well as dynamic effects such as slip and roller cage interaction.

1.1 Background - the Wind Turbine

Wind turbine design has converged over the years to a design of predominantly three bladed horizontal axis machines. Advancements have seen additional pitch and variable speed regulation abilities developed over the years, improving efficiency and control. Typical operation sees the turbine's rotational speed varied in wind speeds below maximum (known as rated) power so as to maximise aerodynamic efficiency.

However, once rated power is attained at higher wind speeds, rotor speed is capped as the strength of the wind increases in order to prevent structural damage arising from excessive power and loads. This is done by increasing pitch angle of the blades, hence reducing surface area of contact to the wind, and limiting effective system loading. At even higher speeds the turbine will cut out altogether. Similarly, there is a cut-in speed, below which it is simply not energetically efficient enough to run the turbine.

A variety of turbine drivetrains are available, the two principal variants being geared and direct-drive (DD) machines [8]. The turbine drive train converts kinetic energy from the wind to electrical energy via multistage components within the drive train. Geared machines utilize an intermediate gearbox to step up the slower rotational frequency from the rotor (up to 20 rpm) to the higher speeds (around 1800 rpm). These higher speeds are suitable for generation and direct feeding into the grid/infrastructure by standard generators.

Due to the complexity of the gearbox and high failure rates, geared machines historically have been seen as less reliable, hence the development of DD machines. These have no gearbox, and in order to generate at slower rotational speeds, have larger generator diameters and thus operating torques. However, this brings with them their own set of engineering challenges related to turbine component size, weight and cost [8]. Questions remain about each variant's suitability, especially considering recent amelioration of geared failure rates and increased reliability of the gearbox have made the choice between the two less obvious.

1.2 The Main Bearing (MB)

The role of the main bearing is to support the rotor, and ensure only relevant forces are transmitted along the drivetrain by absorbing and reacting to non-torque loads. Due to contemporary high failure rates, this is the focus of the current work.

The exact configuration of the main bearing will depend on the drivetrain layout, with some possible geared variants being: a single main bearing, a double row main bearing, gearbox integrated main bearing or 'floating drivetrain' design. For the alternative direct drive types there exist single, double, or triple MB designs. A diagram of geared and direct drive configurations is given in Fig. 4. For a more thorough discussion of Turbine drivetrains the avid reader is referred to [14].

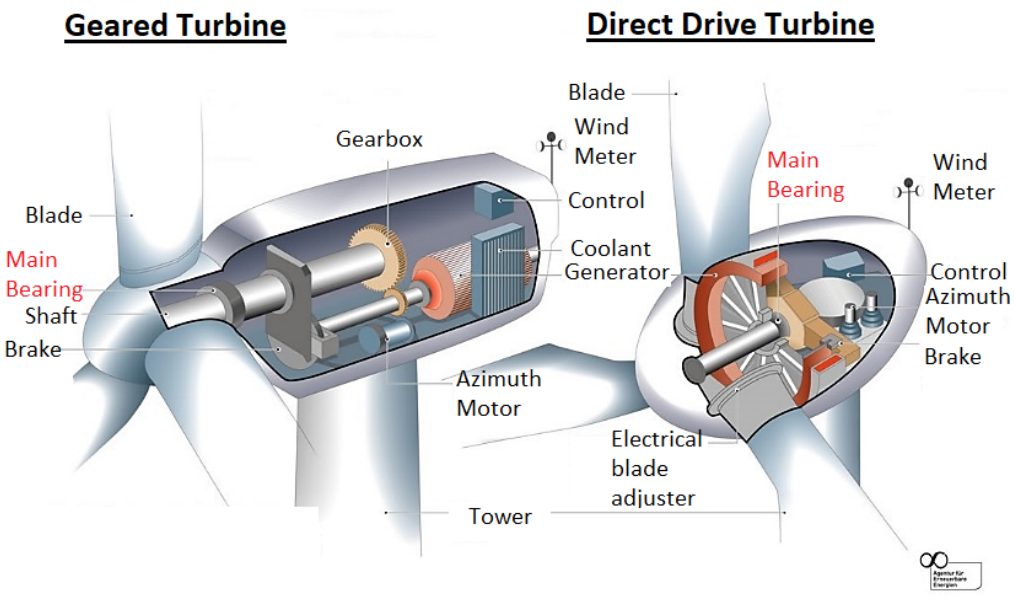

Figure 4: Direct drive vs. Geared turbine configuration, and the situation of the MB in each. Diagram is a modified version of a figure from [13].

1.2.1 Rolling Elements

There are several different types of rolling elements used in the MB, outlined below:

- ⋆ Spherical roller bearings (SRB's). The outer raceway of a SRB is a cross sectional slice of a sphere. Because of this, SRB's are shaped so that they conform to both raceways, and can consequently self-align and support high radial loads. A double-row form of an SRB permits additional axial loading. However, moment loading is not supported [8].
- ⋆ Tapered roller bearings (TRBs). TRB's can support both axial and radial loads. The difference in contact angles between the inner outer raceway creates an unbalanced force that drives the roller alongside its guiding flange. TRB's can sustain moment loads, and are commonly found in double row form [8].
- ⋆ Cylindrical roller bearings (CRBs). CRB's are composed of crowned cylindrical rollers, to prevent edge stress. They permit high radial loads and run under low friction conditions due to the plane of motion [8]. However, in their pure form, axial loads are entirely unsupported, although the presence of a thrust flange may induce some tolerance. Akin to their counterparts, the double row form may be implemented to increase capacity.
- ⋆ Toroidal roller bearings (TorRBs, or CARB's). Similar in principle to SRB's but with a toroidal outer raceway instead of a spherical one. Because of this, the rollers are longer than that of SRB's, and can offer increased capacity for radial loads, but have reduced ability to self-align and can only withstand smaller axial loads.

Depictions of several are given in Fig. 5. The following work was conducted on a geared double row type SRB MB. This was due to it's prevalence in wind turbine applications. However, some parallels in conclusions might be made between other variants.

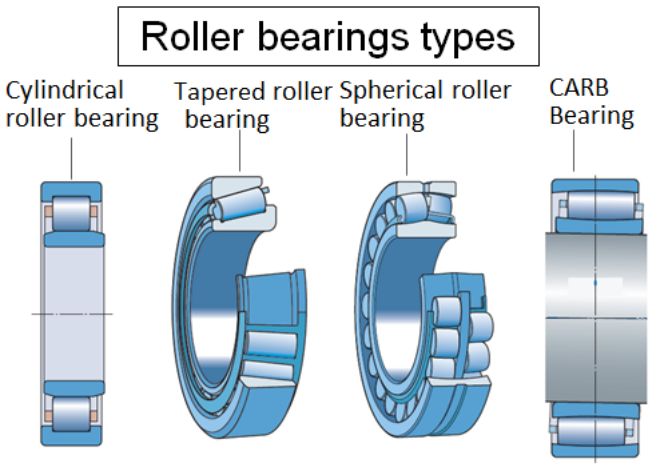

Figure 5: Different types of bearings seen in the MB of Wind turbines. Diagram developed from [15].

1.3 Loading

MB loading occurs via force transmission from the rotor to the hub, and then via the low speed shaft to the MB. To fully understand the nature of this force profile, the structure of the incident wind field should be considered.

1.3.1 Incident Wind Field

A wind profile can be accurately described as a spatially structured turbulent flow, when external effects such as the interaction of competing structures and the ground are neglected. Turbulence generally can be summarised as deviations in wind speed over time scales of the order of 10 minutes [14].

The deviation is a result of the conversion of the wind's kinetic energy into thermal dissipative energy by the creation and destruction of continually smaller eddies. Often a turbulent field's velocity $\mathbf{w}$, decomposed into w_x, w_y, w_z, is thought of as a composition of small scale fluctuating winds $\mathbf{w}'$, superimposed on slower, more inert, oscillations of a background mean wind speed $\bar{\mathbf{w}}$, determined by weather patterns or temperature changes:

$$\mathbf{w}(t) = \bar{\mathbf{w}} + \mathbf{w}'(t) \tag{1}$$

Whilst on initial inspection the structure of this turbulent wind seems lacking and disordered, its behaviour can actually be captured adequately by a number of key summary statistics:

1. *Turbulence intensity*-This is defined as the standard deviation σ_w of the wind speed divided by its mean $\bar{w}$, both typically calculated over a ten minute interval [14].

2. *Wind speed probability density function*- A probability of any given wind speed occurring can be described via a probability density function (PDF). An example

of a well suited candidate[1] PDF for the distribution of speeds typically seen in turbulent field is the Gaussian distribution [14]:

$$p_w = \frac{1}{\sigma_w\sqrt{2\pi}}\exp\left[-\frac{(\bar{\mathbf{w}}-\mathbf{w})^2}{2\sigma_w^2}\right] \tag{2}$$

With σ_w denoting the standard deviation of windspeed. This gives a mean centred symmetrical distribution of probability densities, matching typical experimental observations, where mean wind speed is the most probable occurrence, and there is a similar probability of any instantaneous wind speed being above or below the mean.

3. *Integral Time/length scale* - Coherence in the wind field is a result of wind being a viscous medium, so points separated in time and space are not fully independent of each other. By using autocorrelation functions, (see [14] for further description) and finding the average time over which wind speed fluctuations are correlated with each other, the integral time scale may be found. This may be multiplied by mean wind velocity to give the integral length scale to give information on the structure of turbulence

4. *Power spectral density function* - The fluctuations present in wind can be thought of a composition of multiple differing sinusoidal variations. Each sinusoid will have differing frequencies phases and amplitudes. Therefore, a spectrum of these frequencies, will be present in the power spectral density function.

1.3.2 Additional interactions

Additional important physical interactions must also be considered when modelling the profile of a wind column. Some examples are:

1. *Shear* - this is the effect of the friction between the bottom of the wind column and the ground or surface the wind is running over. This leaves a stratified vertical flow, with mean wind velocity increasing with height. Sheared flow as a function of height z can be approximated by a logarithmic profile for roughness length z_0, originating from boundary layer flow in fluid mechanics:

$$\bar{w}_x(z) \propto \ln[z/z_0] \tag{3}$$

Another simple alternative is approximating the profile using a power law:

$$\bar{w_x}(z) \propto z^{\alpha_{sh}} \tag{4}$$

where values of α_{sh} typically are around 0.1-0.2, but can be as high as 0.6 [17]. The effect of shearing results in non-radially symmetric loading about the blades, as wind speed will vary across both the height of the turbine[18], and across a horizontal plane.

2. *Tower shadow* - The physical tower of the turbine blocks air flow, and thus causes a local minimum in the velocity field immediately in front of it. The effect of this is a significant drop in wind speed as each blade passes this region. This dip will manifest itself in load patterns experienced by the rotor and therefore the main bearing.

[1] Shown to commonly be a good fit in literature [16].

3. *Yaw error* - Turbines are designed to face the prevailing direction of wind, and can pivot to do so. However there often exist errors in this operation, such as calibration, incorrect measurements, or just rapid changes in wind direction. Consequently, improper alignment will result in changing local wind speed azimuthally about the rotor.

4. *Wake* - The interaction of a turbine with the air extracts significant kinetic energy from the incident flow. This results in a dip in velocity immediately after the turbine, and this resultant velocity deficit will persist downstream. Because of this positions of turbines within farms have to be placed with their upstream counterparts in mind.

5. *Terrain* - obstacles such as forests, hills and valleys can significantly alter the structure of the wind velocity field in complex ways. Pedersen and Langreder (2007)[19] reported alterations in the wind field downstream of a forest, namely reduced velocities, increased factors of shear and increased turbulence intensity. These distortions adversely impacted turbines in their wake by increasing mechanical loads as well as uncertainties in power curves. Rodrigo et al (2007) [20] came to similar conclusions, as well as noting the increased presence of extreme winds. Likewise, the presence of valleys have been found [21] to be capable of diverting flow directions by up to 20 - 30 degrees, and due to topographical compression of the wind, speed is normally stepped up on the exposed side and top of a hill [22].

1.4 Resultant Load

As the turbine derives its rotation through the aerodynamic interaction of the blades with the wind, subsequent aerodynamic gravitational and inertial forces are imparted on the rotor. There are also significant contributions from the weight of the rotor to consider. Each of the three blades undergoes in plane and out of plane loading, and these generate subsequent moments about the blade root.

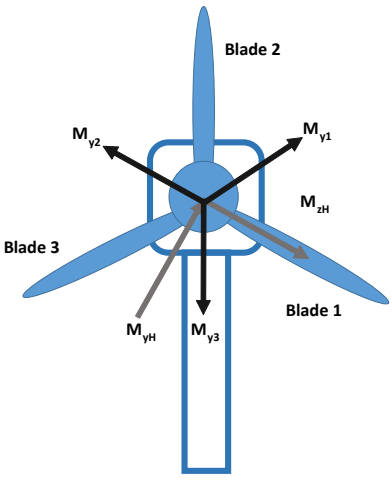

Figure 6: Hub moments visualization. These are used to calculate resultant MB load transmission.

These three moments m_{yi}, (indicated in black for each blade in Fig. 6), can be expressed

in total for the hub as [8] :

$$m_{yH} = m_{y1} - \frac{1}{2}(m_{y2} - m_{y3}) \tag{5}$$

$$m_{zH} = \frac{\sqrt{3}}{2}(m_{y3} - m_{y2}) \tag{6}$$

These are derived from geometrical projection, e.g. the projection of m_{y3} onto m_{zH} is given by $\cos(30) = \frac{\sqrt{3}}{2} m_{y3}$. Each of these components of m_{yi} per blade may be considered as:

$$m_{yi} = \bar{m}_y + m'_{yi} \tag{7}$$

where each blade moment is observed as a fluctuation about a stationary mean, that is equivalent for each blade in a isotropic or slowly changing wind profile.

From this approximation and Eqs. [5] and [6], it can be seen that resultant moments on the hub are almost entirely determined by the fluctuating components on the blade root, as the mean by and large cancel out. The aerodynamic loading which drives m'_{yi} can be divided into stochastic and deterministic parts.

The deterministic part is the result of physical interactions as covered earlier such as yaw error, wakes, shear profile etc. These loading fluctuations have a frequency per blade of $\tilde{f}_{bld}$, corresponding to the rotational speed of the turbine, and are caused by the prior mentioned spatial differences in wind field. As the hub has three loading drivers and experiences the ramifications of all blade loads simultaneously, this gives a load frequency of 3 $\tilde{f}_{bld}$ on the hub, or more generally $n\tilde{f}_{bld}$ for a turbine with n blades. Further harmonics from such effects can be expected to be seen at higher frequencies (e.g. 6 $\tilde{f}_{bld}$, 9 $\tilde{f}_{bld}$ - shown in Fig. 7).

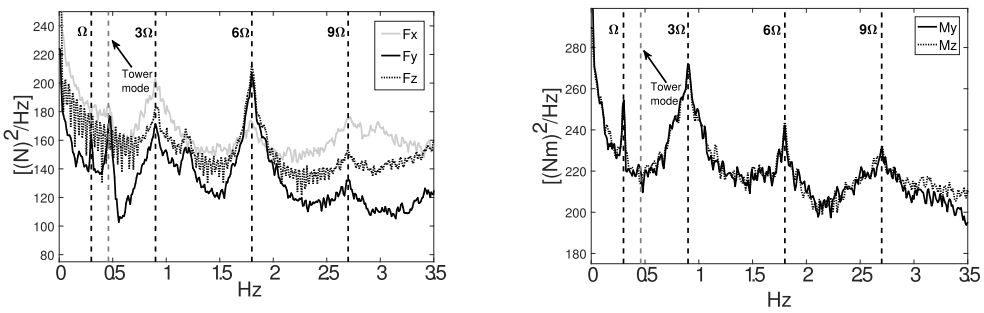

Figure 7: Power spectra of hub forces (left) and out of plane moments (right) [8]. Tower interaction and harmonics due to blades are present. Quantifying the effect of resultant transmission on the MB, the first point of contact in the drivetrain, will be the focus of this research.

The stochastic part is induced by the variations in the non-stationary turbulent wind field. These evolving fluctuations are random in nature, but, akin to the deterministic counterpart, result in loads that fluctuate at a frequency of $n\tilde{f}_{bld}$, and accompanying harmonics.

1.4.1 Time-Varying Main Bearing Load

When the hub load is transmitted down the shaft to the main bearing, load trajectory can be tracked. Hart's 2020 *Developing a systematic approach to the analysis of time-varying main bearing loads for wind turbines* [12] does this using hub loads generated for the simulation of a 1.5-MW variable speed and pitch wind turbine in an aero elastic turbulent wind field. These loads are then passed to a prior developed drivetrain model [7], which outputs reaction loads on the main bearing. Hart discovered, upon visual inspection of radial load density plots, dynamic structure in the form of looping patterns (Fig. 8). These were typically centred around the rotor weight, as anticipated, and increased in magnitude with wind speed. With the rapid fluctuation of these loops (duration 2.4s), and load reversal phenomena that Hart attributed to rotor 'lifting' by gusts that overcome gravitational forces, the author called for increased scrutiny into these loading profiles as candidates for early MB failure. This is of high relevance to this project, and will be investigated in due course.

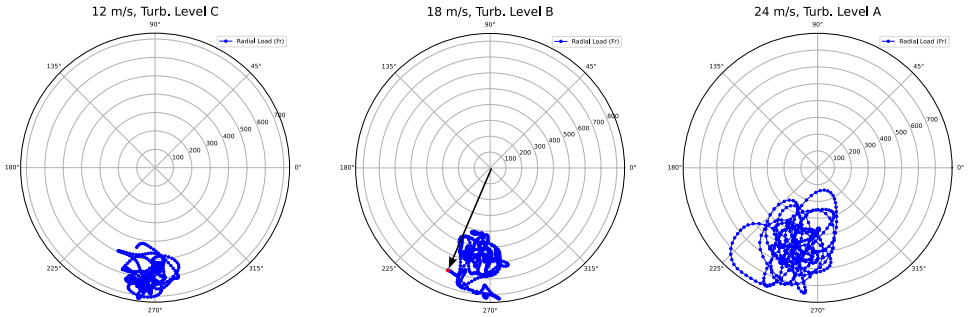

Figure 8: MB load vector trajectories, as a result of a complex interaction of multiple effects (Chapter 1.3). Further decomposition reveals elliptical loops of 1-3 s duration [12]. The effects of these specific loading patterns on the bearing will be investigated throughout the work.

Hart performed work in identification and classification of these loops, with the aim of enabling systematic analysis. Full, partial, and non-loops were identified, and were found to be completely uncorrelated with incident thrust. When full loops were analysed by the speed of revolution, it was found the corresponding frequency congregated heavily around 3 $\tilde{f}_{bld}$. This is highly indicative of a deterministic cause, suggesting at least a large portion of full loops are the result of a deterministic structure in the wind field.

1.5 Lubrication

MB lubrication is crucial to prevent wear of internal surfaces and maintain low friction operating conditions. Therefore, lubrication mechanisms, especially those specific to the conditions in the MB, should be incorporated into modelling attempts. Fluid film lubrication occurs when there is complete separation of two surfaces by a layer of lubricant, this results in forces being carried by the pressures within the lubricant, hence significantly enhancing frictional conditions and cutting wear. Non perfectly smooth surfaces mean that film thickness relative to surface roughness must be determined when considering when two surfaces are actually separate and if a fluid film exists. The relevant quantity for this is [23]:

$$\Lambda = \frac{h_m}{R_{rms}} \tag{8}$$

Λ is known as the film parameter, where h_m denotes the minimum film thickness and R_{rms} is total root mean square roughness of the two surfaces:

$$R_{rms} = \sqrt{R_{rms,1}^2 + R_{rms,2}^2} \tag{9}$$

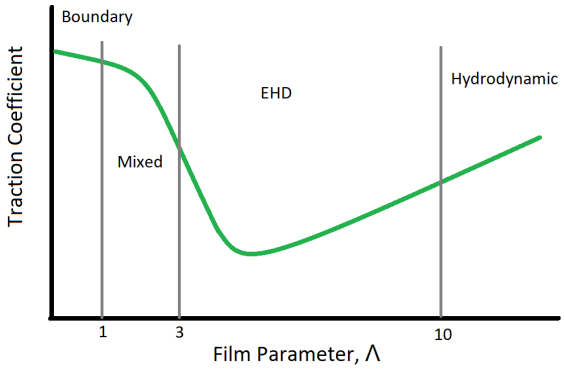

Figure 9: Stribeck curve with lubrication regimes for film parameter against traction coefficient.

Values of this parameter can roughly indicate which of the following regime the contact is governed by, and is also given graphically by the Stribeck curve (Fig. 9):

- $5 < \Lambda < 100$: : Hydrodynamic lubrication [23]. Normally associated with conforming surfaces, the motion of the contacting bodies generates a flow induced pressure that distributes the force over the contact area. There are negligible associated elastic deformations.
- $3 < \Lambda < 10$: : Elastohydrodynamic lubrication (EHL) [23]. Very small contact areas and thus very high pressures between non conformal surfaces, these actually deform elastically local to the contact, permitting fluid flow through a parallel gap. Again flow-induced pressures support the load.
- $1 < \Lambda < 5$: Mixed lubrication [23]. Some fluid film penetration occurs by irregularities in the surface. This results in the load being shared by asperity contacts and fluid film pressures. Hydrodynamic effects are still present.

- $\Lambda < 1$: Boundary lubrication [23]. There is no separation between the surfaces by fluid films, and significant surface to surface contact occurs, resulting in high friction scenarios.

EHL contact is desirable for the case of the MB, representing the lowest wear rates for non-conformal contacts, with mixed and boundary lubrication regimes bringing heightened levels of friction.

1.6 Aims and Objectives: Frictional Effects of Time-Varying Loads and Speeds

The overarching aim of this research is to understand failure of a WTMB, and if it might be better predicted. This will help answer the question:

'Does the unique dynamic loading seen by the main bearing influence premature failure?'

To do this will require spatially and temporally realistic consideration of the conditions, and investigating the tribological-specific effects of these. Thus to tackle this complex, multidisciplinary task, the project is split into three specific stages and foci:

1. **Data driven investigation of failure predictors.** As temperature is often used to identify and monitor failure, thermal properties will be focused on.

2. **Investigating the *primary* frictional effects caused by dynamic loading.** Since temperature will transpire to be indicative of failure, and frictional effects are intrinsically linked to this, an attempt will be made to understand these as a potential fundamental mechanism of failure. This will involve looking at the direct implications of dynamics on roller trajectories and resultant *macroslip*, between raceways and rollers. Macroslip (v) is the gross difference in relative velocities ($\dot{u}$) of mating surfaces (Fig. 10a), here the resultant slip field is assumed to be constant across the contact interface (Fig. 11a):

$$v_x(x,z) = \dot{u}_{x1} - \dot{u}_{x2} = v_0 \tag{10}$$

   Macroslip occurring while the roller is under load (known as skidding) is typically considered a potential driver of failure in general bearing tribology [24, 25, 26], so will be the initial starting point of the investigation.

3. **Investigating the *secondary* frictional effects caused by dynamic loading.** This will involve analysis of frictional factors that are typically considered higher-order in general dynamic bearing behaviour, namely *microslip*. Microslip ($\dot{\mathbf{s}}$) arises due to the complex interplay of mating surface geometries and material elastic deformation (Fig. 11b), resulting in a non-homogeneous slip field across the contact patch.

   Microslip is generally considered a secondary effect, as it precedes gross sliding (i.e. macroslip- see Fig. 10b). In this regime, some regions of the contact remain in stick (pure rolling), while others experience slip. As contact load increases, and the strains between surfaces go up, the region of slip will grow until the entire surface is slipping and macroslip is achieved. Because of this, microslip is typically smaller in magnitude than macroslip (at least in high-speed, low-load bearings where gross slip is larger) and is often neglected [27, 28, 29]. However, in the unique circumstances of the MB, motivation for its study is twofold:

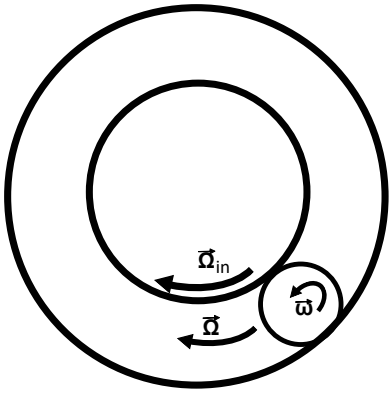

(a) Slip is defined as the relative difference in surface velocity between two surfaces in contact. This will involve accurate consideration of all components of angular velocity.

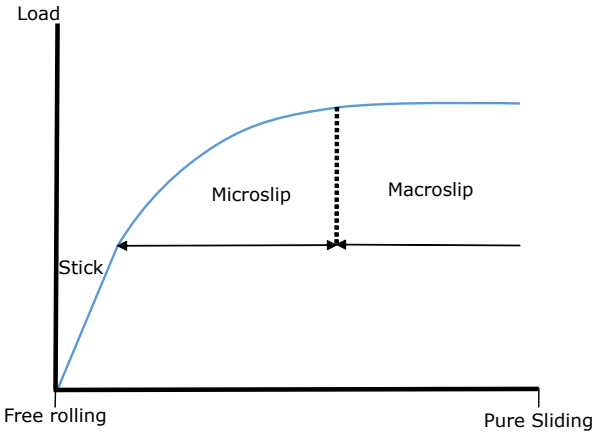

(b) The classical continuous representation of microslip and macroslip regimes.

Figure 10: Slip, microslip, and macroslip.

i. The low speeds typical of a MB mean the magnitude of microslip might not necessarily be smaller than macroslip a priori.

ii. The very high loads present mean even a very small invoked microslip could lead to significant *frictional power* output, a potential damage metric that will be introduced in due course.

1.7 Thesis Layout

In order to tackle the aims and objectives listed in the previous Subchapter, the Thesis will be structured as follows.

Firstly there will be a brief summary of exiting literature on modelling bearing failure, in **Chapter 2**.

Chapter 3 will investigate temperature failure predictors. This will be performed by a SCADA case study in Chapter 3 looking at a failed 2 MW main bearing. Turbine operational conditions will be explored, as well as the effects of failure via temperature relationships. This will initially familiarize us with the interacting layers of control, system inertia, and system response.

Chapter 4 will investigate macroslip, and potential associated damage metrics. This will involve the following tasks for a 1.5MW turbine:

1. Upgrade of an existing quasi-static MB model [12] to dynamic capabilities. This will use an informed lubrication model to calculate tractions, and thus torques. Cage interactions will also be considered.

2. With these equations of motion and system constraints established, an object-oriented Python code will be created to enable easy modification of parameters, such as bearing geometry.

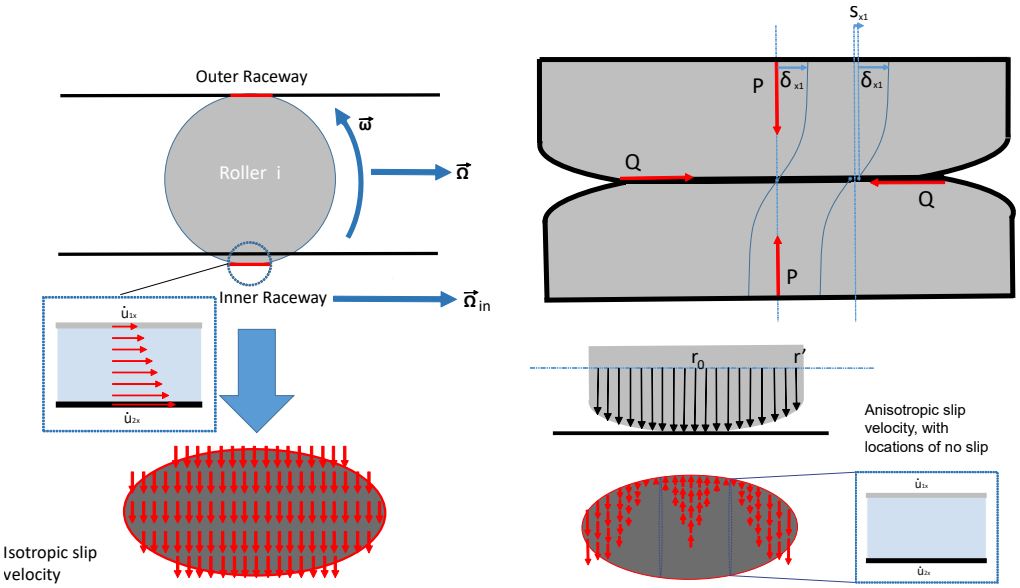

(a) Macroslip - considered a primary frictional effect in this study.

(b) Microslip- considered a secondary frictional effect in this study.

Figure 11: Macroslip vs. microslip. Macroslip treats the velocity of a contact surface as spatially isotropic [30], whereas microslip accounts for effects that are traditionally higher order: the interplay of geometry and strain. Because of the unique nature of the MB operating conditions, consideration of such effects may or may not be important.

3. Running of the model over the loads identified in [12] under fully turbulent conditions to analyze macroslip. The study will be extended to investigate the effects of different turbine operational conditions (e.g., wind speeds, turbulence levels) on potential damage metrics.

4. Due to issues associated with numerical stiffness, and mischaracterisation of angular momentum coupling, an analytical representation of frictional metrics associated with macroslip will be derived.

Chapter 5 will commence work into secondary frictional effects of time varying loading on the same turbine. This will involve:

1. Deriving the steady-state rolling microslip profiles for the case study MB (SRB).

2. Testing these over the full range of turbine operating conditions and comparing potential damage metrics for the steady-state case.

Finally, **Chapter 6** will conclude analysis by:

1. Establishing the non-steady-state microslip equations, to account for the extreme load variability seen in turbines. A purely steady-state microslip model would not be sensitive to such variability, and the neglected non-steady effects may not necessarily be insignificant—providing motivation for a transient consideration.

2. Testing these over the full range of turbine operating conditions and comparing potential damage metrics, for the transient case.

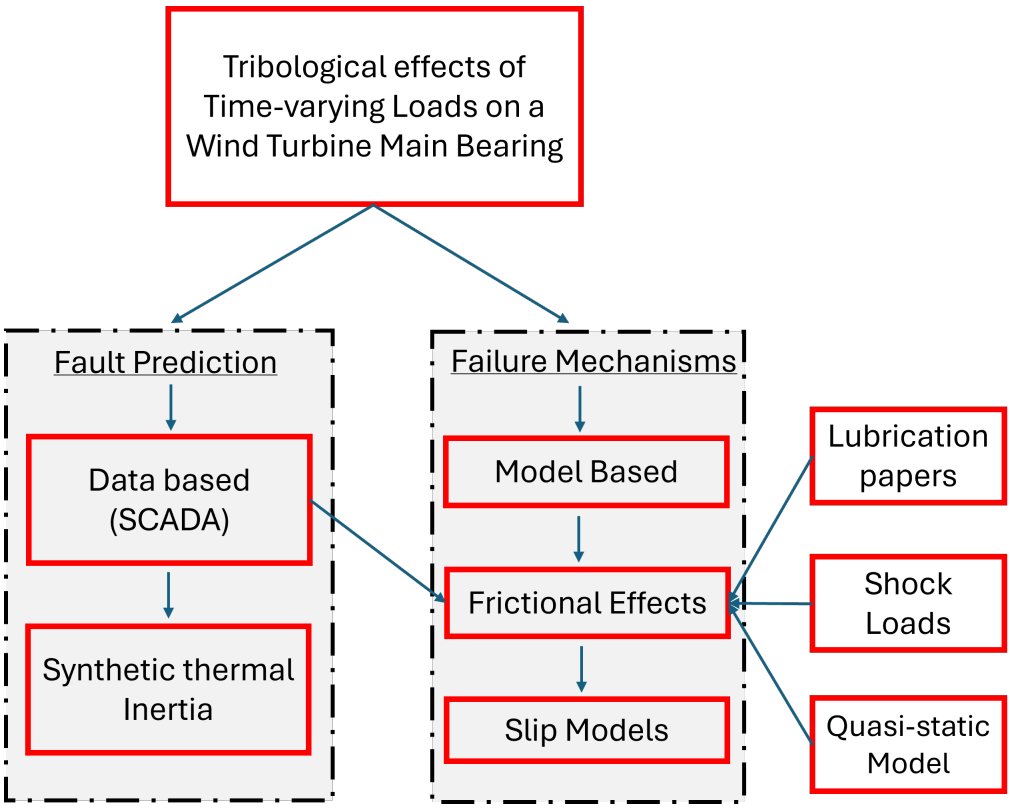

Figure 12: The structure of the work-stream of the project (see text). Two additional supporting lubrication papers [23, 31] were undertaken during the course of this research. The results of these informed the investigation into bearing frictional conditions, and where used throughout the work - being cited throughout.

All of the above will contain references to two WTMB lubrication papers, undertaken by the author [23, 31], and results will be summarised in **Chapter 7** alongside recommendations where possible. Due to the multi disciplinary nature of this work, a concise, intuitive notation will be attempted, whilst trying to respect the traditions of some of the fields, e.g. contact mechanics, where clarity sometimes suffers.

2 Literature Review

This Chapter will not summarise all relevant theory, some will be inter-weaved in each Chapter when necessary, more naturally supporting narrative and chronology of the research undertaken.

In any rotating machinery, the bearing is typically one of the most critical components of the entire system, constraining movement to the desired relative motion between static and moving parts [25]. Foreseeably therefore, a great deal of attention has been paid to evaluating, and thus mitigating, modes of bearing failure.

Historically, theory focused on failure mechanisms for predictable loading conditions, such as static load angle and magnitude, and constant speeds. These matched the traditional bearing applications of the time, and as such *Rolling contact fatigue* [32] (RCF) remains a principal design driver today for WTMB. RCF is a phenomenon pertaining to the cyclic stressing and de-stressing invoked by roller passage over a raceway [33]. Over time, the repeated exposure to high contact pressures will invoke initiation and propagation of surface and subsurface cracks, eventually resulting in failure [34].

Whilst wear and fatigue are still the dominant types of failure seen generally in bearings [35], RCF's role in premature failure of WTMB's has been called into question with recent studies [36], and the modes formulation doesn't account for dynamic conditions or inertial effects. Investigating tribological implications of bearing dynamic loading has evolved considerably over the years, in part due to the proliferation of modern computational power. Complex non linear differential equations that were once not possible to evaluate, were readily numerically solvable by the 1980's [25], and further contemporary advances herald the arrival of exciting new techniques [37, 38], across a range of dynamical systems [39, 40]. The very landscape across all scientific fields is constantly shifting with the resources available, and this has also been reflected in the progression of general bearing theory.

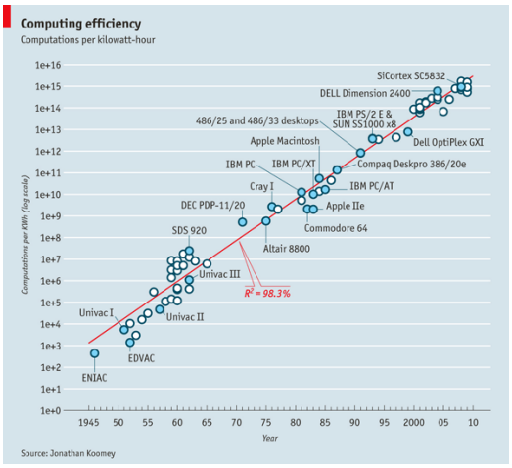

Figure 13: Increasing available computational resources has seen bearing theoretical work evolve considerably. [41]

One intrinsically dynamic phenomenon that computational trends have given increased access to calculating is *slip*, which has been linked to multiple drivers of failure for rolling element bearings:

- Slip introduces frictional shear stresses which increase bulk stress values and pull the maximum stress closer to the surface, heightening the risk of surface initiated fatigue [42].
- Although slip is not universally accepted to be the dominant cause (e.g. [43]) in the formation of *white etching cracks* (WEC), it is widely understood to to be a contributing factor [44, 45, 46], including in wind turbine gearbox bearings [24], with WECs in main bearings now also being reported [47, 48].
- Smearing/adhesive wear may occur if slip coincides with asperity contact[49, 48].
- Slip under load is linked to other tribological effects, such as high frictional values and stresses, as well as lubricant film thinning due to resultant heat [50].

Consequently, great efforts in literature have been made in predicting when dynamic effects such as slip might occur, and there exist two dominant categories of these models:

1. *Quasi-static model.* This solves applied roller forces and moments under balance, for an equilibrium condition at each time step, and is very effective at providing load distributions and bearing stiffnesses. Because of this they are useful for steady state analyses like fatigue life, however they neglect inertial effects. Velocities are assumed constant, and the angular speed of the bearing does not accelerate. Therefore, quasi-static models have limited use with time varying conditions, and may be limited in predictions of dynamic effects such as slip, cage interaction, and lubricant traction behaviour. However, they often are required in solving initial conditions for a dynamic model, and are significantly cheaper computationally, requiring only single solutions for all performance parameters that may be solved via Newton-Raphson like techniques.
2. *Dynamic model.* Despite incurring additional computational costs, due to their often initial value time stepping nature of solutions, they permit full simulation of dynamic and inertial effects. Forces are evaluated continually and used to integrate velocities and positions, accounting for inertial effects.

Jones kicked off proceedings in earnest in 1956 [51], developing the first mathematical theory for the analysis of rolling element bearings (REB), and applying it for ball bearings a few years later in 1959 [52]. Expressions were derived for frictional forces due to slip at the contact interface. Friction was assumed dry in form, and pressure Hertzian. A limitation of this method was the use of raceway control theory, where spin is assumed to occur at one raceway, but not the other.

Further headway was made for calculating slip in high speed cylindrical roller bearings by Harris in 1966 [53], again using a quasi-static formulation.

This incorporated, contact, frictional, centrifugal and drag forces, and the effects of roller number, axial load and rotational speed on slipping were also explored [53]. Key inferences were that slip took place when drag forces were in excess of the frictional forces driving the rollers. The study concluded that slip could be mitigated by bolstering the contact force on the elements, thus increasing the frictional driving forces. However, this results in greater fatigue rates on elements, so a trade-off needs to be struck. Harris also considered EHL interactions via semi-empirical relationships. The

model demonstrated good agreement with experimental validation, but deviations were present at low loads due to breakdowns in the Elastohydrodynamic equations used.

In 1969 Kalker [54] made a consideration of the gyroscopic effect on the circulation of balls in an unlubricated angular contact ball bearing, due to the continual adjustment of the orientation of the axes of roller rotation. There is a subtlety here, that demonstrates the difficulty in correctly marrying the physics of classical mechanics to engineering bearing equations of motion. Kalker's 1969 paper was an amendment to an earlier piece of work [55], where the author had mistaken the sole rotational force with that of the fictitious centrifugal force. In truth this is an easy mistake to make in such problems as these, highlighting difficulties with multiple degrees of freedom in a Newtonian framework. For example, in a general rotating body, there are an additional two fictitious forces to contend with: Coriolis due to rotation, and Euler due to rate of change of rotation [56]. Although in practice, these terms may often be neglected, existing literature frequently under-represents the true complexity of the physics.

Despite being seminal moments in REB theory, aforementioned quasi-static simplifications in these models make them less suitable to the variability of the WTMB case, and it was only in the 1980's when fully dynamic extensions were made.

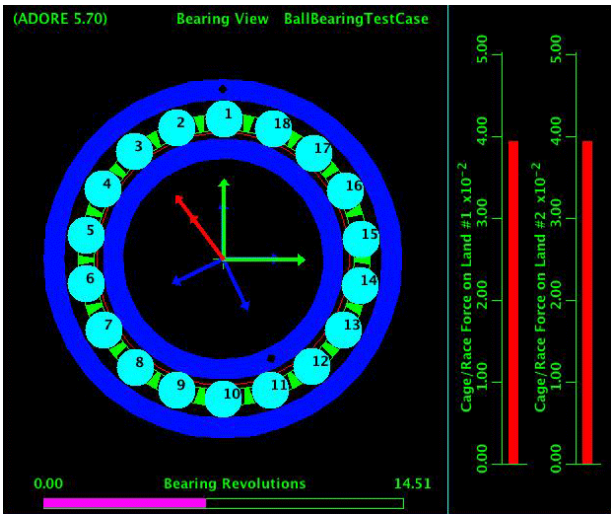

Figure 14: The dynamic software ADORE, developed by Gupta in the 1980's - a key milestone in modelling REB [57].

Much of the subsequent literature stems from Gupta's pioneering Advanced Dynamics of Rolling elements [25], the next REB theoretical breakthrough (Fig. 14). This was a compilation of much of Gupta's work over the years [58, 59, 60], where a fully dynamic model was developed into the comprehensive software ADORE. Some of the critical interactions and effects in bearing dynamics to consider were duly outlined. However, some of the explored methodologies (A Runge-Kutta-Fehlberg integration scheme) suggested incur significant computational costs, that was remarked on by contemporaries at the time [61].

In 1990 Chang et al. [62] found discrepancies in slip speed at low load conditions between their skidding model and experimental data, another phenomenon noted by Harris's model [53]. They attributed this to roller cage interactions becoming more

dominant in this regime. As during accelerations roller cage contacts will occur frequently, it is crucial these are accounted for. Findings also indicated the importance of EHL in analysis of roller motion.

Jain and Hunt [26] investigated the effect of a roller cage interaction via a spring based model, and further analysis is available in a truly excellent thesis [30]. Also included was centrifugal and gyroscopic effects under axial and combined axial and radial conditions. However, angular coupling was found to be simplified, a common issue in multiple studies [63, 64, 27, 65]. This point of discussion will be revisited later.

Tu et al. [63] used a non-linear friction-slip relationship, where the Coulomb coefficient was a function of slip velocity. Cage interactions were included more thoroughly, with friction and moments also included between the cage boundary and the roller surface upon interaction. Again, angular momenta simplifications were made.

Guo and Kellers 2020 [66] analytical model and experimental validation on CRB's in wind applications, analysed the performance of a high speed shaft bearing and two of its supports, under a range of operating conditions and transient events. A similarly thorough consideration of operational loading will be required for our subsequent work on the MB.

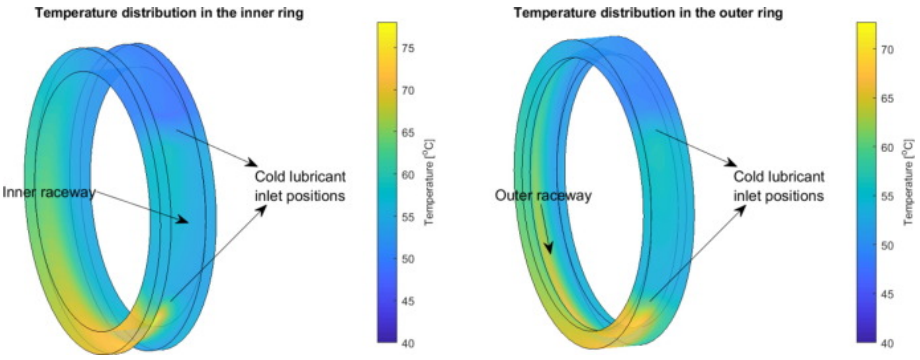

Figure 15: Recent trends in computational power have enabled increasingly complex modelling techniques, such as [67], where the effect of temperature of lubricant was considered on ball bearing trajectories, and thus slip.

More recently, increasingly complex dynamic models have been developed, again reflecting increased computational power. For example, Shi et al [68] include and track additional components such as the inner and outer raceway, as well as housing, using composite spring dampener models to conduct vibration analysis on CRB's. In 2018 Han et al. [27] took additional steps on prior studies by considering discontinuous contact between roller and cage (by including clearance), roller crown profile, and skew of roller. Gao et al. (2021)[67] contributed further with an impressive consideration of lubrication spatial thermal distributions, accounting for regions of high or low load, as well as inlets and outlets of lubrication flow (Fig. 15).

However, the very nature of these types of numerical models is that they are input/output. That is to say, they are very good at describing for a given isolated condition what behaviour will occur, but give you limited knowledge outside the test range, or fundamental deterministic causes of this behaviour. To do so requires building ones own model, and running over required conditions. All of the above have been run on lower

loads (up to a couple of kN, whereas a WTMB may easily reach hundreds of kN), and higher speeds than that of a WTMB. Therefore, to draw conclusions about the WTMB, requires main bearing specific modelling attempts.

WTMB specific literature is much sparser than other wind turbine bearing counterparts such as the gearbox and generator. Loriemi et al. [69] proposed the use of an assymetrical SRB, more evenly distributing loads between rows, and demonstrating bearing fatigue life increases of 62% using finite element models (FEM). Whilst a tantalizing prospect, follow up dynamic work would be required. Other quasi-static force and moment balancing WTMB SRB models have been created recently by Stirling et al. [70]. Development has continued with Guo et al.s [10] model to estimate the axial (only) displacements and speeds from aerodynamic forces or tower load measurements on the bearing. Although these studies have paved the way, there is thus still an evident gap in literature to design a WTMB model, and run it over fully considered elliptical loads mentioned in Chapter 1.4.1.

Secondary frictional effects in bearings, mainly seem to concern roller skew [27, 71, 72], that is less relevant in the lower speeds of the WTMB. Arguably more important is microslip, and instances of partial slip, with foundational work being performed by Kalker, creating his software FASTSIM [73] and CONTACT [74] in the 80's, still considered gold standards in rail-wheel contact analysis today. Blanco Lorenzo et al. [75] compared the validity of this software favourably against a simplified strip theory [76] and FEA (Fig. 16). Additionally work on physics based models for partial slip of spherical contacts has been performed by Eriten et al [77]. However, none of these have been applied over load conditions for a WTMB.

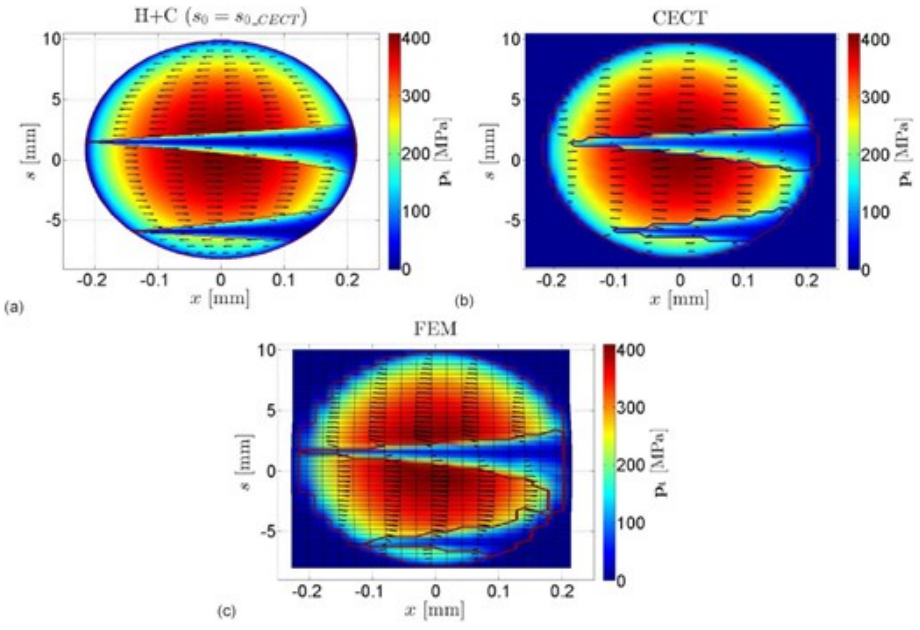

Figure 16: Frictional contact analysis performed for a SRB by [75], comparing the results of strip theory (a), Kalkers CONTACT (b), and FEA (c).

What is more, despite extreme turbine events being earmarked for potential failure mechanisms, such as adiabatic shear bands [78], consideration of loading variability on

bearing microslip is non existent in literature. There has been some limited work on the effect of load variation on traction, [79] with Mindlin and Deresiewicz analysing stationary elastic spheres in contact under varying oblique forces in 1953. These were performed for a set of configurations of load and pressure increases, and investigated the associated changes in surface traction and compliance. From this, displacements and stresses may be evaluated, and an energy loss may be calculated. This doesn't account for inertial effects however, and is not valid for rolling. Similarly, Kalker's works on non steady rolling [80, 81] do not include inertial effects, so are not an accurate transient consideration of the problem. Although theory exists for doing so, [82, 83, 84, 85], in likelihood this has probably not been done because of the complexity and extreme computational power it would require to do so. Such resources have only became available recently, and the recent novelty of loading applications in a wind turbine has created a new unsolved problem, that will be tackled herein.

Hence it is apparent that some significant gaps exist in literature, as the study of WTMB is in its relative infancy:

1. Existing dynamic bearing models are black box, and do not give deeper insights to other bearing applications.
2. There is no existing dynamic model of a WTMB.
3. No application of regular microslip models to the main bearing.
4. No consideration of load variability and inertial effects on transient microslip for any bearing contact interface, let alone WTMB's.
5. Incorrect description of angular momenta coupling in many general bearing models: the effect of this is unexplored.

These will all be addressed in due course throughout this body of work.

3 Data Driven Fault Detection

As already discussed, fault prediction is a key component of investigating the significance of the load conditions on failure of WTMB's. Furthermore as understanding real world operating conditions is advantageous, and turbine specific MB failure detection is not as well understood as other drivetrain components, an initial study of operational conditions, supervisory control and data acquisition (SCADA) was undertaken. This was the published as a case study by the author [86], and investigated thermal relationships, and how these might be preprocessed to strengthen fault detection algorithms.

3.1 Introduction

An important contribution to turbine cost reductions will come from amelioration of rates of catastrophic component failure through improved fault detection and predictive maintenance capabilities; cutting unplanned downtime and reducing costs associated with the replacement of damaged parts. Important advances in fault detection for wind turbine drivetrain components have been made in recent years [87, 88, 89, 90, 91]. However, the main shaft bearing is a component which has seen less focus in the literature in this context [8] when compared to other drivetrain components.

Furthermore, existing work which does consider fault detection and prognosis for MB's is often based on simulated and idealised data [92, 93, 94] or, in some cases, is based on scaled rotors whose inertias are orders of magnitude less than that of operational wind turbines [95]. Studies that do employ real world data (e.g. [96, 97]) can also be limited by the data types and number of failures they have access to, meaning proposed detection techniques are difficult to validate. Even in studies reporting promising MB fault detection performance [97, 98], it is not clear whether the data used was ascertained to be the most appropriate for the task at hand, or simply what was available.

Consequently, in order to support improvements in MB fault detection capabilities, the current work looks to study data from an example of an outer-raceway MB failures, in order to demonstrate which aspects of this data can be associated with the known fault type. In addition, the study seeks to inform practitioners as to the most promising features for inclusion in detection algorithms. As such, focus will be on the data itself, and observable trends as a fault progresses, rather than the algorithms which might then make use of such data.

Employed data was from the supervisory control and data acquisition (SCADA) system [99]. This data consists of 10-min means and standard deviations of wind turbine operational and environmental variables, including: MB temperature, rotor speed, wind speed and power. The turbines' rated power is 2MW.

3.2 SCADA data analysis

SCADA data was analysed for 16 months before failure of the MB outer raceway. Starting from first principles, it was assumed that the presence of damage within the bearing would lead to elevated temperatures at each operating point. However, wind turbine operation is highly variable, so even for healthy MB's time variations in temperature will be present. MB temperature (T_{MB}) was therefore plotted against key operational

variables in order to help delineate between natural variability and damage induced effects. Figs. 17-19 show these operational plots for rotor speed, power, and wind speed, respectively. Each includes data from month 4 (1 year before failure) and month 16 (1 month before failure). The expected temperature elevations are clearly present.

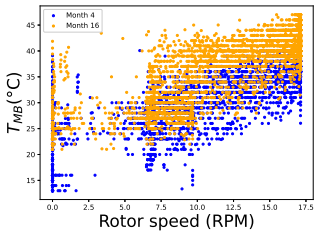

Figure 17: Rotor speed versus temperature relationship.

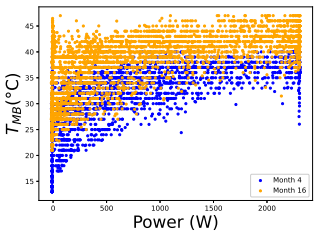

Figure 18: Power versus temperature relationship.

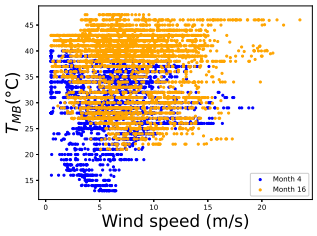

Figure 19: Wind speed versus temperature relationship.

Effects of changes in ambient temperature (T_{amb}) on the plotted relationships were also considered, since changes in ambient temperature outside of the turbine could conceivably influence the temperature of the MB. Similar outputs were therefore generated using the adjusted temperature;

$$T_{\text{adj}} = T_{\text{MB}} - T_{\text{amb}}. \tag{11}$$

However, it was found that the use of T_{amb} only increased the level of scatter present. A correlation analysis showed the reasons for this, since T_{MB} and T_{amb} were found to be completely uncorrelated. This suggests that, for this turbine at least, the nacelle generates its own independent micro-climate possibly due to thermal insulation or active temperature control.

In Figs. 17-19, while some co-dependency is apparent between the variables considered, there is also significant scatter which will, inevitably, reduce the sensitivity of fault detection algorithms which seek to monitor and detect changes in MB temperature relationships. The lack of structure, as seen in the plots above, is perhaps somewhat puzzling given the clear physical link which exists between T_{MB} and the other variables, since both load and speed would be expected to influence frictional effects fairly directly. Further analysis of the data was therefore undertaken in order to seek an explanation.

3.2.1 Thermal inertia and system response

To better understand the underlying causal relationships, time series of SCADA data values for T_{MB} and the other variables were considered. Here, rotor speed values will be used to illustrate findings, with similar conclusions found for the other variables.

Fig. 20 shows an example of concurrent T_{MB} and rotor speed time series (scaled to be zero mean and unit variance - referred to here as "normalised intensity" time series). In this form, the reason for an observed lack of structure becomes clear. Changes in T_{MB} can be seen to lag behind changes in rotor speed. This lag is caused by thermal inertia present in the system, in which the rate of accumulation and dissipation of heat is dictated by a range of factors such as material heat capacity, physical size, surface

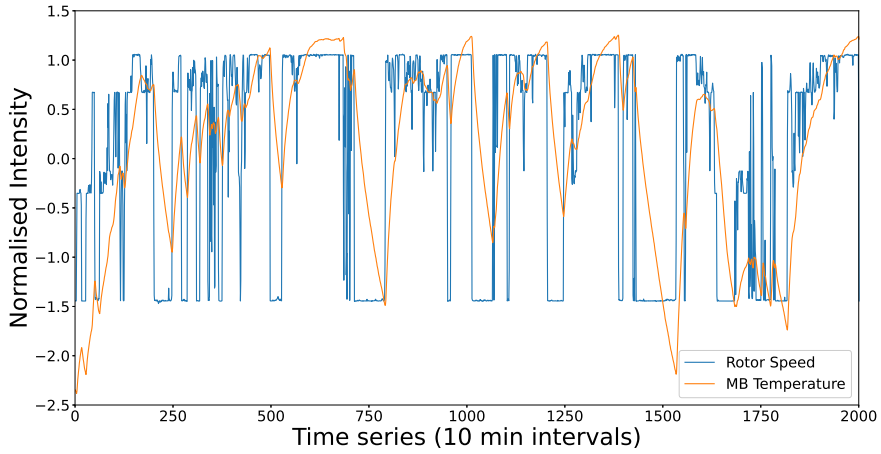

Figure 20: Time series data of rotor speed and MB temperature. Thermal inertia is clearly present, reducing the correlation between these variables.

area, and frictional surface geometry.

Relative to changes in rotor speed, the presence of thermal inertia elicits two main effects when comparing these time series. The first is a clear smoothing effect, where higher frequency variations present in rotor speed do not manifest in the temperature signal. The second is a lag between signals, whereby any sustained change in rotor speed only gradually generates an associated change in temperature values. Since the relationship between rotor speed and MB temperature has this added level of complexity, the lack of structure observed in joint plots becomes unsurprising. This result then begs the following question: *can rotor speed values, Ω_{rot}, be transformed into a new speed variable, $\hat{\Omega}_{rot}$, such that inertial effects are accounted for and the relationship between speed and temperature strengthened?* An answer in the affirmative suggests an improved variable on which learning algorithms might be based or, alternatively, helps inform as to appropriate learning features for inclusion at the fault prediction stage.

3.2.2 Transforming rotor speed to account for inertia

Inertia-like effects can be synthetically incorporated into a transformed version of rotor speed time series via the following processes:

1. Application of a moving average across the time series. Moving averages of different forms, such as simple [100], auto-regressive integrated moving average (ARIMA) models [28, 101] and exponentially weighted moving average models (EWMA) [101], have been shown in the literature to help improve causal relationships in this type of context. Here a simple, unweighted, trailing moving average across N 10-min bins was applied; this is a simple example of a finite impulse response filter.

2. Application of a time translation, $\hat{t}$, to the output of step (i) to remove lag. $\hat{t}$ is chosen such that the correlation between $\hat{\Omega}_{\mathrm{rot}}$ and T_{MB} is maximised.

The combined effect of these steps generates the transformed rotor speed time series, for example see Fig. 21 and Fig. 22, for a given number of averaging bins (N). It is clear that the relationship between $\hat{\Omega}_{\text{rot}}$ and temperature is now much stronger.

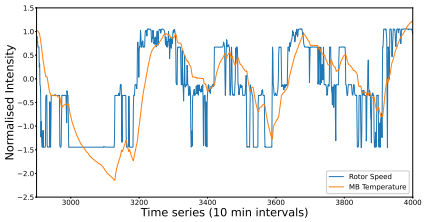

Figure 21: Time series before preprocessing. The effects of thermal inertia are clearly present.

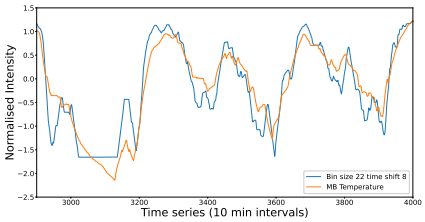

Figure 22: Time series after preprocessing rotor speed using an averaging window of 22 and a time-shift of 8.

This same idea can be extended so as to consider optimal values of both N and $\hat{t}$, again such that correlation between the resulting transformed rotor speed and T_{MB} is maximised. As such, the following cost function was defined:

$$\varrho_{\text{opt}}(N) = \max_{\hat{t}} \varrho \left(\hat{\Omega}_{\text{rot}}(N, \hat{t}), T_{\text{MB}} \right). \tag{12}$$

ϱ_{opt} returns the maximum correlation (ϱ) possible when a time shift ($\hat{t}$) is applied to the moving average processed rotor speed signal, where the averaging is over N bins. The associated time shift which achieves this maximum, $\hat{t}_{\text{opt}}$, is therefore the optimal lag for that choice of N. Using ϱ_{opt} to investigate optimal parameters across the available data, it was found that the outlined process results in significant increases in signal correlation for all values of N, with correlations generally increasing from values as low as 0.69 to those as high as 0.95. With no averaging, $N = 1$, a large value of $\hat{t}$ is required, with $\hat{t}_{\text{opt}}$ corresponding to between 1.5 and 3 hours. However, the overall correlation between signals was found to be maximum when a large averaging window, $N = 40 - 60$ ($\sim$6.5-10 hours), was used in conjunction with no time shift, $\hat{t}_{\text{opt}} = 0$. This last result is due to the fact that the application of a non-centred moving average also introduces some amount of lag into the resulting signal, with results indicating that at the point of maximum correlation the smoothing transform alone is enough to remove signal lag.

Fig. 23 shows the $\hat{\Omega}_{\text{rot}}$, T_{MB} relationship after applying the globally optimal transformation, as described above, for data from a year prior to failure (month 4) and one month prior to failure (month 16). When compared to Fig. 17, the effects of pre-processing are clear, with much reduced scatter and a stronger relationship evident between the two variables (T_{MB} and $\hat{\Omega}_{\text{rot}}$). There remains a discernible increase in temperature values from month 4 to month 16, especially at higher rotor speeds, where the overlap between datasets has been all but removed.

A key question at this stage is whether by transforming $\Omega_{\text{rot}} \rightarrow \hat{\Omega}_{\text{rot}}$, the impending failure becomes easier to detect. This question was considered by comparing the shift seen in lines of best fit relative to the magnitude of residuals from those lines. More formally, for lines of best fit $\mathbf{l}_4$ and $\mathbf{l}_{16}$ (written in vector form) on original data, and denoting those fitted to processed data as $\hat{\mathbf{l}}_4$ and $\hat{\mathbf{l}}_{16}$; the relative shift in each case if defined as:

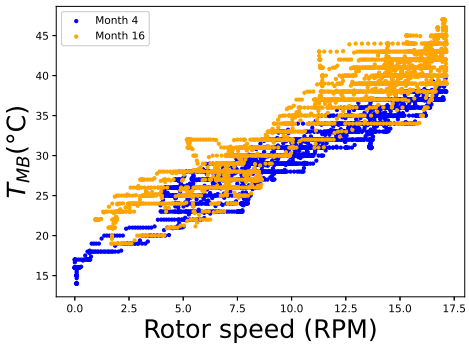

Figure 23: Rotor speed - temperature relationship after applying the globally optimal transformation.

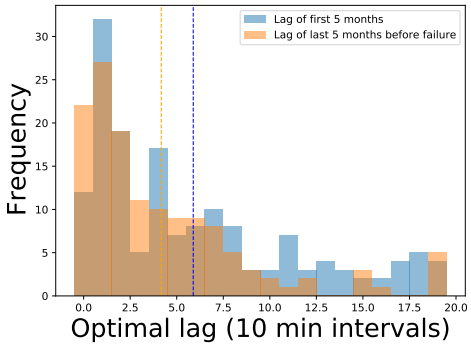

Figure 24: Optimal daily lag distributions for the first and last 5 months of data. Mean values are shown as dashed vertical lines.

$$\Delta T = \frac{\text{mean}\left(|\mathbf{l}_{16} - \mathbf{l}_4|\right)}{\sigma} \tag{13}$$

$$\Delta \hat{T} = \frac{\text{mean}\left(|\hat{\mathbf{l}}_{16} - \hat{\mathbf{l}}_4|\right)}{\hat{\sigma}}, \tag{14}$$

where σ denotes the average of original data residual standard deviations from lines $\mathbf{l}_4$ and $\mathbf{l}_{16}$ respectively, and similarly for $\hat{\sigma}$ with respect to $\hat{\mathbf{l}}_4$ and $\hat{\mathbf{l}}_{16}$ on transformed data.

With these definitions in place, it was found that the relative shift ($\Delta\hat{T}$) after transforming rotor speed values was around 40% larger than that obtained using the original data (ΔT), indicating a significant improvement in sensitivity which could in turn allow for earlier or more reliable detection of impending MB failures. In practise, more sophisticated methods than straight line fits would be used to detect faults. However, the analysis presented here highlights the potential benefits of either pre-processing as outlined, or ensuring such effects are accounted for in learning methodologies.

While correlation can be maximised with a large enough averaging window and no lag, it is also worth considering the possible information revealed when a shorter averaging window is applied, such that non-zero optimal lag values (for the chosen value of N) are obtained. Considering the degrading internal conditions of a failing MB, which in turn lead to higher frictional forces, and so the higher temperatures observed in Figs. 17-19, it would be reasonable to expect rougher surfaces and the presence of metallic debris to also effect the rate at which temperature responds to changes in speed (or load).

The lag applied above can in fact be interpreted as an estimate of the rate at which bearing temperature responds to changes in rotor speed, an estimate learned from the data itself.

Optimal lag values were therefore investigated, using intermediate values of N, in order to ascertain whether a reduction in $\hat{t}_{\text{opt}}$ values tends to occur as the bearing moves closer to failure. On average, this was found to be the case; for example, Fig. 24 shows distributions of daily optimal lag values from the first and last five months of data using an averaging window of $N = 10$. Dashed lines show the average of optimal lag values in

each case. Both with respect to the distributions themselves and their average values, a shift towards the left is evident for the data taken from closer to failure. This in turn implies that optimal lag might itself constitute a useful learning feature to be tracked and fed to fault detection algorithms.

The transformation process outlined in this Chapter can also be applied to power and wind speed signals with similar results. Overall the highest correlations were found to exist in the rotor speed case.

3.3 Discussion

In this study, data from an outer race MB failure was analysed. Results of the SCADA data analysis (Chapter 3.2) indicated that, as expected and in agreement with other studies [101], temperature trends increased as the bearing moved closer to failure (Fig. 23), reflecting increased frictional effects in the system.

However, some subtleties associated with the data were also investigated, with findings indicating that thermal inertia effects should be considered when developing fault detection models. It was further demonstrated that improved relationships between key variables can be obtained by pre-processing measured data to artificially incorporate inertial effects. Such pre-processing procedures might therefore be incorporated into fault detection algorithms in order to improve sensitivities. Alternatively, results could be interpreted as providing insight as to the types of features necessary for inclusion in learning models (removing the need for the data itself to be manipulated outwith the learning procedure). Explicitly, features should be included that allow for inertial type effects to be accounted for, such as smoothed measurements and lags of measured values. The choice between pre-processing or feature-level inclusion of these effects will largely depend on sophistication of the chosen fault detection methodology.

It is also worth noting that while average based smoothing and time shifting of signals has been commonly used to 'clean' data prior to learning in the past, the current study indicates that this step could provide more than just improved input-output correlations.

As shown in Chapter 3.2.2, optimal lags were found to reduce in mean values closer to failure, indicating they may form a useful additional learning feature in their own right. More generally, this could be extended to the use of other measures of system inertia for monitoring of MB health. This suggests that, whilst MB temperature itself is certainly a key indicator of system health, other measurable properties are present which shouldn't be overlooked.

3.4 Conclusions

In this study SCADA datasets were analysed with regards to their fault detection potential on an example of a wind turbine outer raceway fault. It was found that thermal inertia present in the system warranted specific consideration, with changes in inertia associated time-lags potentially offering a new learning variable.

Failure could alternatively be predicted if the fundamental mechanism of failure was understood, and could be modelled. Given that temperature has been found in this Chapter to be inherently linked to failure, this indicates that frictional effects play a

role (increased friction, increased temperature). As it is not currently known what the primary failure modes are, the presence of frictional effects motivates consideration of whether they might also drive this failure process. This will now done in the next Chapter.

4 Macroslip Model

The previous Chapter prompted a consideration of frictional effects. Therefore, in this Chapter, a dynamic model is proposed for the main bearing, considering EHL theory, gyroscopic effects, roller cage interactions, and slip. The first step of the model is to use a quasi-static solver to calculate internal roller load distribution under an applied radial and axial load for the double row-spherical bearing. From this, tractive forces may be found, which can be used to solve the rotational equations of motion and analyse slip.

4.1 Introduction

Slip, the presence of relative motion at contacting surfaces, can be a driver for a number of damage mechanisms in rolling element bearings, as covered in Chapter 2.

Slip may occur at a micro-level, as a result of contact geometries under load, or at a macro-level, as a result of system dynamics. The focus of the current Chapter is dynamically induced macroslip.

Macroslip can be broken into two subcomponents. *Cage slip* refers to instances where macroslip is such that the full rolling element set orbits the bearing centre at a speed which differs from that of pure rolling (therefore resulting in a cage speed which also differs). Macro-level individual *roller slip* also occurs, in addition to cage slip, as rollers enter and exit the loaded zone [48] or are otherwise affected by changes in system loading and speed. It is currently understood that individual roller slip can still occur in the absence of cage slip.

A recent study investigated cage slip in the main bearing of an operational wind turbine as a possible contributor to premature failures [102]. The analysis, using up-tower measurements, concluded that levels of cage slip appeared negligible, likely as a result of high loads and single-cage design between bearing rows, but it was emphasised that individual roller slip may still be present. The current Chapter seeks to build on this previous work by investigating individual roller macroslip in a wind turbine main bearing under realistic operating conditions, in which rapid variations in main bearing load magnitudes and directions are known to occur [12]. In order to computationally analyse this phenomenon, it is necessary to first develop an appropriate dynamic model. As will be described, this transpired to be a non-trivial problem. A detailed model derivation, along with careful treatment of some subtleties which arose, is therefore the initial focus of this Chapter. Results under realistic wind turbine operating conditions are then presented and discussed.

4.2 Quasi-Static Roller Loads

For solving roller normal load distribution around the bearing that is subsequently used to inform dynamic components, a *quasi-static* solver was developed from [12]. This assumes applied shaft loads at a given time-step are balanced by total reaction loads from the roller. As this quasi-static component is used in making roller load assessments through all subsequent investigations of frictional effects (Chapters 3, 4, 5), it is now covered in some detail.

The formulation used in the relevant study [12] is not suitable for dynamic extension, due to the continuous nature of roller distribution. Therefore, a different discrete quasi-static model was created, which can be fully and properly applied to dynamic cases. Initially, a single row is explored, prior to the double-row form, but much of the following is taken from [12].

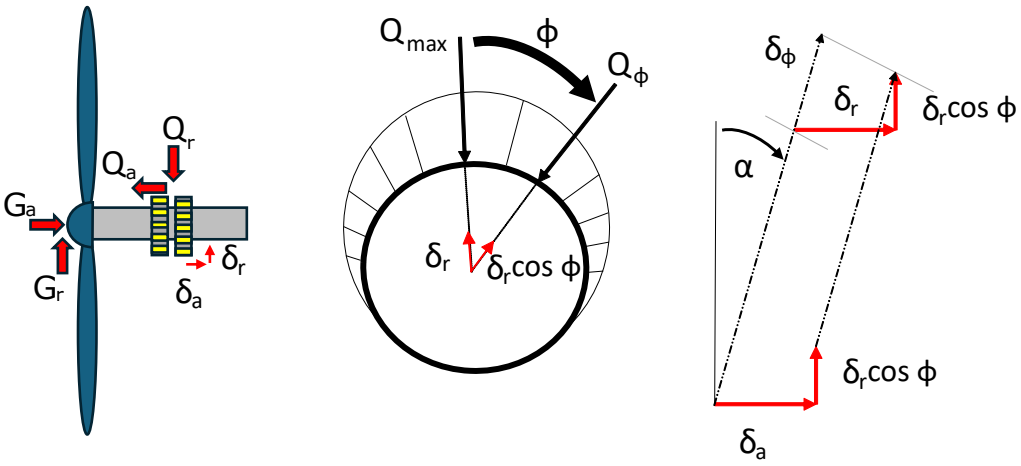

Figure 25: Quasi-static forces and deflections on the MB.

Displacement geometries are given as per Fig. 25, depicting a deflection on a single row of rollers.

These deflections are defined by δ_ϕ, at an angle ϕ around the bearing circumference:

$$\delta_\phi = \delta_{\max}\left(1 - \frac{1}{2}\epsilon(1-\cos\phi)\right) \tag{15}$$

with maximum deflection being given by (at $\phi = 0$):

$$\delta_{\max} = \delta_a \sin\alpha + \delta_r \cos\alpha \tag{16}$$

And where:

$$\epsilon_\phi = \frac{1}{2}\left(1 + \frac{\delta_a \tan\alpha}{\delta_r}\right) \tag{17}$$

is the fraction of the circumference under load. With the roller trapped between the two raceways, it can be treated as a compression-only non-linear spring of form:

$$Q = K_{\text{tot}}\delta^{3/2} \tag{18}$$

where K_{tot} is the combined stiffness of both the inner and outer raceway roller interactions.

Thus, the reaction force (Q) at the angle ϕ takes the form:

$$Q_\phi = Q_{\max}\left(1 - \frac{1}{2}\epsilon(1-\cos\phi)\right)^{3/2} \tag{19}$$

And then this given reaction force can be decomposed into radial and axial components:

$$Q_\phi^r = Q_\phi \cos\phi\cos\alpha, \quad Q_\phi^a = Q_\phi \sin\alpha \tag{20}$$

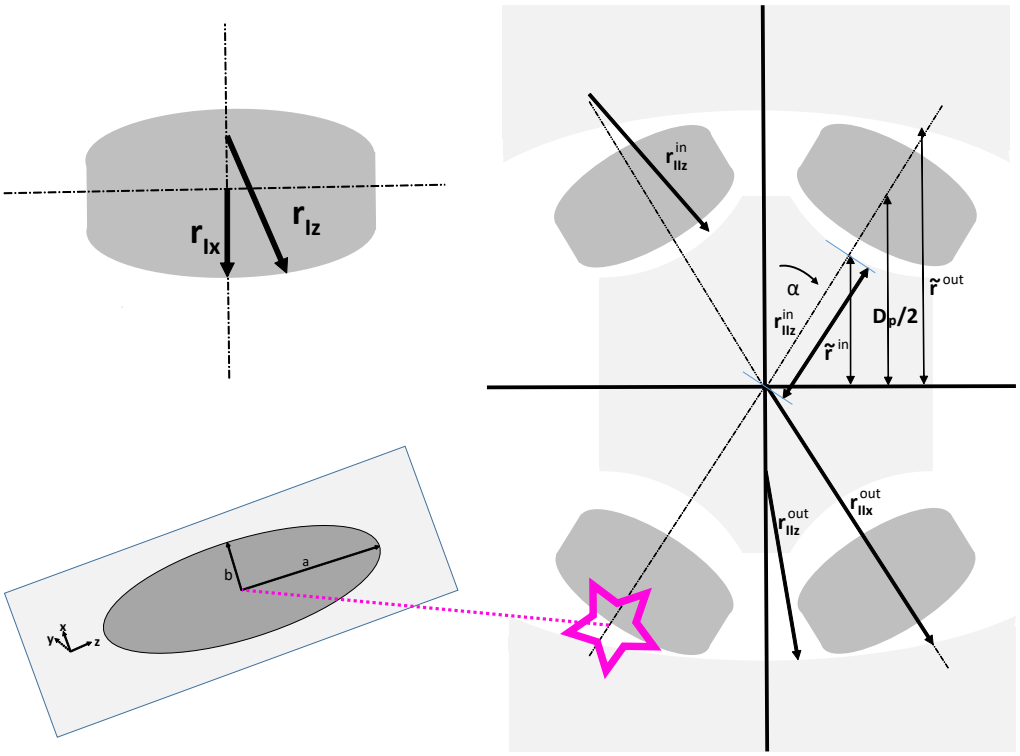

Figure 26: Internal geometry of a spherical roller bearing with accompanying parameters. Two contacting interface produces a contact patch, by Hertzian theory.

By definition of a compression-only spring, any rollers that are outside the roots of Eq. (19), or a limiting angle of:

$$\phi_l = \cos^{-1}\left(-\frac{\delta_a \tan\alpha}{\delta_r}\right) \tag{21}$$

do not supply any reaction force to the bearing.

Therefore, reaction force per roller at any angle of ϕ has been deduced. Hence as there is now an equation where reaction loads are a function of shaft displacement, δ_r and δ_a, reaction can be found for any given applied, axial G_a, and radial G_r, loads; the system is assumed to be at equilibrium. In this case, the problem is reduced to finding values of δ_a and δ_r that minimise:

$$(G_r - Q_r)^2 + (G_a - Q_a)^2 = 0 \tag{22}$$

4.2.1 Double Row Case

When this argument is extended to the double row case, the upstream and downstream rows need to be distinguished between each other, done here by subscripts 1 for upwind/rotor side row and 2 for downwind/generator side row. From Fig. 26 by inspection:

$$\delta_{r1} = \delta_{r2} = \delta_r \tag{23}$$

$$-\delta_{a1} = \delta_{a2} = \delta_a \tag{24}$$

The same procedure can be applied within each row such that the subsequent radial and axial reaction forces ($Q_{r1}, Q_{r2}, Q_{a1}, Q_{a2}$) may be deduced from defined shaft displacements (δ_r and δ_a). Total axial and radial reactions then take the form:

$$Q_r = Q_{r1} + Q_{r2} \tag{25}$$

$$Q_a = Q_{a2} - Q_{a1} \tag{26}$$

As total reaction forces can be evaluated, the same root-finding formulation may be implemented as in Eq.[22], to find the displacements that minimize the system and thus total reaction forces per roller. All that remains to determine the numerical values of these loads is to arrive at values of the spring constant K.

4.2.2 Interface Spring Constant

A curved surface S with radius r, has a scalar curvature value associated with it, given by:

$$\zeta_s = \text{sign}(S)\frac{1}{r} \tag{27}$$

where sign(S) is 1 and -1 for convex and concave surfaces respectively. This gives for two surfaces (I) and (II) in contact during revolution a total curvature sum of:

$$\sum \zeta = \zeta_{Iz} + \zeta_{Ix} + \zeta_{IIz} + \zeta_{IIx} \tag{28}$$

and a curvature difference of:

$$F_\zeta = \frac{(\zeta_{Ix} - \zeta_{Iz}) + (\zeta_{IIx} - \zeta_{IIz})}{\sum \zeta} \tag{29}$$

where the principal axes are x and z, and chosen such that curvature difference is a positive quantity. This is calculated with the internal geometry of a SRB given by Fig. 26. D_p is pitch diameter, r_{1x} roller radius, and $r_{1z}, r^{\text{in}}_{IIz}, r^{\text{out}}_{IIz}$ are contour radii. Other terms are calculated as:

$$r^{\text{in}}_{IIx} = \frac{D_p}{2\cos\alpha} - r_{Ix} \tag{30}$$

$$r_{IIx}^{\text{out}} = \frac{D_p}{2\cos\alpha} + r_{Ix} \tag{31}$$

$$\tilde{r}^{\text{in}} = r_{IIz}^{\text{in}} \cos\alpha \tag{32}$$

$$\tilde{r}^{\text{out}} = r_{IIz}^{\text{out}} \cos\alpha \tag{33}$$

under the assumption that the bearing clearance is zero. Numerical values for all and other bearing geometrical values are all available in Appendix A.

The combined metrics of curvature sum and differences permit the system to be treated as an ellipsoid-plane contact, by *Hertzian contact theory*.

Hertzian Contact Mechanics

Hertzian contact mechanics describes the stress and deformation of two elastic bodies in contact. Governing assumptions are [103, 104, 105]:

1. Strains are small and within the elastic limit.
2. Contacting surfaces are assumed frictionless.
3. The area of contact is much smaller than the dimensions of the contacting bodies.
4. Each body can be considered as an infinite homogenous *elastic half space*.

The results are a set of simple analytical equations, with the following being relevant for an elliptical contact:
Pressure distribution

$$p(x,z) = p_0\sqrt{1 - \frac{x^2}{b^2} - \frac{z^2}{a^2}} \tag{34}$$

Max Pressure

$$p_0 = \frac{3F}{2\pi ab} \tag{35}$$

Semi major ellipse dimension

$$a = \left(\frac{6\kappa^2 F\mathcal{E}}{\pi\sum_\zeta E'}\right)^{1/3} \tag{36}$$

Semi minor ellipse dimension

$$b = \left(\frac{6F\mathcal{E}}{\pi\kappa\sum_\zeta E'}\right)^{1/3} \tag{37}$$

with κ, the ellipticity parameter:

$$\kappa = a/b \tag{38}$$

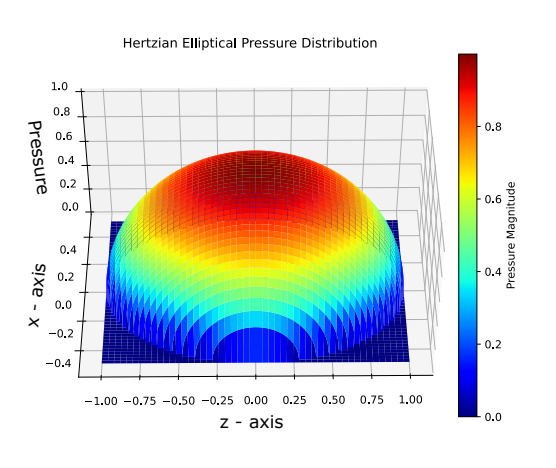

Using Hertzian theory, the ellipticity parameter, κ, can be used to find the spring constant in:

$$Q = \underbrace{\left(\frac{\sqrt{2}\pi E}{3(1-\nu^2)}\kappa\sqrt{\frac{\mathcal{E}}{\mathcal{F}(\kappa)^3\sum_\zeta}}\right)}_{K=\text{spring contact stiffness}}\delta^{3/2} \tag{39}$$

where $\mathcal{F}(\kappa)$ and $\mathcal{E}(\kappa)$ denote *elliptical integrals* of the first and second kind, respectively.

This relationship models a single contacting interface of two elastically identical bodies as a nonlinear compression-only spring.

When bearing material specific values are used, summarised by the following table:

Property	Value
Young's modulus E	2.05×10^{11} Pa
Reduced Elastic modulus E'	2.55×10^{11} Pa
Poisson's ratio ν	0.3
Material	Steel

Table 6: Material Properties for Hertzian Contact Analysis

K simplifies to:

$$K \approx 3.336 \times 10^{11}\kappa\frac{\sqrt{\mathcal{E}(\kappa)}}{\mathcal{F}(\kappa)^3\sum\zeta} \tag{40}$$

-resulting in a calculation solely involving κ.

However, resolving elliptical integrals is an expensive implicit calculation, typically requiring costly methods such as Gauss-Legendre quadrature [106]. This would be an impractical repeat calculation in a time series analysis.

To avoid this issue, an empirical explicit formulation presented by Antoine et al. was used [107], achieving at least 0.003% precision within the range $1 \leq \kappa < 10^{10}$.Other approximations exist, but they perform well only in the range $1 \leq \kappa \leq 10$, which wouldn't suffice in the specific WTMB case here, where $\kappa \approx 40$.

The Hertzian elliptical integrals were shown to be computed as:

$$\mathcal{F}(\kappa) = (\lambda_0 + \lambda_1\kappa^{-2} + \lambda_2\kappa^{-4}) - \ln[\kappa^{-2}](\lambda_3 + \lambda_4\kappa^{-2} + \lambda_5\kappa^{-4}) \tag{41}$$

$$\mathcal{E}(\kappa) = (\beta_0 + \beta_1\kappa^{-2} + \beta_2\kappa^{-4}) - \ln[\kappa^{-2}](\beta_3 + \beta_4\kappa^{-4}) \tag{42}$$

And by defining a new variable X as:

$$X = \frac{1+F_\zeta}{1-F_\zeta} \tag{43}$$

Antoine et. al showed κ can be well approximated as:

$$\kappa(X) = X^{\text{sign}(F_\zeta)\varsigma(\log_{10}X)} \tag{44}$$

with:

$$\varsigma(x) = \frac{2}{3}\left(\frac{1+\mu_1x^2+\mu_2x^4+\mu_3x^6+\mu_4x^8}{1+\mu_5x^2+\mu_6x^4+\mu_7x^6+\mu_8x^8}\right) \tag{45}$$

All coefficients are given in Appendix B for ease of access, taken from [107]. This methodology was used to perform the Hertzian contact analysis.

With the individual roller raceway interface spring constant thus arrived at, now a total spring constant K_{tot} for the combined inner and outer raceway interaction needs to be found. If each interaction is treated like a spring, and the roller becomes a series of two non-linear springs, the forces inside the series must be equal throughout:

$$K_i \delta_i^{3/2} = K_o \delta_o^{3/2} = K_{\text{tot}} (\delta_i + \delta_o)^{3/2} \tag{46}$$

Thus, the combined spring constant of both inner and outer raceway interfaces—i.e., an isolated roller as a whole—is found by rearranging:

$$K_{\text{tot}} = \left(\left(\frac{1}{K_i} \right)^{2/3} + \left(\frac{1}{K_o} \right)^{2/3} \right)^{-3/2} \tag{47}$$

This is then used to inform Eq [46], and thus Eq.[22] may be solved.

It was also found the Quasi-static solver here performed better than the continuous version presented in [12], with the loading zones less narrow in the continuous version due to a spatial averaging effect. The discrete representation here is a more realistic representation of roller loads.

We are now at the point where given input time series shaft loads, axial and radial, individual roller loads may be determined. This was used in all subsequent analysis, that we will now begin.

4.3 Newtonian Dynamic Macroslip Model

The previous Subchapter determined roller loads. These can now be used to determine the tractive forces acting on the roller to solve roller trajectories, and also to determine frictional metrics from slip. This was done initially via a *Newtonian* framework - the standard method in bearing engineering.

Therefore, roller orbital dynamics in the developed model will be captured using rigid-body equations of motion. Note, this approximation is applied only with respect to the dynamic equations themselves. In contrast, all load and contact evaluation aspects of the model do incorporate elastic deflections using Hertzian theory (see Chapter 4.3.6). Since the elastic deformations occurring in such bearings are several orders of magnitude less than the geometric dimensions which determine inertia and momentum, the rigid-body approximation in the context of dynamic equations is valid

4.3.1 General equations of motion for the rotation of a rigid body

The fundamental equation of motion governing the rotation of a rigid body is,

$$\sum_i \mathbf{m}_i = \frac{d\mathbf{l}}{dt}, \tag{48}$$

where the $\mathbf{m}_i$ are moments and $\mathbf{l}$ is the body's angular momentum (both vector quantities). However, this is the case only in an *inertial* frame of reference. As will be seen, it can often be beneficial to express $\mathbf{l}$ in a reference frame whose orientation changes over time, *i.e.* a rotating (*non-inertial*) reference frame. In such cases, the time-rate-of-change of the reference frame basis vectors must be taken into account. The body's angular momentum, $\mathbf{l}$, is the product of its 3×3 moment of inertia tensor, $\mathbf{I}$, with its angular velocity vector, $\boldsymbol{\omega}$. In a non-rotating frame, $\mathbf{I}$ will in general be non-diagonal and time dependent.

If, instead, the reference frame rotates such that its axes maintain the same alignment with respect to the body's mass distribution throughout, $\mathbf{I}$ (as observed in the rotating frame) remains constant. If, in addition, this alignment coincides with the body's principal axes of inertia, $\mathbf{I}$ will also be diagonal here, $\mathbf{I} = \mathbf{I}_p$. Let $\boldsymbol{\gamma}$ denote a choice of reference frame angular velocity which achieves both of these outcomes. It can be shown that:

$$\frac{d\mathbf{l}}{dt} = I_p \left(\frac{d\boldsymbol{\omega}}{dt} - \boldsymbol{\gamma} \times \boldsymbol{\omega} \right) + \quad \boldsymbol{\gamma} \times \mathbf{l}. \tag{49}$$

Expressing all vector/tensor quantities in the inertial (non-rotating) reference frame which has the same orientation as the rotating frame at each given instant in time (in this orientation $\mathbf{I} = \mathbf{I}_p$):

$$\mathbf{m}_i = \begin{bmatrix} m_{i,1} \\ m_{i,2} \\ m_{i,3} \end{bmatrix}, \quad \boldsymbol{\omega} = \begin{bmatrix} \omega_1 \\ \omega_2 \\ \omega_3 \end{bmatrix}, \quad \frac{d\boldsymbol{\omega}}{dt} = \begin{bmatrix} \dot{\omega}_1 \\ \dot{\omega}_2 \\ \dot{\omega}_3 \end{bmatrix}, \quad \boldsymbol{\gamma} = \begin{bmatrix} \gamma_1 \\ \gamma_2 \\ \gamma_3 \end{bmatrix}, \quad \mathbf{l} = \mathbf{I}_p \boldsymbol{\omega} = \begin{bmatrix} I_1 \omega_1 \\ I_2 \omega_2 \\ I_3 \omega_3 \end{bmatrix}. \tag{50}$$

Combining Eqs [48] and [49], the equations of motion for rigid body rotation under these circumstances are therefore:

$$\sum_i m_{1,i} = I_1 \dot{\omega}_1 - I_2 \gamma_3 \omega_2 + I_3 \gamma_2 \omega_3 - I_1 \left[\boldsymbol{\gamma} \times \boldsymbol{\omega} \right]_1 \tag{51}$$

$$\sum_i m_{2,i} = I_2 \dot{\omega}_2 - I_3 \gamma_1 \omega_3 + I_1 \gamma_3 \omega_1 - I_2 \left[\boldsymbol{\gamma} \times \boldsymbol{\omega} \right]_2 \tag{52}$$

$$\sum_i m_{3,i} = I_3 \dot{\omega}_3 - I_1 \gamma_2 \omega_1 + I_2 \gamma_1 \omega_2 - I_3 \left[\boldsymbol{\gamma} \times \boldsymbol{\omega} \right]_3 . \tag{53}$$

A suitable rotating frame can be obtained by fixing the frame in the rigid body so they rotate together in all dimensions. In such cases $\boldsymbol{\gamma} = \boldsymbol{\omega}$, $\boldsymbol{\gamma} \times \boldsymbol{\omega} = \boldsymbol{\omega} \times \boldsymbol{\omega} = 0$, and Eqs [51,53] reduce to the well-known *Euler's equations* of rigid body rotation. However, in the current problem, it transpires that it is convenient to define a rotating frame for which $\boldsymbol{\gamma} \neq \boldsymbol{\omega}$.

4.3.2 Angular momentum decomposition and the parallel axis theorem

The angular momentum, $\mathbf{l}$, of a rigid body with respect to the origin, $\mathcal{O}$, of an inertial reference frame may be shown to decompose as follows [108]:

$$\mathbf{l} = \mathbf{l}_{\mathrm{CoM}} + \tilde{\mathbf{l}}, \tag{54}$$

where $\mathbf{l}_{\mathrm{CoM}}$ is the angular momentum of the body's centre of mass (CoM) relative to $\mathcal{O}$[2], and $\tilde{\mathbf{l}}$ is the angular momentum of the rigid body relative to its COM. Consider the

[2]More specifically, $\mathbf{l}_{\mathrm{CoM}}$ is the angular momentum (relative to $\mathcal{O}$) of a point mass with mass equal to that of the rigid body, and with position and velocity equal to the body CoM at each point in time.

simple case of rotation within a single plane, where an object (of mass M and in-plane moment of inertia $\mathbf{I}$ about its CoM) spins about its own CoM with angular velocity $\boldsymbol{\omega}$, while orbiting the stationary system origin (at a distance R) with angular velocity $\boldsymbol{\Omega}$. The above decomposition in this instance becomes:

$$\mathbf{l} = MR^2\boldsymbol{\Omega} + \mathbf{I}\omega \tag{55}$$

A related result is the *parallel axis theorem*. This states that the moment of inertia of a rigid body about a given axis is equal to the sum of (1) its moment of inertia about the parallel axis which passes through the body's COM, and (2) the product of the body's mass and the square of the distance between parallel axes [108]. For the simple case considered above, the parallel axis theorem gives:

$$\mathbf{I}_{\mathcal{O}} = MR^2 + \mathbf{I}. \tag{56}$$

This theorem deals with strict rigid-body rotation about the given axis, the implication being that for a parallel axis located outside of the body, the body maintains its initial orientation with respect to the origin at all times[3]. In cases where this occurs, the parallel axis theorem actually follows as a specific case of Eq. [55], since one may easily show that $\boldsymbol{\omega} = \boldsymbol{\Omega}$ here. Crucially, the parallel axis theorem is not applicable in more general cases where the orbiting body may experience $\boldsymbol{\omega} \neq \boldsymbol{\Omega}$. In such instances the general form, Eq. [54] or [55], must be used.

4.3.3 Modelling of Bearing slip in the literature

Much work on the modelling and analysis of slip in roller bearings has been undertaken in the literature [26, 63, 64, 27, 65, 66]. This is usually in the context of gross slip (also referred to as cage slip). Particularly relevant to the current work is [26], where an efficient model is presented for the purposes of studying ball-bearing slip behaviour in wind turbine gearboxes. The current modelling work is broadly based on [26].

A drawback of the model used in [26] is the use of the parallel axis theorem, to arrive at the differential equation governing ball-bearing orbital speeds, since this theorem does not apply to bearing balls or rollers which themselves have independent velocity components about an axis parallel to which that they are orbiting (see Chapter 4.3.2). It thus appears that the true angular momentum in the system was not accounted for. The formulation used in [26] allows orbital motion and roller spin to be *decoupled*, greatly simplifying the solving process. However, considering the total system angular momentum (Eqs . [54] or [55]) reveals that these quantities are in fact part of a *coupled system*.

[3] An example of such an orbit being that of the tidally locked moon.

Coupled Systems

Coupling refers to a system of equations, having components interacting with each other. For example in a simple linear system:

$$\frac{dy_1}{dt} = k_1 y_1 + k_2 y_2 \tag{57}$$

$$\frac{dy_2}{dt} = k_3 y_1 + k_4 y_2 \tag{58}$$

Each component y_1, y_2 will effect each other's evolution in time, and solving $\frac{dy_1}{dt}$ and $\frac{dy_2}{dt}$ will need consideration of this. The act of decoupling, and solving each component independently, i.e:

$$\frac{dy_1}{dt} = k_1 y_1 \tag{59}$$

$$\frac{dy_2}{dt} = k_4 y_2 \tag{60}$$

would be an incorrect description of the system. However, in practice if $k_2 \ll k_1$ and $k_3 \ll k_4$, coupling may be negligible, and the simplification may offer an accurate approximation of the system's behaviour. Since k_i have no time dependency, the coupling is static.

Similar issues related to system angular momentum characterisation and the coupling/ decoupling of orbit and spin appears to be widespread in literature, and is present in a number of studies [63, 64, 27, 65]. Further, it appears this error has been carried forward to at least one existing example of commercial software. Whilst these comments on coupling may appear philosophical, with little relevance to the current application, they are important observations, as a decoupled approximation of a coupled system, may not be a good representation of true system behaviour depending on coupling strength (see coupled systems callout). Further work will be conducted to investigate the extent of this coupling, and the relevant importance of it in WTMB simulations.

4.3.4 Numerical Integration

The dynamic equations to be integrated in this work are second order. Such equations may be reformulated as a system of first order differential equations for solving. Such systems are of the form:

$$\frac{d\mathbf{y}}{dt} = f(\mathbf{y}, t). \tag{61}$$

Integration may then be undertaken using any of a variety of numerical procedures of varying complexities, stabilities and accuracies. With respect to stability, if a system of ordinary differential equations is *"stiff"* [109], explicit methods of integration are unstable unless the time-step is made prohibitively small (Fig. 27). In such cases, an implicit method must be used. The most basic numerical integrators falling into each category are the (explicit) Euler method:

$$\mathbf{y}(t + dt) = \mathbf{y}(t) + dt \cdot f(\mathbf{y}(t), t), \tag{62}$$

and (implicit) backward Euler method:

$$\mathbf{y}(t + dt) = \mathbf{y}(t) + dt \cdot f(\mathbf{y}(t + dt), t + dt). \tag{63}$$

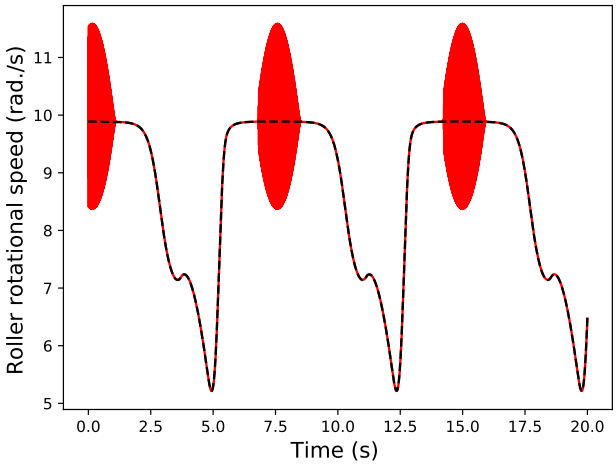

Figure 27: Example of instability in the highly loaded zone when using Euler's method (red). Backward Euler (black) can be seen to avoid this instability issue. This issue is not widely reported in the literature, and may be specific to the WTMB.

In backward Euler, $\mathbf{y}(t + dt)$ appears on both sides of the equation. As such, each integration step requires an additional numerical procedure to solve for the $\mathbf{y}(t + dt)$ which satisfies Eq. (63). Improved stability therefore comes at a computational cost. Numerical stiffness issues don't appear to be greatly reported in the literature, with the author only finding its brief mentioning in an discussion between Pirvics and Gupta [61] on the latter's recent paper. This phenomena's absence is likely due to the novelty of the application and associated very high loads. However, stiffness posed challenges throughout this investigation.

4.3.5 Equations of motion for a spherical roller bearing

Reference frames used in the current work are shown in Fig. 28. The bearing-centre frame is denoted by X_0, Y_0, Z_0. Roller-centric frames are denoted by x, y, z. Subscript "0" (e.g. x_0) indicates axes which translate with the roller centre, but which do not rotate and so maintain their initial orientation with the bearing-centre axes. The x, y, z axes (no sub- or super-scripts) translate with the roller centre, while also rotating such that the y-axis remains aligned with the line from the bearing centreline to the centre of the roller. Primed axes (e.g. y', y'_0) are obtained from their un-primed counterparts by applying a rotation of α (the bearing contact angle) about the corresponding x-axis (x or x_0).

Assuming no skewing or tilting of rollers occurs, and approximating the contact angle as remaining constant, a constant and diagonal moment of inertia tensor is seen in the described (rotating) x', y', z' frame. Note, a rotating frame is necessary to achieve this, as demonstrated by the changing mass distribution observable in the x'_0, y'_0, z'_0 frame (see Fig. 28c) as the roller orbits the bearing centreline. Other notation is as follows: $\boldsymbol{\omega}$ (appropriately sub-scripted) will denote roller angular velocity in the various x, y, z frames. $\boldsymbol{\gamma}$ will denote the angular velocity of the roller-centric rotating frame in the various x, y, z frames. $\boldsymbol{\Omega} = [0, 0, \Omega_{Z0}]^T$ will denote the orbital angular velocity of the

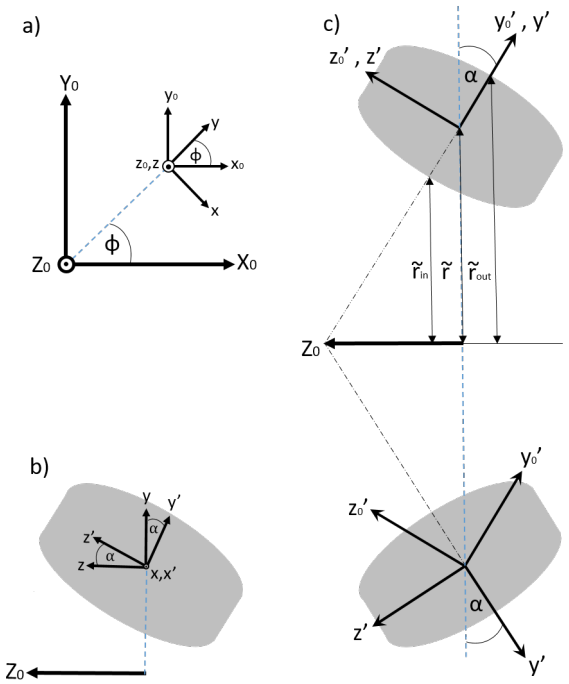

Figure 28: Spherical roller bearing reference frames shown for a single row and roller.

roller centre in the X_0, Y_0, Z_0 frame.

Each roller in the bearing will rotate about its own centre, whilst also orbiting the bearing centreline. The roller is assumed to rotate freely (subject to moments in the system) only about z', and the roller centre is assumed to rotate only about Z_0. The radius of orbit is assumed to remain constant throughout, as is the contact angle α. From the orientation described for the x, y, z frame, it follows that this frame is rotating with angular velocity $\boldsymbol{\gamma}_{xyz} = [0, 0, \Omega_{Z_0}]^T$. It follows that the x', y', z' frame is rotating with angular velocity $\boldsymbol{\gamma}_{x'y'z'} = [0, -\sin\alpha\, \Omega_{Z_0}, \cos\alpha\, \Omega_{Z_0}]^T$. Approximating the roller as a cylinder, the diagonal moment of inertia tensor in this frame is:

$$I_{x'y'z'} = \begin{bmatrix} \frac{1}{4}MR^2 + \frac{1}{12}ML^2 & 0 & 0 \\ 0 & \frac{1}{4}MR^2 + \frac{1}{12}ML^2 & 0 \\ 0 & 0 & \frac{1}{2}MR^2 \end{bmatrix}, \tag{64}$$

where M is roller mass, R is the roller centreline radius and L is roller length. For roller slip analysis, $\omega_{z'}$ is the critical angular velocity component. Since off-design skew and tilt are both assumed not to occur, the roller angular velocity components $\omega_{x'}$ and $\omega_{y'}$ are pre-determined, since they each must be such that the roller follows its design trajectory and orientation while orbiting the bearing centreline. Since the roller experiences a constant contact angle, α, it follows that $\omega_{x'} = 0$ throughout. $\omega_{y'}$ is non-zero, and a function of Ω_{Z_0} and bearing geometry. But, as will be shown, turns out not $\omega_{y'}$ is not needed. Since $\omega_{x'}$ and $\omega_{y'}$ may be considered known, only a single differential

equation must be solved, that of $\omega_{z'}$- Eq. (53). It has been shown that:

$$\boldsymbol{\omega}_{x'y'z'} = \begin{bmatrix} 0 \\ \omega_{y'} \\ \omega_{z'} \end{bmatrix} \quad \text{and} \quad \boldsymbol{\gamma}_{x'y'z'} = \begin{bmatrix} 0 \\ -\sin\alpha\ \Omega_{Z_0} \\ \cos\alpha\ \Omega_{Z_0} \end{bmatrix}, \tag{65}$$

hence:

$$I_{x'x'}\gamma_{y'}\omega_{x'} = I_{y'y'}\Gamma_{x'}\omega_{y'} = I_{z'z'}\left[\boldsymbol{\gamma}_{x'y'z'} \times \boldsymbol{\omega}_{x'y'z'}\right]_{z'} = 0. \tag{66}$$

The roller-centric differential equation to be solved in this case is therefore much simplified,

$$\sum_i m_{z',i} = I_{z'z'}\dot{\omega}_{z'}. \tag{67}$$

Note, whilst this equation initially appears to be independent of the roller orbital speed, Ω_{Z_0}, and the inner-raceway/shaft angular velocity, Ω_{in}, both quantities will influence $\omega_{z'}$ values through the moments acting on the roller. This will be shown explicitly in a later Subchapter. The roller's orbital motion about the bearing centreline, Ω_{Z_0}, is governed by a second differential equation, obtained using Eq. (55) and roller velocity projections onto the z-axis. This takes the form:

$$\sum_i m_{Z_0,i} = MR^2\dot{\Omega}_{Z_0} + I_{zz}\big(\cos(\alpha)\dot{\omega}_{z'} - \sin(\alpha)\dot{\omega}_{y'}\big), \tag{68}$$

where I_{zz} is the lower diagonal element of $I_{x'y'z'}$ after transformation (using rotation matrices) to the x, y, z frame. Eq. (68) shows explicitly the coupling between "roller orbit" and "roller spin" components.

4.3.6 Moments acting on a roller

Integrating rotational equations of motion requires the moments acting on the system to be resolved at each timestep. Bearing roller moments are caused by tractive/friction forces which result from normal forces at roller/raceway and roller/cage contacts. The various forces acting on the roller are shown in Fig. 29. These are as follows:

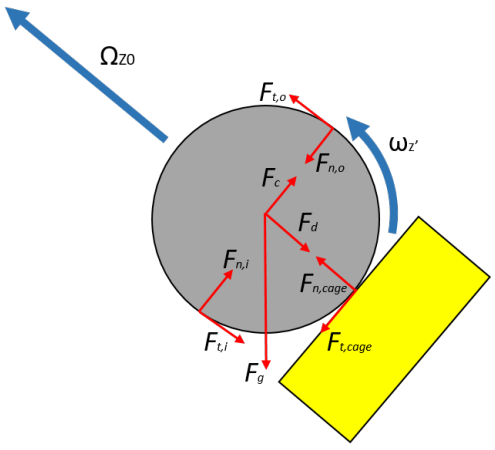

Figure 29: Forces acting on an individual roller.

1. Gravitational force, $\mathbf{f}_g$. In the roller frame,

$$f_{g,x'} = mg\cos\phi \tag{69}$$
$$f_{g,y'} = -mg\cos\alpha\sin\phi \tag{70}$$
$$f_{g,z'} = -mg\sin\alpha\sin\phi \tag{71}$$

where m is roller mass, g acceleration due to gravity, α the roller contact angle, and ϕ the roller orbital position (see Fig. 28).

2. Centrifugal force, $\mathbf{f}_c$. In the roller frame:

$$f_{c,x'} = 0 \tag{72}$$
$$f_{c,y'} = m\Omega_{Z_0}^2\tilde{r}\cos.\alpha \tag{73}$$
$$f_{c,z'} = m\Omega_{Z_0}^2\tilde{r}\sin\alpha, \tag{74}$$

where $\tilde{r}$ is the vertical height from the bearing centreline to the roller centre (see Fig. 28).

3. Fluid (lubricant) resistance drag, $\mathbf{f}_d$. In the roller frame:

$$f_{d,x'} = \mathrm{sign}(v)\frac{1}{2}\rho_{\mathrm{lub}}\epsilon_{\mathrm{fill}}v^2C_DA \tag{75}$$
$$f_{d,y'} = 0 \tag{76}$$
$$f_{d,z'} = 0, \tag{77}$$

where $v = \Omega_{Z_0}\tilde{r}$ is the roller tangential velocity in the bearing frame, ρ is lubricant density, $\epsilon = 0.7$ is a fill factor, A is the cross-sectional area of the roller, and C_D the drag coefficient (taken to be 1 based on approximate Reynolds numbers for the system).

4. Inner- and outer-raceway normal contact forces, $\mathbf{f}_{n,i}$ and $\mathbf{f}_{n,o}$, respectively. These forces consist of a y' component only, and are approximated as follows:

   (a) First a Hertzian contact model (essentially identical to that of [12], but containing discrete representations of rollers) of the bearing is used to perform a static load balance which determines the normal load on each roller required to balance the current bearing load;

   (b) Second, the magnitude of the unbalanced resultant y' body-force, $f_{g,y'} + f_{c,y'}$, is added to the appropriate raceway to balance all non-tractive forces along y'.

   Hertzian theory is then used to determine the resulting contact patch and pressure distribution, if present, at each contact location (required for traction force estimation).

5. The form of the cage normal force, $\mathbf{f}_{n,cage}$, will differ depending on the model implementation. In the current work, the normal cage force will be used to act as a "control" in the system since, ultimately, it will be assumed that it acts to balance all roller forces along x' (see Chapter 4.3.7). Similar to raceway normal forces, Hertzian theory is used to evaluate the contact patch and pressure distribution between roller and cage. The cage is assumed to conform to the roller with the same geometry as between roller and raceways in the lateral direction. In the rolling direction the cage is assumed to also conform to the roller with equal percentage conformity to that defined laterally. Note, in the applied formulation the cage tractive force represents an unbalanced y' force in the system, however, testing has revealed this unbalanced force to be acceptably small.

6. Elastohydrodynamic tractive forces ($\mathbf{f}_{t,i}$, $\mathbf{f}_{t,o}$, $\mathbf{f}_{t,cage}$) at inner raceway, outer raceway and cage contacts, respectively. These are generated from shearing of the lubricant film when slip is present which, in turn, results in surface-stress distributions over each contact patch. At the point (x'_p, z'_p) in a contact patch, the shear stress (τ_{yx}) in a Newtonian fluid separating the two surfaces may be approximated as [110]:

$$\tau_{yx}(x'_p, z'_p) = \frac{\eta(x'_p, z'_p)\Delta\dot{u}_x}{h_c}, \tag{78}$$

The viscosity (η) across the contact patch is affected by local pressure variation and frictional heating which results from lubricant shearing. A closed-form approximation of viscosity variations under these conditions was derived by Crook [110] and also applied in [26]:

$$\eta(x'_p, z'_p) = \eta_0 \exp\left[c_{\eta p} p(x'_p, z'_p)\right] \frac{\ln\left[\sqrt{\chi+1}+\sqrt{\chi}\right]}{\sqrt{\chi(\chi+1)}} \tag{79}$$

where p is the Hertzian pressure distribution $\Delta\dot{u}_x$,the slip speed, h_c central film thickness, and:

$$\chi = \eta_0 \exp[c_{\eta p} p(x', z')] c_{\eta T} \Delta\dot{u}_x^2/(8K_c) \tag{80}$$

with K_c being the lubricant thermal conductivity. Lubrication property values are summarised below. Other lubrication/bearing parameters match that of [31].

Property	**Symbol**	**Value**
Barus Law Pressure-Viscosity Coefficient	$c_{\eta p}$	21 GPa^{-1}
Temperature-Viscosity Coefficient	$c_{\eta T}$	0.04 $^{\circ}\mathrm{C}^{-1}$
Lubricant Thermal Conductivity	$\underline{K}_c$	0.125 $\mathrm{Jkg}^{-1}\mathrm{K}^{-1}$
Lubricant Specific Gravity	$\underline{\rho}_c$	0.9
Lubricant Contact-Inlet Temperature	T_{inlet}	35°C
Surface roughness	R_{rms}	300 nm

Table 7: Lubrication properties used in the analysis.

In this model (Fig. 30), h is assumed constant throughout the contact, as h_c. This was evaluated using an equivalent line contact representation [23, 31] and a central film thickness empirical formula which accounts for surface roughness [111]:

$$h = R_x \cdot 2.691 U^{0.705} G^{0.556} \cdot W_l^{-0.135} \left(1 + 0.2\left(\frac{R_{\mathrm{rms}}}{R_x}\right)^{1.222} \nu^{0.223} W_l^{-0.229} U^{-0.748} G^{-0.842}\right) \tag{81}$$

with dimensionless speed:

$$U = \frac{\eta_0 \cdot \dot{u}_{\mathrm{ent}x}}{E' \cdot R_x} \tag{82}$$

dimensionless load:

$$W_l = \frac{3F}{4a \cdot E' \cdot R_x} \tag{83}$$

and dimensionless material parameter:

$$G = E' \cdot c_p \tag{84}$$

where c_p is the inverse asymptotic isoviscous pressure coefficient (at the inlet temperature- $1/c_p = \int_0^\infty \frac{\eta_0}{\eta}\, dp$).

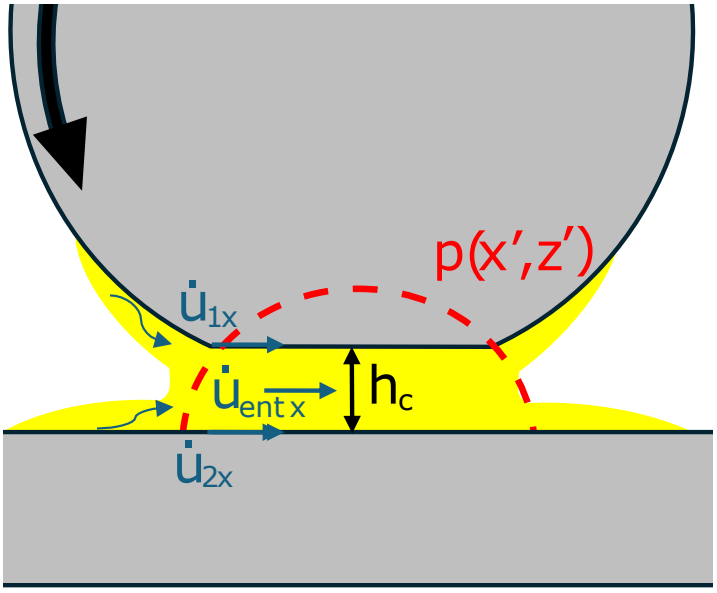

Figure 30: The lubrication model used to calculate tractive forces.

We denote roller and raceway/cage surface tangential velocities as $\dot{u}_{1x}$ and $\dot{u}_{2x}$, respectively. The above formulation requires both entrainment velocity, $\dot{u}_{\text{ent}x} = \frac{1}{2} \mid \dot{u}_{1x} + \dot{u}_{2x} \mid$, and slip speed, $\Delta\dot{u}_x = \dot{u}_{2x} - \dot{u}_{1x}$, to be evaluated at each contact. For convenience, surface tangential velocity expressions were identified such that positive slip values result in positive acceleration of the roller in its local frame, consequently, generating roller moments with the same sign as $\Delta\dot{u}_x$. These are:

$$u_{2,in} = -(\Omega_{in} - \Omega_{Z_0})\tilde{r}_{in} \quad (85)$$

$$u_{2,out} = (\Omega_{out} - \Omega_{Z_0})\tilde{r}_{out} \quad (86)$$

$$u_{2,cage} = 0 \quad (87)$$

$$u_{1,in} = u_{1,out} = u_{1,cage} = \omega_{z'} r. \quad (88)$$

r is the roller centreline radius. The bearing in question has a stationary outer-raceway, $\Omega_{out} = 0$.

Having calculated the traction forces as described above for each case, the moments acting on the roller at each point in time are $\mathbf{m}_{t,i} = R\mathbf{f}_{t,i}$, $\mathbf{m}_{t,o} = R\mathbf{f}_{t,o}$, and $\mathbf{m}_{t,cage} = R\mathbf{f}_{t,cage}$.

4.3.7 Model implementation

Previous sections highlight the complexity of dynamics for the entire system being considered, including the presence of coupled differential equations for $\omega_{z'}$ and Ω_{Z_0}. Results outlined in Chapter 4.1 indicate that some simplification may be possible, since it appears reasonable to assume roller orbital trajectories are maintained at that of pure rolling[4] via cage normal forces (neglecting clearance between cage spars and rollers).

[4]The benefit of this is that at "pure rolling" the orbital speeds becomes a simple function of shaft speed, similar to a gear-speed equation Eqs.[12, 31].

However, even then one would have to ensure that forces/moments are such that both Eqs. [67] and [68] remain satisfied throughout, a complicated task. Furthermore, under high loads which (locally) drive rollers at their pure-rolling speed, it has been found that governing differential equations become stiff, requiring an additional solving procedure at each time-step. Based on the above difficulties, which would require complex nested iterative solving to handle all aspects of the real-world problem, it was deemed sensible to first consider a simplified version of the system which is analogous, but not identical, to the original.

We therefore consider the case where rollers are subject to identical loading, contact geometries, entrainment speeds and surface tangential velocities as those seen in the main bearing (as per Chapter 4.3.6), but where all of this occurs for rollers travelling in a straight line at velocity $\Omega_{Z_0}\tilde{r}$ (for Ω_{Z_0} set equal to the orbital speed under pure-rolling) between parallel raceways, as opposed to orbiting a bearing centre. In this simplified case, there is no longer an orbital component to angular momentum, and hence Eq. (68) falls away, leaving the single differential equation, Eq. (67), to be integrated. Whilst not identical to the real-world problem, it is believed that analysis of this simplified case will still provide insights into the key mechanisms at play in such systems. Additionally, wind turbine rotors have large rotational inertia, and so is it assumed that $\dot{\Omega}_{Z_0}\tilde{r}$ is small/negligible. The cage normal force for each roller is therefore specified such that it balances the other forces acting along x':

$$f_{n,cage} = \mid f_{g,x'} + f_{d,x'} + f_{t,i} - f_{t,o} \mid . \tag{89}$$

Rollers in this system are thus independent of one another, since they interact with their adjacent cage spars only. As a result, dynamic analysis may be undertaken considering just a single roller in the system. Applied load balancing via the Hertzian model still requires knowledge of the orbital position of all rollers, but (since Ω_{Z_0} is now that of pure-rolling) orbital position over time may be easily determined at each point in time, for example see [12].

This model implementation was undertaken using the main bearing and 1.5 MW wind turbine aeroelastic model applied in previous work [12, 31]. Simulated wind conditions contained a shear exponent of 0.2, and aeroelastic simulations were performed at three levels of kinematic turbulence (high - (A), medium - (B) and low - (C), as specified by IEC-61400 design standards). Simulations at each turbulence level were performed for turbulent wind fields with mean wind speeds of 14, 18, and 22 m/s. In total, analysis of individual roller dynamics was undertaken across 10-min turbine simulations. Note, all simulations fall within the turbine's second constant speed region, wherein pitch action is attempting to maintain the shaft speed at its set rated-level. The roller differential equation, Eq. (67), remains stiff. Stable time integration was consequently achieved using the backward Euler method.

4.3.8 Cumulative Frictional Energy

To analyse results in the context of possible damage occurrence, the accumulation of frictional energy was calculated from the obtained dynamic model results. Cumulative frictional energy at a given contact is defined as,

$$E(t) = \int_{t_0}^{t} \mid \mathbf{f}_{trac}(t) \cdot \Delta\dot{u}(t) \mid \quad dt. \tag{90}$$

Cumulative energy results presented in the following section are of the total cumulative energy, *i.e.* $E_{tot} = E_{in} + E_{out} + E_{cage}$. As will be described, E_{tot} values are dominated by E_{cage}.

4.3.9 Results

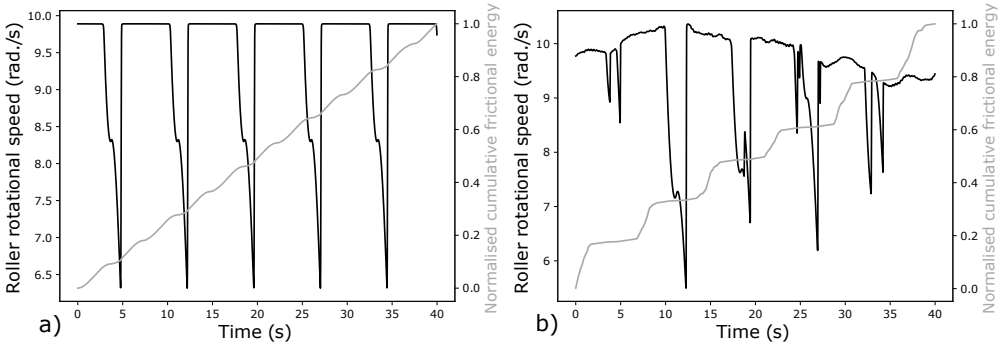

Figure 31: a) Roller rotational speed and normalised cumulative frictional energy under constant load and speed, b) Roller rotational speed and normalised cumulative frictional energy under time-varying conditions.

Fig. 31 shows the roller rotational speed, ω_z', solution after applying the model under conditions of a static downward load and constant speed, set to the mean load and speed seen in the 14m/s mean wind speed case with turbulence level B.

As expected, roller rotational speeds can be seen to remain at pure-rolling throughout the load zone. This is due to high contact forces. As the roller exits the load zone, the braking action of cage contact decelerates the roller. An inflexion point in rotational speed is visible. This occurs as the roller passes over the top of the bearing, where briefly there is no gravitational component acting to push the roller into the cage. Upon re-entering the loaded zone the roller can be seen to rapidly re-accelerate to the pure rolling speed. The cumulative frictional energy from across all contacts (cage, inner- and outer-raceway) is also shown. This variable increases steadily throughout the contact zone. As there is essentially no slip at inner- and outer-raceways towards the centre of the load zone, energy accumulation there is due to roller-cage interaction. This scenario might be crudely taken to represent a roller in a bearing of a conventional power plant turbine.

Fig. 32 provides results under time varying conditions. Note, in this case the cumulative frictional energy values were around two orders of magnitude greater than for the static case. Here, the roller can be seen to track the slowly changing pure rolling speed when loaded. Note, the bearing applied load is also changing in both magnitude and direction throughout. Most of the energy can be seen to accumulate towards the centre of the loaded zone. Again, this energy accumulation is dominated by friction between the roller and its cage, resulting from (brief) high traction forces at inner- and outer-raceways working to force the roller into the cage spar. Raceway traction forces are present due to the slow variations in shaft speed, which in turn are changing the pure-rolling speed. Traction forces therefore develop which drive the roller towards the current pure-rolling $\omega_{z'}$ value.

Cumulative frictional energies were compared across wind speeds and turbulence levels, as shown in Fig. 33. Frictional energy is seen to be highest at the lowest considered wind speed of 14 m/s. This observation was originally thought to be explained as resulting from turbine operation/control, since once rated power is reached at around 12 m/s, excess energy and loads at higher wind speeds are shed by the control system pitching

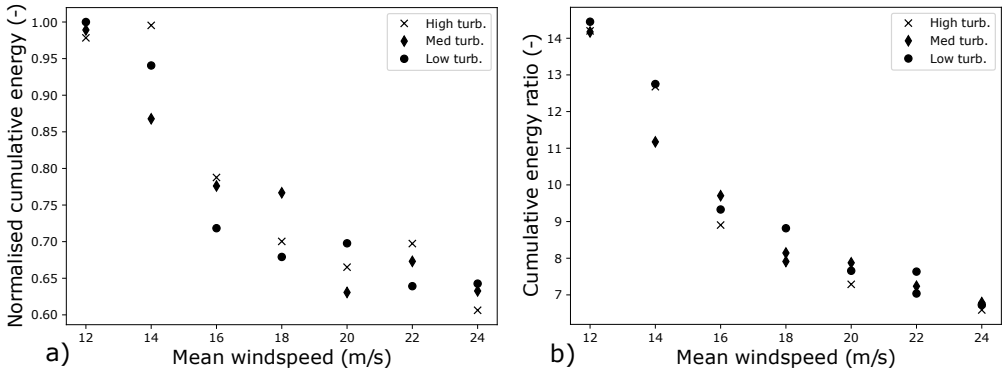

Figure 32: (a) Normalised cumulative frictional energies in the downwind row for each turbine simulation. Results are normalised against the 12 m/s, turbulence C test, (b) Ratios of frictional energy results in the downwind versus upwind main bearing row, $E_{\mathrm{down}}/E_{\mathrm{up}}$.

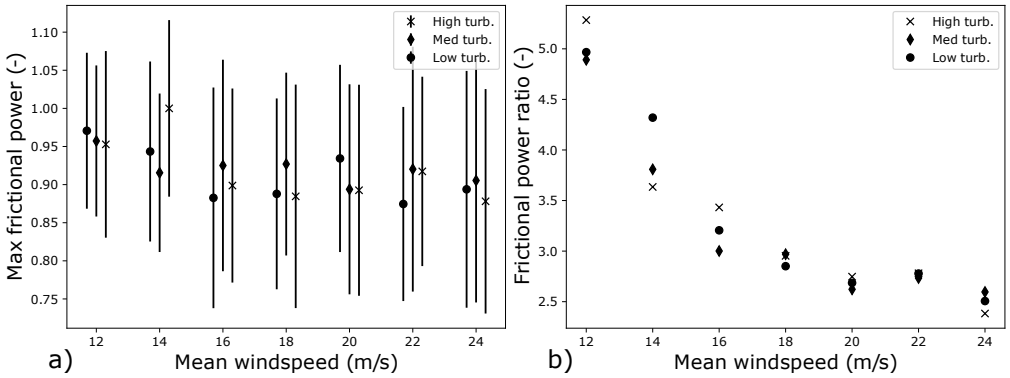

Figure 33: (a) Mean and standard deviation values for the maximum frictional power per roller orbit in the downwind row. Results are normalised against the 14 m/s, turbulence A result. Note, results are staggered about each mean wind speed for clarity. (b) Ratios of mean values of max frictional power per orbit in the downwind versus upwind main bearing rows.

the blades. This would result in design thrust loads which maximise at about 12 m/s, then fall continuously for higher wind speeds. As a result, higher frictional energies might well be expected at points of higher thrust loading. Further comparison was made between upwind and downwind row frictional energy ratios, since discussions with wind farm operators indicate that main bearing failures tend to occur in the downwind main bearing row.

However, upon additional inspection it was found that although results were stable in terms of slip speeds, rapid force fluctuations persisted as an artefact of resolving the stiff dynamics (Fig. 34), meaning a tiny numerical oscillation was yielding erroneously high frictional energies. This was unexpected, considering an implicit method had already been used, and hints at the *extreme stiffness* of the problem: extra caution must be taken in analysing problems of this nature. There are three possible strategies to deal with such residual stiffness:

1. Keep decreasing the time step. With infinite computational power, eventually a

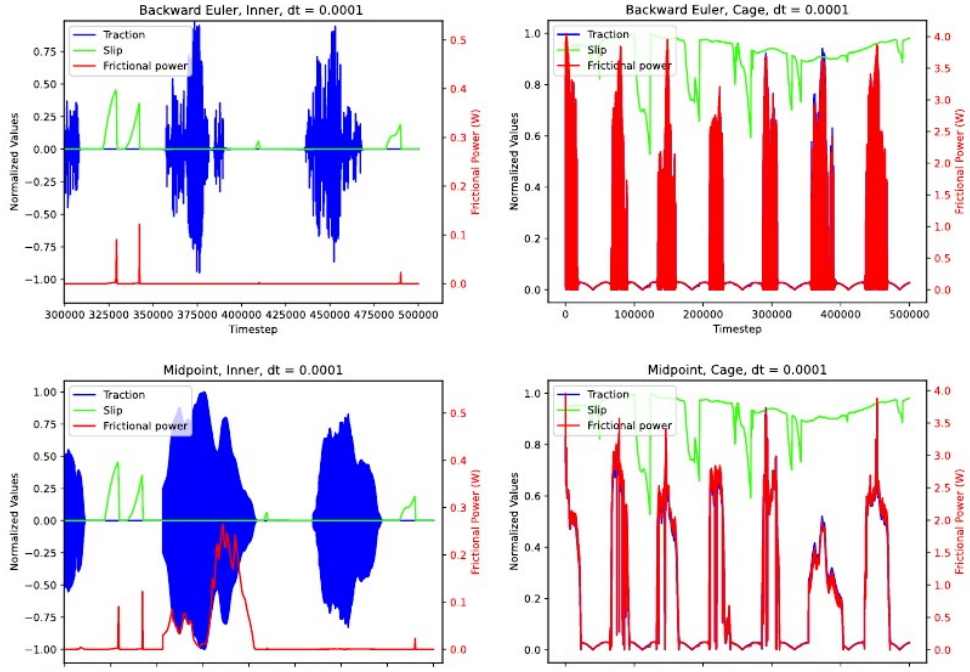

Figure 34: Traction's, slip's, and frictional powers from raceways and cages using two different integration schemes. Stiffness can be seen to cause stark numerical issues.

stable solution will be achieved. This was performed initially up to a timestep of $1\times\ 10^{-5}$. Energy results continued to decrease (Fig. 35), hinting at vanishing frictional energy, but results were still unstable (Fig. 34). Going beyond this for a 10 min interval of real world data, due to the large requisite number of points, is not feasible.

2. Change to a more accurate integration method. An implicit midpoint method was explored, that is better equipped to deal with stiffness.

$$\mathbf{y}(t+\Delta t) = \mathbf{y}(t) + \Delta t \cdot f\left(t + \frac{\Delta t}{2}, \mathbf{y}(t) + \frac{\Delta t}{2} f(t, \mathbf{y}(t))\right) \tag{91}$$

This did improve stability of forces to some extent, however it was also ultimately inconclusive. As it incurred additional computational costs, due to multiple calls of the quasi-static solver, adapting integration method further was deemed impractical without further substantial restructuring of the code.

3. Attempt a different method. An analytical approximation, whereby the different scales of the problem are dealt with separately, might be the best way to proceed.

At this point it is worth discussing if value lies in proceeding with the only remaining strategy available (point 3). Values of frictional energies are low, and negative linear trends with decreasing time-step hint at vanishing frictional energy, so it is arguably reasonable to conclude that macroslip is not significant, and potentially we can crack on with looking to see if microslip is significant instead. However, it was decided to continue, motivated by a few points.

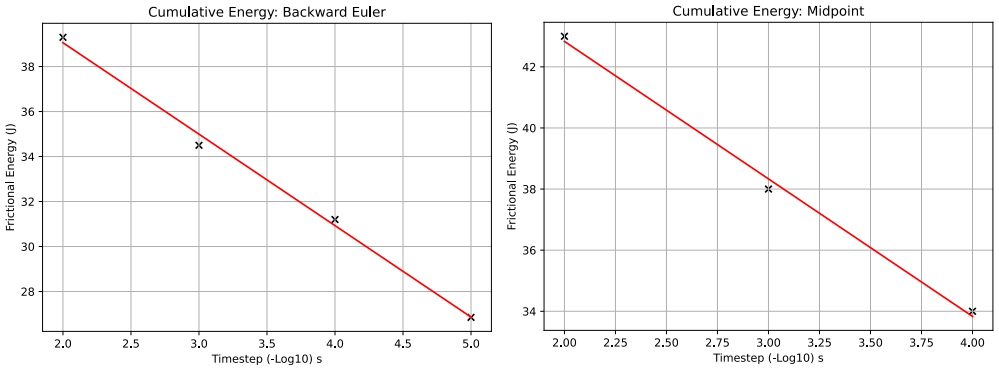

Figure 35: Cumulative frictional energies for backward Euler method and midpoint integration schemes (1 roller). Both hint at vanishing frictional energy, but are inconclusive due to numerical stiffness. A timestep of 1 $\times 10^{-5}$ was not performed for the midpoint method, due to prohibitive computational time.

i. Despite frictional energy decreasing with timestep for both methods, the energy increases when moving between the backward Euler method, and the more accurate midpoint method. This is counter-intuitive, and motivates additional investigation as it leaves the open question:

   'Why is it that increasing accuracy, via decreasing time-step, gives the opposite trend in energy by changing to a supposedly more accurate integration scheme?'

   This leaves a slight lingering doubt that we may conclusively determine that energies vanish.

ii. There is a 2 order magnitude difference in frictional energy between the 'static' load equivalent and the dynamic case. This is likely due to the the system struggling to track with fluctuating value of pure rolling, but we haven't quantified the actual effect of this fluctuation in terms of energy. This will go about answering more fundamentally if there is a difference between the 'static' bearing and a WTMB in terms of macroslip.

iii. Coupling hasn't been investigated, an aim identified earlier and ripe to be tackled using a fresh approach.

iv. Whilst indicative of vanishing frictional energies, residual numerical instability is not conclusive. For reasons of thoroughness an alternative method is required.

4.4 Hamiltonian Dynamic Macroslip Model

The final observation in the previous Subchapter highlights the shortcomings of a Newtonian model for this problem, and motivates an alternative approach. Thus a *Hamiltonian* based method is introduced [112], which has strengths in more complicated dynamic systems with multiple degrees of freedom, such as celestial mechanics [113]. It also has the advantage of removing potential confusion with reference frames, along with inadvertent issues which may arise as such, for example, the previously explored angular momentum coupling mischaracterisation. Further, fictitious forces are no longer required.

It is pertinent to note, that both models applied correctly to absolute precision would describe the same system identically. Consequently, at first, there appears no advantage in the choice of one over the other, and the benefits of the modern computer for solving numerically mean these is unlikely to be any difference using either method. However numerical methods cannot always reveal fundamentals concerning behaviour about the system, e.g. stability [114]. The Hamiltonian is a more fundamental approach for doing so, relying on energy and geometry [115], instead of forces, which are actually derived quantities [116]. Furthermore, forces of constraint can be removed, and the frequencies of complicated motions can be analysed without explicitly solving the exact equation of motion. This enables the study of more complicated motions and non linear effects. Another option would be the Lagrangian [117, 118], a similarly elegant method also founded on variational principles. This was decided against as it yields a set of $n(=2)$ *second order* ordinary differential equations (ODE's), as opposed to $2n(=4)$ *first order* ODE's given by the Hamiltonian. The latter are generally, but not always, easier to handle [119].

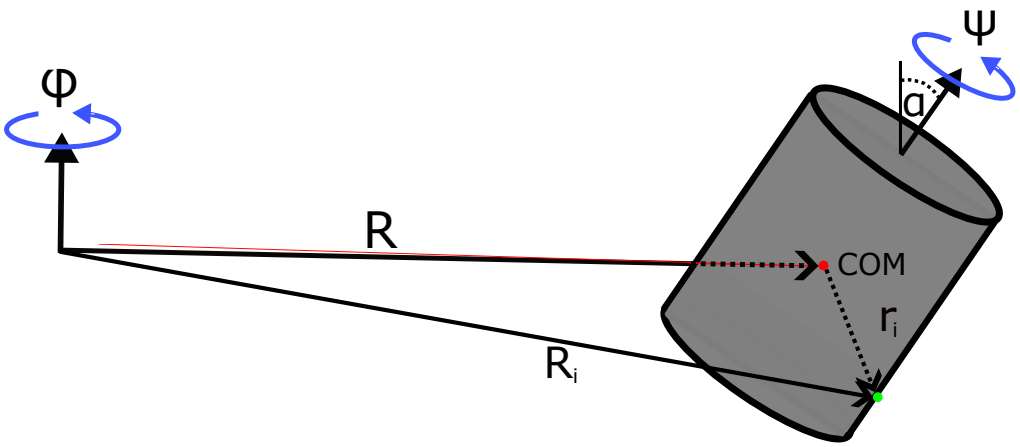

Figure 36: Two degrees of freedom slip coupled spin orbiting system

The derivation of the Hamiltonian set of equations are given in Appendix C. Again, a 2 degrees of freedom (DOF) system was analysed, with skew and tilt being ignored. However, a 4 DOF version is available in Appendix C for future development, with the strengths of the formulation becoming more obvious as the DOF's increase, due to increasing complexity of coupled ODE's associated with complicated changes of angular velocity in time.

Before continuing we should mention the fundamental aim of this model is to characterise the behaviour of the system, specifically how frictional energy, is influenced by

variations of loads and speeds, in order to answer questions and uncertainties raised at the end of Chapter 4.3. This will conclusively determine if macroslip energy truly goes to ≈ 0.

Aim: Analytical Model

We seek an analytical approximation due to numerical stiffness in the Newtonian model:

$$\text{Newtonian Model} \xrightarrow{\text{Stiffness Issues}} \text{Analytical Approximation}$$

$$\text{Goals:} \begin{cases} \text{Leading-order behaviour in extreme load limit} \\ \text{No stiffness issues} \\ \text{Capturing coupling effects} \end{cases}$$

4.4.1 The Lagrangian

The focus will be on one given rolling element, again assuming a cylindrical profile, and for simplicity cage interactions will be neglected. The first step in establishing the Hamiltonian is to find the Lagrangian $\mathcal{L}$, given by [115, 112]:

$$\mathcal{L} = \mathcal{T} - \mathcal{V} \tag{92}$$

where $\mathcal{V}$ denotes potential energy, which in this case is a function of the position around the circumference of the bearing:

$$\mathcal{V} = MgR(1 - \cos\phi) \tag{93}$$

With M denoting mass of roller, g gravitational constant, and R radius of orbit. $\mathcal{T}$ is given by the kinetic energy of the element, fully generally by integrating the velocity (v_i) over the body of the roller (see [120]):

$$\mathcal{T} = \frac{1}{2}\int (v_i)^2 \, dm \tag{94}$$

with the position vector of a given point on the body written as $\vec{R}_i = \vec{r}_i + \vec{R}$, and geometrical symbols depicted in Fig. 36. Due to the additive nature of vectors, the total angular velocity of the element can be decomposed into body and orbital form respectively, $\vec{\omega} = \vec{\omega}_b + \vec{\Omega}$. Then the velocity of an element on the surface is expressed vectorially as:

$$\vec{v}_i = \frac{d\vec{R}_i}{dt} = \frac{d\vec{R}}{dt} + \frac{d\vec{r}_i}{dt} = \vec{\Omega} \times \vec{R} + \vec{\omega} \times \vec{r}_i \tag{95}$$

This is then plugged into Eq. (94), resulting in [120]:

$$\begin{aligned} \mathcal{T} = \frac{1}{2}\int \Big[&\Big(\vec{\Omega} \times \vec{R}\Big) \cdot \Big(\vec{\Omega} \times \vec{R}\Big) + 2\Big(\vec{\Omega} \times \vec{R}\Big) \cdot \Big(\vec{\omega}_b \times \vec{r}_i\Big) + 2\Big(\vec{\Omega} \times \vec{R}\Big) \cdot \Big(\vec{\Omega} \times \vec{r}_i\Big) \\ &+ \Big(\vec{\omega}_b \times \vec{r}_i\Big) \cdot \Big(\vec{\omega}_b \times \vec{r}_i\Big) + 2\Big(\vec{\omega}_b \times \vec{r}_i\Big) \cdot \Big(\vec{\Omega} \times \vec{r}_i\Big) + \Big(\vec{\Omega} \times \vec{r}_i\Big) \cdot \Big(\vec{\Omega} \times \vec{r}_i\Big) \Big] \, dm \end{aligned} \tag{96}$$

Hence, it is evident how complex angular momentum coupling is in multiple DOF systems, and the potential for its oversimplification.

Fortunately, in this case:

$$\vec{\Omega} = (0, 0, \dot{\phi}) \quad \text{(Global frame)} \tag{97}$$

$$\vec{\omega}_b = (0, 0, \dot{\psi}) \quad \text{(Body frame)} \tag{98}$$

and further, due to symmetry about a rotational point in all principal axes:

$$\int \vec{r}_i \, dm = 0 \tag{99}$$

meaning terms 2 and 3 drop from Eq. (96), leaving:

$$\int (\vec{\Omega} \times \vec{R}) \cdot (\vec{\Omega} \times \vec{R}) \, dm = MR^2\Omega^2 \tag{100}$$

$$\int (\vec{\omega}_b \times \vec{r}_i) \cdot (\vec{\omega}_b \times \vec{r}_i) \, dm = \vec{\omega}_b \cdot \int \vec{r}_i \times \vec{\omega}_b \times \vec{r}_i \, dm = \vec{\omega}_b \cdot \mathbf{I}\vec{\omega}_b \tag{101}$$

$$\int (\vec{\omega}_b \times \vec{r}_i) \cdot (\vec{\Omega} \times \vec{r}_i) \, dm = \vec{\Omega} \cdot \int \vec{r}_i \times \vec{\omega}_b \times \vec{r}_i \, dm = \vec{\Omega} \cdot \mathbf{I}\vec{\omega}_b \tag{102}$$

$$\int (\vec{\Omega} \times \vec{R}_i) \cdot (\vec{\Omega} \times \vec{R}_i) \, dm = \Omega^2 I_{zz} \tag{103}$$

where $\mathbf{I}$ denotes the moment of inertia tensor through its top, and I_{zz} the moment of inertia about a vertical axis through its pivot, related by:

$$\mathbf{I} = \begin{bmatrix} I_{xx} & I_{xy} & I_{xz} \\ I_{yx} & I_{yy} & I_{yz} \\ I_{zx} & I_{zy} & I_{zz} \end{bmatrix} = \mathbf{C} \begin{bmatrix} I_1 & 0 & 0 \\ 0 & I_2 & 0 \\ 0 & 0 & I_3 \end{bmatrix} \mathbf{C}^T \tag{104}$$

[5]

where $\mathbf{C}$ is the passive transformation matrix from lab to roller frame, shown in Appendix C, giving:

$$I_{zz} = I_1 \sin^2\alpha + I_3 \cos^2\alpha \tag{105}$$

Combining the above, in the body frame of reference, we find the free body Lagrangian as:

$$\mathcal{L} = \frac{1}{2} I_3 \dot{\psi}^2 + \frac{1}{2} MR^2 \dot{\phi}^2 + \frac{1}{2} \dot{\phi}^2 (I_1 \sin^2\alpha + I_3 \cos^2\alpha) + \dot{\phi}\dot{\psi} I_3 \cos\alpha - MgR(1 - \cos\phi) \tag{106}$$

With all angles being defined by Fig. 36.

Whilst the method presented seems excessively formal, it outlines the natural framework for an accurate description of more complex configurations (e.g. [120], 4 DOF, inclusion of clearance dynamics, defects in mass distribution due to wear).

[5] $I_1 = I_2$ in the case here due to symmetry in the two principal axes of rotation.

4.4.2 Hamilton's Equations

Each coordinate q_i, has a corresponding *conjugate momenta*[6] p_i, given by $\frac{\partial \mathcal{L}}{\partial \dot{q}_i}$. These momenta don't have a physically intuitive meaning, not necessarily corresponding to linear or angular momentum. Instead, they are a more general and fundamental concept of momenta [121], being specifically associated with each co-ordinate, and should be thought of as variables to help solve the system:

$$p_\psi = \frac{\partial \mathcal{L}}{\partial \dot{\psi}} = I_3\dot{\psi} + I_3\dot{\phi}\cos\alpha \tag{107}$$

$$p_\phi = \frac{\partial \mathcal{L}}{\partial \dot{\phi}} = \dot{\phi}(MR^2 + I_1\sin^2\alpha + I_3\cos^2\alpha) + I_3\dot{\psi}\cos\alpha \tag{108}$$

As the Hamiltonian $\mathcal{H}$ is given by:

$$\mathcal{H} = \sum_i \dot{q}_i p_i - \mathcal{L} \tag{109}$$

and:

$$\dot{q}_i = \frac{\partial \mathcal{H}}{\partial p} \tag{110}$$

$$\dot{p}_i = -\frac{\partial \mathcal{H}}{\partial q} \tag{111}$$

Then rearranging Eqs. (107, 108) to find $\dot{\psi}$ and $\dot{\phi}$ in terms of p_ψ and p_ϕ, and plugging into $\mathcal{L}$, to find $\mathcal{H}$ as:

$$\mathcal{H} = -\frac{p_\psi^2}{2I_3} + gMR(1-\cos\phi) + \frac{p_\psi p_\phi}{I_3} - \frac{(p_\phi - p_\psi\cos\alpha)(p_\phi - p_\psi\cos\alpha - 2p_\phi + 2\cos\alpha p_\psi)}{2(MR^2 + I_1\sin^2\alpha)} \tag{112}$$

with accompanying equations of motion (EOMs):

$$\dot{\phi} = \frac{p_\phi - p_\psi\cos\alpha}{MR^2 + I_1\sin^2\alpha} \tag{113}$$

$$\dot{\psi} = \frac{p_\psi}{I_3} - \frac{\cos\alpha(p_\phi - p_\psi\cos\alpha)}{MR^2 + I_1\sin^2\alpha} \tag{114}$$

$$\dot{p}_\psi = 0 \tag{115}$$

$$\dot{p}_\phi = -MgR\sin\phi \tag{116}$$

However, in its current form, this system isn't of particular interest or relevance, having no driving terms. As $\dot{p}_\psi = 0$, and thus p_ψ is conserved, ψ is a cyclic co-ordinate, meaning we only have a 1 DOF system.

[6] Sometimes referred to as Canonical momenta.

4.4.3 Rayleigh Dissipation Function

Obviously, the free body representation of the system is vastly different from the real world. Dissipative influences and the energy being transferred into the system need to be accounted for.

To do this, the *Rayleigh dissipation function*[7] is introduced [115], an 'effective' potential of velocities, $\mathcal{R}(\dot{q}_i)$:

$$\mathcal{R}(\dot{q}_i) = \sum_i k_i \frac{\dot{q}_i^n}{n} \tag{117}$$

where k_i is the coefficient of velocity-dependent friction. This modifies Hamilton's equations of motion:

$$\dot{q}_i = \frac{\partial \mathcal{H}}{\partial p_i} \tag{118}$$

$$\dot{p}_i = -\frac{\partial \mathcal{H}}{\partial q_i} - \frac{\partial \mathcal{R}}{\partial \dot{q}_i} \tag{119}$$

Historically, the function has often been regarded as something of a curiosity, without real-world applications. This unease can perhaps be explained by the variational foundations of Hamiltonian and Lagrangian dynamics and the violation of these principles due to the non-conservative nature of the dissipation function. Furthermore, k_i often could only be found in practice from back-working from the forces present[8], further going against the grain of the foundation of these mechanical methods. However, renewed contemporary interest has demonstrated its suitability in linear and non-linear forms for frictional problems [122, 123], including the presence of lubrication [124], as well as other dissipative physical mechanisms [125, 126, 127].

Whilst the problem is non-variational[9], and thus not a 'true' Hamiltonian system, it may still be viewed as a flow of energy. Therefore, system variables may still be tracked and analysed through considering energy transfer and balances.

The function can be split into the driving slip term and the dissipative drag term. Drag is assigned the same quadratic profile as in the previous Subchapter, with $n = 3$.

The slip term requires a little more work. The example presented in the previous Subchapter was an advanced model for modelling traction. However, in the knowledge that loads are so high that rollers are unlikely to exit the linear region of the traction curve (Fig. 37), we can take the limiting behaviour of Eq. (79), when $\Delta\dot{u}_x \to 0$, $\chi \to 0$, Taylor expanding [129]:

$$\underset{\chi\to 0}{\eta} \approx \eta_0 \exp\left[c_{\eta P} p(x,z)\right] \left(1 + \frac{2}{3}\chi + O(\chi^2)\right) \tag{120}$$

[7] The use of the term dissipation is perhaps misleading in this instance, as friction can drive the system as well, that it does here.

[8] Although on a deeper level the two are identical.

[9] It can be reformulated as a variational one by doubling the DOF and reducing to an effectively conservative system- see [128]. This trick is not done here.

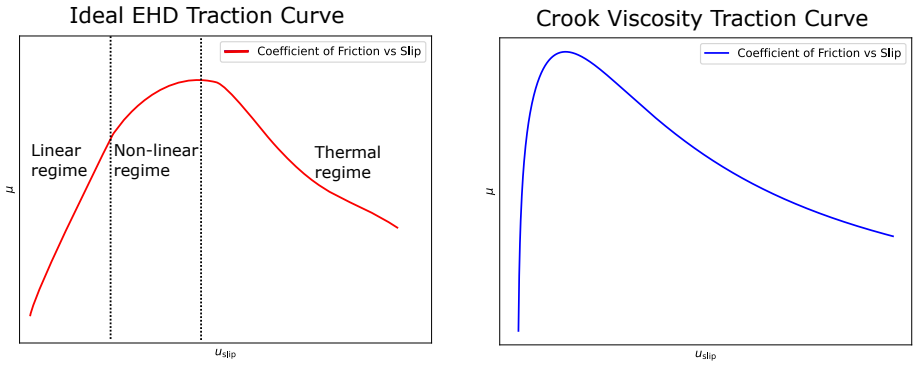

Figure 37: Ideal traction curve (left) and the Crook traction model (right) used in the Newtonian model in Chapter 4.3. The gradient is so steep in the Crook curve, due to high pressures in the application, that slip is minimal, and unlikely to leave the linear regime.

Then, if we keep only the dominant, linear, term and integrate spatially over shear stress (that would give us force as in Chapter 4.3) from Eq. (78).

$$\int_{-a}^{a}\int_{-b}^{b}\tau_{yx}(x,z)dxdz \approx \Delta\dot{u}_x \underbrace{\int_{-a}^{a}\int_{-b}^{b}\frac{\eta_0}{h}\exp\left[c_{\eta P}p(x,z)\right]\,dx\,dz}_{\text{Rayleigh coeff: } k_{\text{slip}}} \tag{121}$$

With the right hand sides linearity in $\Delta\dot{u}_x$, it is obvious this serves as an effective potential in slip speed, and the integral term is our Rayleigh coefficient associated with slip k_{slip}. This can also be seen as the slope of the traction curve, around $\dot{u}_{\text{slip}} = 0$, multiplied by force.

k_{slip} can be found from Eq. (121) numerically, as in Chapter 4.3. However doing so would require to establish a contact patch and integrate at each time step, which doesn't really align with the desired 'quick and dirty' philosophy of the model.

Although the expression does not have a closed form, in the knowledge that pressures are huge, and the term in the exponent $\to \infty$, we may utilise Laplaces method to a second and fourth order, to attain asymptotic approximations of k_{slop}. The second order form is stated:

$$k_{2\text{nd}} = \frac{\eta_0 2\pi ba}{h_c c_{\eta P} p_0}\exp\left[c_{\eta P}p_0\right] \tag{122}$$

The fourth order is more involved, and is available in the Appendix D, along with workings for both asymptotic forms.

These analytical expressions, which are purely in terms of Hertzian parameters, were found to perform within typically 5-10% accuracy of the numerical (Fig. 38), for 5.63 % and 5.72% of the computational time respectively. The second order term was deemed appropriate for subsequent analysis in determining leading order behaviour, $k_{\text{slip}} = k_{2nd}$.

Our Rayleigh dissipation function is thus defined as:

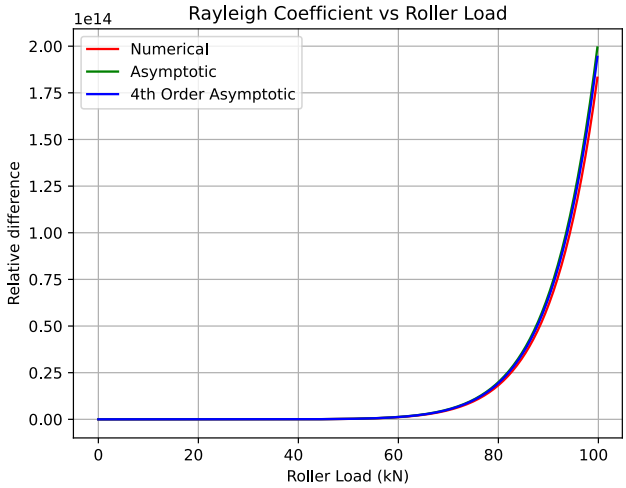

Figure 38: Numerical vs. asymptotic approximations of Rayleigh dissipation function coefficient. A value on the graph represents the gradient of the linear region of μ (coefficient of friction) vs. slip speed, for a given load. The numerical version was used in Chapter 4.3, showing the goodness of fit between the assumptions made here (Eqs. (120, 122)).

$$\mathcal{R} = \frac{k_{\text{slip}}}{2}(\phi,t)\Bigg(\underbrace{\left(\mathrm{c}\alpha\, r_{out}\dot{\phi} + r\dot{\psi}\right)^2}_{\text{(Outer slip term)}} + \underbrace{\left(c\alpha\left(r_{in}\dot{\phi} - r_{in}\omega_{in}\right) - r\dot{\psi}\right)^2}_{\text{(Inner slip term)}}\Bigg) - \frac{1}{3}\underbrace{\left(\frac{1}{2}\epsilon\rho C_D R\dot{\phi}\right)^3}_{\text{(Drag energy term)}} \tag{123}$$

where a ϕ and t dependence arise generally as the roller will have a load dependence on position and load. A short hand of c and s has been used in place of cos and sin for brevity.

4.4.4 System Behaviour

Using the Rayleigh dissipation function, we now have a set of fully coupled equations, giving a general description of the evolution of the system. The same interactions to the previous Newtonian model used have been considered, (apart from neglecting dissipation due to roller cage interface), and a small discrepancy in using an asymptotic form of the traction. The governing equations can be found from subbing Eq. (123) into Eqs. (118, 119), arriving at:

$$\begin{aligned}
\dot{\phi} &= \frac{p_\phi - p_\psi \mathrm{c}\alpha}{MR^2 + I_1 \mathrm{s}^2\alpha} \\
\dot{\psi} &= \frac{p_\psi}{I_3} - \frac{\mathrm{c}\alpha(p_\phi - p_\psi \mathrm{c}\alpha)}{MR^2 + I_1 \mathrm{s}^2\alpha} \\
\dot{p_\psi} &= -k_{\text{slip}}(\phi,t) r\left(\frac{\mathrm{c}\alpha(r_{out} - r_{in} - 2r)}{MR^2 + I_1\mathrm{s}^2\alpha}p_\phi + \left(\frac{\mathrm{c}^2\alpha(r_{in} - r_{out} + 2r)}{MR^2 + I_1\mathrm{s}^2\alpha} + \frac{2r}{I_3}\right)p_\psi + \mathrm{c}\alpha r_{in}\omega_{in}\right) \\
\dot{p_\phi} &= -k_{\text{slip}}(\phi,t)\mathrm{c}\alpha\left(\frac{\mathrm{c}\alpha\left(r_{out}^2 + r_{in}^2 + r(r_{in} - r_{out})\right)}{MR^2 + I_1\sin^2\alpha}p_\phi + \left(\frac{\mathrm{c}^2\alpha\left(r(r_{out} - r_{in}) - r_{out}^2 - r_{in}^2\right)}{MR^2 + I_1\mathrm{s}^2\alpha} + \frac{r(r_{out} - r_{in})}{I_3}\right)p_\psi \right. \\
&\quad \left. -\mathrm{c}\alpha r_{in}^2\omega_{in}\right) + \frac{1}{2}\epsilon\rho C_D R^3 \frac{p_\phi^2 - 2p_\phi p_\psi \mathrm{c}\alpha + p_\psi^2\mathrm{c}^2\alpha}{(MR^2 + I_1\mathrm{s}^2\alpha)^2} - gMR\mathrm{s}\phi
\end{aligned} \tag{124}$$

These were integrated using an initial value problem approach (Scipy's Radau method),

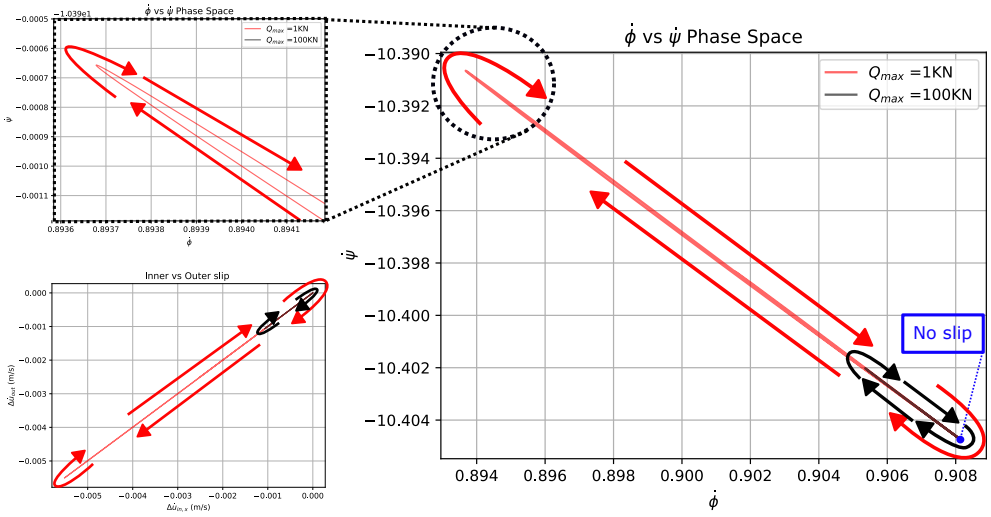

Figure 39: Phase portraits of orbital, rotational, and slip motions of roller, using Eqs. (124), for 1 kN and 100 kN constant load constant speed bearing conditions.

for a simple azimuthal load distribution from [130], at a constant load and speed[10]. This revealed the extent of the coupling seen in Fig. 39.

Velocities were found to be fundamentally interlinked, constrained to move along an orbit when slipping, with a constant orientation of this orbit in phase space. The inclination of this orbit was found to be unaffected by load magnitude and other properties, only being influenced by geometrical ones, such as contact angle. This is due to the strength of the coupling and transferral of energy.

Therefore, the two velocity components should not be considered individually (see Chapter 4.3.3), and a change in one component is strictly associated with a change in another. If the two were independent, the phase plot in Fig. 39 would have vertical or horizontal lines, indicating independent motions, instead there are diagonal and curved lines. This has implications for studies that apply a decoupling approximation, and goes against the earlier assertion in Chapter 4.1 which stated that roller slip may occur without cage slip [102].

The full intricacy of the coupled motion for variable operating conditions is seen in Fig. 40. Further to the coupling between orbital and rotational motions, is an additional layer of complexity, via the time variation in the driving rotational speed. This changes the no slip condition in Fig. 39 from a point, to a time varying motion up and down a constrained line, defined by the pure rolling ratio at that given time point. The deviations from this pure rolling line are events where the roller undergoes slip.

It was also found that synthetically introducing additional orbital inertia (i.e. a presence of cage interaction, by multiplying all factors of MR^2 in Eq's.[124] by λ_{cage}) effected the phase trajectories in a complex non linear manner Fig. 40b, as it changes coupling strengths. For example: a cage inertia of 0 M, indicates the roller is free from cage

[10]Gravity was set to 0 to make Fig. 39 clearer.

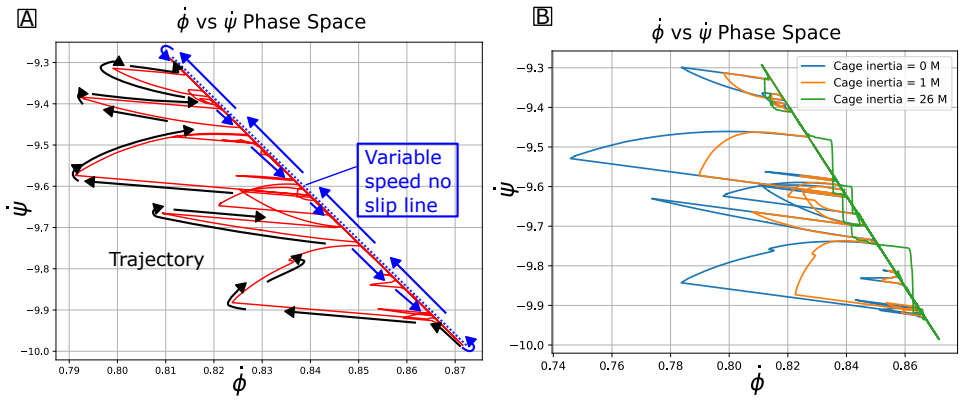

Figure 40: (A) Phase portraits of orbital and rotational speeds, using Eqs. (124), for variable loading (2 mins of 12 A). (B) Shows the effect of inclusion of additional cage inertia on coupling.

interaction, 1 M means it is interacting with a cage inertia equal to its own mass, and 26 M indicates being entirely driven by, or driving the cage. It is likely an accurate understanding of cage- roller interactions and its effect on slip, would require a full account of the behaviour of all other rollers. Without this it is not clear to what extent the roller is interacting with the cage (pushing/being pushed by). This could be done by simulating all 27 rollers, or alternatively giving this synthetic inertia a time dependence ($\lambda_{\text{cage}} \rightarrow \lambda_{\text{cage}}(t)$), potentially dependent on the extent of other loaded rollers.

What phase plots doesn't represent or capture is the quantity of time the roller spends under slip. This is comparatively small against the time it is under pure rolling. Moreover this is whilst mostly unloaded, giving minimal contribution to frictional metrics.

Thus it would appear that slip in the two motions does not occur separately, being fundamentally interlinked. When this is combined with earlier reported field evidence of minimal measured operational cage slip [102], we can begin to conclude that there is therefore likely to be minimal macroslip of either cage or roller present in WTMBs.

However, at this point the system still requires numerical methods to evaluate, and hasn't offered any improvements on the results in Chapter 4.3 in terms of evaluating frictional energies invoked by changes in operating speed in the highly loaded stiff region.

As it is specifically this factor that is of interest, and the knowledge that drag and gravity are markedly smaller than the driving raceway interaction, these terms can be neglected for frictional calculations.

Next, in order to better represent the system, we take k as a constant. It should be emphasised this is merely an intermediate point, intended for analysing the state of the system at an instantaneous snapshot in time: $k(\phi, t) \rightarrow k$. As ϕ and ψ now don't appear explicitly appear, our system of Eqs. (124), can be reduced to a two by two, linear, matrix equation:

$$\begin{bmatrix}\dot{p_\phi}\\ \dot{p_\psi}\end{bmatrix} = -k_{\text{slip}}\begin{bmatrix} \mathrm{c}\alpha\left(\frac{\mathrm{c}\alpha\left(r_{out}^2+r_{in}^2+r(r_{in}-r_{out})\right)}{MR^2+I_1\mathrm{s}^2\alpha}\right) & \mathrm{c}\alpha\left(\frac{\mathrm{c}^2\alpha\left(r(r_{out}-r_{in})-r_{out}^2-r_{in}^2\right)}{MR^2+I_1\mathrm{s}^2\alpha}+\frac{r(r_{out}-r_{in})}{I_3}\right)\\ r\left(\frac{\mathrm{c}\alpha(r_{out}-r_{in}-2r)}{MR^2+I_1\mathrm{s}^2\alpha}\right) & r\left(\frac{\mathrm{c}^2\alpha(r_{in}-r_{out}+2r)}{MR^2+I_1\mathrm{s}^2\alpha}+\frac{2r}{I_3}\right)\end{bmatrix}\begin{bmatrix}p_\phi\\ p_\psi\end{bmatrix}$$

$$+ k_{\text{slip}}\begin{bmatrix}\mathrm{c}^2\alpha r_{in}^2\Omega_{in}(t)\\ -r\mathrm{c}\alpha r_{in}\Omega_{in}(t)\end{bmatrix} \tag{125}$$

That may be represented as:

$$\dot{\mathbf{x}} = \mathbf{A}\mathbf{x}(t) + \mathbf{f}(t) \tag{126}$$

Where $\mathbf{A}$ is the system matrix and $\mathbf{f}(t)$ the forcing term.

This is an inhomogenous linear time invariant (LTI) system, and has a solution of the form [131]:

$$\mathbf{x}(t) = \underbrace{e^{\mathbf{A}t}\mathbf{x}(0)}_{\text{homogeneous}} + \underbrace{\int_0^t e^{\mathbf{A}(t-\tau)}\mathbf{f}(\tau)\,d\tau}_{\text{particular}} \tag{127}$$

For bearing geometries,

$$\mathbf{A} = k_{\text{slip}}\begin{bmatrix}-0.59442 & -0.60587\\ 9.7379\times10^{-5} & -1.2344\end{bmatrix},\quad \mathbf{f}(t) = k_{\text{slip}}\begin{bmatrix}0.11934\,\Omega_{in}(t)\\ -0.012523\,\Omega_{in}(t)\end{bmatrix} \tag{128}$$

For later convenience we will define $\mathbf{A} = k_{\text{slip}}\mathbf{A}_1$. The equilibrium state (pure rolling) value can be found from the values of p_ϕ, p_ψ at pure rolling, by plugging $\dot{\phi}_{roll} = \frac{\Omega_{in}(t)r_{in}}{r_{in}+r_{out}}$, $\dot{\psi}_{roll} = -\frac{r_{out}\Omega_{in}(t)r_{in}\mathrm{c}\alpha}{r(r_{in}+r_{out})}$ into Eqs. (107,108), or by linear algebra taking the product of the inverse of the system matrix with $\mathbf{f}(t)$:

$$\begin{aligned}\begin{bmatrix}p_{\psi,roll}\\ p_{\phi,roll}\end{bmatrix} &= \begin{bmatrix}I_3\dot{\psi}_{roll} + I_3\dot{\phi}_{roll}\cos\alpha\\ \dot{\phi}_{roll}(MR^2 + I_1\sin^2\alpha + I_3\cos^2\alpha) + I_3\dot{\psi}_{roll}\cos\alpha\end{bmatrix}\\ &= \begin{bmatrix}0.2110817\\ -0.01012796\end{bmatrix}\Omega_{in}(t)\\ &= \mathbf{A}^{-1}\mathbf{f}(t)\end{aligned} \tag{129}$$

where checking that the last and first line in Eq. (129), both give the middle numerical value, indicating the system is logically well defined and consistent[11]. If the two were not identical, a mistake would have been made, and this verification process is reassuring given the abstract nature of the previous steps.

The real benefit of a linearised system is the ability to use standard linear methods on them [132], giving eigenvalues and eigenvectors of:

$$\lambda_1 = -0.59452\,k_{\text{slip}},\quad \lambda_2 = -1.2343\,k_{\text{slip}} \tag{130}$$

$$\mathbf{v}_1 = \begin{bmatrix}1.0000\\ 1.5218\times10^{-4}\end{bmatrix},\quad \mathbf{v}_2 = \begin{bmatrix}0.68754\\ 0.72615\end{bmatrix} \tag{131}$$

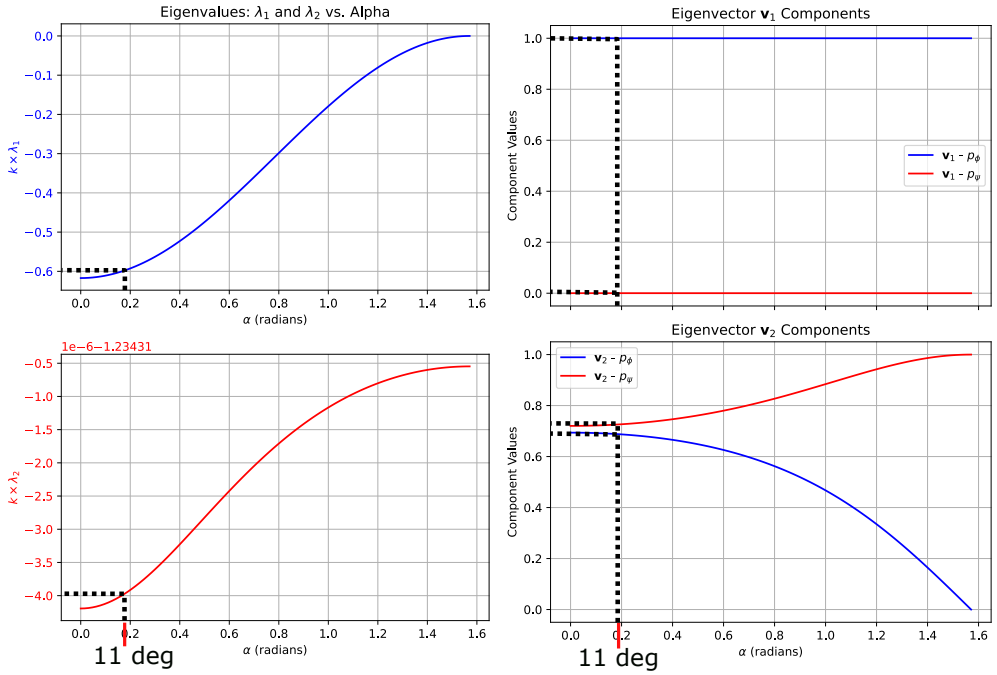

Figure 41: Eigenvalues and vectors vs. contact angle for the bearing. Specific geometry contact angle (11 degrees) is marked, corresponding to the values provided in the text.

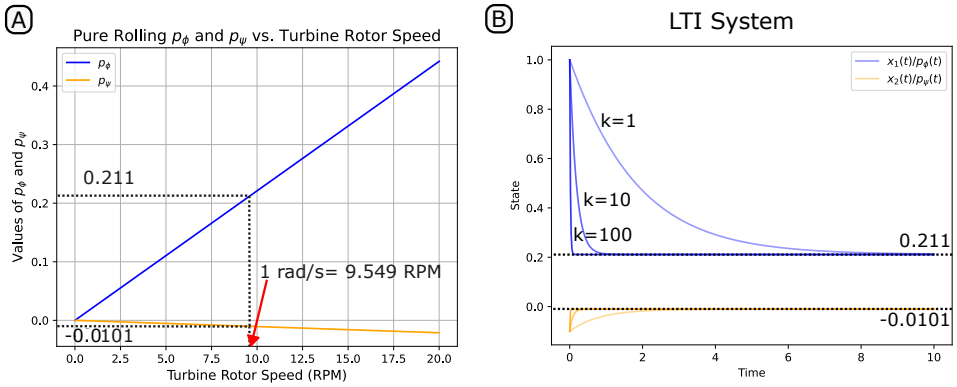

Figure 42: LTI representation of the system (B), for a 1 rad/s rolling speed. Increasing values of k_{slip} lead to increasingly rapid decays to the instantaneous pure rolling value, dictated by turbine rotor speed, Ω_{in} (A). In (B) Ω_{in}, and thus $\mathbf{f}(t)$ are kept constant for clarity.

These eigenvalues and vectors are a function of bearing geometry, and are always negative and real, apart from at $\alpha = 90\,\text{deg}$, when the motions become uncoupled (Fig. 41). This indicates a decay, without oscillation, of $e^{-\|\lambda_i\|t}$ along each respective node, and as $k_{\text{slip}} \to \infty$, $\lambda_i \to \infty$, this decay becomes practically instantaneous. This means, albeit in a rather formal and abstract definition, slip only exists for a very small time period in the system. Fig. 42b provides a good demonstration of this, as k_{slip} gets larger, the

[11] If the reader wishes to confirm for themselves, they would require a full definition of both than Eq. (128), i.e. higher than the 5SF provided.

system more rapidly settles to the pure rolling values of the conjugate momenta.

The eigenvalues can also be used to evaluate the observed numerical stiffness. Stiffness is not an exact mathematical property per se [133], and it can be difficult to predict when numerical issues will or won't occur. Therefore, indications, as opposed to exact definitions, of stiffness are often given, a popular one being [133]:

"A linear constant coefficient system is stiff if all of its eigenvalues have negative real part(s) and the stiffness ratio is large." (page 217)

With the stiffness ratio for our system being given by :

$$\frac{|\lambda_2|}{|\lambda_1|} \approx 2 \tag{132}$$

this statement is not fulfilled. However, another possible precursor for stiffness is given by [134]:

"Stiff differential equations are characterized as those whose exact solution has a term of the form e^{-ct}, where c is a large positive constant." (page 348)

Since the value of k_{slip} can be as large as 2×10^{14} (see Fig. 38), this condition is satisfied. In our preceding Newtonian method we would of required a characteristic timescale of $dt \sim 1/\lambda$ to solve. Further, when we consider our system state variables are of order 1×10^{-1} - 1×10^{-2} (Fig. 42a), these issues become even more apparent. There is up to a 15-16 order of magnitude difference between the state variables and their eigenvalues.

Since Numpy float64, used here, follows the IEEE 754 double-precision floating-point standard [135], with 15 decimal places available, we are nearing the limit of what numerically can be solved due to the extreme difference in scales involved. This formally captures why the system struggles with stiffness: extremely large decay rates, due to very high roller loads, combined with very small variable values, due to very low operational speeds. Numerically, the perfect storm.

However, k_{slip} is not constant, so the current derivation is not accurate outside the immediate local location in ϕ and t. To characterise global behaviour we must consider the fully general case, where k_{slip} is a function of both the roller position round the bearing, and also time, due to changing load angle (e.g. due to gusts of wind), and also speed:

$$k(\phi,t)_{2\text{nd}} = \eta_0 \frac{2\pi b(\phi,t)a(\phi,t)}{c_{\eta P}p_0(\phi,t)} \exp[c_{\eta P}p_0(\phi,t)] \tag{133}$$

This means there exists a similar dependence for the system matrix $\mathbf{A}(\phi,t)$, making the system highly non-linear, and potentially very difficult to resolve or understand behaviour[12].

However, non-linear systems are widely tackled, where appropriate, with linear methods [119]. In many cases this may be the only viable method to use. Fortunately, we may do this to a high precision here.

Noting that the decay rate time scale, $\sim 1/\lambda_i$, is negligible compared to the timescale of the evolution of $k_{\text{slip}}(\phi,t)$ and to the driving timescale $\Omega_{in}(t)$, the *fast dynamics* of the

[12]The minimum for a system to exhibit chaotic behaviour is three independent variables, with non-linearity present [115]

slip can be analysed independently from the *slow dynamics* [114, 136] of the rest of the system. Slip can be taken to have minimal influence on the overall dynamics and trajectory of ϕ, and hence $k_{\text{slip}}(\phi, t)$ can be simplified to $k_{\text{slip}}(t)$: i.e. purely a time dependent input as the roller tracks with pure rolling, apart from very small slip displacements with rapid decays.

This then leaves a system of inhomogeneous linear time variant (LTV) equations:

$$\dot{\mathbf{x}} = \mathbf{A}(t)\mathbf{x} + \mathbf{B}(t)\mathbf{f}(t) \tag{134}$$

where $\mathbf{B}(t)$, known as the control or input matrix, in this case is the identity matrix, $\mathbb{I}$, scaled by $k_{\text{slip}}(t)$.

This LTV approximation is a very good representation of the system, due to the already mentioned 15-16 order of magnitude difference between the respective timescales. Furthermore, when the timescales do approach each other in size, as they are changing, this region may be neglected due to its minimal contribution to frictional energy (under light load). This comes back to the underlying aim of the model, to investigate frictional energies due to operational load and speed variability.

Solving Eq. (134) in general is more involved [119, 137] than the LTI variant in Eq. (126), and is given by:

$$\mathbf{x}(t) = \mathbf{\Phi}(t, t_0)\mathbf{x}(t_0) + \int_{t_0}^{t} \mathbf{\Phi}(t, \tau)\mathbf{B}(\tau)\mathbf{f}(\tau)d\tau \tag{135}$$

This involves resolution of the *state transition matrix* [138] $\mathbf{\Phi}(t, t1)$, which is often challenging, and unlikely to be of closed form [137]. However, in the special case of $\mathbf{A}(t)\mathbf{A}(\tau) = \mathbf{A}(\tau)\mathbf{A}(t)$ [139, 137]:

$$\mathbf{\Phi}(t, \tau) = \exp\left[\int_{\tau}^{t} \mathbf{A}(s)\, ds\right] \tag{136}$$

where it should be noted that this expression is not equivalent to $\exp[\mathbf{A}t]$.

Since the matrix $\mathbf{A}(t) = k_{\text{slip}}(t)\mathbf{A}_1$, and $k_{\text{slip}}(t)$ is a scalar:

$$\mathbf{A}(t_1)\mathbf{A}(t_2) = k_{\text{slip}}(t_1)k_{\text{slip}}(t_2)\mathbf{A}_1\mathbf{A}_1 = \mathbf{A}(t_2)\mathbf{A}(t_1) \tag{137}$$

since $\mathbf{A}_1$, as a square matrix, commutes with itself. As a result the form of Eq. (136) may be applied, resulting in:

$$\mathbf{x}(t) = \underbrace{\exp\left[\int_{t_0}^{t} k(s)\mathbf{A}_1\, ds\right]\mathbf{x}(t_0)}_{\text{homogeneous}} + \underbrace{\int_{t_0}^{t} \exp\left[\int_{\tau}^{t} k(s)\mathbf{A}_1\, ds\right] k(\tau)\mathbb{I}\mathbf{f}(\tau)d\tau}_{\text{particular}} \tag{138}$$

where subscript slip has been dropped for brevity.

The behaviour of this solution is captured in Fig 43. System state depends on a complex interaction of both load, (k_{slip}) and speed, (Ω_{in}). As load increases the system better tracks with the fluctuating state of the pure rolling momenta.

Mathematically, this is due to an increasing negative integral over $k(s)ds$, which is necessarily always a real positive value. This means the exponential kills off contributions;

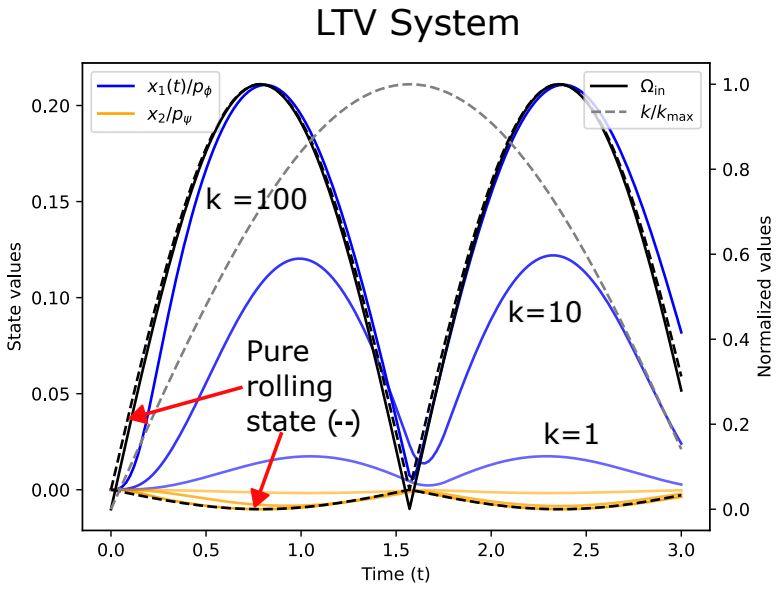

Figure 43: LTV representation of the system for different values of k_{slip}.

the previous system states of the become less and less important in calculating the current state. By reasoning, times further back, and closer to, t_0, will have an increasingly negative exponential exponent, so will have negligible contributions to the overall state of the system.

We now appeal to the knowledge of the shear magnitude of k in our system. By reasoning, times further back, and closer to t_0, will have an increasingly negative exponential exponent as the result of the inner integral getting increasingly negative in Eq. (138). This kills off the homogeneous term:

$$\mathbf{x}(t) \approx \int_{t_0}^{t} \exp\left[\int_{\tau}^{t} k(s)\mathbf{A}_1\, ds\right] \mathbb{I} k(\tau)\mathbf{f}(\tau) d\tau \tag{139}$$

Furthermore, principal contributions will come from when $t \approx \tau$ [129, 140]. Therefore, performing a Taylor expansion around the vicinity of $t - \tau$ [13]:

$$\mathbf{x}(t) \approx \int_{t_0}^{t} \mathbb{I} \exp\left[\left(k(t)(t-\tau) + O\left((t-\tau)^2\right)\right)\mathbf{A}_1\right] \cdot \left(\mathbf{f}(t) + (t-\tau)\mathbf{f}'(t) + O\left((t-\tau)^2\right)\right) \cdot \left(k(t) + (t-\tau)k'(t) + O\left((t-\tau)^2\right)\right) d\tau \tag{140}$$

neglecting higher order terms:

$$\mathbf{x}(t) \approx \int_{t_0}^{t} \mathbb{I} \exp\left[\left(k(t)(t-\tau)\right)\mathbf{A}_1\right] \cdot \left(\mathbf{f}(t) + (t-\tau)\mathbf{f}'(t)\right) \cdot \left(k(t) + (t-\tau)k'(t)\right) d\tau \tag{141}$$

[13] The expansion is backwards in time so is slightly different from the familiar form.

making the substitution of $s = t - \tau$:

$$\mathbf{x}(t) \approx -\int_{t-t_0}^{0} \mathbb{I}\exp\left[\big(k(t)(s)\big)\mathbf{A}_1\right] \cdot \Big(\mathbf{f}(t)k(t) + s(\mathbf{f}'(t)k(t) + k'(t)\mathbf{f}(t))\Big) ds \tag{142}$$

The limits can be swapped, and as k is very large and negative, the upper bound can be extended to infinity, $t - t_0 \to \infty$, as these contributions are exponentially suppressed [129, 140], leaving to leading order:

$$\begin{aligned}\mathbf{x}(t) &\approx \int_0^{\infty} \mathbb{I}\exp\left[k(t)s\mathbf{A}_1\right]\mathbf{f}(t)k(t)\,ds + \int_0^{\infty} \mathbb{I}\exp\left[k(t)s\mathbf{A}_1\right] s\Big(\mathbf{f}'(t)k(t) + k'(t)\mathbf{f}(t)\Big)\,ds \\ &= \underbrace{\mathbf{A}_1^{-1}\mathbf{f}(t)}_{\text{Equilibrium term}} + \underbrace{\frac{1}{k(t)^2}\mathbf{A}_1^{-2}\big(\mathbf{f}'(t)k(t) + k'(t)\mathbf{f}(t)\big)}_{\text{First order term.}}\end{aligned} \tag{143}$$

where the exponential matrix integral has been used in the final step.

Finding the frictional energy from the system state at this point is simply arrived at by using the definitions of the conjugate variables, and of kinetic energy from the Hamiltonian:

$$T = \sum_i \dot{q}_i p_i \tag{144}$$

meaning that the frictional power is:

$$\dot{E}_f(t) = \big\|(\mathbf{x}_{\text{roll}}(t) - \mathbf{x}(t)) \cdot \dot{\mathbf{q}}(t)\big\| = \left\|\frac{1}{k(t)^2}\mathbf{A}^{-2}\big(\mathbf{f}'(t)k(t) + k'(t)\mathbf{f}(t)\big) \cdot \dot{\mathbf{q}}(t)\right\| \tag{145}$$

and the cumulative frictional energy is given by:

$$E_f(t) = \int_{t_0}^{t} \left\|\frac{1}{k(t)^2}\mathbf{A}^{-2}\big(\mathbf{f}'(t)k(t) + k'(t)\mathbf{f}(t)\big) \cdot \dot{\mathbf{q}}(t)\right\| dt \tag{146}$$

It can thus be seen, to first order, that frictional energies are a combination of an interplay of load and speed variability. In the case:

$$k^2(t) \gg \|\mathbf{f}'(t)k(t) + k'(t)\mathbf{f}(t)\| \quad \Rightarrow \quad E_f,\, \dot{E}_f \to 0. \tag{147}$$

This condition was found to be the reflective of the problem here; when this expression was ran over the same turbine conditions used in the previous Subchapter, very low resultant frictional metrics were found. This finding is due to the extremely high operational loads, and slower associated timescales with load and speed variability satisfying Eq. (147).

Therefore we can conclude that there is fundamentally a theoretical effect present in macroslip frictional metrics, due to the variability in loads and speeds of the bearing. This is evident from the form of Eqs. (145,146) alone, as well as powers and energies increasing across wind-speeds with increased variability of conditions Fig. 44. Similarly, we see a difference present between the static and dynamic loading cases [14]. If we break down the contributions of frictional energy for one roller, we see the greater contribution to $E_f, \dot{E}_f$ is from the load variability term in our system, with speed variability having

[14] There is a nuance here, in that if speed does not vary, the solution to the problem is ill posed as it is no longer an LTV system. Therefore, Eqs. (145, 146) can't truly be used, and alternative methods would be required. However, we can instead view this is a description of the static loading with an additional infinitesimal speed fluctuation $\Omega_{in}(t) = \Omega_{in,0} + \delta\Omega_{in}(t)$.

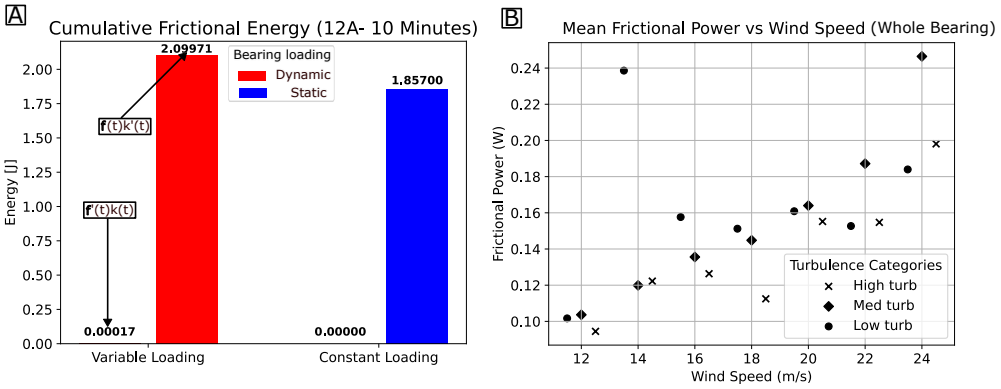

Figure 44: The leading order behaviour of frictional energies and powers due to macroslip for the system was found conclusively to approach 0. Although theoretical differences exist in frictional metrics due to load and speed variability (see text), in practice this has no demonstrable effect in a WTMB, and the values vanish. (A) is presented for one roller, (B) for the whole bearing.

a negligible contribution. However, in practice, this theoretical difference has no meaningful energetic consequence on our case, with very low frictional outputs. Therefore we conclude that macro level slip, due to dynamic loads and speeds, is unlikely to be a factor in premature WTMB failure.

The limitations of the assumptions of this analytical expression should be understood, as it is designed specifically for the low speed high load case of a WTMB. With higher speeds, non linear forces (drag) would make the linearisation less accurate, and with lower loads, the Taylor expansion performed in Eq. (140) would also lose validity, meaning loads further back in time would start to have greater influence on the contemporary state of the system. A cut off for smaller values of $k \sim 1/dt$ was applied for the results in Fig. 44 so as not to surpass these regions of validity for the Taylor expansion.

It might appear that we have undertaken a rather self-indulgent exercise in analytical mechanics, producing a simulacrum of the original problem, so far detached from its origin that it has lost all meaning and usefulness [141].

This concern is worth addressing. The Newtonian model provided can be considered a 'black box', giving a case-by-case solution, describing how a system will evolve, but not necessarily why. This makes it harder to understand fundamental behaviour and structures of the system, consequently when novel applications are encountered bringing with them novel issues, deeper insight is required.

The analytical 'glass box' model provides this. It is in fact a good representation of the system, due to the operational load and speed extremes, validating simplifications and assumptions. Furthermore, it targets gaps in understanding, explaining why stiffness occurs and the importance of correctly applied momenta coupling. It specifically targets the region the Newtonian model cannot, load and speed fluctuation under highest load, answering questions about this frictional contribution left open at the end of the previous Subchapter. In engineering, philosophically, such methods should only be developed if they are useful. That is, they meet these requirements:

1. There is a need to develop them, since the simpler method doesn't give the intended

outcomes.

2. There is a meaningful outcome and results may be interpreted and used to inform the engineering task.

As both conditions are satisfied, this exercise has been a valuable contribution.

4.5 Conclusions

This Chapter began by developing a quasi-static Hertzian based load solver, for discrete distributions of rollers in a case study SRB. This solver was used for calculating the roller loads used in Chapters 4, 5 and 6.

With macroslip being identified as a key factor in other turbine bearings wear and failure, a Newtonian dynamic model was developed to track this proposed cause of failure for WTMB. Major influences on dynamics were incorporated, including gyroscopic effects, roller cage interactions, and EHL. The lubrication model used assumed Hertzian pressure distributions inside the contact, and a spatially constant film thickness, calculated from an empirical formula.

Results hinted at low associated frictional metrics, although extreme numerical stiffness made firm conclusions difficult. In fact, trends between cases might be misinterpreted due to artefacts associated with stiffness, and extreme care should be taken interpreting systems such as these in future work.

After some deliberation, it was decided to develop an alternative method to conclusively determine if the indications given by the Newtonian model were correct. Therefore a Hamiltonian representation was derived, with an asymptotic approximation of the lubrication model. This approach also targeted gaps in literature due to angular momenta mischaracterisation. Analysis revealed the difference in time scales were so extreme in the system, that the standard limit of decimal places available (15) is approached, making it numerically challenging to solve, especially for the previous Newtonian model. Furthermore, neglecting angular momentum coupling was found to be a poor simplification of a slip coupled spin orbiting system.

Nevertheless, extremely low frictional metrics were found, supporting the findings of the Newtonian model. Since the Newtonian model included a higher fidelity depiction of lubrication effects (preferable), and the Hamiltonian method only captured leading order behaviour, the two models really should be ultimately viewed as supporting each other. Moreover, both need interpreting together covering weaknesses/left by of the other: in unison providing exceptional value answering a difficult problem.

This Chapter found that macro level slip was unlikely to be a factor in premature WTMB failure. As macroslip is insignificant, and small displacements under high loads might invoke considerable frictional dissipation, consideration of higher order displacements between surfaces should now be undertaken.

5 Steady State Microslip

The following Chapter will run through the derivation of steady state microslip for the case study bearing. Tests will be run over parallel conditions in Chapters 4, and the Chapter will terminate with the findings of the frictional implications of these.

5.1 Introduction

Prior to this gross slip was considered, as a driver for failure. This analysis had assumed that the relative motion between contact surfaces was uniform throughout the patch, and for many bearing applications this is a suitable simplification [142]. In the WTMB case, difficulties were encountered due to the stiffness of the system, nevertheless two separate analyses types concluded that the invoked frictional energies and powers due to macroslip were extremely low. However, considering the extremely high load conditions of the main bearing, a very small relative motion could invoke a very high dissipation of frictional energy, and this is considered in more depth here.

Thus undertaking a higher order accuracy assessment in relative surface displacements would be prudent. Therefore *microslip* is introduced, where the interplay of effects such as strain and geometry are considered. These result in a non-uniform displacement field throughout the contact.

This Chapter's analysis considers micro-slip under steady state tractive rolling, where there is no acceleration present. Therefore the system is analysed as a sequence of equilibrium states, and effects arising due to transitions between are ignored. There is no inherent reliance on time, except from resolving the state under an immediate applied condition, whereas in reality, transient effects will be present in some form, and may or may not be significant. The neglect of transient effects poses concerns about the usefulness of steady state methods. However, steady state methods are often analytical, elegant, and don't rely on excessive computational power that was often unavailable at their time of development. Furthermore, they give insight into the inner workings of the system, and may have additional value in techniques where deviations from the stable state are considered (e.g. perturbative analysis).

The structure of the Chapter is as follows: We will firstly revisit contact mechanics via Carters strip theory [143], applying some modifications to derive an equivalent for a SRB, making various idle comments and observations along the way. Then the derived equations will be used to assess the effect of microslip on frictional metrics, over the full range of wind conditions, to make conclusions on damage and failure predictions.

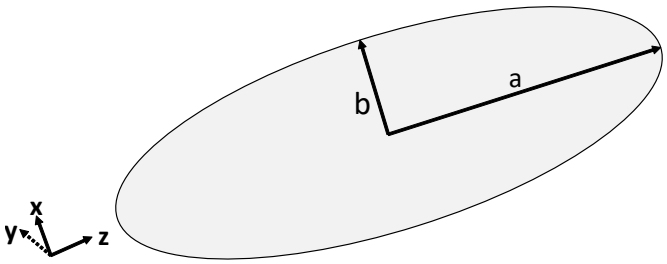

Figure 45: The right hand side Cartesian contact patch co-ordinate frame with elliptical geometries used in the following two Chapters. Care should be taken, as differences exist between classical contact mechanics texts (e.g. [105]) in axes and denotion of a and b.

5.2 Establishing Boundary Conditions

Rolling is a relative angular motion between two bodies in contact about an axis to a common tangent plane. This angular motion will give an absolute motion of surfaces, and any difference between these two surface in various properties, e.g. material, geometry, strain, will accordingly evoke a relative motion.

If a reference frame is used which moves with the point of contact (Fig. 45), the surfaces flow through the contact zone with tangential velocity V_1 and V_2. The bodies may also fully generally have angular velocity ω_{z1} and ω_{z2}. If each of these velocities are unequal, sliding and spin will respectively occur.

Additionally, an effect known as *creep* may also eventuate, in which the difference between strains tangentially leads to an effectively enlarged circumference of rotation for one of the bodies. This is a geometric effect and creep velocities are denoted by δV.

When using a Eulerian view, in which the reference frame is moving with the point of contact: the material moves whilst the field of deformation remains fixed in space. If tangential displacements at a surface point are denoted by $u_x(x,z,t)$ and $u_y(x,z,t)$, this is captured via:

$$\frac{du_x}{dt} = V\frac{\partial u_x}{\partial x} + \frac{\partial u_x}{\partial t} \tag{148}$$

and

$$\frac{du_z}{dt} = V\frac{\partial u_z}{\partial x} + \frac{\partial u_z}{\partial t} \tag{149}$$

Hence particle velocities in the field are given by:

$$v_x(x,z) = V + \delta V_x - \omega_y z + V\frac{\partial u_x}{\partial x} + \frac{\partial u_x}{\partial t} \tag{150}$$

$$v_z(x,z) = \delta V_z + \omega_y x + V\frac{\partial u_z}{\partial x} + \frac{\partial u_z}{\partial t} \tag{151}$$

If the strain field does not change with time, as in steady rolling, the final partial is dropped from both of these expressions [15]. The remaining partials arise purely from strain in the surface, and can be deduced if surface tractions are known, as will subsequently be done. Therefore, the velocities of microslip of points on the surface for

[15] These terms will become important later when exploring transient effects

steady rolling are given by:

$$\dot{s}_x(x,z) = v_{x1} - v_{x2} = (\delta V_{x1} - \delta V_{x2}) - (\omega_{y1} - \omega_{y2})z + V\left(\frac{\partial u_{x1}}{\partial x} - \frac{\partial u_{x2}}{\partial x}\right) \tag{152}$$

$$\dot{s}_z(x,z) = v_{z1} - v_{z2} = (\delta V_{z1} - \delta V_{z2}) + (\omega_{y1} - \omega_{y2})x + V\left(\frac{\partial u_{z1}}{\partial x} - \frac{\partial u_{z2}}{\partial x}\right) \tag{153}$$

These may also be represented in non-dimensional form for an elliptical contact:

$$\dot{s}_x(x,z)/V = \xi_x - \psi z/c + \left(\frac{\partial u_{x1}}{\partial x} - \frac{\partial u_{x2}}{\partial x}\right) \tag{154}$$

$$\dot{s}_z(x,z)/V = \xi_y - \psi x/c + \left(\frac{\partial u_{z1}}{\partial x} - \frac{\partial u_{z2}}{\partial x}\right) \tag{155}$$

where $\xi_{x/z} = (\delta V_{x1/z1} - \delta V_{x2/z2})/V$ is the creep ratio, and ψ is the spin parameter $(\omega_{y1} - \omega_{y2})c/V$ in which $c = (ab)^{1/2}$, with the following boundary equations applying:

$$\dot{s}(x,z) = \begin{cases} 0 & \text{(In a stick region: } |q(x,z)| < \mu p(x,z)) \\ \mu p(x,z) \cdot \frac{-\dot{s}(x,z)}{|\dot{s}(x,z)|} & \text{(In a slip region: } |q(x,z)| = \mu p(x,z)) \end{cases} \tag{156}$$

Where p denotes pressure and q surface traction, not to be confused with conjugate momenta p_i and position q_i used in Chapter 4.4.

Eq. (156) states that in a stick region, where there is no relative motion, the traction must not exceed the Couloumb force, and in a slip region the traction will equal the magnitude of the coulomb force but oppose the direction of slip. As before, we will focus only on motion in the x (rolling) direction.

These preceding equations define our problem, and will be solved for the rolling case of a cylinder, then ball bearing, before we are in a position to do so for a full SRB case. We will also stick to b representing semi minor axes (aligned with x), and a the semi major (z).[16]

5.3 Cattaneo-Mindilin's problem

As discussed in the previous Subchapter, there may be regions of slip and stick occurring simultaneously across the contact, first identified via Cattaneo- Mindilin's problem [104]. The problem is that of a static Hertzian pressure contact, subject to a constant tangential force per unit length across the contact. In an age preceding numerical techniques, this elegant argument noted that for a no slip $Q < \mu P$, this would necessitate a singular μ at the edge of the contact (Fig. 46).

The reader is referred to [104] or [105] for a full treatment of the problem, but the results are stated below and are useful in aiding understanding of the rest of the Chapter.

The solution of distribution of tangential traction in the static case is solved by the distribution of two elliptical tractions:

$$q'(x) = \mu p_0 (1 - x^2/b^2)^{1/2}, \quad |x| < b \tag{157}$$

[16] This differs from some notable literature- see ref.[105].

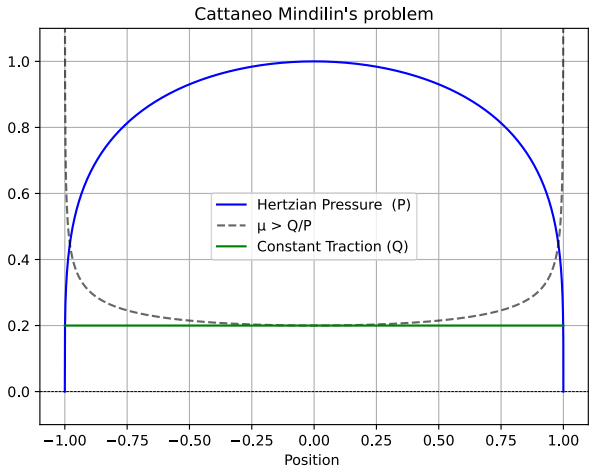

Figure 46: Cattaneo- Mindilin's problem- for no slip and a constant traction an infinite coefficient of friction is required at the edges of the contact. This is unphysical, so stick and slip zones must arise.

$$q''(x) = -\frac{c}{b}\mu p_0 (1 - x^2/c^2)^{1/2}, \quad |x| < c \tag{158}$$

Primed notation corresponds to the distribution that causes slip, and double primed the stick. These tractions cause strains of:

$$\frac{\partial u_x'}{\partial x} = -\frac{2(1-\nu^2)}{bE}\mu p_0 x, \quad |x| < b \tag{159}$$

$$\frac{\partial u_x''}{\partial x} = \frac{2(1-\nu^2)}{bE}\mu p_0 x, \quad |x| < c \tag{160}$$

These strains cancel inside the region $|x| < c$, giving no displacement(stick) within this annulus, and the size of this stick region can be determined by integrating over the distributions to find the magnitude of the force:

$$Q = \int_{-b}^{b} q(x)dx = \int_{-b}^{b} q'(x)dx + \int_{-c}^{c} q''(x)dx \tag{161}$$

giving:

$$\frac{c}{b} = \left(1 - \frac{Q}{\mu P}\right)^{1/2} \tag{162}$$

The behaviour of this solution is, for a constant P, steadily increasing Q from 0, microslip begins at the edges of the contact and moves inwards (Fig. 47). As Q approaches the limiting value of μ, gross sliding will occur, as the stick region shrinks to a radius of $c = 0$.

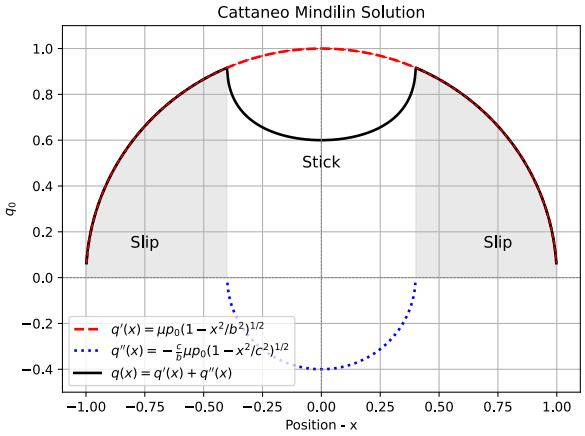

Figure 47: The solution is found by prescribing two opposing Hertzian form tractions.

5.4 Rolling Elastic Cylinders

We now move onto the case of steady rolling between two cylinders, upon which a tractive force is being applied. This could represent the driving or braking of a wheel.

Similar to Cattaneo- Mindilin's static problem, we expect the cylinders to be divided into stick and slip zones as in the configuration of Fig. 47.

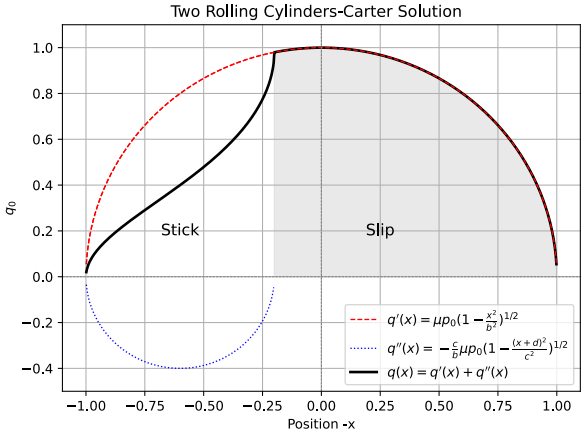

Figure 48: In the case of rolling cylinders the distributions used for Cattaneo-Mindilin's problem are shifted to satisfy Eq. (156). This is known as Carter's solution.

as in the rolling case, we expect an occurrence of both regions, however Eq. (156) is violated, as the leading slip edge in the contact, doesn't oppose the traction direction.

Here arises a chief problem in such analysis, finding the configurations of slip and stick generally is very difficult for even the simplest of cases. For rolling cylinders, it was initially tackled by Carter, by shifting the stick region $q''(x)$ to the leading edge by a distance $d\,(= b - c)$, and solving resultant tractions and strain distributions.

Slip is now conveniently confined to the single zone at the trailing edge (Fig. 48), where boundary conditions are satisfied. Following the same reasoning from the preceding Subchapter, if the stick traction $q''(x)$ distribution is displaced by $d\,(= b - c)$ so that it now aligns with the leading edge, the resultant traction and strains become:

$$\begin{aligned}
q'(x) &= \mu p_0 (1 - \frac{x^2}{b^2})^{1/2}, && |x| < b, \\
q''(x) &= -\frac{c}{b} \mu p_0 (1 - \frac{(x+d)^2}{c^2})^{1/2}, && -b \le x \le c - d, \\
\frac{\partial u_x'}{\partial x} &= -\frac{2(1-\nu^2)}{bE} \mu p_0 x, && |x| < b, \\
\frac{\partial u_x''}{\partial x} &= \frac{c}{b} \frac{2(1-\nu^2)}{cE} \mu p_0 (x+d), && -b \le x \le c - d.
\end{aligned} \tag{163}$$

If these two strains are combined, within the strip ($-b \le x \le c - d$) the resultant tangential strain is

$$\frac{\partial u_x}{\partial x} = \frac{2(1-\nu^2)}{bE} \mu p_0 d = \text{constant} \tag{164}$$

The tractions on each surface are equal and opposite, so therefore the tangential strains are both equal and opposite. For the slip velocity to be zero this means that when the above expression is plugged into Eq. (154), under no spin and no slip ($\dot{s} = 0$), results in a creep ratio of

$$\xi_x = -4(1-\nu^2) \mu p_0 d / bE \tag{165}$$

Accordingly the required boundary conditions are satisfied. As with the static case, the width of the stick region is dependent on the tangential force:

$$\frac{d}{b} = 1 - \frac{c}{b} = 1 - (1 - Q_x / \mu P)^{1/2} \tag{166}$$

Consequently if the Hertzian relationship is used for p_0, we can make a substitution of Eq. (165) into Eq. (166) :

$$\xi_x = -\frac{\mu b}{R} [1 - (1 - Q_x / \mu P)^{1/2}] \tag{167}$$

where 1/R is the linear combination of the two surface curvatures. This means any presence of tractive force will cause microslip in the trailing edge, which will grow until when $Q = \mu P$, gross sliding occurs.

The results of this analysis only apply to elastically similar solids in contact, else additional effects are present. We now have a tractable equation for microslip in the contact, involving only forces and geometries. This strip theory is now used for the case of a roller bearing in a raceway, where the radius of curvature varies along the non-rolling direction.

5.5 A Ball Rolling in a Conforming Groove

The next extension of the problem is solving over a curved surface, where the problem goes from the 1D line contact form to 2D. Tackled by Johnson, a pre-eminent figure in contact mechanics, surface points across a curved body will necessarily have different local velocities. This differential can be roughly approximated by using a Taylor expansion:

$$V_1 \approx \omega(R - z^2/2R) \tag{168}$$

This geometrical velocity differential is known as Heathcote slip [104] Therefore from the definition of creep in Eq. (154), across the contact the ratio is

$$\xi(z) = \frac{V_1 - V_2}{\omega R} = \left(1 - \frac{V_2}{\omega R}\right) - \frac{z^2}{2R^2} = \xi_0 - \frac{z^2}{2R^2} \tag{169}$$

If the creep ratio previously found for Eq. (165) a cylindrical slice is substituted into this expression:

$$\frac{d}{b} = \Gamma(\gamma^2 - z^2/a^2) \tag{170}$$

where:

$$\Gamma = \frac{a^2 E'}{4\mu p_0 R^2} \tag{171}$$

and:

$$\gamma^2 = 2R^2\xi_0/a^2 \tag{172}$$

No slip will occur at strips located at $z = \pm\gamma a$ (Fig. 49). From Eq. (166) the tractive force per strip may be expressed as:

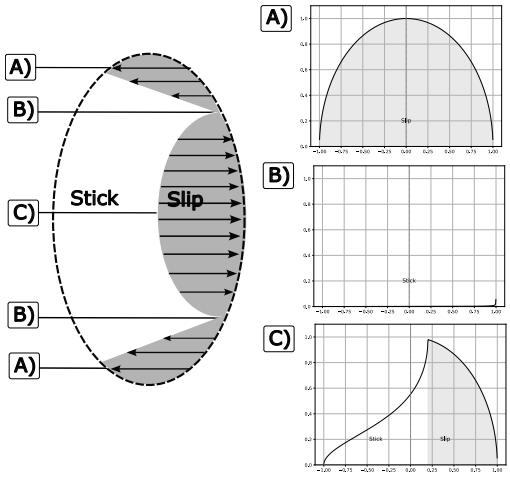

Figure 49: The regions of stick and slip required by evaluating every 'Carter slice' and solving the resultant force to be zero Eq. (174), over a curved surface in the non-rolling direction.

$$Q* = \frac{\pi}{2}\mu p_0^* b_* \frac{d}{b_*}\left(2 - \frac{d}{b_*}\right) = \frac{\pi}{2}\mu p_0 b \frac{d}{b}\left(2\frac{b_*}{b} - \frac{d}{b}\right) \tag{173}$$

For, free, steady, rolling the total traction force satisfies:

$$Q = \int_{-b}^{b} Q * dy = 0 \tag{174}$$

This will determine the position of the no slip bands, γ, and has to be solved numerically by minimizing the integral.

5.6 Wind Turbine SRB Steady Microslip

For a spherical roller bearing the configuration will be different to that of a ball rolling in a groove as given by Johnson [105]. The two differences that are present and which will need consideration are :

1. Modification of peripheral velocity due to the combination of both degrees of angular velocity, (the orbit about the bearing centre and the rotation of the roller around its own principal axes of rotation). This is different from the classically considered cases, as the conforming groove was assumed static.
2. Modification of geometry, to account for contact angle and adequate consideration of differing surface radii. Before, the roller assumed perfect conformity of contacting surfaces, and no angle was present.

Both of these are shown visually in Fig. 50. With the effect of these differences on microslip and frictional metrics not being fully clear, and considering the tolerances required due to the extremely high loads, a full investigation will now be carried out to determine the implications of these.

The effective radii (r' and r'_{in}) for a particle in the contact are illustrated in the diagram below:

First it is instructive to have a look at the peripheral velocity distribution due to the curvature of the roller about the z axes of the roller, depicted in figure 2 and denoted by r'.

For a point z along the surface, where z=0 is centred with the roller, it can be seen that the effective radius $r'(z)$ varies.

This is given vectorially by:

$$r'(z) = (r_{1z}^2 - z^2)^{1/2} - (r_{1z} - r_{1x}) \tag{175}$$

assuming $r_{1z} >> z$, a Taylor expansion may be used. This results in:

$$r'(z) \approx r_{1z}\left(1 - \frac{z^2}{2r_{1z}^2} + \mathcal{O}(z^4)\right) - (r_{1z} - r_{1x}) \tag{176}$$

Thus the velocity distribution due to the curvature of a roller bearing, with just rotational velocity ω, is given by:

$$\omega r'(z) \approx \omega\left(r_{1x} - \frac{z^2}{2r_{1z}}\right) \tag{177}$$

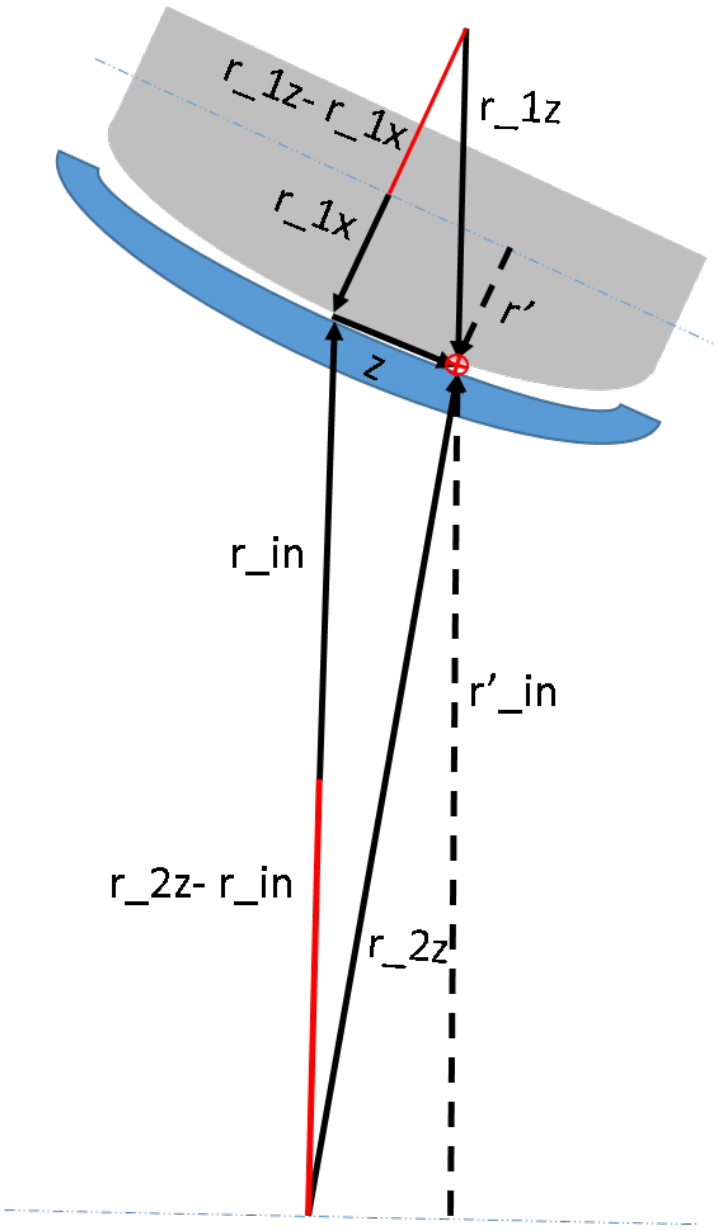

Figure 50: Velocity differences due to geometrical variation across mating surfaces

A similar argument can be made for the velocity distribution on the raceway. Without the presence of a contact angle, this would be:

$$r'_{in}(z) \approx r_{in} + \frac{z^2}{2r_{2z}} \tag{178}$$

Here, the second order term is additive, as the curvature of the raceway is negative, so the point along the surface is getting further away from the axis of orbit, along z.

However, there is also an additional effect due to the contact angle, so the second order term is modified by a factor of $\cos\alpha$, and an additional asymmetrical term is introduced that reduces the effective radius with displacement along z. This gives:

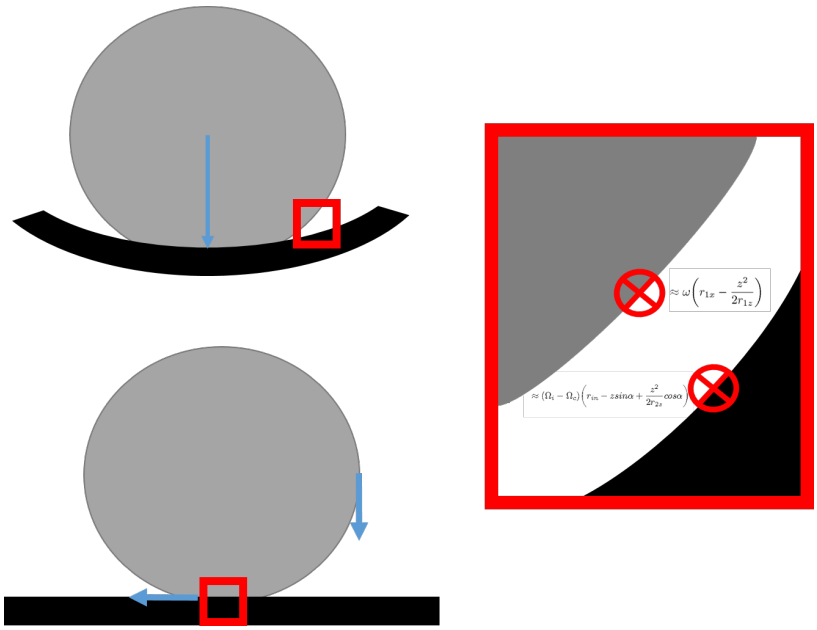

Figure 51: Reference frames of the velocity differences in the patch frame.

$$r'_{in}(z) \approx r_{in} - z\sin\alpha + \frac{z^2}{2r_{2z}}\cos\alpha \tag{179}$$

As the roller is both rotating and orbiting, it is helpful to consider the problem in the patch reference frame, which moves with the contact.

This is done by subtracting the orbital (cage) velocity, Ω_c, from the inner raceway and roller. This would give the velocities of a mating surface point on the roller and inner raceway respectively as:

$$\approx \omega\left(r_{1x} - \frac{z^2}{2r_{1z}}\right) \tag{180}$$

$$\approx (\Omega_i - \Omega_c)\left(r_{in} - z\sin\alpha + \frac{z^2}{2r_{2z}}\cos\alpha\right) \tag{181}$$

This is illustrated in Fig. 51.

The condition of pure rolling [31], an assumption made largely throughout this Chapter, gives that:

$$\Omega_c = \Omega_i \frac{\tilde{r}_{in}}{\tilde{r}_{in} + \tilde{r}_{out}} \tag{182}$$

using,

$$\tilde{r}_{out} = \tilde{r}_{in} + 2r_{1x} \tag{183}$$

and the condition for pure rolling:

$$\omega r_{1x} = \frac{\tilde{r}_{in}\tilde{r}_{out}}{\tilde{r}_{in} + \tilde{r}_{out}} \tag{184}$$

A substitution may be made for the inner raceway's velocity profile of:

$$(\Omega_i - \Omega_c) = \frac{\omega r_{1x}}{\tilde{r}_{in}} \tag{185}$$

giving an inner raceway surface velocity of:

$$\omega\left(r_{1x} - z\sin\alpha\frac{r_{1x}}{\tilde{r}_{in}} + \frac{z^2 r_{1x}}{2r_{2z}\tilde{r}_{in}}\cos\alpha\right) \tag{186}$$

and thus (subtracting Eq. (186) from Eq. (180) and dividing by ωr_{1x}) the creep ratio (Fig. 52) is:

$$\xi = \xi_0 + z\frac{\sin\alpha}{\tilde{r}_{in}} - z^2\left(\frac{1}{2r_{1z}r_{1x}} + \frac{cos\alpha}{2r_{2z}\tilde{r}_{in}}\right) \tag{187}$$

Following the parallel argument to 3.4, if the creep ratio per strip is given by:

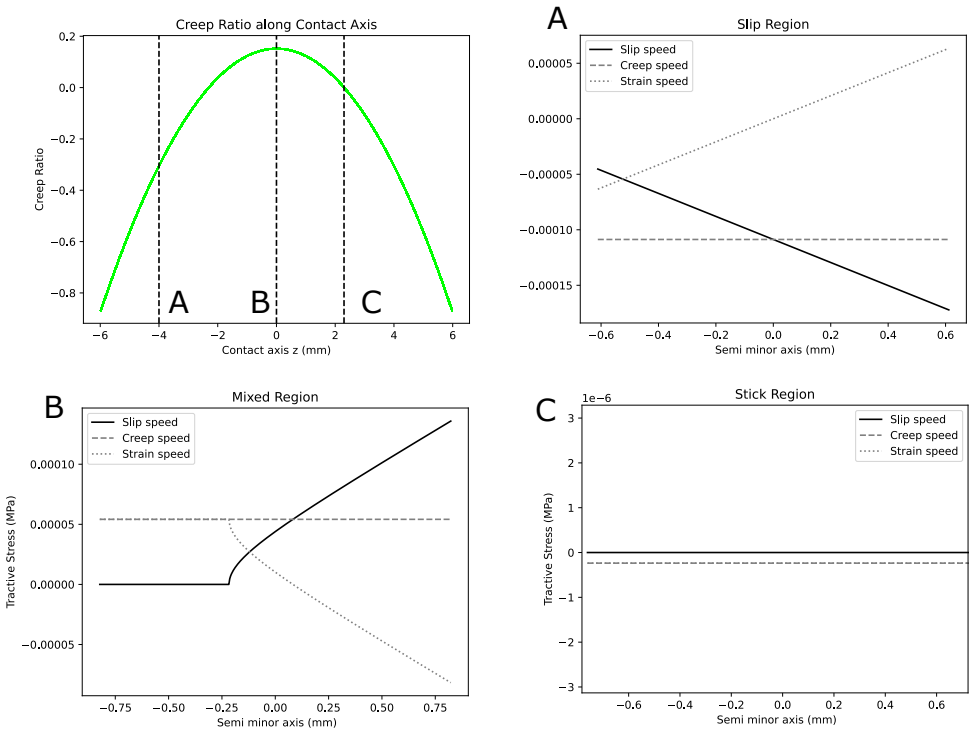

Figure 52: Top left- the creep ratio along contact for SRB. The resultant micro slip speeds from combining geometrical terms (ξ), and strain.

$$\xi = -4(1-\nu^2)\mu p_0 d/aE \tag{188}$$

By equating and rearranging, the ratio of stick region per strip is given by:

$$\frac{d}{b} = \frac{E}{4(1-\nu^2)\mu p_0}\left(\xi_0 + z\frac{\sin\alpha}{\tilde{r}_{in}} - z^2\left(\frac{1}{2r_{1z}r_{1x}} + \frac{\cos\alpha}{2r_{2z}\tilde{r}_{in}}\right)\right) \tag{189}$$

Johnson's formulation for a ball bearing uses a conformity factor, Γ to express the ratio in a symmetric quadratic.

$$\frac{d}{b} = \Gamma(\gamma^2 - z^2/a^2) \tag{190}$$

$$\Gamma = \frac{a^2 E'}{4\mu p_0 R^2} = \frac{a^2 E}{8(1-\nu^2)\mu p_0 R^2} \tag{191}$$

To compare results, an 'equivalent' Gamma must be used. This equivalent expression is

$$\frac{d}{b} = \Gamma' \left(\frac{2r_{1z}r_{1x}\xi_0}{a^2} + z\frac{2r_{1x}r_{1z}\sin\alpha}{a^2\tilde{r}_{in}} - \frac{z^2}{a^2}\left(1 + \frac{r_{1x}r_{1z}cos\alpha}{r_{2z}\tilde{r}_{in}}\right)\right) \tag{192}$$

where:

$$\Gamma' = \frac{a^2 E}{8(1-\nu^2)\mu p_0 r_{1x} r_{1z}} \tag{193}$$

The moment resisting rolling is given by:

$$m_z = \int_{-b}^{b} Q^* \left(r_{1x} - \frac{z^2}{2r_{1z}} \right) dz \tag{194}$$

Due to the assymetry of the slip profiles invoked by an angular contact, a skewing moment will also be generated:

$$m_y = \int_{-b}^{b} Q^* \cdot z \; dz \tag{195}$$

If the effect of these moments is to be evaluated, the outer race patch must also be considered. Using the same reasoning, the velocity of the mating surfaces on the roller and outer race:

$$\approx -\omega \left(r_{1x} - \frac{z^2}{2r_{1z}} \right) \tag{196}$$

$$\approx -\Omega_c \left(\tilde{r}_{out} - zsin\alpha - \frac{z^2}{2r_{2z(out)}} cos\alpha \right) \tag{197}$$

If the same co-ordinate system is used.

Using the outer race pure rolling identity:

$$\Omega_c = \frac{\omega r_{1x}}{\tilde{r}_{out}} \tag{198}$$

Thus the outer raceway velocity is given by:

$$-\omega \left(r_{1x} - z\sin\alpha \frac{r_{1x}}{\tilde{r}_{out}} - \frac{z^2 r_{1x}}{2r_{2z(out)}\tilde{r}_{out}} \cos\alpha \right) \tag{199}$$

Therefore the creep ratio on the outer raceway is:

$$\xi = \xi_0 - z\frac{\sin\alpha}{\tilde{r}_{out}} + z^2 \left(\frac{1}{2r_{1z}r_{1x}} - \frac{\cos\alpha}{2r_{2z(out)}\tilde{r}_{out}} \right) \tag{200}$$

The remaining task required to find the total microslip is to identify the strains between the surfaces. This follows the same protocol as before, by using strip theory and superposing two elliptical distributions.

5.6.1 Strain Terms

The strains in a surface for a Hertzian contact are given by [105]:

$$\frac{\partial u_{x_0}}{\partial x} = -\frac{(1-2\nu)(1+\nu)}{E}p(x) - \frac{2(1-\nu^2)}{\pi E}\int_{-b}^{b}\frac{q(s)}{x-s}d(s) \tag{201}$$

The contact of the two surfaces results in the symmetrical pressure terms cancelling each other out for the resultant strain between surfaces. The remaining integral may be evaluated via the real part of:

$$\int_{-b}^{b}\left(1-\frac{s^2}{b^2}\right)^{0.5}\frac{ds}{x+iy-s} = \pi\left(\frac{x+iy}{b} - \left[\left(\frac{x+iy}{b}\right)^2 - 1\right]^{0.5}\right) \tag{202}$$

In the case that $x^2 < b^2$, the second contribution from this integral is purely imaginary, and disregarded, giving only a real contribution of:

$$\pi\frac{x}{b} \tag{203}$$

In the instance that $x^2 > b^2$:

$$\pi\left(\frac{x}{b} - \left[\frac{x^2}{b^2} - 1\right]^{0.5}\right) \tag{204}$$

Therefore, when $q(s) = \mu P_0(1-\frac{s^2}{b^2})^{0.5}$ is used, this gives the result of the integral outside the contact as:

$$-\frac{2(1-\nu^2)\mu P_0}{E}\left[\frac{x}{b} - \left(\frac{x^2}{b^2} - 1\right)^{0.5}\right] \tag{205}$$

and inside the contact as:

$$-\frac{2(1-\nu^2)\mu P_0}{E}\left[\frac{x}{b}\right] \tag{206}$$

To find the precise total strain for the combined =slip and stick regions, these two must be superposed for the two distributions defined earlier

$$\frac{\partial u}{\partial x} = \frac{\partial u'}{\partial x} + \frac{\partial u''}{\partial x} = \frac{2(1-\nu^2)\mu P_0}{E}\left[-\frac{x}{b} + \frac{c}{b}\left(\frac{x+d}{c} - \left(\frac{(x+d)^2}{c^2} - 1\right)^{0.5}\right)\right] \tag{207}$$

with the resultant strain throughout given by:

$$\frac{\partial u}{\partial x} = \frac{2(1-\nu^2)\mu P_0}{Eb}\left[d - c\left(\frac{(x+d)^2}{c^2} - 1\right)^{0.5}\right] \tag{208}$$

The term in the square root becomes real and provides a contribution to net strain when $-d + c < x$.

With the direction of the total strain being additive between the two surfaces, equal and opposite, the total slip ratio for the inner and outer raceway and zero spin is given as (Eqs. (154,187,200,208)):

$$\frac{\dot{s}_{xin}(x,y)}{\omega r_{1x}} = \xi_0 + z\frac{\sin\alpha}{\tilde{r}_{in}} - z^2\left(\frac{1}{2r_{1z}r_{1x}} + \frac{\cos\alpha}{2r_{2z}\tilde{r}_{in}}\right) - \frac{4(1-\nu^2)\mu P_0}{Eb}\left[d - c\sqrt{\frac{(x+d)^2}{c^2} - 1}\right] \tag{209}$$

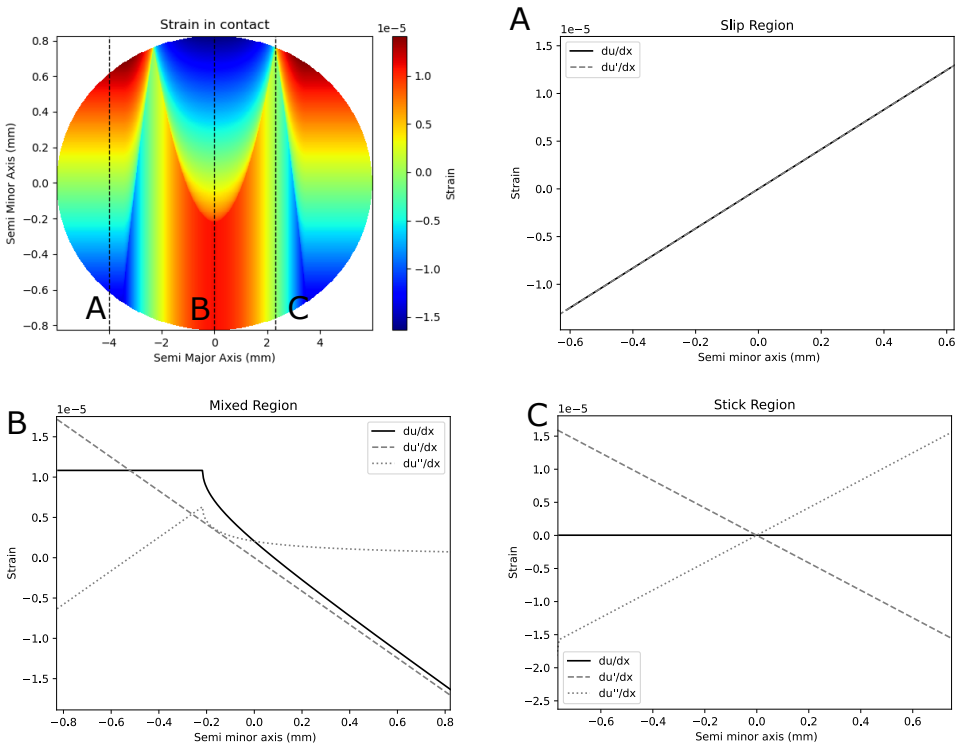

Figure 53: Strain distributions for case study SRB. Slices are taken at the three regimes of -(A) only slip, (B) -regions of stick and slip, (C) -only stick.

$$\frac{\dot{s}_{xout}(x,y)}{\omega r_{1x}} = \xi_0 - z\frac{\sin\alpha}{\tilde{r}_{out}} + z^2\left(\frac{1}{2r_{1z}r_{1x}} - \frac{\cos\alpha}{2r_{2z(out)}\tilde{r}_{out}}\right) - \frac{4(1-\nu^2)\mu P_0}{Eb}\left[d - c\sqrt{\frac{(x+d)^2}{c^2} - 1}\right] \tag{210}$$

The $\frac{1}{c}$ term inside the brackets may not be taken out; elsewhere, $d - c = a$ has been made use of. Resultant strain and traction distributions are portrayed in Fig. 53 and Fig. 54 respectively.

However, the use of these forms is only valid in regions where there is both stick and slip, not in areas of pure sliding. Having outlined microslip for more general bearing geometries, we will next analyse some initial implications of these matters.

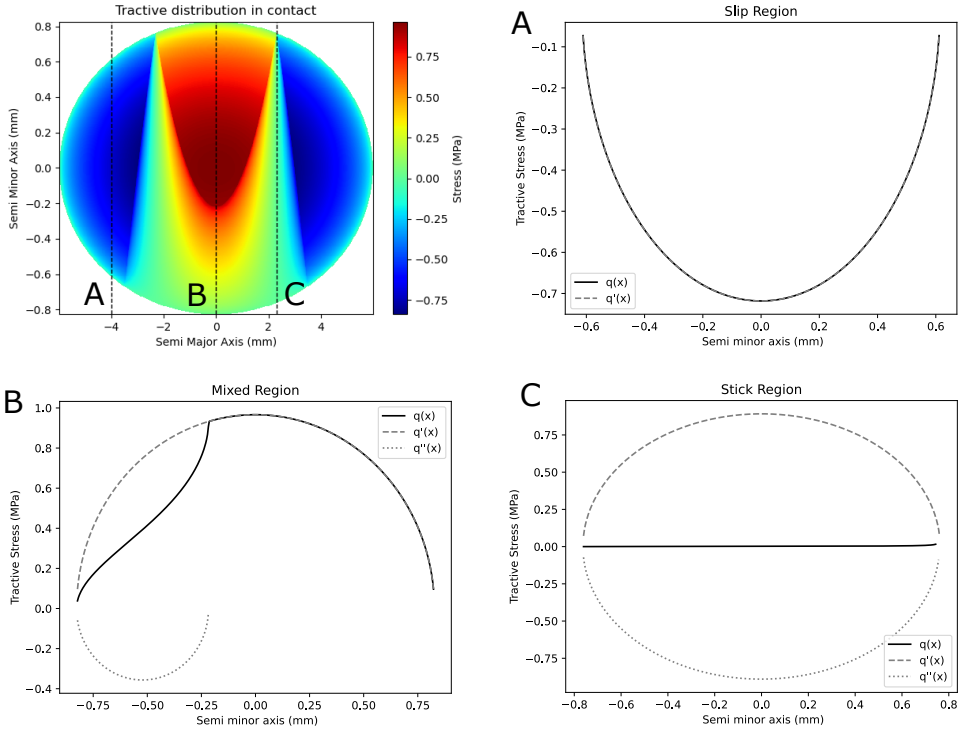

Figure 54: Tractive distributions for case study SRB. Slices are taken at the three regimes of- (A) only slip, (B) regions of stick and slip, (C) only stick. q"(x) becomes imaginary in certain regions, leaving partial, or full slip with its complete absence.

5.7 Results

The classic form of slip/stick is observable for our case, with regions of opposing slip either side of a central region, and narrow bands of stick (Fig. 56).

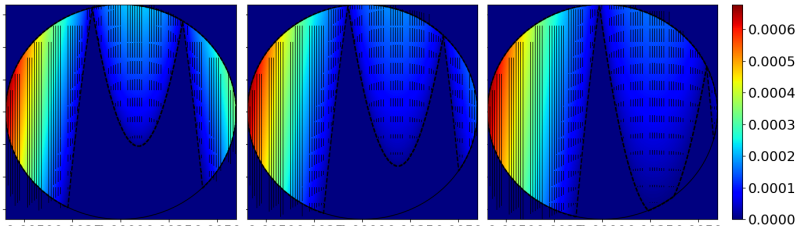

Figure 55: The effect of increasing α on steady state microslip. Shown here are 5, 10, and 15 degrees (from left to right). Increasing asymmetry and size of velocity differential. The net skewing effect of this is investigated in Fig. 56.

The contact angle appears to have a strong effect on microslip distributions in general, and might have potential implications on race failure if steady state microslip is a failure driver (Fig. 55). The asymmetry and velocity differential concentrated frictional power dissipation on the contact side furthest from the axis of orbit, by roughly a factor of 2-3 (Fig. 57) of that of the mean spatial value. Under the above proviso this would

accelerate damage in this region, and reduce bearing life as a whole, according to linear damage theory.

It only took between 150 - 200 points to convincingly discretize the problem on the semiminor axes, typical of most regular elliptical problems (Fig. 57). However a mere twenty or so points also gave a pretty accurate signal (Fig. 57).

The classic resisting moment curve was plotted over different scenarios. There seemed to be little difference due to the moving raceway and static, indicating the ball in a conforming groove is a good approximation for pure rolling in this sense.

Heathcote's resisting moment of $0.08 m_z R/(\mu F a^2)$ is treated in the literature as the limiting case of Γ, however results here instead indicate resisting moment is sensitive to contact angle α, and does not converge on this widely reported value (Fig. 58).

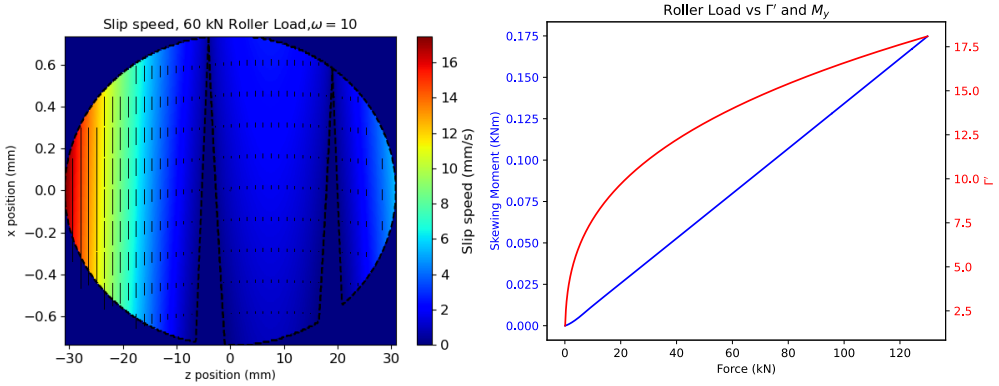

Figure 56: Case study SRB: Left- Stick/slip regions, marked by black outline. Right- Skewing moment (negligible) and Γ' vs. roller Load.

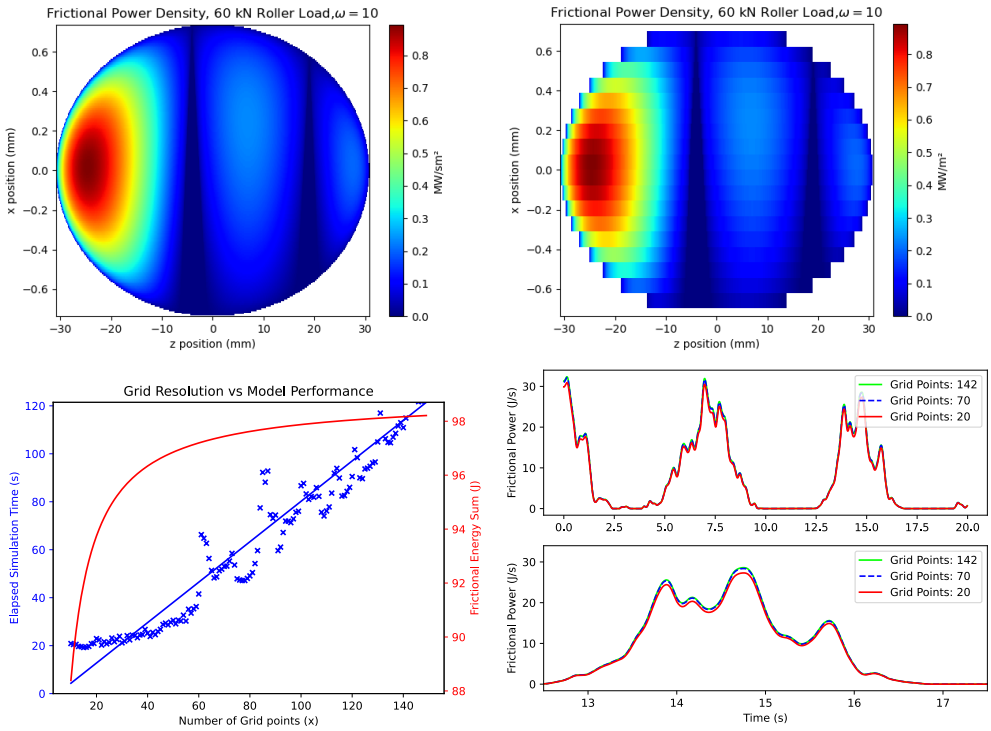

Figure 57: Higher resolution and lower resolution outputs. Even as few as 20 points along x provides adequate convergence.

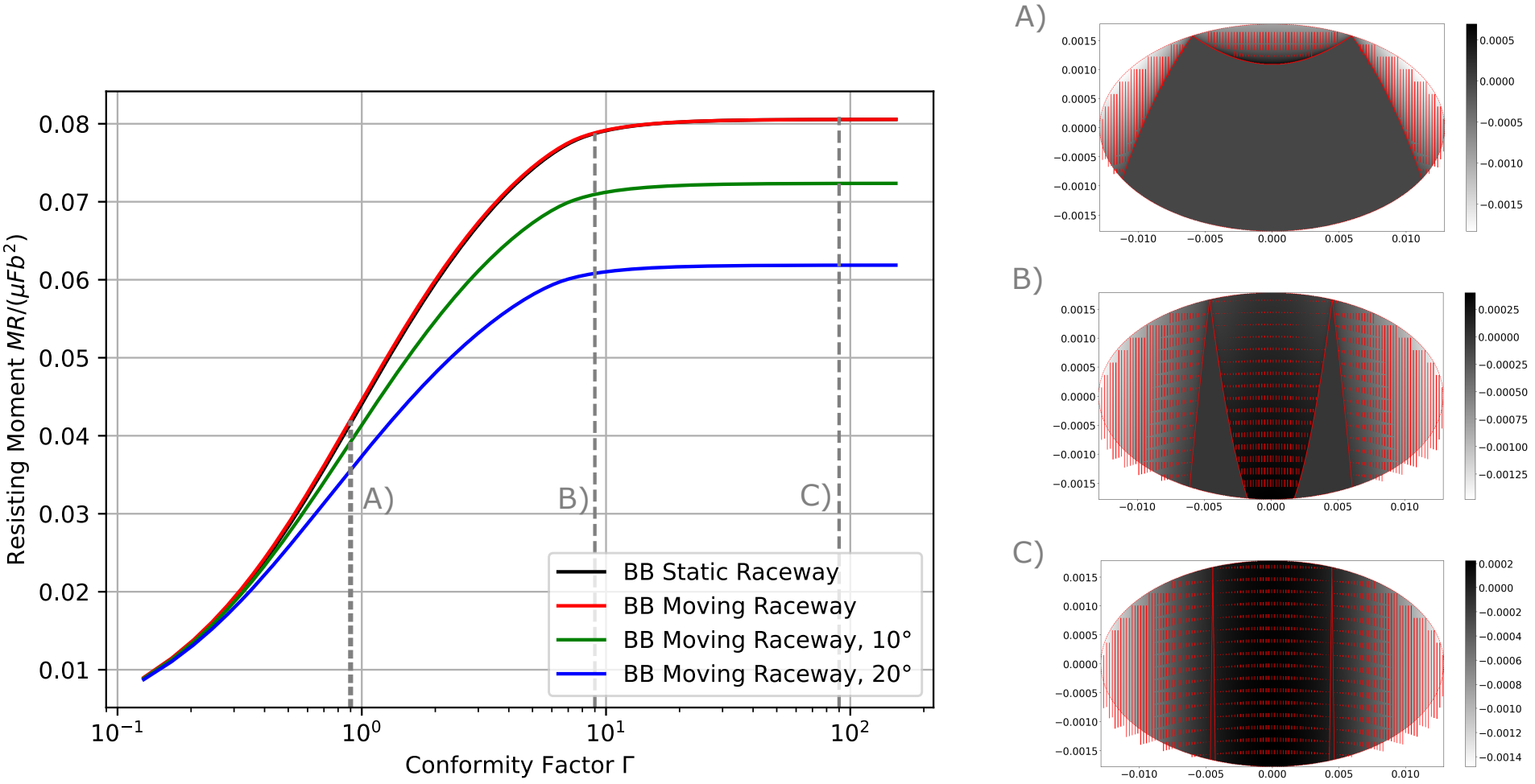

Figure 58: Classical resisting moment vs. Gamma for different scenarios: (1) Ball in static groove, (2) Ball in moving raceway, (3) Ball in moving raceway for 10 degree contact angle, (4) Ball in moving raceway for 20 degree contact angle. Slip profiles for case 1 $\Gamma = 0.9$ (A), 9 (B) and 90 (C) are given. This demonstrates that for case (C), full Heathcote slip is reproduced, converging on a resisting moment of 0.08 $m_z R/(\mu F b^2)$. This is indicated in the slip profile also, with stick being confined to two narrow lines. We note that the Heathcote dimensionless quantity of 0.08 is not a universal quantity. This can be demonstrated by considering the limiting case of Eq. (194), when the roller is cylindrical, $r_{1z} \to \infty$, and the integral becomes symmetric and vanishes.

The effect of skewing was also considered, with the moment m_y identified earlier by Eq. (195). This required consideration of both the skewing on the inner and outer patches. The contribution was found to be higher order, as both opposed each other $m_y = m_{y,in} - m_{y,out}$, resulting in a small relative skewing moment, which was linear with both load (Fig. 56), and angular speed. Whilst this effect is perhaps worth considering in higher fidelity simulations, to do so would require a better description of angular momentum coupling not seen in most rigid body models (Chapter.4).

It was also apparent for typical load ranges (0-130 kN), mean Γ' in the case study's typical load range is around 10. This indicates the turbine SRB's are mostly operating in the majority slip regime (Fig. 56, Fig. 58).

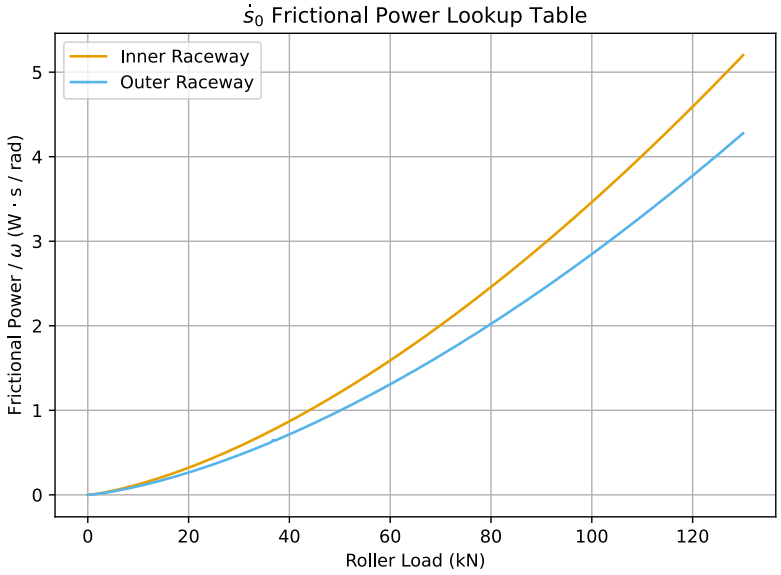

Figure 59: The look up Frictional Power per rads^{-1} scheme used for steady state microslip (henceforth denoted as $\dot{s}_0$). As power values are non-linearly dependent on geometry and applied load, simulations would involve numerous expensive repeat calculations. Recognizing this, significant time savings can be made, for increased accuracy (using higher N in table definition).

The results of this model were tested over different wind conditions, for both the upstream and downstream rows (Fig. 60), using a high resolution look-up table[17] and linear interpolation (Fig. 59).

Similar trends to initial macroslip results were found, with a peak in frictional metrics being associated with the operational thrust strategy of the turbine [18]. Unlike the initial macroslip investigation, this is not an artefact of the numerical process and does in fact indicate higher frictional powers and energies at these speeds.

[17] Eqs. (209, 210) both have linear dependence on angular velocity, and only are dependent on applied load and geometries, a repeat calculation for a memoryless system.

[18] Cumulative energy isn't presented here, as it is a simple conversion from power, the more fundamental quantity, and will accordingly have the same trends. Furthermore, since reported literature values are dimension specific [24], that of an energy value as opposed to an energy density, making comparisons for different sized geometries is not possible.

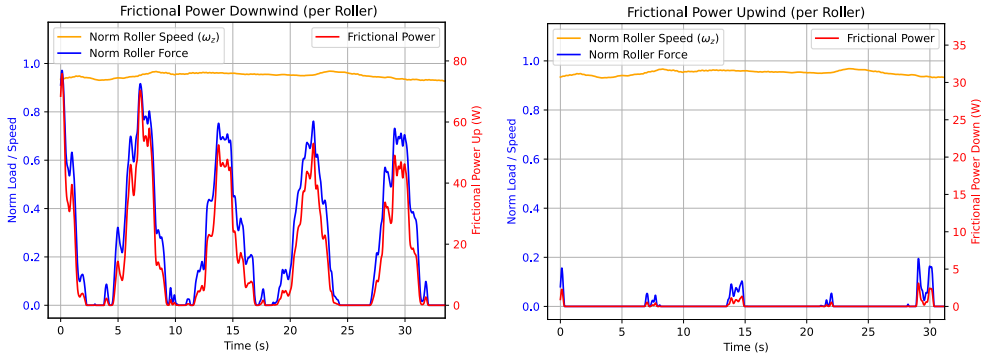

Figure 60: Real time results for 12A m/s. Power is most sensitive to force, due to rotational speed being kept fairly constant by control. Due to asymmetry the upwind row experiences significantly less force and thus lower frictional powers.

Assuming mean conditions in time are the same, powers were scaled by the total number of rollers[19], shown in Fig. 61. At peak values of ≈ 500 W, this is 3-4 orders of magnitude greater than the powers found by the macroslip model, indicating in this application microslip is a more important effect. The value of power densities however was still much less (Fig. 57) than the reported criterion for smearing damage ([48] - $1.5 \times 10^8 W/m$), even in the peak area due to angular asymmetry. The power also represented 0.03% of the total power of the 1.5MW turbine, a conservative absolute value, with literature placing values between 0.1 - 5% [144, 145].

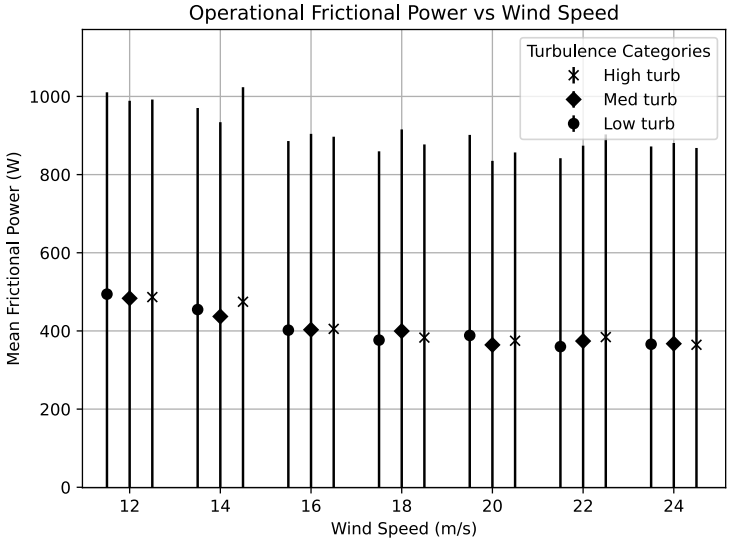

Figure 61: Frictional power results vs. windspeed's and conditions for steady state microslip results. Powers peak at 12 m/s, corresponding to the thrust strategy of the turbine and max roller load.

[19] 27

5.8 Conclusion

It can be concluded that steady state microslip is a more important consideration in bearing damage than macroslip in this instance, simply from the observations that frictional metric's are orders of magnitude higher, whilst the macroslip ones appear to effectively vanish. Interestingly, the trends between the two models are very different, further indicating the importance of selecting an appropriate model. Whilst energies and powers for the macroslip model were ultimately found to go up with wind speed, the model here found the opposite trend. This arises since there is no consideration of inertial effects or transients, solely being dependent on the magnitude of applied force, and rotational speed at a given time step. As a result, the 'most damaging' conditions, correspond to where there is the greatest roller load, i.e. the peak of the turbines thrust strategy.

Consequently, with no sensitivity to dynamics and applied load on average being similar between dynamic and static load cases, this model would predict similar frictional energies between cases. However, limitations exist due to the neglect of transient terms in microslip Eqs. (150,151), that due to the variability of wind loading conditions might require consideration. This will now be performed in the next Chapter.

6 Transient Microslip

The following Chapter will demonstrate the extreme differences in loading variability in a WTMB and a conventional power plant alternative: a motivation for a transient consideration of microslip. Due to the novelty and difficulty of doing so, methodology will be extensively covered, before frictional results over all wind conditions are analysed.

6.1 Introduction

The microslip model presented in the previous Chapter was steady state, meaning system conditions are solved as a succession of quasi-static steady states. Therefore, sudden changes in system state are not represented, and there is no knowledge of behaviour between the 'start' and 'end' points of the two quasistatic steps (Fig. 62). In many cases this is a very good approximation [75]. However inherently transient problems, such as those occurring in the main bearing, might require a full consideration to determine if such a steady state approach is appropriate.

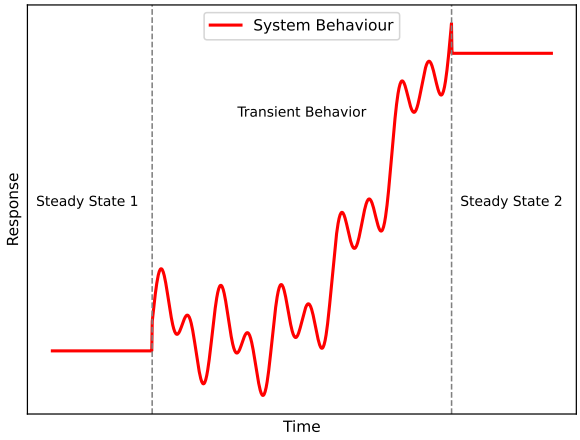

Figure 62: Steady state analysis disregards the period between the two regions. The accuracy of this approach will depend on the magnitude and time period of the transient domain.

Motivation for such a consideration will be provided in the following Subchapter, that provides a further brief study on loading characteristics of the MB. A transient model will then be developed and applied over a range of wind conditions.

6.2 Main Bearing Load Rates and Shock loading

Attention has already been drawn to the unique spatial, and high absolute, loads experienced by the main bearing [12]. However the rate of change of loading, hasn't received any attention, possibly in part because doing so would call for a treatment of the problem, that it will turn out is very challenging. These MB load rates will now initially be characterised.

The following summary statistics are compiled from the roller normal loads from the quasi-static model, when implemented across a range of aeroelastic model conditions. Simulated wind conditions (mean speeds 12-24 m/s) contained a shear exponent of 0.2, and were performed at three levels of kinematic turbulence (high - A, medium - B, and low - C, (as specified by IEC-61400 design standards). It is worth noting that the quasi-static model assumes instant load transmission, so might in parts overestimate the rate of applied load due to effects such as shaft flexibility. On the other hand, resonance and other dynamics are also ignored, and their absence could lead to an under representation of rate of applied load.

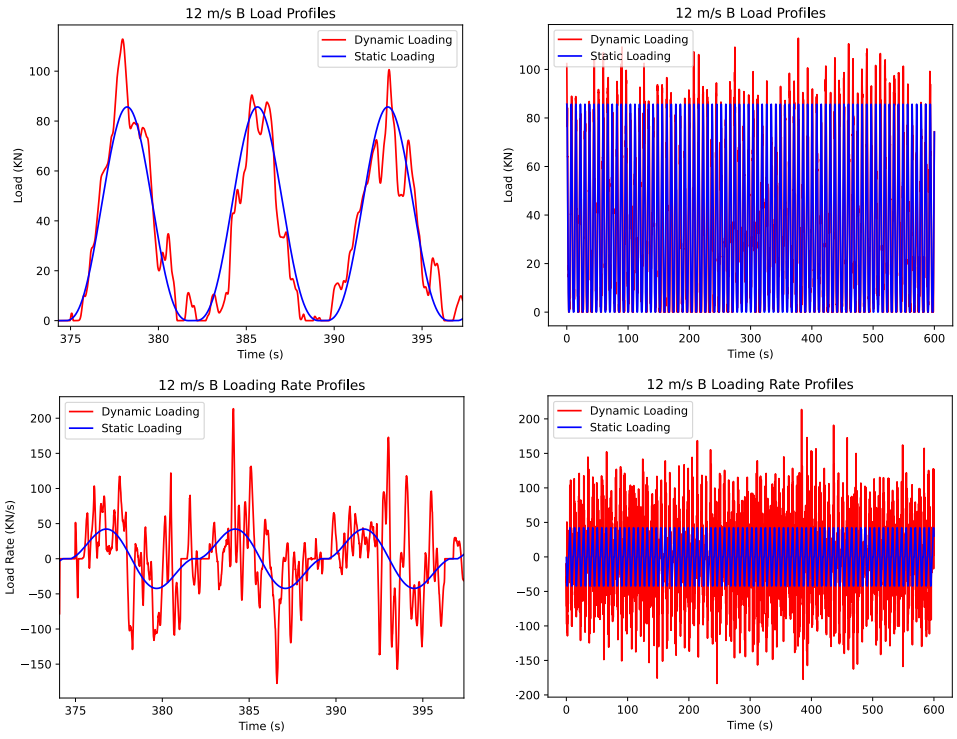

Figure 63: Absolute loads and load rates between a 'Static' load scenario (blue), i.e. a conventional power plant MB analogue, and a WTMB (shown in red). It is clear that whilst absolute load values are similar, the time derivatives vary significantly between cases.

The 12B case is explored as a benchmark for demonstrative purposes. 12 m/s- as this was identified as the highest frictional energy scenario by the microslip model due to the turbine control's thrust strategy. Level B was used as this is the median of the three turbulence groups. A constant load constant speed equivalent was used for comparison

purposes. This is henceforth referred as a 'static' configuration, due to the static nature of the bearing load vector, and is intended as a crude representation of a conventional power plant analogue.

Whilst the mean load values and gross load profiles are very similar between constant and dynamic cases (36.0 kN and 36.8 kN), there is a significant time based deviation present in the dynamic form (Fig. 63). Whilst the relative size of this fluctuation is not necessarily massive, its frequency is several times higher than that of the roller loading cycle.

Digging deeper we notice this rapid fluctuation means the time derivative of load $\dot{F}$ might be a better suited comparison metric. These can be seen to be vastly different (Table 8), with mean values of (23.1 kN/s, 34.0 kN/s) and maximum of (42.3 kN/s, 213.6 kN/s) between the static and dynamic case respectively. In fact, further investigation for a 10 minute simulation window, showed that approximately 1/3rd of the roller time is spent at loading rates higher than the max. loading rate in the static case. This is inclusive of the time the roller is unloaded.

These conditions are something the steady state microslip model is not sensitive to, instead relying only on absolute roller load at each step. Due to similar mean values between the constant and dynamic cases, it would struggle to distinguish between them, resulting in similar, and potentially erroneously low, predictions of frictional energies.

This max. value loading rate at 12 m/s B is chosen as a threshold for a comparison over the remaining conditions, and a 3 SD limit was applied to obtain subsequent maximum values, in order to not over represent noise.

The choice of threshold is arbitrary (justified in part by being associated with the highest frictional energies, and therefore most damaging with a non-transient consideration) but is kept consistent for demonstration. Future work might apply more advanced statistics.

At first glance it is immediately apparent that whilst the mean roller load is higher for the lower speeds, (resulting in higher frictional energies when compared to the steady state approach), loading rate increases substantially as windspeed climbs (indicated in mean and max), as does the roller time above threshold. These effects are captured in Fig. 64.

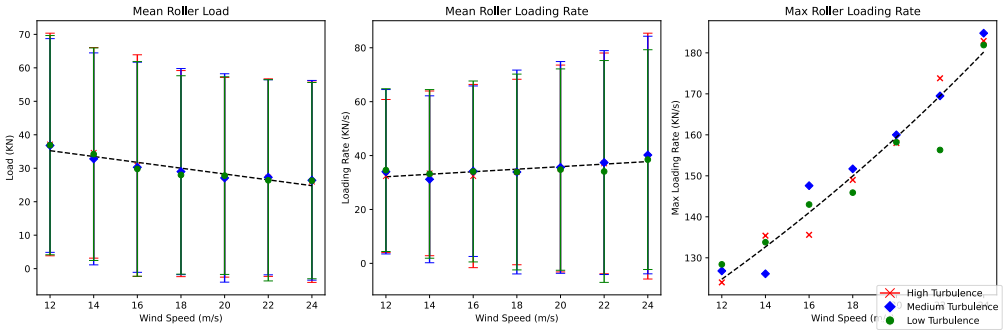

Figure 64: Trends in mean roller loads: F decreases across wind speeds, but rate of load, $\dot{F}$ goes up. This motivates the development of a model that is sensitive to these conditions.

Wind Condition Roller Load Summary Statistics					
Wind Speed	Turbulence Level	Mean Roller Load (kN)	Mean Roller Loading Rate (kN/s)	Max Roller Loading Rate (kN/s)	Roller time above Loading rate threshold (%)
12	A	37.1	32.4	124.0	31.5
12	B	36.8	34.0	126.8	33.2
12	C	36.9	34.6	128.4	34.1
14	A	34.6	33.4	135.4	33.3
14	B	32.8	31.2	126.1	30.9
14	C	34.2	33.2	133.8	32.8
16	A	30.8	32.4	135.6	32.1
16	B	30.3	34.2	147.6	33.4
16	C	29.8	34.1	143.0	33.4
18	A	28.4	33.9	149.0	33.2
18	B	29.0	33.9	151.7	33.4
18	C	28.0	33.9	145.9	33.9
20	A	27.3	35.2	158.0	33.8
20	B	27.1	35.6	160.0	34.0
20	C	27.8	34.8	158.2	33.3
22	A	27.2	37.1	173.8	34.9
22	B	27.3	37.4	169.5	35.6
22	C	26.4	34.1	156.3	32.3
24	A	26.0	39.8	182.9	36.6
24	B	26.4	40.2	184.8	37.2
24	C	26.3	38.5	181.9	35.5

Table 8: Table of roller loads and rates of loads over wind conditions.

This reflects the increasingly chaotic nature of the wind leading to greater rates of change. Increasingly violent and abrupt changes in the wind-field, direction and magnitude, result in high impulses being imparted on the bearing. Counter-intuitively turbulence level don't seem to have significant effects apart from perhaps producing slight increases in variability of loading rates at higher wind speeds. This could be down to the simplicity of the turbulence model or non-linearity of the wind drivetrain interaction, but is otherwise unexplainable and would be an area ripe for further work.

Another interesting feature found by manually sifting through the data (Table 8) is the occasional existence of exceptionally large max. values, corresponding to the presence of what are known as *load reversal events*, where a gust of wind lifts the shaft up, before slamming it back down, resulting in huge peak instantaneous accelerations, at least two orders of magnitude above threshold. These only seem to occur at higher wind speeds, and don't appear to correlate in magnitude, possibly due to the combined effects of their low frequency, the length of observed window, and the stochastic nature of wind. Whilst it was not possible to consider such matters here due to the 3 σ threshold, investigating the effect of such loading events on the health of the bearing should be a matter of future investigation.

Large loading rates may be important for system health. *Shock loading*, loading that is characterised by rapid rates of change of force with time [146], could be very important for system health and longevity. Mechanical shock has several associated routes to premature failure. A given single shock may not appear to cause damage, but repeated low-level shock expose could invoke fatigue failure [147]. Alternatively a single high shock could breach a threshold and invoke accelerated material failure [148]. Both of these two mechanisms respectively can be crudely captured by the mean and max rates of loading already presented. They will be explored further by the model later on.

Examples of other operating conditions transients where such high load rates might occur are controlled and emergency stops - found to be three times more damaging than normal stops on the drivetrain in one fatigue analysis study on such events [149]. Due to 80-90% of the turbines relative inertia being upstream in the blades [150], such stops are accompanied by huge and rapid oscillations in torque on the low speed shaft and bearings [151].

Care should be taken at this point to state: the systems sensitivity to sudden applied loads is *not currently known* and we are not claiming to make any conclusions from simply these observed load rate trends a-priori. That is to say, these rates of load application might not be high enough, or conversely the constant load case in itself may already meet the requirements to be damaging.

However, the lack of failure of similarly highly loaded static industrial equivalents (e.g. conventional power plants) and the stark difference in loading rates between the two provides significant motivation for further analysis. It is interesting to note at this point that a model accounting for loading rates could give very different conclusions to the micro/macroslip results, depending on the systems sensitivity, and this sensitivity should now be determined.

Although effects of high loading rates could well have significant consequences on interior material mechanics, and should be investigated in future, the key area of interest here is restricted to the frictional interface for a few reasons. Firstly, to maintain consistency, secondly because 67% of wave energy is radiated via the surface [152], and finally

due to the presence of large tractions on the surface, which will mean that this relative displacement will radiate significant energy.

6.3 Elastodynamics

Again, the problem will be a consideration of relative slip between surfaces, but this time how loading transients effect it. This involves consideration of the full non steady microslip equation, e.g.:

$$\dot{s}_x(x,y)/V = \xi_x - \psi y/c + \left(\frac{\partial u_{x1}}{\partial x} - \frac{\partial u_{x2}}{\partial x}\right) + \left(\frac{\partial u_{x1}}{\partial t} - \frac{\partial u_{x2}}{\partial t}\right)/V \tag{211}$$

that, it transpires, can be decomposed into:

$$\dot{s} = \dot{s}_0 + \dot{s}' \tag{212}$$

where $\dot{s}_0$ is given by the earlier steady rolling equation (Eqs.[154-157]), and $\dot{s}'$:

$$\dot{s}' = V\left(\frac{\partial u_{x1}}{\partial x} - \frac{\partial u_{x2}}{\partial x}\right)' + \left(\frac{\partial u_{x1}}{\partial t} - \frac{\partial u_{x2}}{\partial t}\right) \tag{213}$$

The primed indicates this is the decoupled dynamic strain.

The presence of the two final terms significantly complicates solving this equation, as the conventional, previously used, elastostatic problem, goes from parabolic, to hyperbolic and time dependent [82, 83], -a field of study known as Linear *Elastodynamics* [153]. Additionally, the strain field is now also non-steady, and needs to be evaluated accordingly. This level of complexity perhaps explains the lack of literature on microslip transients.

Kalker produced a series of influential papers on transient effects in mircoslip [80, 81, 154, 155], but neglected inertial effects. The importance of these inertial effects was highlighted by Gurrutxaga-Lerma in two impressive papers on slip in the presence of friction in dynamic contacts of planar and antiplanar half spaces [82, 83]. In these the author stated [82] *'there exist a considerable number of practical applications where loading transients affect contacting interfaces. Such situations are found in the* ***bearings of rotating machinery*** *(e.g.... **wind turbine shafts**'*, and,[83] *'Elasto dynamic contact is of particular relevance at high strain rates, under* ***shock or ramp loading****....'*. These mathematically involved (common to the field) papers were an elastodynamic (ED) version of the Cattaneo- Mindinlin problem, and despite some consideration of dynamic deformations in rolling contacts (e.g. Tyres [156]), and effects such as outer ring flexibility on bearing power losses [157], there appears to be a gap in knowledge on specific roller raceway elastodynamic interaction. At the time of writing, it the author is unaware of any existing consideration of inertial effects applied to bearing frictional interfaces [158], and certainly no application to highly relevant Wind Turbine Main Bearing engineering. Before proceeding, it is worth stating that the worth of this model presented herein will lie in it's novelty; it tackles this complex, overlooked problem, in an easy to follow form, and thus justified simplifications will be present. That being said, fairly standard methods will be applied.

6.4 Governing Equations

Evaluating the temporal partial in Eq. (213), and how displacements u_x evolve with time for the two contact surfaces, involves revisiting linear elasticity. Linear elasticity has already been used in the previous Chapter in the elastostatic case, which involved solving the displacements for the Navier Cauchy equation for equilibrium:

$$(\underline{K} + \frac{1}{3}\underline{G})\nabla(\nabla.u) + \underline{G}\nabla^2 u = 0 \tag{214}$$

Where $\underline{K}$ and $\underline{G}$ are the bulk and shear moduli. There are numerous ways this equation can be solved subject to appropriate boundary conditions, e.g. green functions [105], separation of variables [159] and bi-harmonic potentials [160] to name a few.

The elastodynamic case is an extension of the same theory, and so it maintains a consistency and ease of comparison between the two Chapters. Due to the complexity involved and resultant text brevity, results will merely be stated, but the reader is referred to a highly recommended accompanying introduction in [159]. This provides an accessible, but detailed, modern background on the topic. Displacements are given by the linear wave equation:

$$\rho\frac{\partial^2 u}{\partial t^2} = (\underline{K} + \frac{1}{3}\underline{G})\nabla(\nabla.u) + \underline{G}\nabla^2 u \tag{215}$$

Where ρ is the mediums density.

Although most dynamical systems are intrinsically non-linear, the act of *linearisation* simplifies the problem substantially. Linearisation is the act of expansion over a small physical quantity about an equilibrium point, here displacement, where only resultant first order linear terms are retained. This implies that at no point do the strains (dynamic or static) surpass the elastic threshold, past which the theory becomes non-linear and invalid. Therefore, all deformations are perfectly elastically reversible.

The benefit of linearisation cannot be understated: the nodes of discretized domains can be solved independently [20] and superposed, enabling the strength of modern computational techniques such as vectorized approaches in Python, and parallelisation/ use of clusters. All such methods were implemented here. This makes solving problems in large scale systems tractable, and known fundamental solutions can be combined to give a representation of problems of more complex general configurations. Considering the difficulty in finding static slip distributions (Chapter 5.3), this enables an easier numerical description of our dynamic problem.

[20] Unlike interdependent non linear systems, which often require sequential operations with significant overhead.

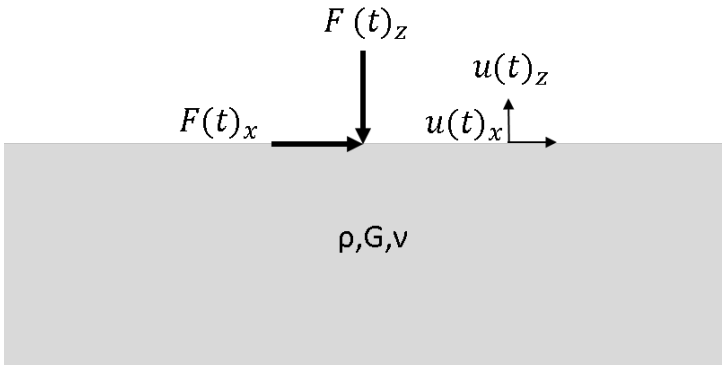

Figure 65: Lambs problem describes the transient surface displacements along an infinite elastic half space (a common method to contact mechanics [104, 105]), upon application of a unit step force point load (Eq. (216)) at a distance x. This displacement response is a fundamental solution. From this time evolving displacement, surface velocities and strains can be deduced.

6.5 Lambs Problem

The next simplification which will be made is the use of the infinite elastic half-space approximation. This simplifies boundary conditions significantly, as it only requires the wave amplitude to be finite at large distances [159]. It should be recognised this is a simplification, and in actuality there will be other wave phenomena such as elastodynamic reflections, and interactions from neighbouring rollers. However, we are concerned with the dominant dynamics in the contact from the primary roller, and again, the half space approximation was made use of in [105], from which the earlier steady-state microslip model was used. Furthermore, due to the $1/r^2$ decay of amplitude present, local effects will invariably dominate.

Fundamental solutions (known as *displacement responses*[21] exist to describe how the surface of this elastic half space material will behave and deform upon the application of an instantaneous unit step function point load on the surface of the form:

$$f(x,z,t) = F\delta(x,z)\mathscr{H}(t) \tag{216}$$

Where F, δ and $\mathscr{H}$ denote the force magnitude, Dirac delta and Heaviside function respectively. A visual of the problem statement can be seen in Fig. 65.

This problem is familiar to, and of interest in geophysics, where it is used in modelling earthquakes, but applies for general ν of linearly elastic materials (i.e. Steel), and is known as Lambs problem, after the original paper [162].

The speeds of the three stress waves (shear C_s, pressure C_p, and Rayleigh C_r) mediating a disturbance on the surface a linear isotropic half-space, are found from the three roots $\underline{\kappa}_1^2, \underline{\kappa}_2^2, \underline{\kappa}_3^2$ of Rayleigh's Bi-cubic function [22] :

$$16(1-\underline{a})\underline{\kappa}^6 - 8(3-2\underline{a}^2)\underline{\kappa}^4 + 8\underline{\kappa}^2 - 1 = 0 \tag{217}$$

Where $\underline{a}$ denotes the ratio of speed of S to P waves C_s/C_p. Here is an unintended consequence of traversing multiple fields, as both symbols appearing above are distinctly

[21] See Achenbach [161] for a well detailed derivation

[22] See Eringen and Suhubi's magnum opus *Elastodynamics* [153] for more information on this function.

different from the non underlined representation in Hertzian contact theory.

The first root is real and true- and has a physically meaningful value (the ratio of R and S waves). The last two are false and turn to complex conjugates when Poisson's ratio exceeds 0.2631. There are interesting implications for additional roots of this equation in proving the dynamic instability of elastic media above the unphysical limit of $\nu > 1$ [163].

Initially the method explored was via the 3D displacement responses[23] from the remarkably accessible Kausel's *'Lamb's problem at its simplest'*[85], which provides 3 dimensional solutions to the problem in a concise form[24]. The text is worth highlighting to the (likely un) interested reader, for its clear presentation and modern explanation of a challenging field. However, due to the unique challenges of the application this method was discarded in favour of the 2D version of Lamb's problem. These issues are set out, in order to assist any future development.

Unique numerical challenges

1. High wave speeds combined with small spatial distances of interest mean very high frequency discretization is required, due to a CFL-like relationship [a], common to wave propagation problems.
2. Singularities in the displacement response functions mean detailed resolution must be used.
3. High rates of load further necessitate a high frequency resolution, else *aliasing* will occur.
4. High spatial gradients in load rate (high variation over a small area) require a very fine spatial discretization between grid points.
5. High contact ellipticity: whilst interest is in the motion in the x direction, so a suitable resolution was required for dx; typically one should match step size over both axes ($dx = dz$), for simulation stability. This necessitates many total grid points, despite primary interest in displacement parallel to rolling direction. Furthermore, it turns out, this mandated running simulations until the slowest mode of vibration had traversed from the full length of the contact $2a$, $\kappa(40)$ times the length scale of actual interest ($2b$). With the $\mathcal{O}(N^2)$ computational cost of convolution, this becomes a prohibitively costly calculation.
6. There is no far-field approximation in such a problem, as there commonly are in simulating other long-range forces such as electromagnetism or gravity. Despite a $1/r$ decay being present, all points in the contact have to be fully considered for a knowledge of displacements interior to the contact[b]. This is because, despite this decay, the interacting number of loaded points for a circle increases as r^2, so will behave similarly for an ellipse.

[a] This is not strictly the CFL condition, as we are not using an explicit time-stepping method to integrate the wave equation of motion.

[b] Far field approximations could be used if looking outside the contact.

To summarise, the primary issue with this uniquely challenging simulation, is that there

[23] Elastodynamic displacement versions of Boussinesq Cerruti.

[24] It is worth noting that alternatives exist [164, 165, 166].

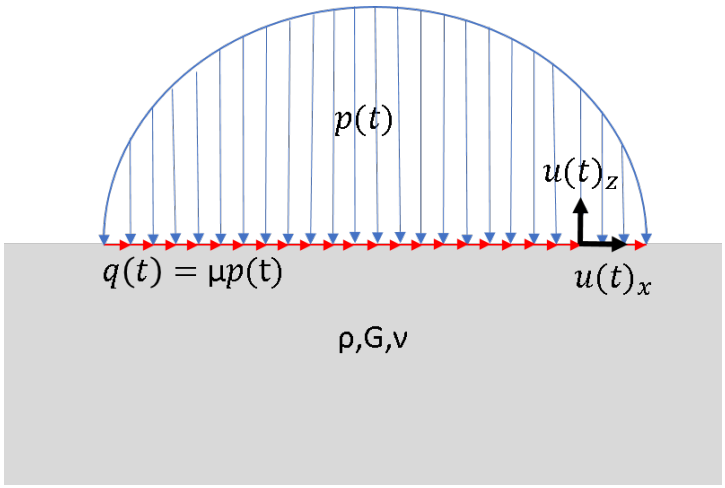

Figure 66: The displacement solution to Lamb's problem (Fig. 65), can be used to linearly superpose pressure distributions to find a solution to a general time evolving distribution. The analysis presented does this numerically, although there are significant challenges. In this way, the time evolving displacement for a given point inside a contact patch may be found.

is an area of interest spanning several different scales of both time, and space[25]. Both the short distances required for high fidelity under high rates of load, as well as the very small time-steps for accurate wave propagation, when combined with the relatively much longer length scale of $2a$, and the respectively long simulation time for all 3 waves to have fully interacted over this, invoked expensive costs.

All of the above problems posed significant challenges throughout the course of code development and in attaining a stable set of results. Quite often the results were not stable, and it was not immediately apparent why. It transpired that any of a number of the above could cause numerical issues, despite manifesting as similar looking 'symptoms' in unstable results. Greater detail is given in the Appendix F, which discuss how accuracy was ensured and these issues overcome.

Thus, the 2D solutions to Lamb's problem [84] were implemented. This reduced dimensionality, was more efficient, and so we could now collapse the area of interest to time and length scales of b, increasing efficieny by $\kappa^3 = 64000$ [26]. Considering the planar nature of the problem, and the parallel formulation of the steady state version, this was deemed an adequate approach.

[25] Something of a recurring theme, with the stiffness issues encountered in Chapter 4 due to the vastly different scales in dynamics.

[26] Spatial points reduced by factor κ, simulation duration cut by factor κ - giving a convolution reduction of κ^2. A naive reduction if equivalent methods were used, that they weren't. A full investigation into the 3D coupled problem is possible, with time, and should be performed in future. Code has partially been developed to do so, using high resolution HDF55 displacement function look up tables, adaptive temporal resampling, hybrid parabolic spatial discretization to match pressure rate profiles, as well as condensed representation of u_n waveforms.

6.5.1 2D Displacements

Due to high ellipticity, the problem can be approximated as a line contact. This enables increased spatial resolution with the same available resources, and use of the 2D planar wave approximation: the special case of a wave or field where the displacement is constant over the direction parallel to the propagation.[27]

Thus, the piecewise displacement functions for the 2-dimensional variant of Lamb's problem can be used, in which displacements are solved for a distance, x, from a source on a 2D lower elastic half-space. The source has dimensions:

$[F][T]/[L] = [\text{Impulse}]/[\text{Length in } y \text{ direction}]$

There are four different surface motions invoked from a normal and a tangential load (Figs. 65). Thus, four different response functions exist for a force of the form of Eq. (216): u_{xx}, u_{xz}, u_{zz} and u_{zx}. For each displacement response, u_n generally, the first subscript indicates the direction of the, load, vertical z or horizontal x, and the second the direction of the displacement. Time $\tau = tC_s/|x|$ is dimensionless and was transformed too when evaluating numerically.

$$u_{xx} = \frac{1}{\pi \underline{G}|x|} \begin{cases} 0, & \tau < \underline{a}, \\ \frac{4\tau^2(1-\tau^2)\sqrt{\tau^2-\underline{a}^2}}{(2\tau^2-1)^4+16\tau^4(\tau^2-\underline{a}^2)(1-\tau^2)}, & \underline{a} \leq \tau \leq 1, \\ \frac{-\sqrt{\tau^2-1}}{(2\tau^2-1)^2+4\tau^2\sqrt{\tau^2-\underline{a}^2}\sqrt{1-\tau^2}} & 1 < \tau, \end{cases} \tag{218}$$

Only u_{xx} is used, being the only relevant displacement for tracking the moving relative dislocation parallel to the surface of the roller and the raceway[28]. The form of u_{xx} is visually explored in Fig. 67, showing the decay of the moving wave at different distances. These displacement fields are the dynamic analogue of the elastostatic Flamant solutions [104], though by construction, these static limits are not recovered as $t \to \infty$. See [82, 83] for a discussion of this. This means these equations model solely the dynamic components of displacement, the perturbation from the static. Thus, to find net microslip involves superposing the elastostatic solutions with the elastodynamic, justification for Eq. (212).

Therefore, for an impulse of form Eq. (216), by symmetry of Eq. (213):

$$\dot{s}' = 2\left(V\frac{\partial u_{xx}}{\partial x} + \frac{\partial u_{xx}}{\partial t}\right) \tag{219}$$

This can be analysed by using a simple finite difference method and can be implemented for a given point relative to an origin at, and along, x and t.

However, this is only representative of the slip wave moving between two surfaces due to an idealised instantaneous point load. Obviously this needs to be modified to represent a rapidly applied, but non instantaneous, load distribution, as of the type seen in Fig. 66. The natural question then arises, how might a transient load profile look, and how might it be represented?

[27] A true plane wave cannot physically exist, as it would have to fill all space; however, it is a widely used physical approximation.

[28] u_{zz}, u_{zx} represent out of plane vibrations, and u_{xz} is discarded via the same reasoning in going from Eq. (201) to Eq. (202).

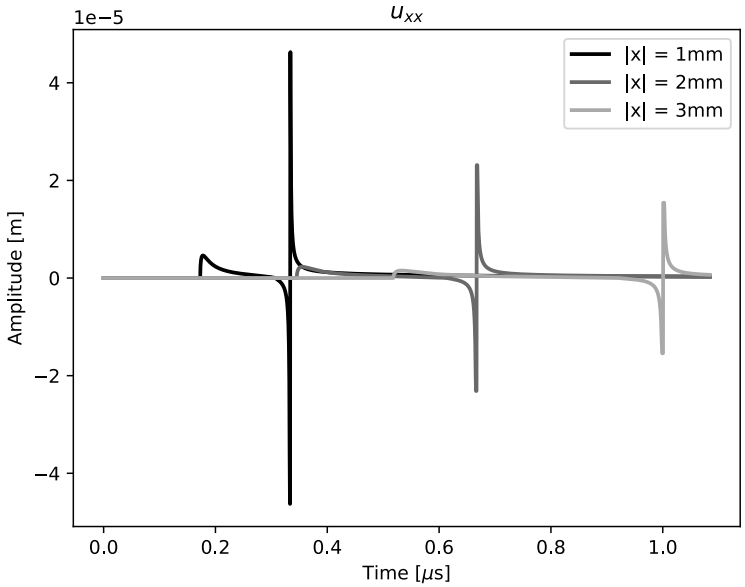

Figure 67: The form of the 2D displacement function for an impulse at different distances. Note the moving singularity at $\tau = C_s/C_r$.

6.6 Rate of Loading Profile

Ultimately this model will take the roller loading history, from that imparted by the quasi-static module in the previous parts of this work. Therefore, loads and, loading rates from finite differences, are already known. The next step is finding the pressure rate profile for applying to displacement functions, as the line contact will be discretized. Consequently a given force input, $\dot{F}$ needs to be transformed to a transient pressure distribution $\dot{p}(x)$. Then a transient traction distribution, from this needs to be established, $\dot{q}$, relevant for for finding displacements. How this is done will now be outlined.

Full understanding of a transient pressure profile is a difficult task, especially if lubrication is considered [167, 168]. Not only is the pressure profile complex, but the area will expand, bringing additional regions into contact, subsequently interacting elastodynamically. Therefore assumptions and simplifications are necessarily made [29]. The first of these being :

$$\frac{dp}{dt} \approx \frac{p(x,y,t+\Delta t) - p(x,y,t)}{\Delta t} = \frac{p_0(t+\Delta t) - p_0(t)}{\Delta t}\left(1 - \frac{x^2}{b^2}\right)^{\frac{1}{2}} = \frac{\Delta p}{\Delta t} \tag{220}$$

I.e. pressure rate, like absolute pressure, is also of Hertzian and parabolic form.

The next simplification, is that a, and b, and thus $\dot{p}$ remain constant, throughout the simulation time-step, Δt. Therefore they are resolved from the absolute force at the end of the previous/start of the new time-step. This simplification is motivated as the

[29] It is worth taking a moment to distinguish between the two. A simplification: a purposeful reduction in complexity to make problem more tractable, being aware of the limitations of making it. An assumption - where necessary adjustments are made without proof, due to a lack of data, knowledge, or an impossible computational complexity, in order to progress a model.

rate of pressure change increase far outstrips the rate that the area of the contact patch grows, as, for a line contact equivalent [23]:

$$b = \left(\frac{8FR_x}{\pi\tilde{E}'}\right)^{1/2} = k_1 F^{1/2} \tag{221}$$

and:

$$p_0 = \left(\frac{2F\tilde{E}'}{\pi R_x}\right)^{1/2} = k_2 F^{1/2} \tag{222}$$

Where $\tilde{E}' = (1 + R_x/R_z)\mathcal{E}(\kappa)^{-1}E'$ is the adjusted reduced modulus. By making the comparison that k_2/k_1 for our bearing is very large ($\tilde{E}'^2/4R_x^2$), we can see the rate of growth of b is dwarfed by that of p.

Such assumptions as these do have precedents in other practical applications in literature [104], and will increase in accuracy as Δt gets smaller. This is part of a larger issue in discretization, and will be kept in mind going forward. As long as the steps are small enough, results should be acceptable for initial analysis.

The last assumption made is that traction is of Coulomb form:

$$q = \mu p \tag{223}$$

and by similar logic/reasoning to above :

$$\frac{dq}{dt} \approx \mu \frac{\Delta p}{\Delta t} \tag{224}$$

The first is a regularly made assumption in contact and numerical mechanics [75], and as the system will turn out be slipping due to vibrational dislocations between surfaces, it is assumed sufficient to take μ as 0.1, the dynamic value, in the ensuing investigation. It should be remarked, it is known that the coefficient of friction will vary spatially across the contact (see [169, 170, 171]), and also with slip speed. This should be taken into account when interpreting results.

The next Subchapter will look at taking the forms of $\dot{p}$, and $\dot{q}$, and looking at how they might be represented in the time domain to find resultant displacements.

6.7 Temporal Regularisation

u_{xx} is formulated for a Heaviside load. This is a load applied suddenly in time, $\mathscr{H}(t)$. As this is an applied Chapter, actual time will be used instead of dimensionless time in the explanation, since it is easier to match up with real world variables such as pressure rates and powers. The model enumerated here switches between both.

As prior discussed, this is not a physical representation of loading, as loads are applied over a finite timescale, and do not have discontinuities in gradient. Therefore a smooth approximation to this function is required, that converges on $\mathscr{H}(t)$ when a regularisation parameter $\epsilon_t \to 0$. A common approximation is an arctan load [172, 173, 174] (see Fig. 68), a loading profile approximation that will be used here:

$$\mathscr{H}(t) \approx g_\epsilon(t) = \frac{1}{2} + \frac{1}{\pi}\arctan(t/\epsilon_t) \tag{225}$$

which approaches $\mathscr{H}(t)$'s true form as $\epsilon_t \to 0$.

It is therefore the gradient of the Heaviside approximation $g_\epsilon(t)$, which determines the rate at which the load is applied with time- a quantity sometimes denoted in physics and mechanics as *Yank*[30]. This is:

$$\frac{dg_\epsilon(t)}{dt} = \frac{\epsilon_t}{\pi(t^2+\epsilon_t^2)} = f_\epsilon(t) \tag{226}$$

This converges on the delta functions true form as $\epsilon_t \to 0$ (Fig. 68), and is a smoothed approximation.

Assuming load is applied at $t = 0$, ϵ_t may be configured to match with instantaneous load rate, i.e. the maximum of $f_\epsilon(0)$. Practically speaking $\epsilon_{i,t} = (\pi\dot{q}_i)^{-1}$ for the local load location i, [31]. These may be inferred from global loading rates and Eq. (224). It can be seen with smaller ϵ_t, corresponding to higher loading rates, steeper step load approximations arise, and higher derivatives of these (peaks of f_ϵ) are present. However, the integral of f_ϵ (physically speaking the total applied force), is by definition unity.

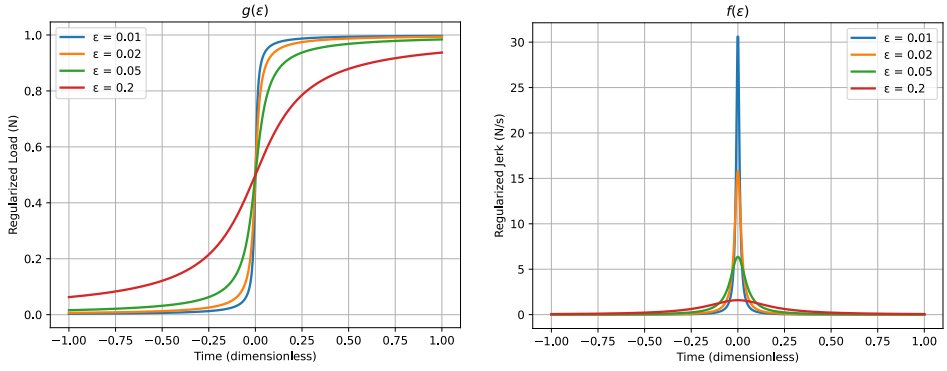

Figure 68: The effect of ϵ_t on load profile (g_ϵ), and on the rate of change of load profile (f_ϵ).

[30] *Jerk* [175] is the only slightly more commonly used massless equivalent- i.e. an analogue of what acceleration is to force.

[31] $C_s/\dot{q}_i$ if dimensionless time is explicitly used.

Since the elastic wave equation is linear, and u_{xx} is a response to a Heaviside load, the smoothed displacement u_ϵ to the loading profile of $g_\epsilon(t)$, or equivalently $f_\epsilon(t) * \mathscr{H}(t)$, is given by [172]:

$$u_\epsilon(x,t) = \int_{-\infty}^{\infty} f_\epsilon(t-t')u_{xx}(x,t')dt' \tag{227}$$

Since this identity isn't immediately obvious or readily available in literature, a proof is in the Appendix E, to which the reader is referred. The results of this convolution for several different values of $f_\epsilon(t)$ is given in Fig. 69.

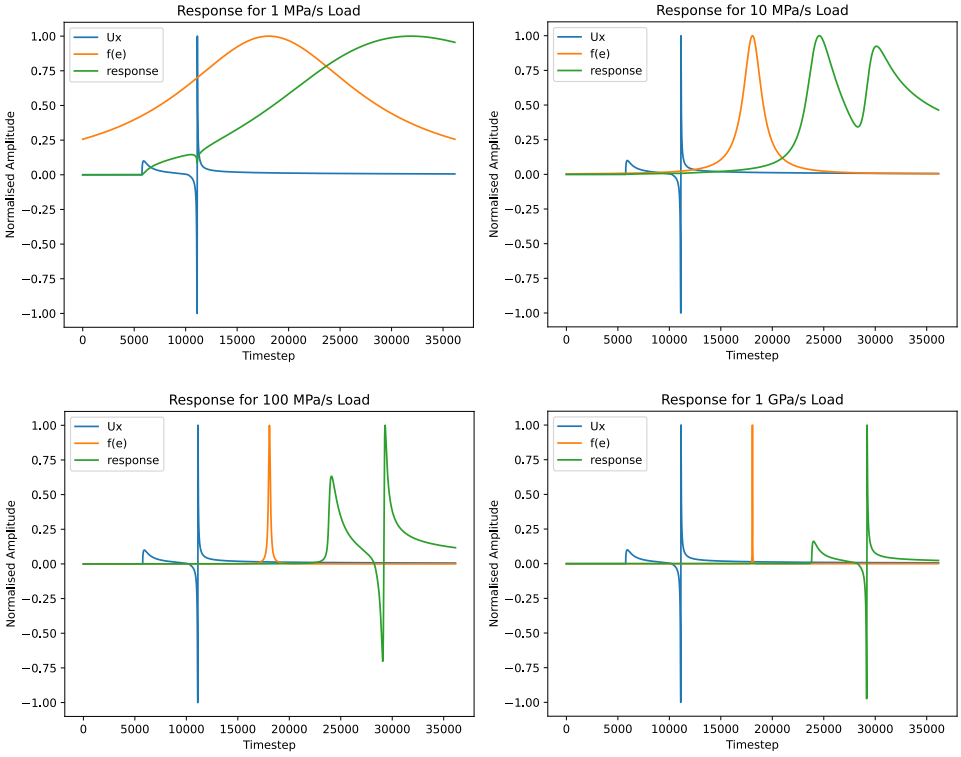

Figure 69: Impulse, response function, and resultant displacement response from different loading rates. Results are normalised, but reduce in width and increase in amplitude with larger load rates.

However, additional complex and important issues need consideration. As u_{xx} is formulated for a unit load, in practice an additional factor of dF, the total force of the loaded element over the time-step Δt, will need to be accounted for.

Now, each $f_{\epsilon,i}$ is representative of a tractive load increase, of unity, being applied over a discrete element, at a relevant load rate. For a local element, that has a pressure rate of $\dot{q}_i$ for a given simulation time Δt, there therefore is a net pressure increase of:

$$\Delta q_i = \frac{dq_i}{dt} * \Delta t \tag{228}$$

As each $f_{\epsilon,i}$ is representative of a pressure increase of unity there needs to be a total number N_ϵ of Δq_i of $f_{\epsilon,i}$, each separated by a unit in time of $\dot{q}_i^{-1}$, i.e. the reciprocal of

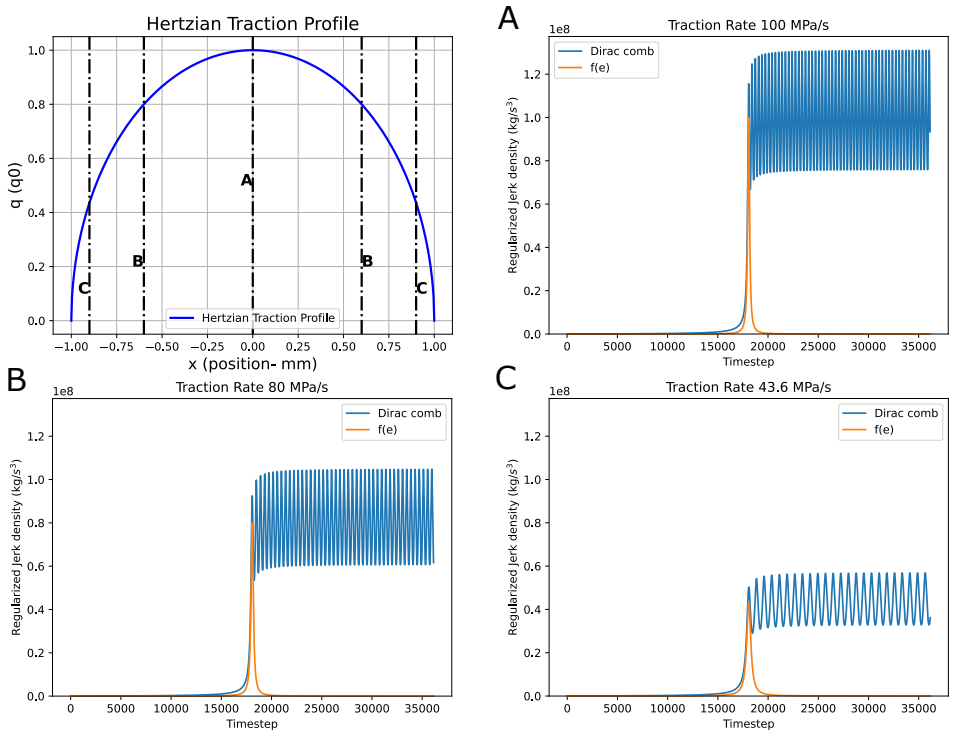

Figure 70: Spatial variation of Ш_ϵ across a transient traction profile.

the tractive load rate:

$$\text{Ш}_{\epsilon,i} = \sum_{K=0}^{N_{\epsilon,i}} (f_{\epsilon,i} - KT_i), \quad T_i = \left(\frac{dq_i}{dt}\right)^{-1} \tag{229}$$

This is a smoothed approximation of a *Dirac comb* Ш, that converges on the true form as $\epsilon_t \to 0$:

$$\text{Ш}_{\epsilon=0} = \sum_{n=-\infty}^{\infty} \delta(x - nT) \tag{230}$$

Again, $\text{Ш}_{\epsilon,i}$ will vary for each loaded element inside the contact patch, and needs to be configured according to the local value of ϵ_t (Fig. 70).

Therefore, the total effect of a loaded element, at x, from a transient pressure impulse lasting duration Δt, can be approximated as:

$$u_\epsilon(x,t) = \int_{-\infty}^{\Delta t} \text{Ш}_\epsilon(t - t')u_{xx}(x,t')dt' \tag{231}$$

This is extended over the entire line contact to describe the state of the system between time-steps as:

$$\int_{-b}^{b}\int_{0}^{\Delta t} \text{Ш}_\epsilon(x, t - t')u_{xx}(x,t')dt'dx \tag{232}$$

A discretized version of this equation was subsequently solved for, where each independent element i had its own Ш_i, dependent on its local traction rate $\dot{q}_i$, varying over the contact. Thus the entire problem over the domain of N elements becomes a set of N time evolving linear equations, that can be solved in parallel [119, 159]. This is compatible with a vectorized, parallelised method in Python.

6.8 Simulation Time

The duration of this simulated time-step in its most complete form would be that matching the quasi-static/shaft loads model input frequency, hitherto 50 Hz 0.02 s. With the necessary frequencies required to avoid aliasing and ensure stability, even running a 0.02 s simulation would be invoke considerable computational expense.

However computational cost can be minimized by recognizing that after the two furthest most points have exchanged Rayleigh waves with each other in the domain (i.e. opposite points along the semi-minor), outputs will start to become reflective of the rest of the duration of the remaining simulation time-step Δt. This is why a 2D method is more efficient, as $b \ll a$. The entire domain will now be fully internally interacting. However, a snapshot of instantaneous values at this point ($t = 2b/C_r$), shouldn't strictly be used, due to the complex nature of wave interaction, and the set of different frequencies in loading rates over the domain. Instead, the system will be in a *dynamic equilibrium*, in which metrics fluctuate, around a mean value over some characteristic time period (Δt_{char}). Hence, the minimum time scale of simulation, Δt_{min} [32], is given by:

$$\Delta t_{\text{min}} = 2b/C_r + \Delta t_{\text{char}} \tag{233}$$

as Rayleigh waves are the slowest moving interaction of the three wave-speeds. This time period will be much smaller than Δt.

Nonetheless, once the system has reached this state it will maintain a fluctuating, but on average constant, rate of energy transfer, via the mechanical loading, into kinetic and elastic. This is as load rate can only be approximated as linear between simulation steps, as there is no additional information available due to limitations with sampling frequency.

Once the timescale Δt_{char} is established, which is characteristic of the systems behaviour for the rest of the step, relevant metrics (e.g. frictional energy) could be assumed by taking the mean (denoted with a bar) over Δt_{char}, and extrapolating over Δt. i.e.:

$$E_{\Delta t} \approx \frac{\Delta t}{\Delta t_{char}} . \bar{E}_{\Delta t,\text{char}} \tag{234}$$

This may be resolved by tracking relevant system variables in Eq. (232). However, when using an instantaneous metric like power, it would be assumed to be the same throughout the time-step:

$$\dot{E}_{\Delta t} \approx \dot{\bar{E}}_{\Delta t,\text{char}} \tag{235}$$

[32] For a correct physical description, the initial transitory period of $2b/C_r$ cannot be skipped, due to the nature of the convolution. If the convolution was initialised at the start of Δt_{char}, the system would have no memory of previous events in the past that contribute to the evolution and establishment of dynamic equilibrium, breaking causality. The nuances of this will be revisited later.

6.9 Wind turbine SRB Transient Microslip

The physics of the method was tested and verified for a uniform load rate and a Hertzian load rate distribution, (see Appendix G). As previously discussed, this was a numerically challenging investigation, and various techniques were required to achieve numerical stability (see the Appendix F). Future work might look at analytical forms of Lamb's problem, some headway was made into using a near field asymptotic expansion [176], but had to be dropped for time constraints.

Having established the workings of the model, it was put to use on test conditions that spanned the domain of all possible turbine operating points. Therefore, a test matrix was defined as the outer product of:

$$\mathbf{M} = \vec{F} \otimes \dot{\vec{F}} \tag{236}$$

Where

$$\vec{F} = \{5, 10, 20, 30, 40, 50, 60, 70, 80, 90, 100, 110, 120, 130\}(\text{kN}) \tag{237}$$

and

$$\dot{\vec{F}} = \{5, 10, 20, 30, 40, 50, 60, 70, 80, 90, 100, 120, 140, 160, 180, 200\}^{\mathrm{T}}\,(\text{kN/s}) \tag{238}$$

Table 9: Parameters and Values for test matrix $\mathbf{M}$.

Parameter	**Value**
System Memory	b/C_r
N	500
Δt_{char}	$4b/C_r$
κ	40
μ	0.1

This spanned the effective parameter space of observed loads and load rates for the case study SRB. Outputs were solved for the central slice of the contact.

For our application, using the same simplifications previously encountered,(pure rolling and symmetry of contacting surfaces), micro-slip is given as:

$$\dot{s}' = 2\left(\omega r_{1x} \frac{\partial {u_x}'}{\partial x} + \frac{\partial u_x}{\partial t}\right) \tag{239}$$

However, although dynamic strain may be a useful metric to monitor material integrity, it contributes minimally to dynamic microslip in our case ($\omega \sim 10$), as $\omega \cdot r_{1x} \cdot \frac{\partial u_x'}{\partial x} << \frac{\partial u_t}{\partial t}$ (see Appendix H).

Consequently, only the final term of Eq. (239) was used in calculating frictional power, with the mean ellipticities of the outer and inner contact ($\kappa \sim 40$) used to configure simulations. As mentioned earlier, it should be stressed that these dynamic values are by construction separate from the steady state case, and a full description of strains and velocities would be made by recombining both, that is:

$$u_x = u_{x,0} + u_x' \tag{240}$$

And then using full displacements to solve for velocities and strains, and establishing frictional powers. However, due to the large difference in magnitude between both cases, we are simply decoupling the two and analysing separately. It would be tedious and not particularly valuable to perform such a recombination. The frictional energy in results are then given by:

$$\dot{E}' \approx q \cdot \frac{\partial u_x}{\partial t} \tag{241}$$

where the approximation arises since there is no exact knowledge of the form of tractional distribution in transient slip; it is assumed as the full slip profile.

Results from text matrix $\mathbf{M}$ were compiled and are now summarised below.

There is a strong linear relationship between dynamic strains and load rate (Figs. 71(a, b), with results indicating that at lowest force values, the highest rates of change of force could cause the bearing to approach the elastic limit of steel. This possibility was also raised in the Appendix G.2 with preliminary evaluation of Hertzian load rates.

These findings applied in the field, predict that an initially lightly loaded bearing, subject to a sudden very high load rate, would be at increased risk of damage. This could be the results of a sudden alteration in wind direction changing the load location, invoking local surface yield, and gradual failure. However, as mentioned before, the model is least accurate in these regions, as it assumes the patch size is kept constant throughout a time-step. Therefore it is unclear for how long such high dynamic strains would be present with the growth of the patch, and some caution should always be taken when interpreting these findings. Furthermore, limitations in assuming a constant μ could be significant in such scenarios. Additionally, although we have compiled tests over the complete set of co-ords in the matrix $\mathbf{M}$. Although some combinations of load and load rate are indeed possible, this doesn't mean they occur, i.e. a smaller area of matrix elements is covered in the field. Real time analysis will give additional insight into this.

A highly significant finding was that frictional powers are independent of applied forces, having a linear dependence on $\dot{F}$ only. This validates the assumption used of keeping b constant, outlined in Chapter 6.6, as change of patch size is irrelevant, as $\dot{F}$ is constant, although $\dot{p}_0$ is not. Whilst this implies net power output over Δt is not dependent on initial load F, the same is not true of power density, that could be a better failure metric, as it is independent of geometry. It is noted that the limit for smearing [48] could be possible under certain scenarios, indicated in Fig. 71c. An algorithm methodology exploring the potential effects of cumulative energy densities on survivability was developed, and left in Appendix I. Because of the observed linear relationships, power results have been normalised by μ^2, meaning that relationships and dynamic powers may consequently be calculated for different values of μ, e.g: different lubrication regimes. This is useful outcome, since if it turns out using that $\mu = 0.1$ is too high or low, results may easily be rescaled.

There is slight noise present in the frictional metrics at the higher load rates, due to aliasing. This could be overcome by running the simulations with higher N, but due to the aforementioned CFL like relationship, would also necessitate a smaller dt. With the time scope this was not possible, but might be performed with more work.

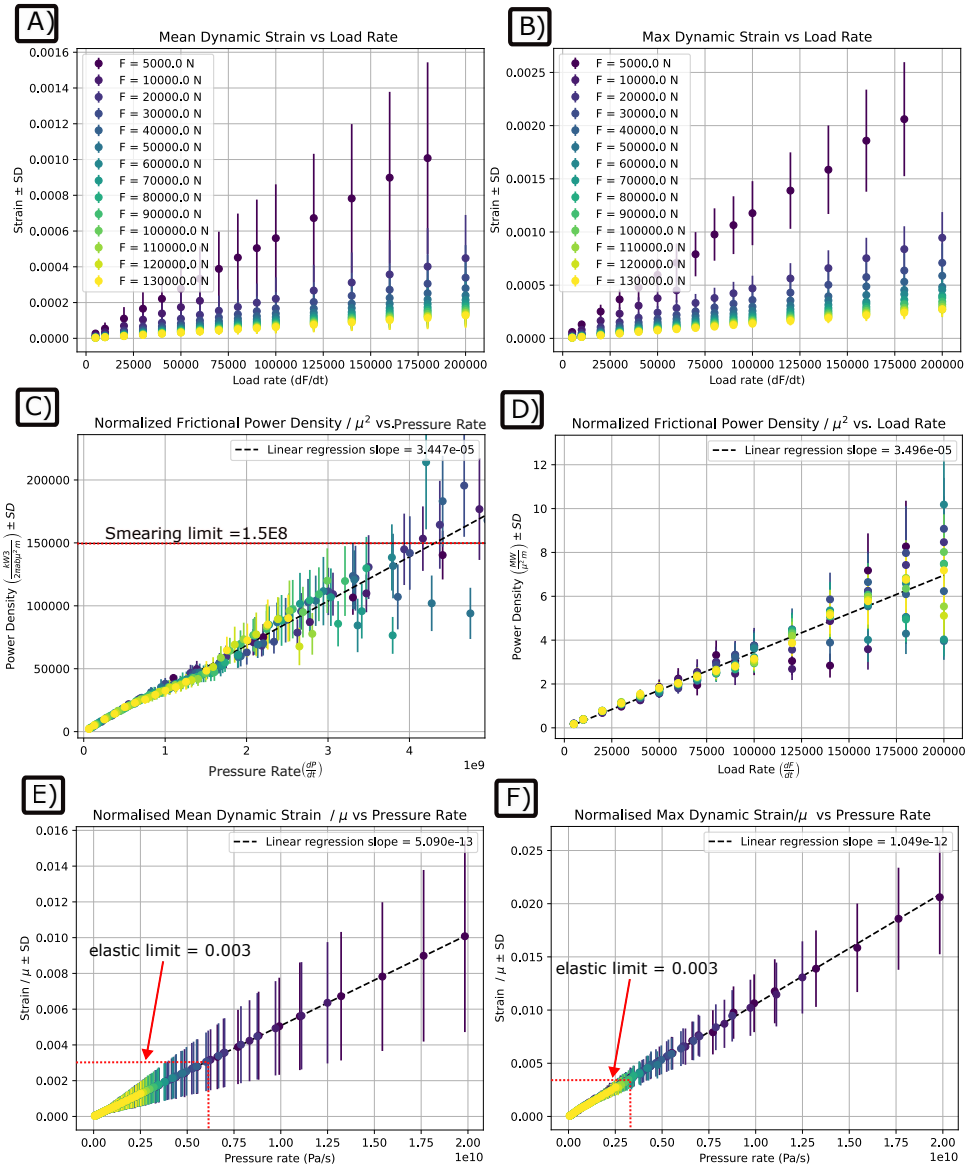

Figure 71: The linear relationships deduced over test case bearing operating conditions **M**. Variance (1SD indicated) is in large due to inherent system dynamics (see Chapter.6.7 or Appendix G.2). Relationships were used to establish semi-analytic equations for subsequent analysis. There is some spatial aliasing present at the higher load rates for powers.

6.9.1 Numerical-Analytical Equations

Making predictions from the test matrix outcome was straightforward, due to the linear nature of theory and thus results.

If fricional power density for a central line contact is related to roller load rate by:

$$\dot{E}_{\ell,0} = m \cdot \dot{F}\mu^2 \tag{242}$$

As suggested by Figs. 71(c, d), with m being found by linear regression. This gives the frictional power per slice of the contact, in terms of the rate of change of central pressure as:

$$\dot{E}_{\ell,0} = m \cdot \mu^2 \dot{p_0} \frac{2\pi ab}{3} \tag{243}$$

This line integral can be extended into a surface one, and integrated along the semi major axis to give total frictional power of the contact:

$$\dot{E} = m\mu^2 \dot{p_0} \frac{2\pi ab}{3} \int_{-a}^{a} [1 - z^2/a^2]^{\frac{1}{2}} dz \tag{244}$$

The integral is solved by a trigonometric substitution, $z = a\sin\theta$, $d\theta = a\cos\theta\, dz$, and using the double angle formula, $\cos^2\theta = \frac{1+\cos 2\theta}{2}$, on the resultant form to give:

$$\int [1 - z^2/a^2]^{\frac{1}{2}} dz = \frac{2\theta + \sin 2\theta}{4} = \frac{1}{2}\left(z\sqrt{1 - \frac{z^2}{a^2}} + a\sin^{-1}\frac{z}{a} \right) \tag{245}$$

When limits are plugged in, this simplifies to:

$$\dot{E} = m\mu^2 \dot{P_0} \frac{2\pi^2 a^2 b}{6} \; = m\mu^2 \dot{F} \frac{\pi a}{2} \tag{246}$$

that is the frictional power associated with transient microslip for an elliptical contact.

Qualitatively, by taking the gradient, it can be reasoned that the intercept, $+c$, is associated with a systematic error from the spatial regularisation, and keeping the same dx, gradient can be used accurately.

Similarly, as steady state strain inside the contact is proportional to traction (Eq. (159)), dynamic strain should be proportional to traction rate. Results supported this, enabling a set of predictive hybrid numerical-analytical equations to be applied over operational conditions:

$$\dot{E} = m_1^* \mu^2 \dot{F} \frac{\pi a}{2} \tag{247}$$

$$\overline{\frac{\partial u}{\partial x}} = m_2 \mu \dot{p_0} \frac{\pi}{4} \tag{248}$$

$$\frac{\partial u}{\partial x}_{\max} = m_3 \mu \dot{p_0} \tag{249}$$

where the mean and max values of strain are calculated by normalising the integral and the max. of the central value respectively. Each of the three gradients are specific to this bearing.

Additional processing was applied to m_1^*, to account for noise present due to aliasing. This was done by finding the slope associated with:

$$\dot{E}_\ell \cdot \frac{3}{2\pi ab} = m_{12} \dot{P}_0 \tag{250}$$

and leveraging the two slopes to get an average slope and uncertainty

$$m_1^* = (m_{11} + m_{12})/2 \pm |m_{11} - m_{12}|/2 \tag{251}$$

These equations were then verified against the frictional energy found by running a simulation over all strips, and integrating for total frictional energy for a 30 kN/10 kN/s

load case, at a time $t = 0.301\mu s$. The results of this full simulation are given on the next page, with the full complexity of all three surface wave interaction being evident. Notably, the frictional power results are an order of magnitude above the steady state (Fig. on next page). Comparing the derived semi analytical equations for the same scenario we find:

$$\dot{E} = 3.472 \pm 0.025 \cdot 0.1^2 \cdot 10\text{e}3\,\text{N/s} \cdot \frac{\pi * 24.4\,\text{mm}}{2} = 133.30 \pm 0.96\,\text{W} \tag{252}$$

This is a favourable comparison (full simulation 129.5 W) with the discrepancy of 2-3% explainable from comparing mean and instantaneous metrics, despite the relatively low N used. These simple, fitted equations were then used in actual analysis of wind files. This is an incredibly quick method; performing a step by step integration of transient system explicitly would not be possible in a realistic timescale, due to the complexity of the calculations.

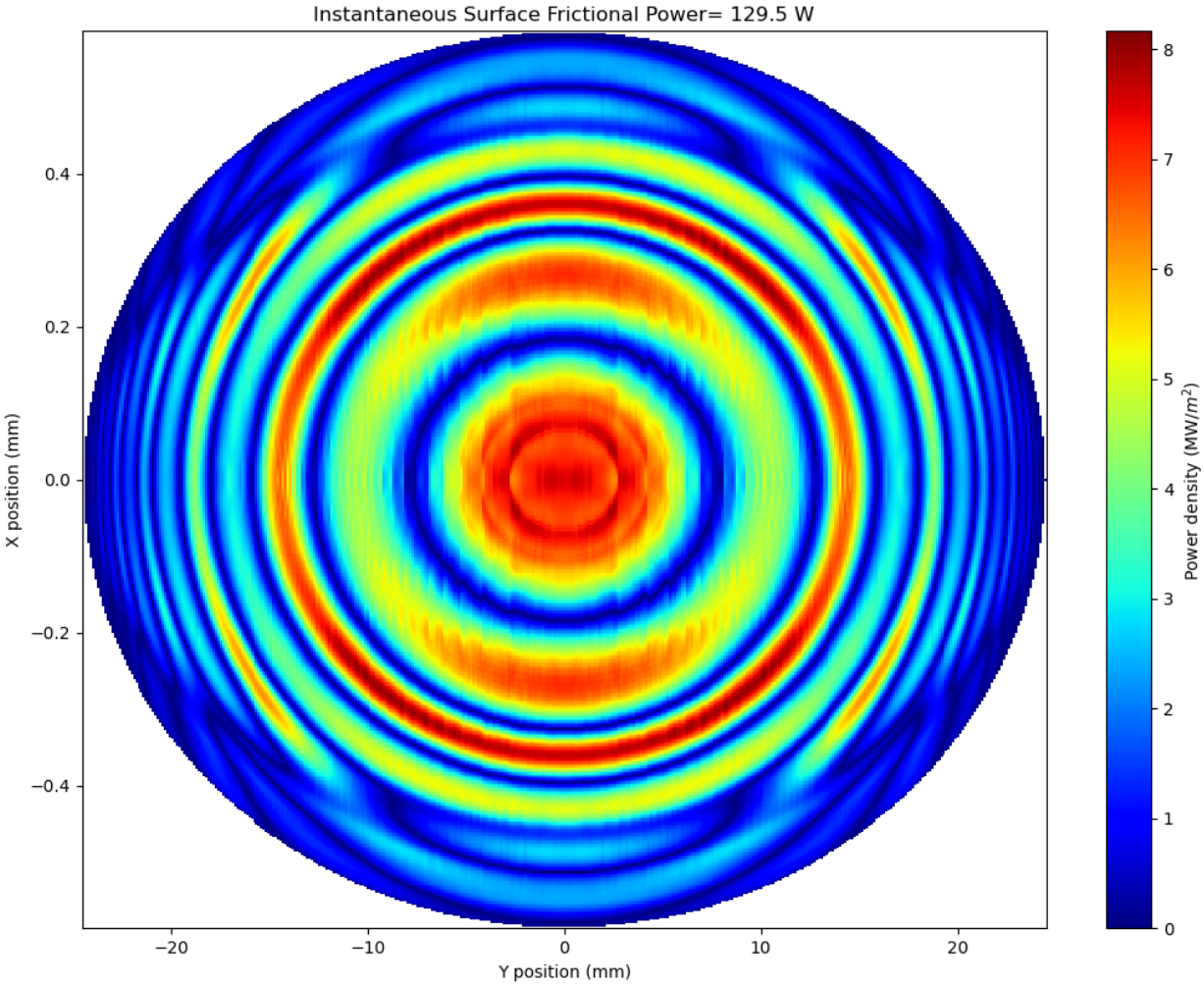
Instantaneous Surface Frictional Power= 129.5 W
X position (mm)
Y position (mm)
Power density (MW/m²)

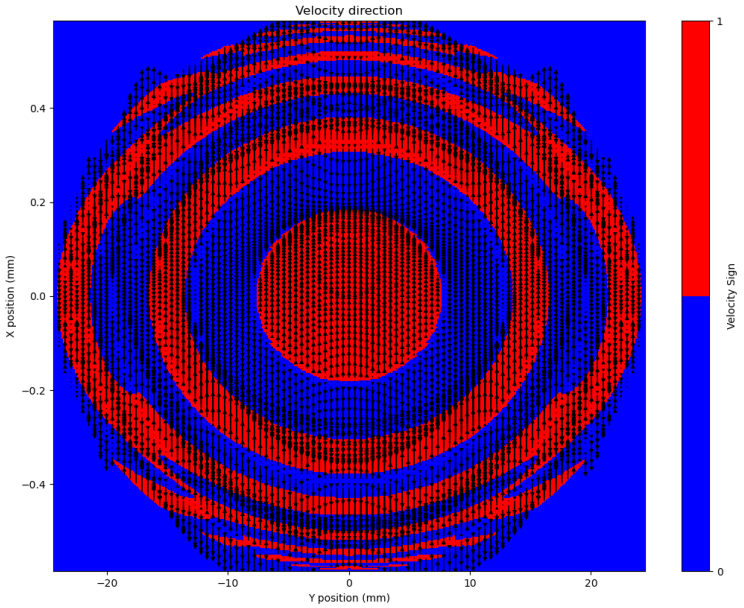
Velocity direction
X position (mm)
Y position (mm)
Velocity Sign

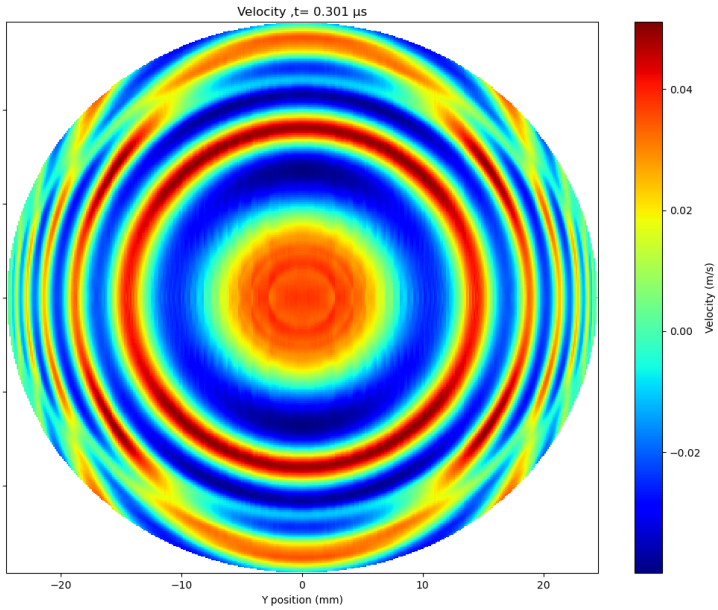
Velocity ,t= 0.301 µs
Y position (mm)
Velocity (m/s)

6.10 Results

These equations were applied over the full range of wind conditions, using a centred finite difference method to reduce noise (Fig. 72), capping $\dot{F}$ at a limit of 3 standard deviations (SDs), and conservatively neglecting strain terms below 5 kN, due to potential divergence caused by the $\frac{1}{ab}$ dependence in $\dot{p}$.

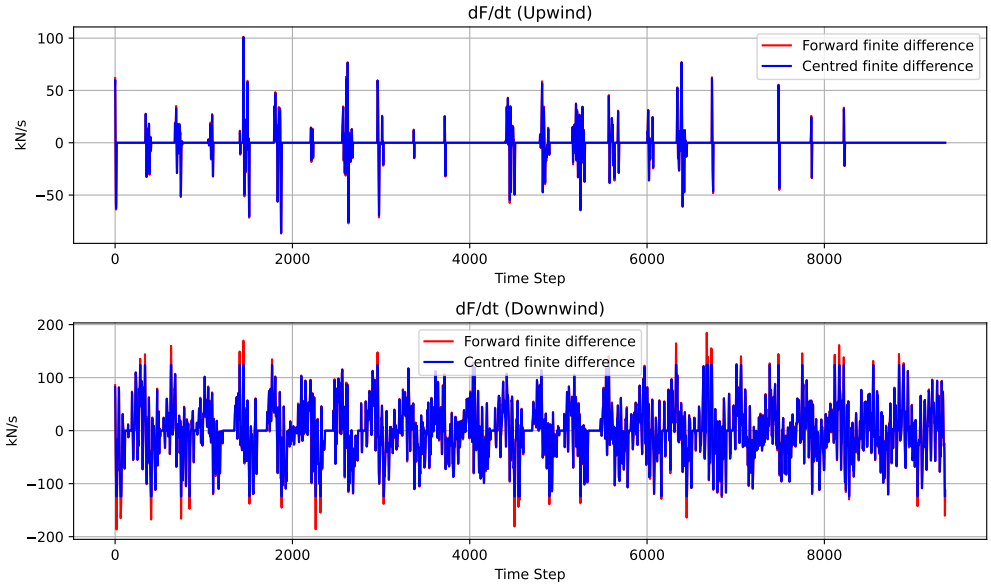

Figure 72: Centred finite difference with 3SD cap vs. forward finite difference effect on roller load rate

The same idea was used as in the macroslip Chapter 4, using a benchmark, constant load, constant speed 'static' equivalent to make a comparison against. This serves as an analogue for a conventional power plant turbine, in which observed failure rates are lower.

50Hz time series results for 12 m/s A are presented in Fig. 73. Because of the linearity, and thus rapid solve time of Eqs.[247-249], a plethora of data is available for all four load locations (upstream/downstream, inner and outer). The transient analysis shows a complex dependency on F and $\dot{F}$, and there is significant fluctuation present in power and strain outputs (Figs. 73(a, b, e)). The static equivalent upwind row is unloaded and experiences significantly lower powers and strains.

Interestingly, the area of peak power dissipation coincides roughly halfway between the rollers' peak load and the exit of the load zone (Fig. 73c). This is where the product of $\dot{F}$ and F is at its highest. This may be used to explain more complex relationships in the dynamic case.

The distribution of strains between the two cases is explored in Fig. 74e, with Seaborn's Gaussian Kernel Density Estimate (KDE) representation of the strains present in all four contact points over time. Zero strains have been removed to make relationships clearer. What becomes apparent is the longer tail of the dynamic case in strains. On the other hand, strains in the static case have no probability of such extremes and are

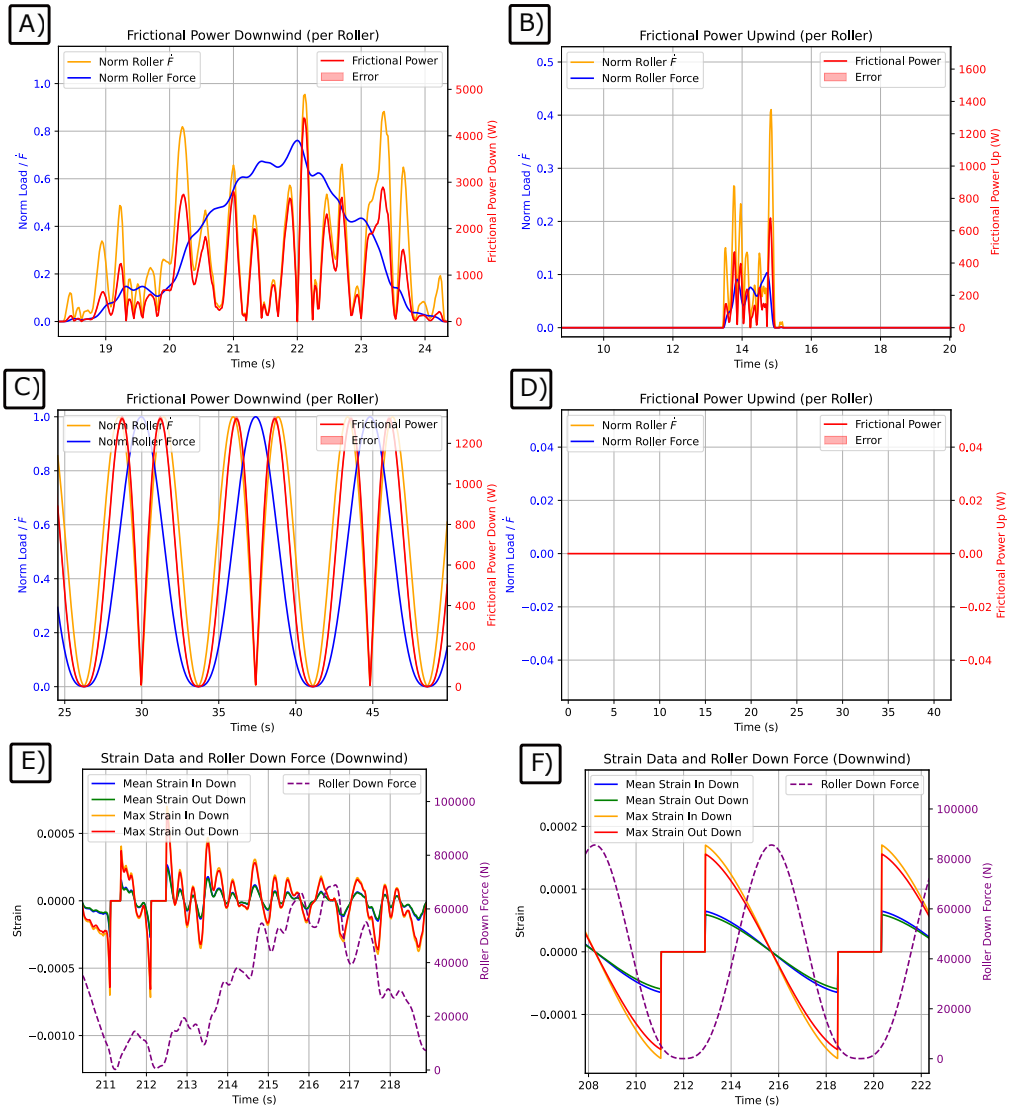

Figure 73: 12A run. Frictional power has a complex dependency on both roller force and $\dot{F}$, with a greater sensitivity to the latter. There is, like in earlier analysis, an imbalance in powers between rows.

confined to a narrow range, well within the elastic limit. Thus, the two are characterized by completely different distributions.

The frictional power outputs were scaled to the power of the turbine for all 27 rollers and displayed in histograms 74(a- d). This demonstrated that the mean power loss is higher by more than 50% in the wind turbine case than in the static case. Furthermore, the distribution is radically different between cases, with much higher instantaneous powers occurring on the right tail of the dynamic loading case. It isn't just that these higher powers are more frequent between cases, there is a significant portion of power loads in the wind case that would never occur in the static equivalent. It can be seen as we move to 24 m/s, this trend increases in the dynamic case, with the length of the histogram

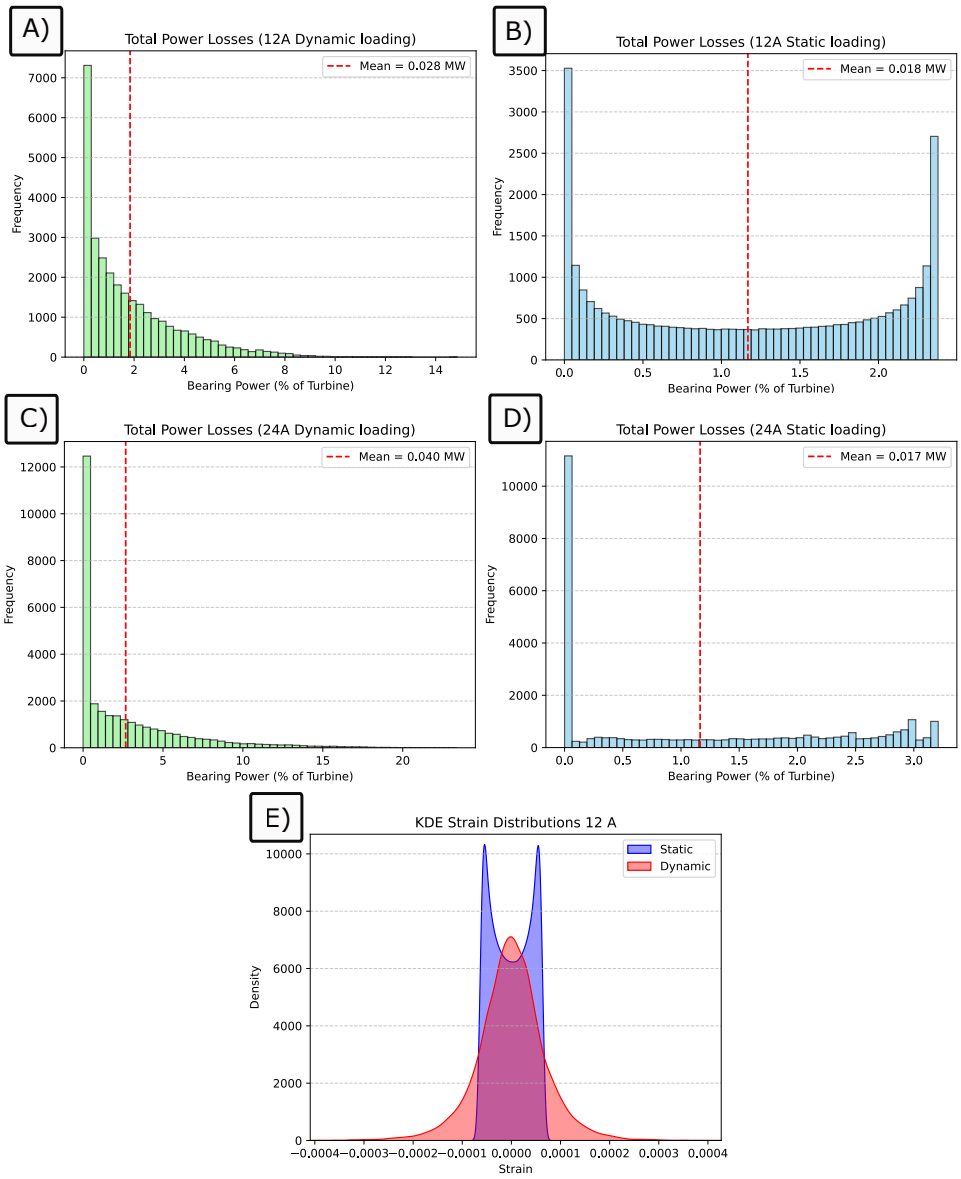

Figure 74: Power distributions between 'static' and dynamic cases are seen to be significantly different when a transient model is used. These are represented in terms of total operational power of the turbine. These differences can be characterised as fundamental statistical ones - see text.

extending, whilst in the static it remains relatively similar. Linking back to the idea of shock loading overcoming a threshold and invoking material damage, such high power events could be associated with increased risks of this occurring.

This finding is further supported when the analysis was extended over all of the operational conditions (Fig. 75). Maximum powers (Fig. 75b), and upper limit powers (Mean + 3SD- see Fig. 75a) were compiled, revealing a constant increase with wind speed, although no particular correlation with turbulence levels. The rate of increase

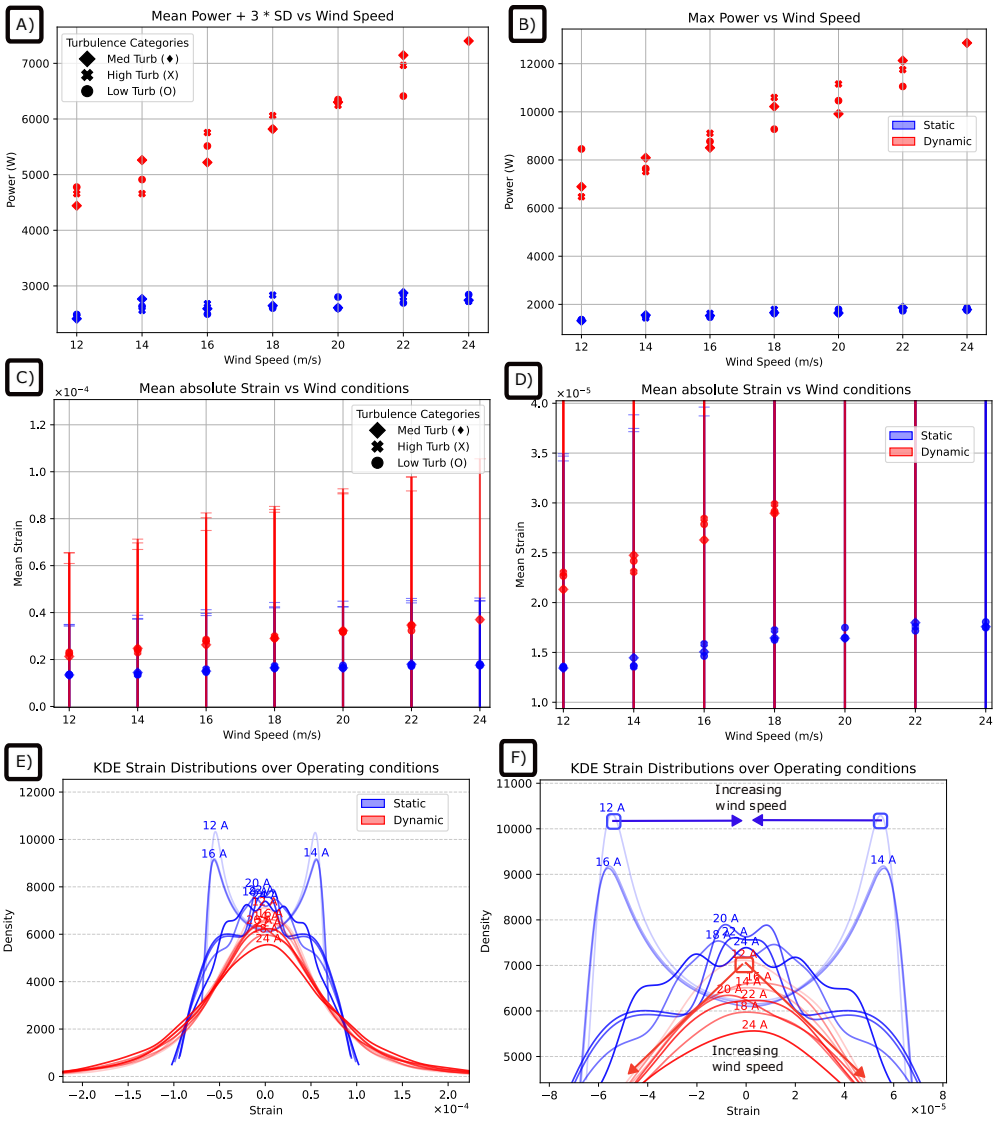

Figure 75: Maximum powers and strain KDE distributions over all wind conditions. The two sets of results are markedly statistically different, and a steady state analysis would not have been sensitive to this, giving very different predictions.

is greater in the dynamic case, for both powers and strains. The lack of signal with turbulence, is confusing, and warrants additional exploration in future work.

What is extremely intriguing from these findings, is that in the static case, the observed max. power is actually lower than the 3SD limit. On the other hand, the dynamic max powers are significantly higher than the upper 3SD limit. This reveals that the powers distributions seen between these two cases are fundamentally statistically different. The dynamic case experiences an extended tail behaviour, indicating an increased likelihood of extreme events. On the other hand, the morphology of the static equivalent is compactly supported, meaning that relative extreme events have a 0 probability of occurring. Such extreme events are deterministically related to shock, and could be

linked to premature failure.

This trend is also reflected in the strains seen in Figs. 75(e, f). As wind speed increases, the extremes become more densely populated in the dynamic case, further illustrating the distinct bearing behaviour under dynamic conditions and wind applications, compared to the power plant 'static' analogue.

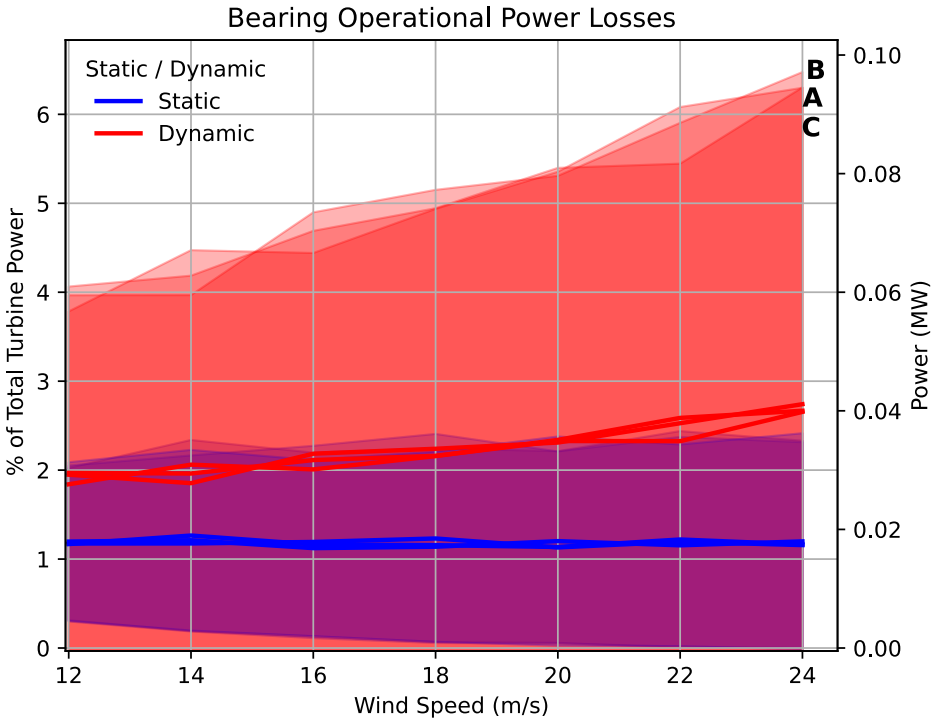

Figure 76: Operational Power losses between the two scenarios. Extreme powers are directly related to wind speed in the dynamic case, whereas they aren't present in the static case.

The fundamental differences between the transient to the steady state micro slip analysis is demonstrated in Fig. 76. Unlike the steady state microslip analysis, there really is a demonstrable and distinct difference between the static and dynamic simulations in terms of frictional power. The dynamic mean value is roughly double that of the static, and goes up with wind-speeds, due to increase variability. Furthermore, extreme power events become more likely to occur, indicated by the shaded area. These values compare more favourably with literature [144, 145] for operational power losses, than those of the steady state microslip frictional model.

If the raceway is unwrapped, and cumulative energy densities plotted over a 10-minute time period between both sets, this makes stark differences between the two cases become even more pronounced: shown in Fig. 77. As already suggested by [24], this could be an indicator of WEC occurrence. One method which could be used to investigate this more deeply is to use spatial distributions of cumulative frictional energy densities to predict failure, or to better inform fault detection algorithms. One such method is explored in Appendix I.

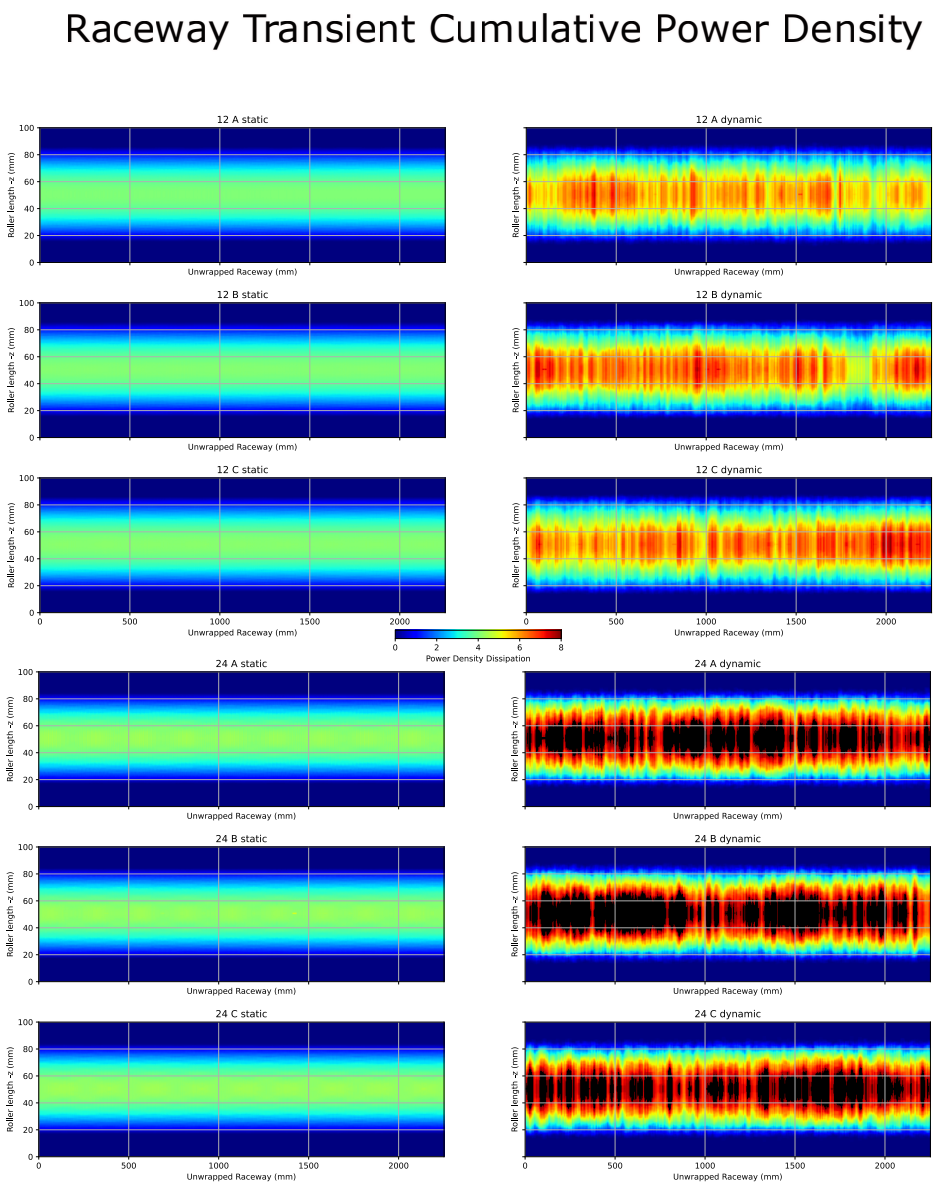

Figure 77: Dissipated frictional energies densities imparted over 10-minute simulations on inner raceways between cases. Values above the max of 12 A- C dynamic have been coloured in as black, for visual effect. In 24 A-C they reached as high as 20MJ m^2.

6.11 Conclusion

To summarise, we have seen that transient microslip looks to be important when considering WTMB failure, giving larger, and very different results to a steady state analysis. Furthermore, it is sensitive to differences between a power plant MB analogue and a WTMB, suggesting that transient conditions in loading require a methodology with transient considerations, rather than a steady state analysis.

7 Conclusion: Findings and Recommendations

Was it not Heraclitus, the great Greek philosopher, who was once heard to say [177]?

"No man ever steps in the same river twice. For it's not the same river, and he's not the same man."

And thus we are at the end of our journey.

The aim of this research was to investigate the tribological effects of time-varying loads on a rolling element WTMB so as to better understand and predict failure. The first attempt to do this was via a data-driven approach, which informed how physics might be better embedded in systems analysis to improve predictions on behaviour and propensity for failure. This then led to further work investigating the fundamental causes behind temperature changes and potential mechanisms of failure; here proposed initially as macroslip and microslip. Further, since it is known that WTMB exhibit higher failure rates than those of power plant equivalents, and that the loading patterns and dynamics differ significantly, these were fully considered throughout, to determine if these load dynamics were a factor in failure. The findings are listed below, for each Chapter.

7.1 Findings

7.1.1 Chapter 3

i) Thermal inertia is clearly present in SCADA data and should be accounted for in preprocessing methods for MB fault detection algorithms.

ii) Changes in MB thermal response are present with accrued damage and these could henceforth be used as an indicator for failure.

iii) Changes in thermal properties linked with failure motivate investigation of deterministic causes of these, i.e. frictional effects.

7.1.2 Chapter 4

iv) Frictional powers and cumulative energies, dissipated at the contact interface, have been linked in literature to failure via WEC and smearing. Thus, this was explored as a potential damage metric.

v) Equations of motion of WTMB dynamics are extremely numerically stiff. This can lead to misleading conclusions on behaviour and trends between windspeeds of frictional metrics.

vi) A classical Newtonian rigid body dynamic method suggests low associated frictional metrics, but couldn't fully resolve the required values due to aforementioned stiffness. In fact, it appears that such an implementation may not be able to resolve macroslip to an adequate level of precision (at least using naive methods due to numerical decimal limitations), even when implicit integration schemes are used.

vii) Alternative methods exist which are better equipped to tackle these regions of extreme stiffness. One of these is the linearised Hamiltonian method presented here. This enabled characterisation of the problem as an LTV system, and a first order semi-analytical approximation of this conclusively found very low operational macroslip frictional metrics.

viii) Angular momenta coupling is important. This is often ignored and decoupled in existing analyses, but the current study conclusively demonstrates such coupling should not, in future, be neglected.

ix) Both 'roller slip' and 'cage slip' must be considered together to accurately model a WTMB system. Although clearance effects are not included, the current work clearly demonstrates that individual 'roller slip' will not be present in the absence of 'cage slip', and the two relative motions must be considered together to accurately model the system. This is widely not performed in the literature, and the findings indicates its importance in ensuring accurate and comprehensive consideration of all potential failure mechanisms.

x) Macroslip produces insignificant frictional energies and powers. This is clear when point (ix) is considered with empirical field observations, that report minimal cage slip. This is further supported by findings (vi) and (vii). Consequently macroslip is unlikely to be a driver for premature bearing failure, unlike other WT bearings such as the gearbox.

7.1.3 Chapter 5

xi) Steady state microslip appears more significant than macroslip in the frictional metrics of highly loaded rollers, such as those in the WTMB.

xii) Asymmetry due to contact angle could accelerate failure at roller/raceway interface, as it leads to regions of higher frictional energy/power densities.

xiii) Heathcote's resisting moment curve is not universal.

xiv) WTMB's mostly operate in the majority 'slip' regime, with bands of 'stick' being narrow, due to the high loads.

xv) Steady state methods predict higher frictional metrics with lower wind speeds, peaking at 12 m/s, corresponding to the operational thrust strategy of the turbine. However, these methods would not be sensitive to and would struggle in distinguishing between, a dynamic load condition of a WT and the 'static' loading on a conventional power plant's MB.

7.1.4 Chapter 6

xvi) Roller absolute loads in WT are similar to those in conventional power plants, however rates of change of load between the two differ greatly. Previous work has not accounted for these rates of change of load (shock loading) so consequently a transient consideration of microslip is needed to determine if such differences are manifested in frictional effects.

xvii) Analysis of transient microslip indicated linear relationships existed between frictional power and the rate of loading, independent of initial contact load.

xviii) The relationship between dynamic strains was linear with central pressure rate. Dynamic strains could near the elastic limit under certain conditions, however this may be overestimated by taking $\mu = 0.1$, and the frequency of these extreme strains could be limited.

xix) There is a one order of magnitude difference in frictional metrics between the transient and steady state microslip case results. Power densities may, at time, reach a literature threshold for smearing. This suggests that transient microslip may be more important than steady state in WTMB failure, further work should be performed to examine this issue in more depth.

xx) There are significant differences present in both higher material (dynamic strains) and frictional (powers and energies) metrics between a power plant MB analogue and WTMB. These differences arise principally due to the transient model's sensitivity to load variability which demonstrated that the statistical distributions of strain and power are fundamentally different between the two. In particular, power plant MBs exhibit closed and compact distributions, whereas those of WTMBs show open distributions indicating a nonzero probability of extreme load and strain events.

xxi) Converse to the steady state model, the transient case indicates an increase in frictional metrics with wind speed, as loading becomes more variable. This highlights the importance of selecting an appropriate modelling approach, as different models capture distinct physical effects and can lead to vastly different and potentially inadequate conclusions.

7.2 Recommendations

The scope of this study has been limited to the rated power section of the operational curve, for one isolated turbine dataset. These limits should be extended to include more turbine datasets of differing designs and site locations, of which there are several impressive open source examples online [178, 179, 180].

Furthermore, solely limiting the model to rated power, where offshore turbines are estimated to spend 30-40% of their life [181], neglects a large portion of operational conditions, and potential damage that may arise. Likewise, case studies of transient events would be pertinent, where bearings of the low speed stage are thought to be particularly vulnerable [149]. Ideally the transient microslip model should be applied to these regimes, where load rates are the highest. However, care needs to be taken here, as if the high load rates exceed the elastic limit, as indicated by some of the dynamic strains in Chapter 6.9 and Appendix G.2, the linear elastodynamic assumption will not be valid, necessitating the use of more advanced theory.

The main recommendations in this thesis swing on the significance of the high frictional powers associated with transient microslip, as the steady state case, and macroslip even more so were shown to be significantly smaller and less relevant. Naturally therefore, follow up work should be performed to investigate.

The shortcomings of the numerical approach for the method explored in Chapter 6 were primarily due to singularities present in Eq. (218), that resulted in excessive computational times and numerical instabilities. This makes full interpretation of results challenging, and alternative methods should be explored.

One obvious candidate is finite element analysis (FEA) [182]. As an industry standard solution FEA is well equipped for parametric studies, and preliminary work may focus on a simplified case of different load rates for a rolling contact, avoiding the less accurate interpolation scheme used here and solving in full.

An alternative that should be performed in alongside an FEA analysis is seeking analytical closed form approximations of Eq. (227). This was attempted, based on work that found an infinite series of cylindrical wave-functions [176, 183] to describe Lambs problem. From this, leading order terms could be used to give quick and accurate calculations for internal displacements for transient Hertzian contact, that would have uses in multiple classes of engineering problems.

If subsequent further work supports the findings of this study, showing that such powers are greater than those of the steady state (or even of a similar order of magnitude), then unique load patterns and dynamics could be a risk factor for failure.

However if the contrary is found, then load patterns and dynamics of a wind turbine will not be a risk factor of failure, although high absolute loads and pressures could be.

The implications of the former could require more radical turbine re-design to mitigate either shocks, or the effects of shocks which impart large pressure impulses on the MB. The former could be done by a systems level approach, modifying the turbine so shock loads are less likely to occur. Due to the inherent chaotic nature of the wind, and more extensive requisite work, this would not be preferable. The latter, looking at mitigating the effects of shock within the existing turbine design, could be achieved by a localized approach, redesigning the bearing so larger contact areas are accommodated, meaning pressures and thus pressure rates would be reduced. An obvious choice is a form of Journal bearing [130], and contemporary work on variants for wind specific application has already begun [184, 185, 186].

A more philosophical recommendation arising from this thesis, is that of a more comprehensive consideration of the fundamental physics underpinning bearing behaviour. Better, more unified notation, [33], would support this, easing the difficulties in traversing and combining interdisciplinary fields, and the use of SI should be used where possible.

Numerical methods aren't necessarily bulletproof, as shown by the issues encountered herein with stiffness, but analytical and semi analytical tools have great use and should continue to be developed. Unfortunately, a deeper understanding of mathematical techniques in engineering is not as prevalent as it was in an age predating the modern computer. This is a natural consequence of the rise of, and increasing reliance on, all powerful computational software like finite element analysis (FEA), computational fluid dynamics (CFD), and computer aided design (CAD). Whilst stopping short of calling for the destruction of computational tools, cotton mills, and general progress in fits of blind rage (Fig. 78), an increased familiarity with traditional analytical tools would aid the problem solving mindset and foster the intuition required for tackling novel engineering applications such as these. Such considerations will further assist in the development of appropriate models, being used in conjunction with and to inform numerical tools. Considering the relevant and dominant physics of the system, as discussed above in finding (xxi), is crucial for making accurate assessments of findings.

[33] Admittedly this is easier said than done, but should be moved towards.

Figure 78: All hail King Ludd [187].

Appendix A: Bearing Geometrical Parameters

Given are the bearing geometrical parameters for the case study 1.5 MW turbine SRB, up to 5 significant figures places. For higher accuracy calculations relevant formula are available in text.

Parameter	**Description**	**Value**
r_{Ix}	Roller radius (rolling-direction)	0.03625 m
r_{Iz}	Roller non-rolling radius	0.41756 m
r_{IIz}^{in}	Inner race non-rolling radius	0.43047 m
r_{IIz}^{out}	Outer race non-rolling radius	0.43047 m
α	Contact angle	0.19199 rad (11 deg)
D_p	Pitch diameter	0.775 m
N_{rollers}	Number of rollers	27
r_{IIx}^{in}	Inner race radius (rolling-direction)	0.35850 m
r_{IIx}^{out}	Outer race radius (rolling-direction)	0.43100 m
$\tilde{r}^{\text{in}}$	Inner race radius of contact	0.35192 m
$\tilde{r}^{\text{out}}$	Outer race radius of contact	0.42308 m
l_{roller}	Roller length	0.1 m
M_{roller}	Roller mass	3.2407 kg
$I_{x'}(I_1) = I_{y'}(I_2)$	Roller non-rolling axes moment of Inertia	0.0037652 kg m^2
$I_{z'}$ (I_3)	Roller rolling axis moment of Inertia	0.0021292 kg m^2

Table 10: SRB Geometrical Parameters used.

Appendix B: Hertzian Empirical Explicit Coefficients

Table 11: Parameter Values for Empirical explicit formula in calculating Hertzian contact terms.

Parameter	**Value**	**Parameter**	**Value**
λ_0	1.3862944	λ_1	0.1119723
λ_2	0.0725296	λ_3	0.5
λ_4	0.1213478	λ_5	0.0288729
β_0	1	β_1	0.4630151
β_2	0.1077812	β_3	0.2452727
β_4	0.041496	μ_1	0.40227436
μ_2	3.7491752×10^{-2}	μ_3	7.4855761×10^{-4}
μ_4	2.1667028×10^{-6}	μ_5	0.42678878
μ_6	4.2605401×10^{-2}	μ_7	9.0786922×10^{-4}
μ_8	2.7868927×10^{-6}		

Appendix C: 4DOF Free Body Hamiltonian

The following has been derived using the same methodology in Chapter 4.4, but for a 4 DOF system.

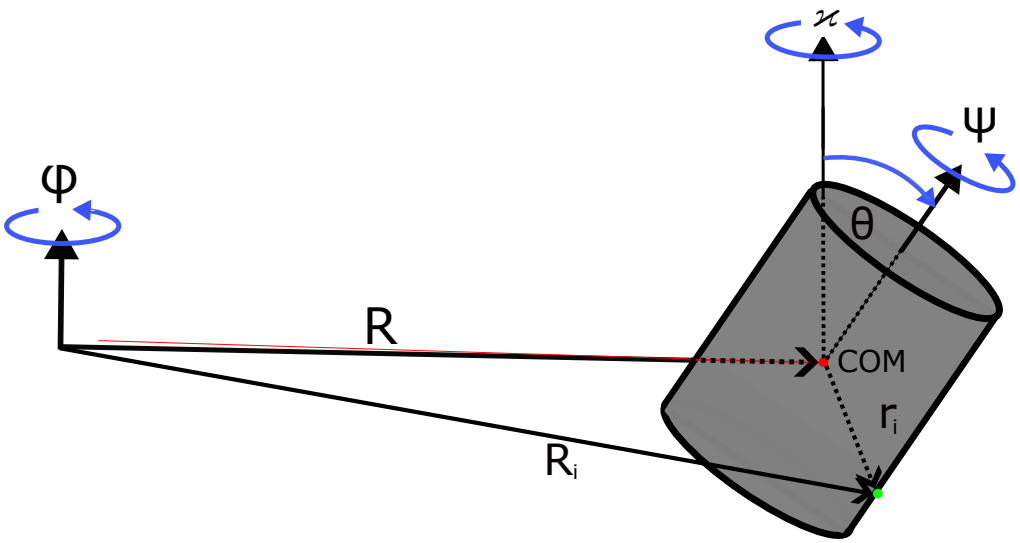

Figure 79: 4 DOF system.

The use of the passive transformation matrix was required.

$$\mathbf{A} = \begin{bmatrix} \mathrm{c}\psi\mathrm{c}\varkappa - \mathrm{c}\theta\mathrm{s}\varkappa\mathrm{s}\psi, & \mathrm{c}\psi\mathrm{s}\varkappa + \mathrm{c}\theta\mathrm{c}\varkappa\mathrm{s}\psi, & \mathrm{s}\psi\mathrm{s}\theta \\ -\mathrm{s}\psi\mathrm{c}\varkappa - \mathrm{c}\theta\mathrm{s}\varkappa\mathrm{c}\psi, & -\mathrm{s}\psi\mathrm{s}\varkappa + \mathrm{c}\theta\mathrm{c}\varkappa\mathrm{c}\psi, & \mathrm{c}\psi\mathrm{s}\theta \\ \mathrm{s}\theta\mathrm{s}\varkappa, & -\mathrm{s}\theta\mathrm{c}\varkappa, & \mathrm{c}\theta \end{bmatrix} \tag{253}$$

The order in which each angle is applied is important, and follows the *Euler angle* notation. Shorthand notation has been used for the trigonometric functions, c- cos, s- sin.

Such a method is the natural way of formulating more complex problems, such as increasing DOF (skew, tilt) and including additional clearance dynamics, without neglecting complex coupling. To extract results for the driven and damped case would require the

same method as Chapter 4.4:

$$
\begin{aligned}
H = {} & gMR(1-\mathrm{c}\phi) + \frac{p_\theta^2}{I_1} - \frac{p_\psi(I_3\mathrm{c}\theta p_\varkappa - I_1\mathrm{s}^2\theta p_\psi - I_3\mathrm{c}^2\theta p_\psi)}{I_1 I_3 \mathrm{s}^2\theta} \\
& - \frac{(p_\varkappa - p_\phi)\mathrm{c}\theta}{I_1 MR^2}\left(\frac{I_3\mathrm{c}\theta p_\varkappa}{\mathrm{s}^2\theta} - I_1 p_\psi - \frac{I_3\mathrm{c}^2\theta p_\psi}{\mathrm{s}^2\theta}\right) - \frac{(p_\varkappa - p_\phi)^2}{2MR^2} \\
& - \frac{(p_\varkappa - p_\phi)p_\phi}{MR^2} - \frac{p_\varkappa}{I_1 MR^2}\left(-I_1 p_\varkappa - \frac{MR^2 p_\varkappa}{\mathrm{s}^2\theta} + \frac{MR^2\mathrm{c}\theta p_\psi}{\mathrm{s}^2\theta} + I_1 p_\phi\right) \\
& - \frac{I_3}{2}\left(\frac{I_3\mathrm{c}\theta p_\varkappa - I_1\mathrm{s}^2\theta p_\psi - I_3\mathrm{c}^2\theta p_\psi}{I_1 I_3\mathrm{s}^2\theta} - \frac{\mathrm{c}\theta}{I_1 MR^2}\big(-I_1 p_\varkappa - \frac{MR^2 p_\varkappa}{\mathrm{s}^2\theta} + \frac{MR^2\mathrm{c}\theta p_\psi}{\mathrm{s}^2\theta} + I_1 p_\phi\big)\right)^2 \\
& - (I_3\mathrm{c}^2\theta + I_1\mathrm{s}^2\theta)\left(\frac{(p_\varkappa - p_\phi)^2}{2M^2R^4} + \frac{(p_\varkappa - p_\phi)}{I_1 M^2 R^4}\big(-I_1 p_\varkappa - \frac{MR^2 p_\varkappa}{\mathrm{s}^2\theta} + \frac{MR^2 c\theta p_\psi}{\mathrm{s}^2\theta} + I_1 p_\phi\big)\right) \\
& - \frac{I_1}{2}\left(\frac{p_\theta^2}{I_1^2} + \frac{\mathrm{s}^2\theta}{I_1^2 M^2 R^4}\big(-I_1 p_\varkappa - \frac{MR^2 p_\varkappa}{\mathrm{s}^2\theta} + \frac{MR^2\mathrm{c}\theta p_\psi}{\mathrm{s}^2\theta} + I_1 p_\phi\big)^2\right)
\end{aligned}
\tag{254}
$$

Appendix D: Asymptotic Forms of Rayleigh Dissipation Slip Coefficient

We are looking to find the integral of:

$$\Delta \dot{u}_x \int_{-a}^{a} \int_{-b}^{b} \frac{\eta_0}{h} \exp\left[c_{\eta P} p(x,z)\right] \, dx \, dz \tag{255}$$

Under the knowledge that p is very large.

Laplaces method states, for an integral of the form [188]:

$$\int_a^b e^{Mf(x)} \, dx \tag{256}$$

if $f(x)$ is at least twice differentiable, and has a maximum at x_0, where $a < c < b$, then the integral will be dominated by regions very close to x_0 as $M \to \infty$.

Then $f(x)$ may be Taylor expanded around this region, too:

$$f(x) \approx f(x_0) + f^{(1)}(x_0)(x-x_0) + \frac{f^{(2)}(x_0)}{2!}(x-x_0)^2 + \frac{f^{(3)}(x_0)}{3!}(x-x_0)^3 + \frac{f^{(4)}(x_0)}{4!}(x-x_0)^4 \tag{257}$$

With (n) denoting the order of derivative with respect too x in this case. $f(x)$ is a Hertzian profile in our case here. Due to the antisymmetry of the integral, the first and 3rd derivative vanish. We may then extend the limits of the integral to infinity, since they will contribute minimally, leaving:

$$\int_a^b e^{Mf(x)} g(x) \, dx \approx e^{Mf(x_0)} \int_{-\infty}^{\infty} e^{\frac{Mf^{(2)}(x_0)}{2!}(x-x_0)^2 + \frac{Mf^{(4)}(x_0)}{4!}(x-x_0)^4} dx \tag{258}$$

If only the second order term is kept, a Gaussian integral may be used, yielding

$$\int_a^b e^{Mf(x)} \, dx \approx e^{Mf(x_0)} \sqrt{\frac{2\pi}{M|f''(x_0)|}} \quad \text{as } M \to \infty, \tag{259}$$

When a Hertzian pressure profile is used, this yields:

$$k_{\text{2nd}} = \frac{\eta_0 2\pi b a}{h_c c_{\eta P} p_0} \exp\left[c_{\eta P} p_0\right] \tag{260}$$

If the fourth order term is kept, this was found to be also analytically solvable, via Mathematica software, giving us an improved asymptotic estimate:

$$k_{\text{4th}} = \exp\left[c_p p_0 \left(\frac{A^2}{8C} + \frac{B^2}{8D}\right)\right] K_{\frac{1}{4}}\left(\frac{A^2}{8C}\right) K_{\frac{1}{4}}\left(\frac{B^2}{8D}\right) \frac{\eta_0}{h_c} \tag{261}$$

with:

$$A = \frac{c_{\eta p} p_0}{2b^2}, \quad B = \frac{c_{\eta p} p_0}{2a^2}, \tag{262}$$

$$C = \frac{c_{\eta p} p_0}{7b^4}, \quad D = \frac{c_{\eta p} p_0}{7a^4}. \tag{263}$$

where $K_{\frac{1}{4}}(x)$ is a *modified Bessel function* of the second kind [140, 129].

Appendix E: Proof Of Regularized Displacement Convolution

The full proof is given here for the sake of completeness, and also as it seems to be absent from other applied sources.

We are given that u_n is the response (output) to the Heaviside ($\mathscr{H}(t)$) function, therefore, for a linear system, we may express:

$$u_n = (y(t) * \mathscr{H}(t)) \tag{264}$$

Where $y(t)$ is some undefined linear impulse response to the system, and $(*)$ denotes the convolution operation.

Invoking the fundamental properties of convolution, for differentiation:

$$\frac{d}{dt}(\tilde{g} * \tilde{f}) = \frac{d\tilde{g}}{dt} * \tilde{f} = \tilde{g} * \frac{d\tilde{f}}{dt} \tag{265}$$

Using our prior definitions (Eq. (225)), we can substitute $\tilde{g} \to g_\epsilon, \tilde{f} \to \mathscr{H}$.

We can express $g_\epsilon(t)$ as :

$$\int_{-\infty}^{\infty} f_\epsilon(t)\mathscr{H}(t-t')dt' = \int_{-\infty}^{\infty} g_\epsilon(t)\delta(t-t')dt' = g_\epsilon(t) \tag{266}$$

Where we have made use of Eq. (227), and:

$$\delta(t) = \frac{d\mathscr{H}(t)}{dt} \tag{267}$$

and the sifting properties of the delta function.

We are trying to find the system response to our smoothed Heaviside approximation, g_ϵ, or formally:

$$u_e = (y(t) * g_\epsilon(t)) \tag{268}$$

Ergo, subbing in Eq. (266):

$$u_e = (y(t) * (f_\epsilon(t) * \mathscr{H}(t))) \tag{269}$$

Due to the commutative property of convolution, we may swap the order of any of the functions, giving:

$$u_e = ((y(t) * \mathscr{H}(t)) * (f_\epsilon(t))) \tag{270}$$

That leaves from Eq. (264), and commutativity again;

$$u_e = (u_n(t) * f_\epsilon(t)) = (f_\epsilon(t) * u_n(t)) \tag{271}$$

as required.

Appendix F: Ensuring Numerical Accuracy

Due to the aforementioned challenges in Subchapter 6.4, combined with the novelty of the investigation, extra care must be taken with accuracy. There are two main factors to consider for numerical accuracy of results.

Appendix F.1: Aliasing

Aliasing is a common issue when representing and processing continuous data as discrete forms. It occurs when the sampling rate is insufficient to capture the true nature of the waveform in signal processing, leaving a distorted version where the higher frequencies are misidentified into lower ones. The Shannon Nyquist sampling theorem is commonly used to overcome this, stating that the sampling rate must be at least twice the rate of the maximum frequency present in the signals [189, 190].

$$f_{Nyq} \geq 2f_{max} \tag{272}$$

However, the Fourier transform of f_ϵ is ([191]):

$$\hat{f}_\epsilon(\omega) = \mathscr{F}\{f_\epsilon(t)\} = \frac{1}{\sqrt{2\pi}} \int_{-\infty}^{\infty} f_\epsilon(t) e^{-i\omega t}\, dt = \frac{1}{\sqrt{2\pi}} \int_{-\infty}^{\infty} \frac{\epsilon e^{-i\omega t}}{\pi(t^2+\epsilon^2)}\, dt = \frac{e^{-\epsilon\omega}}{\sqrt{2\pi}} \tag{273}$$

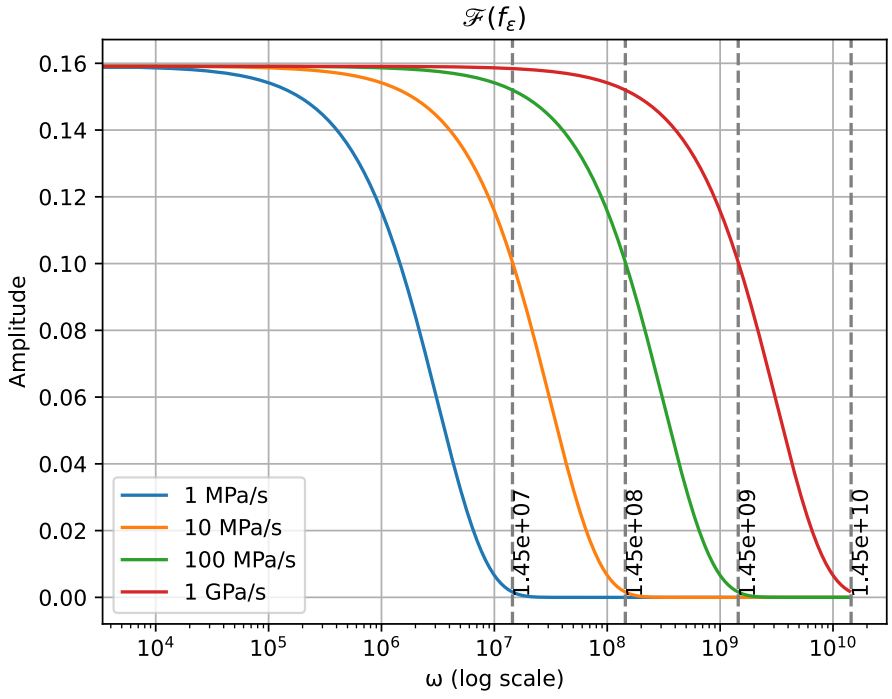

Figure 80: Fourier transform of different values of f_ϵ. The higher the load rate, the greater the frequency content in higher frequencies, meaning a higher frequency cut off ω_{99} is required.

Therefore, this is an open frequency function, meaning there is no maximum frequency, and the smaller ϵ is, (high load rates) the more frequency content present in higher frequencies. Strictly speaking the Shannon-Nyquist theorem cannot be used, as is often the case in real life applications. Instead, a limit of 99% of the maximum frequency amplitude is chosen as a cut off limit, ω_{99}. This is defined as the frequency when$\hat{f_\epsilon \omega}$ falls to 1% of its maximum value (at $\omega = 0$), $\frac{1}{2\pi}$:

$$\omega_{99} = \frac{\ln 0.01}{-\epsilon} \tag{274}$$

The corresponding frequency is:

$$f_{99} = \frac{\omega_{99}}{2\pi} \tag{275}$$

and therefore the corresponding Nyquist rate:

$$dt_{Nyq} = \frac{1}{2f_{99}} = -\frac{\epsilon\pi}{\ln[0.01]} \tag{276}$$

As the Nyquist frequency is the absolute minimum sampling rate required to capture the frequency features of a signal, for smoother signals a minimum timestep of:

$$dt = \frac{dt_{Nyq}}{4} = -\frac{\epsilon\pi}{4\ln[0.01]} \tag{277}$$

was used.

Similiarly, if the grid size is not sufficiently fine, due to the steep nature of a parabolic profile, neighbouring elements will have too high a difference in load rates, and thus in wave frequencies, to result in smooth resultant displacements: the spatial form of aliasing. It was subsequently found whilst for establishing summed results like total (or mean) surface velocity, or total (mean) strain, $N \approx 300$ tended to suffice, but for a clear signal of an individual elements evolution $N \approx 500$ was necessary.

Appendix F.2: Stability

Secondly, *stability* is also required. Whereas with aliasing convergence may be attained, but will not be representative of a true solution, stability is a prerequisite for convergent results. Without it, errors will propagate. One type of convergence condition is the CFL [192] like relationship:

$$C_{CFL} = \Delta t \sum_{i}^{n} \frac{V_i}{\Delta x_i} \leq C_{max} \tag{278}$$

where V denotes the max wave speed (C_p),and simulation grid sizes must give a dimensionless Courant number (C_{CFL}) under $C_{max} = 1$ for convergence.
Using an insufficient time-step leads to the wavespeed propagating over multiple grid points between successive steps, resulting in a loss of information. A ratio of 3 was selected here.

Additionally, there are complexities involved with the singularities in Eq. (218), as set out below.

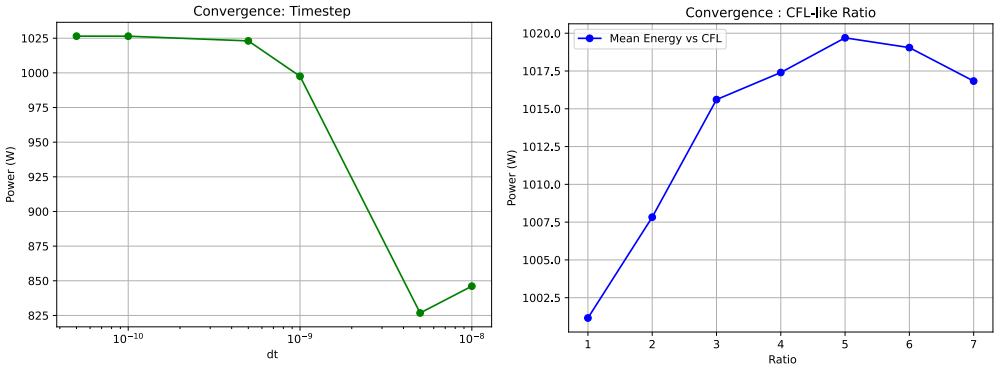

Figure 81: Convergence was taken very seriously in this study, and tested over multiple factors

1. Singularity around $1/|x|$. As spatial sampling decreases and $|x|$ between neighbouring elements gets increasingly small, contributions will diverge. This was dealt with by using a a conservative spatial regularisation parameter ε_x. This was 2-3 orders of magnitude lower than the finest spacing between grid points, and modified $x \to (x^2 + \varepsilon_x^2)^{0.5}$ This is a common method in problems of these nature [193, 194, 195, 196], and increased resultant stability and sped up convergence.

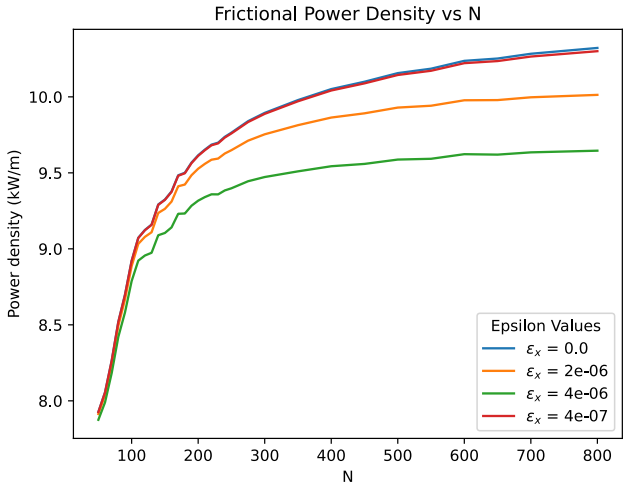

Figure 82: Convergence is slower than that of typical elliptical geometry- at between 500-800 elements, with mild oscillatory behaviour. This can be attributed to the complex dynamics of vibration. ε_x speeds up convergence, but at the loss of information, by effectively reducing the minimum scale and blurring resolution.

2. Singularity around $\tau = C_s/C_r$ (see Fig. 67). Whilst the 3D displacement functions were found to be successfully regularized by convolution [172] [34], the 2D versions are trickier, as the strength of the singularity is greater in the latter, and diverges at a greater rate. This is as the Rayleigh function, which features in the denominator,

[34] And in work on the initial 3D model performed here.

vanishes. Eringen and Suhubi on page 617 [153], regard an integration over this domain as taking a Cauchy Principal Value. Formally this is defined as excluding the problematic region in the integral:

$$\text{C.P.V.} \int_a^b f(z)\,dz = \lim_{\epsilon \to 0} \left(\int_a^{z_0-\epsilon} f(z)\,dz + \int_{z_0+\epsilon}^b f(z)\,dz \right) \tag{279}$$

In the spirit of Occam's razor, this was done by simply truncating u_{xx} when it exceeded the magnitude of the first peak in the displacement function, invoked by the pressure wave, that can be viewed as a physically motivated limit. This involved finding the local maxima of $u_{xx} \in \underline{a} \leq \tau \leq 1$, solving $\frac{\partial u_{xx}}{\partial \tau} = 0$. I.e.:

$$\begin{aligned}
\frac{\partial u_{xx}}{\partial \tau} &= \frac{8(1-\tau^2)\sqrt{\tau^2-\underline{a}^2}\tau}{(2\tau^2-1)^4 + 16(1-\tau^2)(\tau^2-\underline{a}^2)\tau^4} - \frac{8\sqrt{\tau^2-\underline{a}^2}\tau^3}{(2\tau^2-1)^4 + 16(1-\tau^2)(\tau^2-\underline{a}^2)\tau^4} \\
&+ \frac{4(1-\tau^2)\tau^3}{\sqrt{\tau^2-\underline{a}^2}\left((2\tau^2-1)^4 + 16(1-\tau^2)(\tau^2-\underline{a}^2)\tau^4\right)} \\
&- \frac{1}{\left((2\tau^2-1)^4 + 16(1-\tau^2)(\tau^2-\underline{a}^2)\tau^4\right)^2} \Big[4(1-\tau^2)\sqrt{\tau^2-\underline{a}^2} \cdot 16(2\tau^2-1)^3\tau \\
&+ 32(1-\tau^2)\tau^5 - 32(\tau^2-\underline{a}^2)\tau^5 + 64(1-\tau^2)(\tau^2-\underline{a}^2)\cdot\tau^3\tau^2 \Big] = 0
\end{aligned} \tag{280}$$

This had to be solved numerically, as polynomials above order 4 can't generally be solved [197], and was done via a Mathematica script. For steel $\underline{a} \approx 0.56$ gave a root in $\tau \approx 0.577245$. Tethering the limit of the displacement to different multiples of $n \cdot u_{xx}(\tau = 0.577245)$ was experimented with (figure $n = 1, 5, 10$). It was found this didn't effect overall mean power values, just the speed of convergence. In the end $n = 1$ was selected, thus excluding the problematic region previously identified.

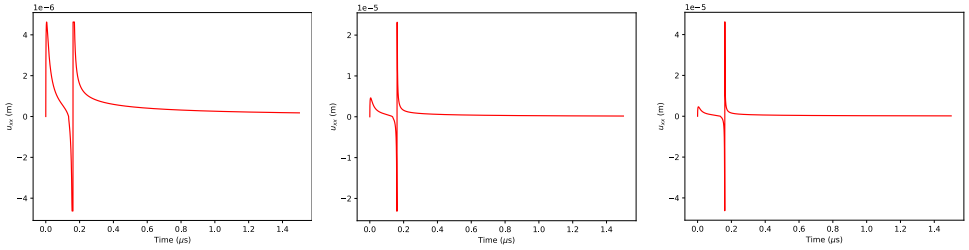

Figure 83: Different limits of truncation n. Final mean power results weren't effected, but speed of convergence was slowed, the higher the truncation.

Numerically, this was still a challenging situation, and an analytical solution to the problem, if one exists, should be the focus of future work.

Appendix G: Pressure Rate Profiles

Appendix G.1: Uniform Pressure Rate Profile

The case of uniform applied pressure is a classic elastostatic example explored in many texts in contact mechanics. Here the transient example is explored, as it explains the working of the model.

Pressure rate, and traction rate are taken as:

$$\frac{\mathrm{d}p}{\mathrm{d}t} = \frac{\mathrm{d}p_0}{\mathrm{d}t}, \quad \frac{\mathrm{d}q}{\mathrm{d}t} = \mu\frac{\mathrm{d}p_0}{\mathrm{d}t} \tag{281}$$

The cases below were for the dimensions of a Hertzian line contact formed for the bearing test case geometries under a load of $F = 10\,\mathrm{kN}$, with $\dot{F} = 10\,\mathrm{kN\ s^{-1}}$.
$\dot{p}_0$, $\dot{q}_0$ were calculated from the central point of the equivalent elliptical distribution line contact.

Only 200 grid points were required for satisfactory convergence, a number typical for regular (static) elliptical integration problems. This is due to the spatial coherence of the wavefronts- all points on the surface in contact are in phase in displacements (Fig. 84), at just after impact $t \approx 0$ [35]. This gives a smooth displacement field. As will be covered, in Hertzian load rates later a far higher number of points is required. There is then an initial transitory phase, of duration $2b/C_r$. There are two things going on here:

1. Instability due to edge effects of convolution. Since the window of convolution is initially very small, numerical inaccuracies associated with discretisation are amplified, as the sample size is very small. With sufficient discretization this effect quickly becomes negligible into the simulation.

2. Ongoing interaction of surface vibrations. At time $2b/C_r$, the furthermost points at the edges of line contact become fully connected, having exchanged Rayleigh waves with each other. After this outputs will start to become reflective of the rest of the duration of the simulation time, as the system converges on dynamic equilibrium. Before this point however, the system is in a transient phase, and larger changes in behaviour can be observed. This can be observed at multiples of b divided by the three speeds, when the different waves from the two further most points of the contact first encounter each other at the midpoint, then in full at $2b$. This is best illustrated on the average surface strain graph (Fig. 85), where changes in gradient can be linked with these multiples.

[35] At $t = 0$ u_{xx} is undefined.

Symbol	Definition	Value
$\underline{G}$	Shear modulus	79 MPa
μ	Coefficient of friction	0.1
C_p	Primary/Pressure wave speed (P-wave)	5790
$\underline{K}$	Bulk modulus	200 Mpa
C_s	Secondary/Shear wave speed (S-wave)	3250 m/s
C_r	Rayleigh wave speed	2770 m/s
$\underline{\nu}$	Poisson's ratio	0.27
$\underline{\rho}$	Density	7850 kg/m^3
$\dot{q}, (= \dot{q}_0)$	Traction rate	69.4 MPa/s
b	Semi minor contact width	0.406 mm

Table 12: Simulation Parameters for Uniform Load Rate Tests

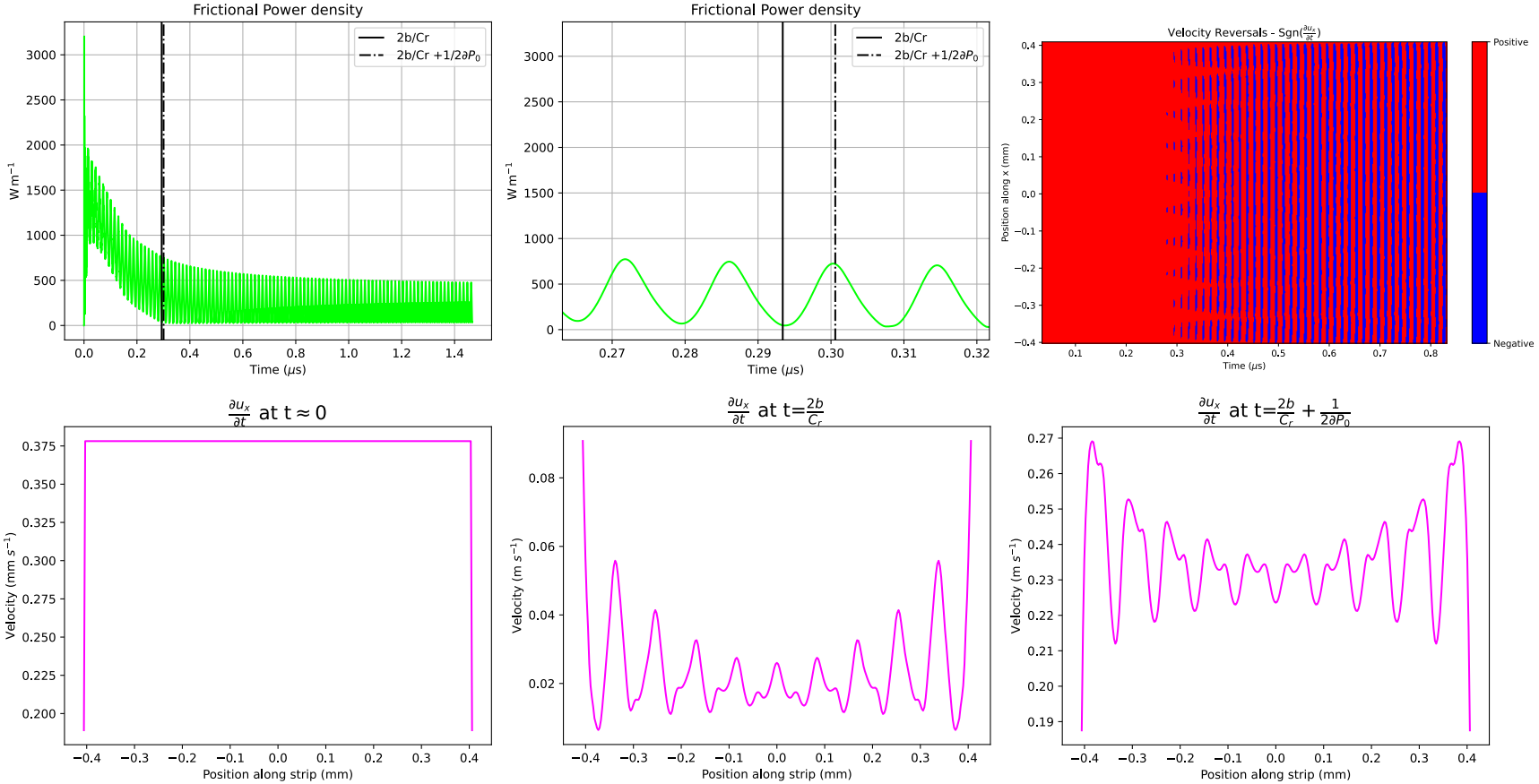

Figure 84: Velocity and frictional power profiles. There is a clear single frequency and associated time period, in which the velocity oscillates in time and space, due to there being only one loading frequency present. Powers settle to a constant output, as dynamic equilibrium is reached. The long-term velocity sign of slip is spatially planar in the uniform load rate case.

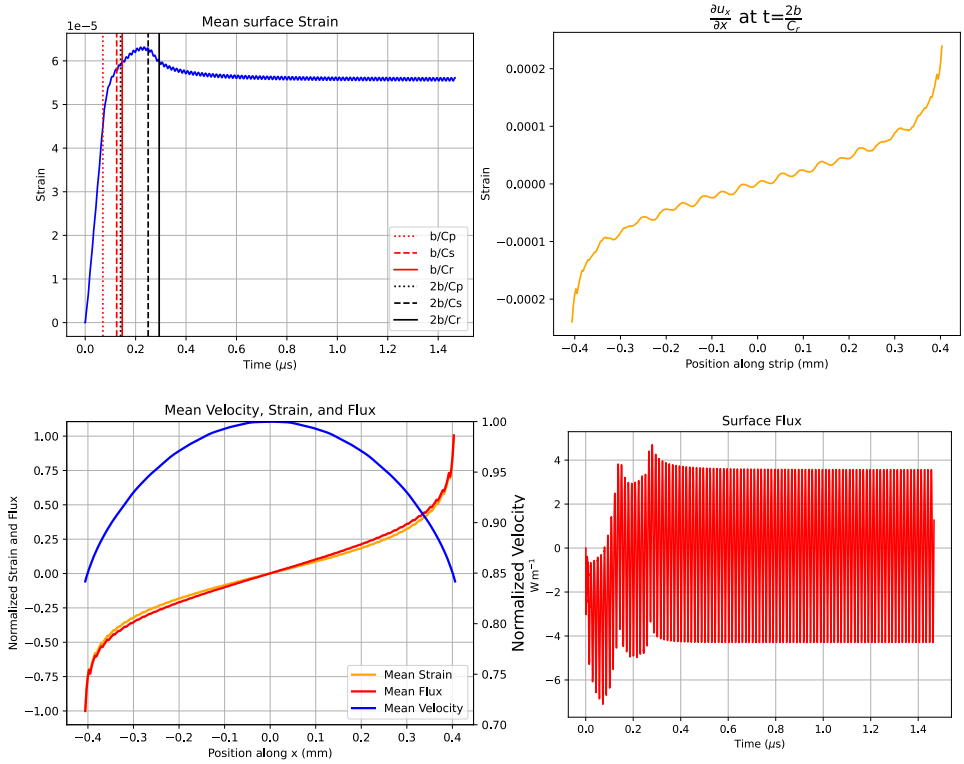

Figure 85: Average dynamic strain in time can be seen to have key behaviour changes corresponding to multiples of wave speeds over the length of the contact. Surface flux helps explain the physics of the problem, via equipartition of energy

Some observations worth stating:

- Dynamic strain approaches a smooth form at $t = 2b/C_r$, after which there is a mild oscillation about this form. The overall amplitude of this dynamic strain does not increase after this point, as the system approaches dynamic equilibrium.
- The dynamic velocity term is symmetric. This is because the elastic force is equal and opposite between two interacting points. Such a pair will push or pull each other equally in the same direction.
- The velocity exhibits complex, dynamic behaviour. Naively, it might be expected that it retains the same form as at $t \approx 0$ throughout the simulation. However, this is a complex spatial problem. The forces are long range, and because it is a closed system with $1/x$ decay. For the locations at the edge, whilst experiencing the same pressure rate as the central point, will experience a different integrated effect of this, as they have fewer immediately neighbouring elements at the boundary. This imbalance, results in variations in surface velocity, and this effect is propagated by the three waves.

  This is graphically explained in Fig. 86. Initially, the velocity is isotropic spatially. If the system were an infinite line, then there would be no spatial variations in velocity at a given time-step and it would be perfectly in phase[36]. However, a front moves in from the edge of the contact, as here is where the imbalance is present.

[36] The system would still oscillate in time, but spatially in phase

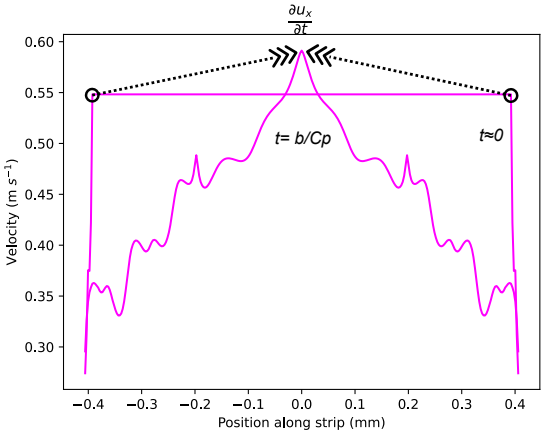

Figure 86: Velocity profile at $t \approx 0$ and $t = b/C_p$. The spike carried by the pressure wave is due to imbalance at the edge of the contact, and moves inwards to meet at the centre.

This sharp peak meets at the midpoint, at $t = \frac{b}{C_p}$, and then the vibrations begin a state of superposition to form a resultant vibration for the rest of the simulation. Shear and Rayleigh waves also undergo the same processes, and this superposition is fully established when they have covered the entire length of the contact, $2b$.

The spatial gradient in load rates will invoke complex variations across the velocity profile, and will be important for Hertzian load rate analysis.

- The time between successive peaks in both frictional power (due to velocity) and strain is $\dot{q}^{-1}$. This is as expected, as there is only one frequency present, and is used in constructing the separation between successive f_ϵ of Ш_ϵ.
- Slip reversal is predicted by the model [37]. Due to the presence of the negative displacement region in the displacement function, and the in-phase nature of the load rate, negative slip (opposing the direction of traction) will occur. Aside from in the transient phase $t < 2b/C_r$, this doesn't occur in a concurrently spatial manner, and the long term behaviour of slip direction is planar.
- All wave motion has an associated energy flux. In ED, volumetrically this can be expressed as [159][38]:

$$\mathbf{s} = -\underline{K}(\Theta)\dot{u}_i - 2\underline{G}\Sigma_{ij}\dot{u}_j \tag{282}$$

where:

  - Θ is the trace of the strain tensor.
  - Σ_{ij} is the off diagonal components of the shear tensor.

[37] This could be an unavoidable artefact due to the use of Ш, and caution should be taken in its analysis. In reality, the load rate profile won't be a succession of peaks on an infinitesimal scale, but a constant 'block' of load rate. However, the displacement functions are not formulated for this, and whilst there is scope for excessive 'waviness' to be introduced in solutions, this won't effect magnitude of slip results. Furthermore, the two will become identical with reduction in separation between delta peaks, and such a delta train is commonly used as a representation of more complex loads [131].

[38] Analogous to the Poynting vector in Electrodynamics.

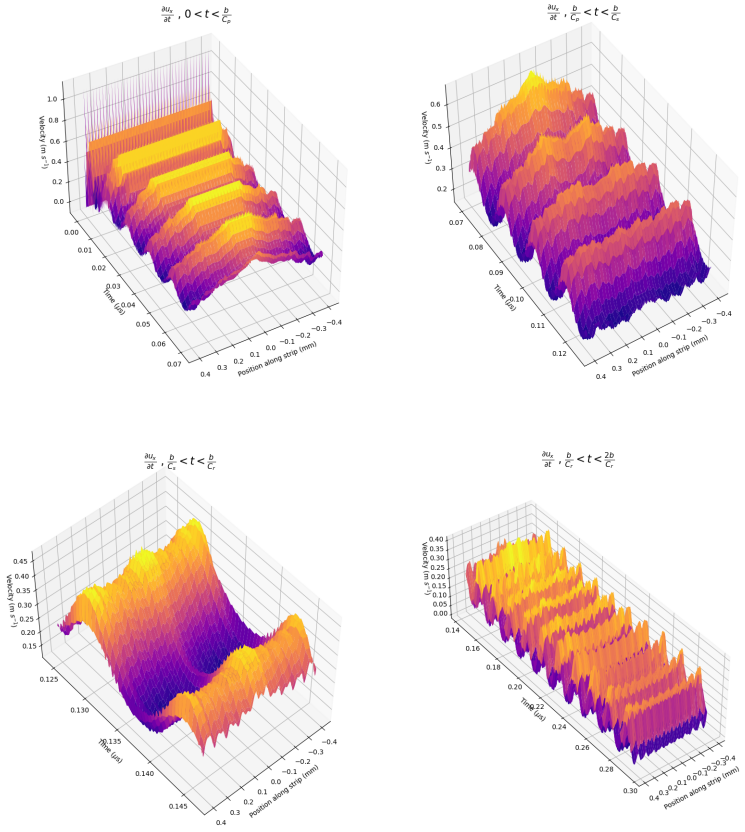

Figure 87: Transient components of surface velocity waveform in multiples of length of contact over wave speed. Pressure spikes are initially observable moving inwards, then superposing. Shear, then Rayleigh, wave interaction introduces extra degrees of complexity. The system then begins to approach its long-term form (bottom right).

Accordingly, the surface flux s_{xx} associated with u_{xx} is simply the product of $\underline{K}$, $\frac{\partial u_x}{\partial t}$ and $\frac{\partial u_x}{\partial x}$. The time series plot of this line flux underlines the physics of the simulation. Flux is initially negative following impact, as net energy is going into the system due to the large applied impulse, and then it is absorbed as elastic potential energy. This excess energy is carried out of the system by elastodynamic waves exiting the contact. As dynamic equilibrium is approached, flux fluctuates between negative and positive values, due to a constant exchange of energy between elastic and kinetic (equipartition of energy). Eventually, energy exiting the contact balances energy coming in from loading, thus establishing dynamic equilibrium.

- True dynamic equilibrium isn't reached instantly after $2b/C_r$, and values continue to level off slowly. This is because the form of u_{xx} never truly reaches 0, and as convolution is a causal operation, the system will have an infinite memory of past events. Since it is dynamic equilibrium which will be representative of the long-term behaviour of the system, representing the majority of the time-step Δt in practical analysis, care needs to be taken with system memory. Initialisation could introduce artefacts in analysis, and will need to be accounted for. Here this was done by truncating the displacement function above the characteristic timescale

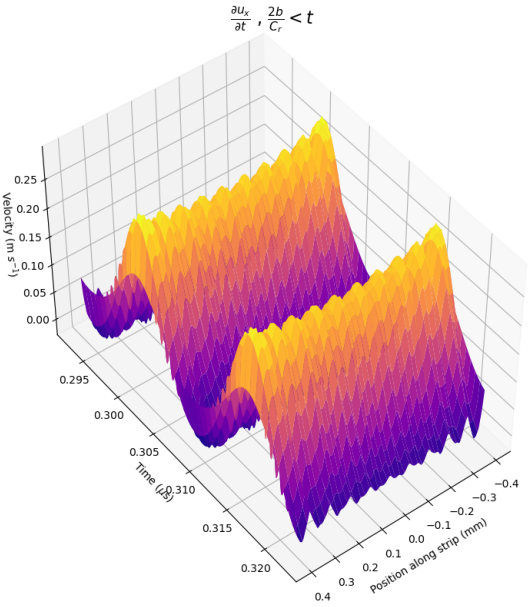

Figure 88: Long term behaviour of surface velocity waveform.

of the problem, i.e. $u_{xx}(t > 2b/C_r) = 0$. As this is dependent on global time, and thus time of wave propagation, it is an unbiased operation.

Despite the simplicity of the 2D loading profile, the complexity of results highlight the highly deterministic nature of the system. We now move onto the more complex Hertzian loading profile, which forms the basis of the real-world WTMB SRB analysis.

Appendix G.2: Hertzian Pressure Rate Profile

With the demonstrative uniform pressure case explored, the velocities and dynamic strains of a Hertzian profile was explored. This is the load rate our real word bearing is predicted to have. Three different load rates, 10 kN/s, 50 kN/s, 100 kN/s, were simulated for an applied load of 30 kN:

The transient and dynamic equilibrium period is different from the uniform traction rate profile, as instead of a single load rate frequency there are now a set of frequencies, corresponding to the parabolic profile of load rate. In the uniform load case, with finite system memory, history can be clearly split into two periods, of an initial transient phase, and followed by subsequent dynamic equilibrium.

A sampling window of $\dot{q}_0^{-1}$ (t_0) would be sufficient to capture the entire ensuing history at this point, since what follows is just a repetition over this period, due to the single frequency present. Establishing an equivalent period for the Hertzian load rate is not so obvious. In practice, it was found that the frequency produced by the central load rate dominated the energy, and a sampling period, $t_{\text{char}} \approx 3 - 10\,\dot{q}_0^{-1}$ tended to suffice

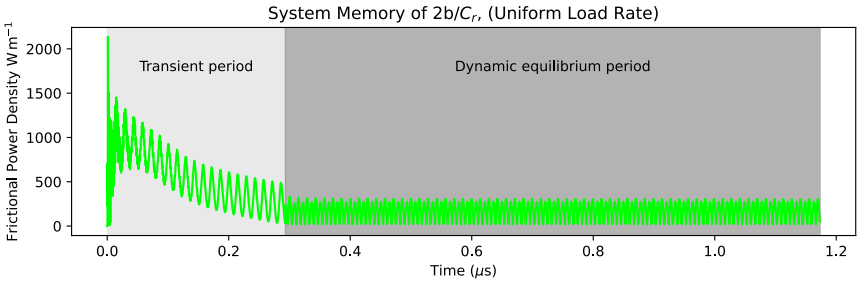

Figure 89: Imposing a finite system memory forces a decay at $t = 2b/C_r$ onto the true dynamic equilibrium state. The discontinuity at this time shows that residual effects from an impact event are significant, and do need to be accounted for to avoid artefacts when making assessments of metrics via extrapolation (Eq. (234)).

[39]. A longer, more rigorous period was used for wind analysis.

Dynamic equilibrium mean behaviour is thus adequately captured. Running longer lengths than this would not provide a great deal of extra information.

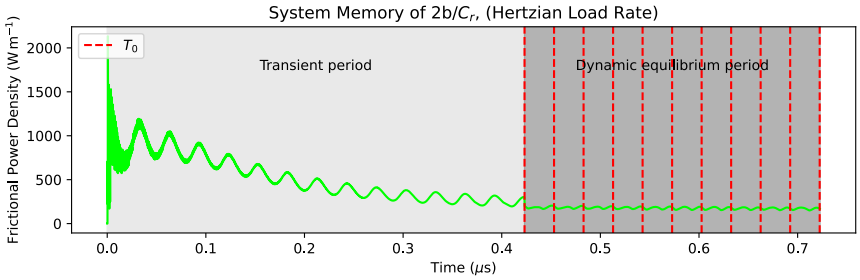

Figure 90: A sampling time over the dynamic equilibrium period of between 3-10 of the central load rate frequency t_0 ($\dot{q}_0^{-1}$) was deemed adequate for assessments of power and energy for a Hertzian profile.

The results of the three different load rates are now explored. System memory of impact was still present in the following tests, capturing the residual effects of impact (e.g. sudden gusts of wind imparting impulse loads on the bearing). However, for wind condition case studies this effect will be negated, as the load rates will on average be more gradual.

Simulation	b	$\frac{dF}{dt}$	$\frac{dq_0}{dt}$	N	dt
Sim 1	0.585 mm	10 kN/s	33.4 MPa/s	500	0.135 ns
Sim 2	0.585 mm	50 kN/s	167 MPa/s	1000	0.068 ns
Sim 3	0.585 mm	100 kN/s	334 MPa/s	1000	0.068 ns

Table 13: Simulation Parameters for three simulated Hertzian Load Rate Tests.

Observations:

[39] Although the true period of repetition (Δt_{char}) of a discrete set of periods would be given by the lowest common multiple of them, $t_0 = \text{lcm}(t_i)$.

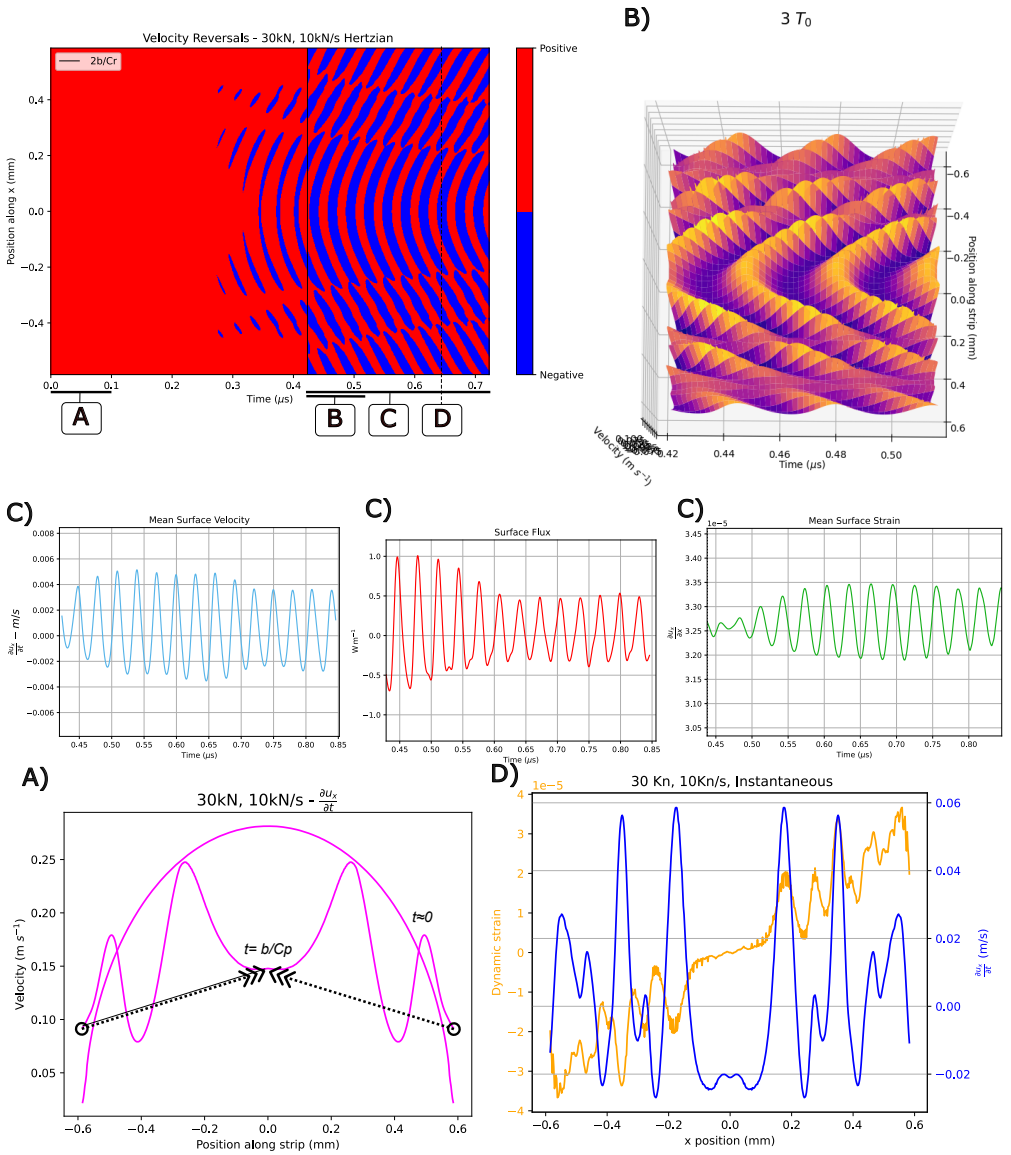

Figure 91: Showing how metrics over dynamic Hertzian loads rates are more complex than for the uniform case, due to the associated frequency spectrum. It can be seen that $\frac{\partial u_x}{\partial x}$, $\frac{\partial u_x}{\partial t}$ and thus flux (C) oscillate around a long term stable value, with the highest frequency component dominating dynamics. The resultant vibration over t_{char} is shown in (B).

- Strain and velocity terms are highly dynamic, propagating across the contact with time. Strain now also varies spatially in time. This was not the case with uniform pressure rates. This is due to the variation in $\dot{q}$ across the contact.
- Peak values of strain and velocity appear linear with load rates between the same absolute load conditions. This is unsuprising considering our use of linear theory.
- The elastic strain limit of steel is 0.3-0.1% (0.001-0.003). After this point the material will permanently deform and surface damage will occur. The highest

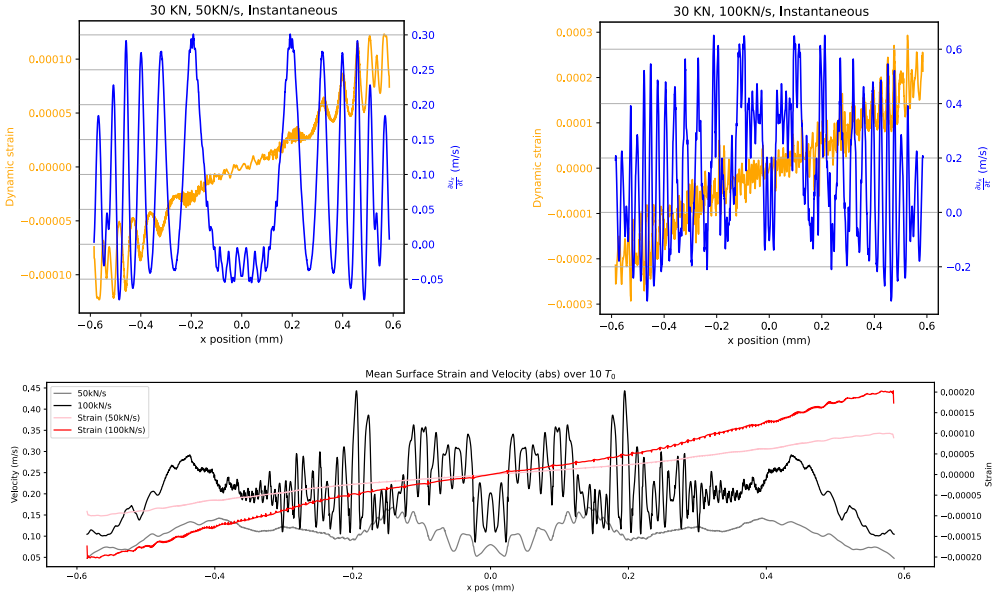

Figure 92: Simulation 2 and 3 results have high frequency load rates, and thus complex higher frequency vibrations.

risk of this happening is at low loads and highest load rates, thus the highest instantaneous pressure rates. This might correspond to an unloaded or lightly loaded bearing suddenly being loaded by a gust of wind. However, it should be noted that high values of μ might contribute too higher than expected outputs. Furthermore, the assumption of constant contact dimensions will be least valid at low loads, meaning the model is least sensitive. It is at this points that the contact patch grows quickest, potentially relieving high pressure rates. Further work is required to determine if dynamic strains do approach the elastic strain limit of steel.

- Regions of spatially concurrent reverse slip are clearly predicted, and these regions become less separated in both time and space with increases in load rate. The mechanical implications of this are currently unclear, but should be investigated in future, as these matters indicate local compressions and extensions of surface material, and thus concentrations of strain tips. This is not something that can be predicted by steady state microslip.

- Spatial aliasing starts to become an issue at higher load rates, and thus higher grid numbers are required. This is because there are steeper spatial gradients in local load rates. Future work should look at analytical methods, or frequency domain calculations (being computationally cheaper due to N log N).

- It should be noted that there is again a constant exchange of energy between elastic (strain $\times$ bulk), and kinetic. Because of the wide set of load frequencies it would require an unfeasibly long time to capture the full dynamics of the simulation. However, average strain and velocity settle quickly, after which they exhibit a complex oscillation about dynamic equilibrium state values.

Appendix H: Dynamic Strain Transient Microslip Contribution

This figure shows how little dynamic strain in practice contributes to microslip, with rotational speed of roller. Because of this it can effectively be disregarded in calculation of frictional energy.

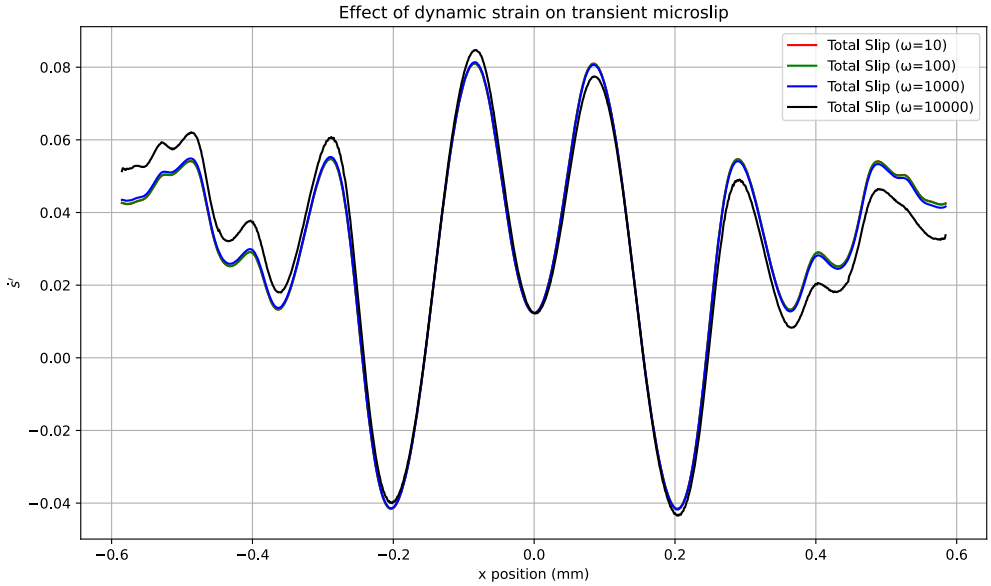

Figure 93: Dynamic strain is seen to contribute minimally to net microslip, apart from very high angular speeds. Therefore only $\frac{\partial u_x}{\partial t}$ was used in calculations of test matrix **M**.

Appendix I: Proposed Cumulative Frictional Energy Density Failure Prediction Algorithm

The following section explores how cumulative energy densities might be used to predict bearing lifetimes, using analyses of the frictional effects of repeated low level shock exposure. The value of this lies in its exploration of the spatial distribution of these densities on individual element failure, a feature available through the presented transient model, which accesses the full spatial complexity of frictional dissipation. The methodology is general and preliminary, and other failure methods such as rolling contact fatigue (RCF) are ignored. A full assessment of actual life would involve a combined consideration of these, not possible within the time-frame of current work.

It only takes one element of the raceway to fail, to cause a failure of the entire bearing[198]. Alternatively, this expression is equivalent to the probability of the whole bearing surviving, being the product of the probabilities of the survival of its components, that are themselves a product of probabilities of the survivals of their individual surface elements:

$$S_{\text{bearing}} = \prod_{i=1}^{n_{\text{comp}}} S_{\text{comp}} \approx \prod_{k}^{in} S_k \cdot \prod_{k}^{out} S_k \cdot \prod_{j}^{roll} S_j \tag{283}$$

focusing only on the inner raceway for demonstrative purposes.

The start point is assuming that survivability of an element, is related to cumulation of frictional power density, by a Lundberg-Palmgren like relationship:

$$\ln \frac{1}{S_k} \propto \left(\int_0^t \dot{E}_k dt \right)^n dxdz \tag{284}$$

where n is some underdetermined parameter. The integral represents energy, leaving a resultant energy density, the same SI units as the original Lundberg-Palmgren model, and based on Weibull statistics [36]. This is just a formal representation of the previously used assumption that cumulative frictional energy density can serve as a proxy for failure likelihood, similar to how the Lundberg-Palmgren model treats stress cycles for RCF. Only the most basic form of Eq. (284) is considered, with n being set to 1.

Thus, the survivability of the inner race as a whole is given by:

$$\ln \frac{1}{S_{\text{in}}} \propto \sum_{k}^{\text{in}} (E_k)^n dxdz \tag{285}$$

and the survivability of the inner raceway is given by:

$$S_{\text{in}} \propto e^{C \sum_k^{\text{in}} E_k^n} \tag{286}$$

where dx, dz have been absorbed into an arbitrary constant C, by design.

However, C and n remain free parameters. Although their absolute values are unknown, we can compare observed (field) survivability under different operating conditions to find and use them for future predictions. Again, for brevity and demonstrative purposes, we are just assuming $S \approx S_{\text{in}}$, ignoring the other components of the bearing.

To find C and n, we must choose a reference set of conditions where an associated survivability is known and then take the ratio of survivabilities:

$$\frac{S_{\text{ref}}}{S_i} = e^{C\left(\sum_k E_{\text{ref}}^n - \sum_k^{\text{in}} E_i^n\right)} \tag{287}$$

If S_{ref} has an associated $L10$, due to its inverse proportionality, we may express the $L10$ life of sub-condition i as:

$$L10_i = L10_{\text{ref}} e^{C\left(\sum_k E_{\text{ref}}^n - \sum_k^{\text{in}} E_i^n\right)} \tag{288}$$

Then, using strict series reliability or linear damage theory, the combined lifetime is:

$$L10_{\text{comb}} = \frac{1}{\sum_i \phi_i / L10_i} = L10_{\text{ref}} \frac{e^{C\sum_k E_{\text{ref}}^n}}{\sum_i \phi_i e^{C\sum_k E_i^n}} \tag{289}$$

where ϕ_i represents the total proportional time spent in each operational sub-condition, which may be derived from operational data or a Weibull wind profile.

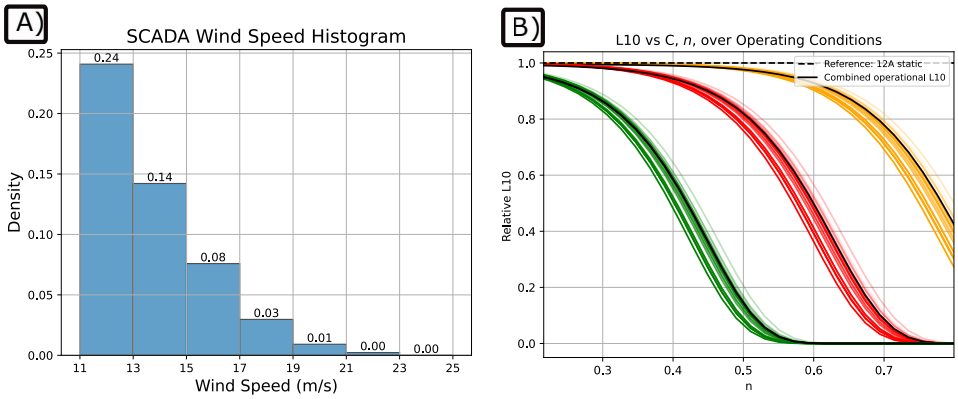

Figure 94: (A): Weighting used, from SCADA wind speed distributions from Chapter 2. This is used to combine the different $L10_i$ over the 12-24m/s wind speeds in (B), to arrive at a combined L10 (black line), for that C (red, orange, green). Each individual $L10_i$ is displayed by a single coloured line, for each wind condition (e.g. 14m/s C). These were calculated from applying Eq. (289) over the relevant dataset (Fig. 95)

This equation can be minimized against field observations (e.g., using a Nelder-Mead solver with a sum-of-squares implementation) to infer parameters C and n, thereby quantifying the system's sensitivity to power densities.

Examples are given below in fig, of how this could be done, for field L10's corresponding to 10% and 90% of a reference L10, by using the 12 A static file as a reference, and the same weighting in Fig. 94(A), to uniquely determine values of C and n.

It should be noted that C and n are uniquely determined, if there is both an observed failure rate, and wind condition distribution with associated frictional energy dataset, and in an ideal case should be identical for a given bearing.

Any reference L10 could be selected, for example field data of wind-speeds and observed failure rates in themselves, to predict L10's of different field conditions.

For example, using the 12 A dynamic condition as a reference, shows there is a big difference in densities, or associated failure chances, between the static and dynamic

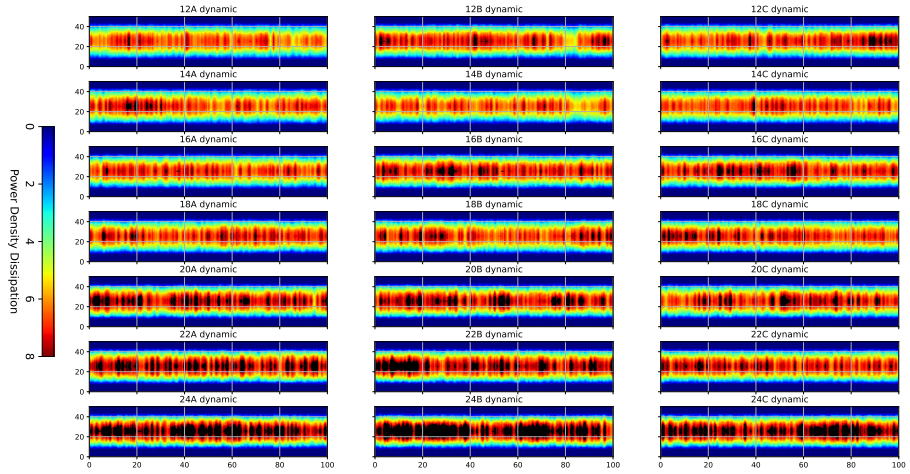

Figure 95: Dataset used in the life analysis model demonstrating densities of frictional energy increase with windspeed.

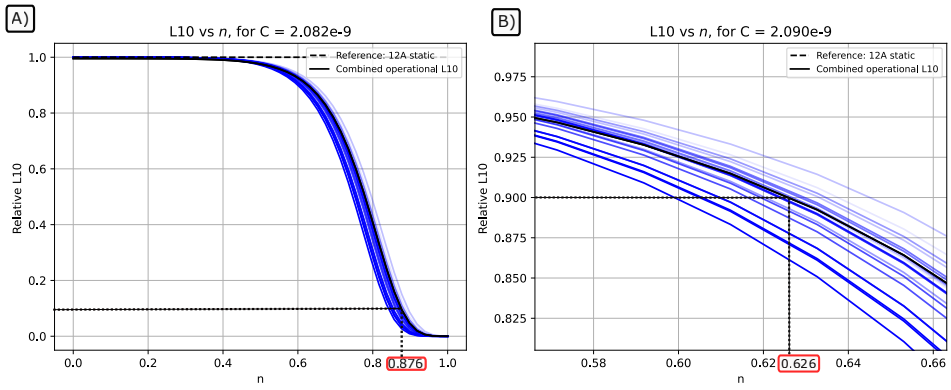

Figure 96: L10 composition for failures rates corresponding to 10% of L10 reference (A) and 90% of reference (B).

cases. This is as here, there is now no longer a narrow grouping between windspeeds (e.g. compared to Fig. 94b or Fig. 96). This indicates there isn't a large difference in energy densities between individual dynamic cases, when compared to the difference there is between static and dynamic ones.

Such methods may be used to predict lifetimes for different wind distributions, or to test the hypothesis that microslip and frictional energy is a driver of failure. In reality, this would need to be combined with weighting in algorithms for other known modes of failure to make valid predictions (RCF). Higher resolution datasets and calculations, across both differing wind conditions and spatially along the raceway would be required to train this model. This would necessitate the use of fairly powerful numerical methods [199] (Fig. 98).

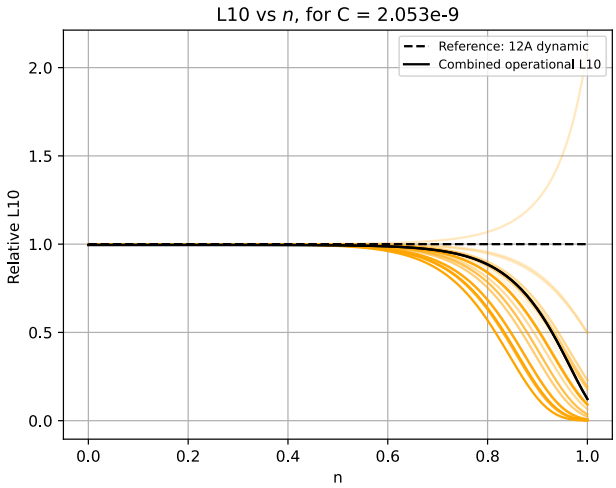

Figure 97: The spread in relative L10's when 12A is used as a reference L10.

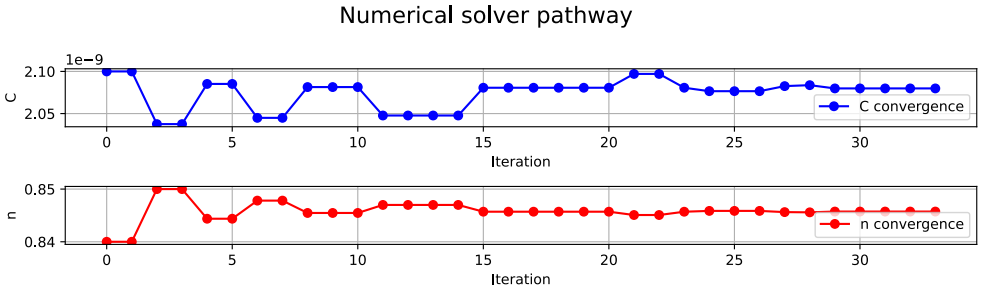

Figure 98: Due to the large number of cell elements, and datafiles, solving Eq. (289) is a sensitive calculation. When combining this with large sets of field data, advanced numerical methods will be required.

References

[1] WindEurope. Wind Energy in Europe in 2019. https://windeurope.org/about-wind/statistics/european/wind-energy-in-europe-in-2019/, 2019.

[2] P. S. Arrhenius. XXXI. On the Influence of Carbonic Acid in the Air upon the Temperature of the Ground. *The London, Edinburgh, and Dublin Philosophical Magazine and Journal of Science*, 41(251):237–276, 1896.

[3] E. J. R. de Mello. Personal communication, 2023. Conversation on 15th March 2023 Regarding the Impending Environmental Calamity.

[4] X. Lu, M. B. McElroy, and J. Kiviluoma. Global Potential for Wind-Generated Electricity. *Proceedings of the National Academy of Sciences*, 106(27):10933–10938, 2009.

[5] GOV.UK. Wind of Change for the Humber Region. https://www.gov.uk/government/news/wind-of-change-for-the-humber-region, n.d. [Accessed 31 August 2021].

[6] Windpowerengineering. Windpower Engineering & Development. http://windpowerengineering.com, No Date. Accessed: 1 September 2021.

[7] E. Hart, A. Turnbull, JuJ.lian Feuchtwang, D. McMillan, E. Golysheva, and R. Elliott. Wind Turbine Main-Bearing Loading and Wind Field Characteristics. *Wind Energy*, 22(11):1534–1547, 2019.

[8] E. Hart, B. Clarke, G. Nicholas, A. Kazemi Amiri, J. Stirling, J. Carroll, R. Dwyer-Joyce, A. McDonald, and H. Long. A Review of Wind Turbine Main Bearings: Design, Operation, Modelling, Damage Mechanisms and Fault Detection. *Wind Energy Science*, 5(1):105–124, 2020.

[9] A. R. Nejad, J. Keller, Y. Guo, S. Sheng, H. Polinder, S. Watson, J. Dong, Z. Qin, A. Ebrahimi, R. Schelenz, F. Gutiérrez Guzmán, D. Cornel, R. Golafshan, G. Jacobs, B. Blockmans, J. Bosmans, B. Pluymers, J. Carroll, S. Koukoura, E. Hart, A. McDonald, A. Natarajan, J. Torsvik, F. K. Moghadam, P.-J. Daems, T. Verstraeten, C. Peeters, and J. Helsen. Wind Turbine Drivetrains: State-of-the-Art Technologies and Future Development Trends. *Wind Energy Science*, 7(1):387–411, 2022.

[10] Y. Guo, O. Bankestrom, R. Bergua, J. Keller, and M. Dunn. Investigation of main Bearing Operating Conditions in a Three-Point Mount Wind Turbine Drivetrain. *Forschung im Ingenieurwesen*, 85(2):405–415, 2021.

[11] L. Sethuraman, Y. Guo, and S. Sheng. Main Bearing Dynamics in Three-Point Suspension Drivetrains for Wind Turbines. National Renewable Energy Lab. (NREL), Golden, CO (United States), May 2015.

[12] E. Hart. Developing a Systematic Approach to the Analysis of Time-Varying Main Bearing Loads for Wind Turbines. *Wind Energy*, 23(12):2150–2165, 2020.

[13] No Author. Nacelle - Innovative Outcomes: Energy I-SPARK. https://ei-spark.lbl.gov/generation/onshore-wind/turb/nacelle/innov/, No Date. Accessed: 1 September 2021.

[14] J. F. Manwell, J. G. McGowan, and A. L. Rogers. *Wind Energy Explained: Theory, Design and Application*. John Wiley & Sons, Ltd, Chichester, U.K., 2nd edition, 2011. [Accessed 8 August 2021].

[15] The Engineering Blog. Rolling Element Bearing Types, Functions, Application & Designation System. `https://theengineeringblog.com/rolling-element-bearing-types-functions-application-designation-system/`, 2020. [Accessed: 1 September 2021].

[16] Adam H. Monahan. The Gaussian Statistical Predictability of Wind Speeds. *Journal of Climate*, 26(15):5563–5577, 2013.

[17] E. Hart, M. Keegan, and D. McMillan. A lookup table approach to determining wind turbine operational fatigue loading from wind field measurements. In *AS-RANet International Conference on Offshore Renewable Energy*, GBR, September 2016.

[18] T. Burton. *Wind Energy Handbook*. Wiley, Chichester, West Sussex, 2011.

[19] H. Pedersen and W. Langreder. Forest - Added Turbulence: A Parametric Study on Turbulence Intensity in and Around Forests. *Journal of Physics: Conference Series*, 75:012062, 08 2007.

[20] J. Sanz Rodrigo, J. van Beeck, and G. Dezsö-Weidinger. Wind Tunnel Simulation of the Wind Conditions Inside Bidimensional Forest Clear-Cuts. Application to Wind Turbine Siting. *Journal of Wind Engineering and Industrial Aerodynamics*, 95(7):609–634, 2007.

[21] P.A. Taylor. Wind Flow over Conical Hills: Computer Model Results. *Journal of Wind Engineering and Industrial Aerodynamics*, 16(1):119–124, 1984.

[22] J-C. Ruel, D. Pin, and And Cooper. Effect of Topography on Wind Behaviour in a Complex Terrain. *Forestry*, 71, 01 1998.

[23] E. Hart, E. de Mello, and R. Dwyer-Joyce. Wind Turbine Main-Bearing Lubrication – Part 1: An Introductory Review of Elastohydrodynamic Lubrication Theory. *Wind Energy Science*, 7(3):1021–1042, 2022.

[24] B. Gould and A. Greco. The Influence of Sliding and Contact Severity on the Generation of White Etching Cracks. *Tribology Letters*, 60:1–13, Oct 2015.

[25] P. K. Gupta. *Advanced Dynamics of Rolling Elements*. Springer-Verlag New York Inc., New York, 1 edition, 1984.

[26] S. Jain and H. Hunt. A Dynamic Model to Predict the Occurrence of Skidding in Wind-Turbine Bearings. In *Journal of physics: conference series*, volume 305, page 012027. IOP Publishing, 2011.

[27] Q. Han, X. Li, and F. Chu. Skidding Behavior of Cylindrical Roller Bearings Under Time-Variable Load Conditions. *International Journal of Mechanical Sciences*, 135:203–214, 2018.

[28] P. Chen, T. Pedersen, B. Bak-Jensen, and Z. Chen. ARIMA-Based Time Series Model of Stochastic Wind Power Generation. *IEEE Transactions on Power Systems*, 25(2):667–676, 2010.

[29] Y. Wang, W. Wang, S. Zhang, and Z. Zhao. Investigation of Skidding in Angular Contact Ball Bearings Under High Speed. *Tribology International*, 92:404–417, 2015.

[30] S. Jain. *Skidding and Fault Detection in the Bearings of Wind-Turbine Gearboxes*. PhD thesis, University of Cambridge, 2013. Thesis.

[31] E. Hart, E. de Mello, and R. Dwyer-Joyce. Wind Turbine Main-Bearing Lubrication – Part 2: Simulation-Based Results For a Double-Row Spherical Roller Main Bearing in a 1.5 MW Wind Turbine. *Wind Energy Science*, 7(4):1533–1550, 2022.

[32] A. Palmgren. *Ball and Roller Bearing Engineering*. S. K. F. Industries, Philadelphia, 1945.

[33] O. Menck and M. Stammler. Review of Rolling Contact Fatigue Life Calculation for Oscillating Bearings and Application-Dependent Recommendations for use. *Wind Energy Science*, 9(4):777–798, 2024.

[34] A. Kapoor, Iman Salehi, and Anna Maria Sri Asih. *Rolling Contact Fatigue (RCF)*, pages 2904–2910. Springer US, Boston, MA, 2013.

[35] F. Xu, N. Ding, N. Li, L. Liu, N. Hou, N. Xu, W. Guo, L. Tian, H. Xu, Chi-Man Lawrence Wu, X. Wu, and X. Chen. A Review of Bearing Failure Modes, Mechanisms and Causes. *Engineering Failure Analysis*, 152:107518, 2023.

[36] J. Kenworthy, E. Hart, J. Stirling, A. Stock, J. Keller, Y. Guo, J. Brasseur, and R. Evans. Wind Turbine Main Bearing Rating Lives as Determined by IEC 61400-1 and ISO 281: A Critical Review and Exploratory Case Study. *Wind Energy*, 27(2):179–197, 2024.

[37] C. Sobie, C. Freitas, and M. Nicolai. Simulation-Driven Machine Learning: Bearing Fault Classification. *Mechanical Systems and Signal Processing*, 99:403–419, 2018.

[38] C. C. Wang and C. J. Lin. Dynamic Analysis and Machine Learning Prediction of a Nonuniform Slot Air Bearing System. *Journal of Computational and Nonlinear Dynamics*, 18(1):011007, 11 2022.

[39] B. R. Noack S. L. Brunton and P. Koumoutsakos. Machine Learning for Fluid Mechanics. *Annual Review of Fluid Mechanics*, (Volume 52, 2020):477–508, 2020.

[40] S. L. Brunton, J. L. Proctor, and J. N. Kutz. Discovering Governing Equations from Data by Sparse Identification of Nonlinear Dynamical Systems. *Proceedings of the National Academy of Sciences*, 113(15):3932–3937, 2016.

[41] The Economist. A Deeper Law than Moore's, 2011. Accessed: 2025-03-26.

[42] M. N. Kotzalas and G. L. Doll. Tribological Advancements for Reliable Wind Turbine Performance. *Philosophical Transactions of the Royal Society A: Mathematical, Physical and Engineering Sciences*, 368(1929):4829–4850, 2010.

[43] Francesco Manieri, Kenred Stadler, Guillermo E. Morales-Espejel, and Amir Kadiric. The Origins of White Etching Cracks and Their Significance to Rolling Bearing Failures. *International Journal of Fatigue*, 120:107–133, 2019.

[44] Yan Zhou, Ji liang Mo, Zhen bing Cai, Chang guang Deng, Jin fang Peng, and Min hao Zhu. Third-body and crack behavior in white etching layer induced by sliding–rolling friction. *Tribology International*, 140:105882, 2019.

[45] Walter Holweger, Marcus Wolf, Daniel Merk, Toni Blass, Matthias Goss, Joerg Loos, Soeren Barteldes, and Andris Jakovics. White Etching Crack Root Cause Investigations. *Tribology Transactions*, 58(1):59–69, 2015.

[46] Mohanchand Paladugu, Douglas R. Lucas, and R. Scott Hyde. Effect of Lubricants on Bearing Damage in Rolling-Sliding Conditions: Evolution of White Etching Cracks. *Wear*, 398-399:165–177, 2018.

[47] A. Greco, N. Demas, R. Erck, B. Gould, J. Keller, S. Sheng, and Y. Guo. Wind Turbine Drivetrain Reliability, 2022.

[48] G.L. Doll. Surface Engineering in Wind Turbine Tribology. *Surface and Coatings Technology*, 442:128545, 2022. Special Issue of Surface and Coatings Technology Celebrating the Pioneering Research Career of Professor Allan Matthews in the Field of "Plasma-Based Surface Engineering".

[49] M. van Drogen B. Han C. Matta V. Brizmer, K. Stadler and E. Piras. The Tribological Performance of Black Oxide Coating in Rolling/Sliding Contacts. *Tribology Transactions*, 60(3):557–574, 2017.

[50] B. A. Tassone. Roller Bearing Slip and Skidding Damage. *Journal of Aircraft*, 12(4):281–287, 1975.

[51] A. B. Jones. The Mathematical Theory of Rolling-Element Bearings. In *Mechanical Design and Systems Handbook*. 1956.

[52] A. B. Jones. Ball Motion and Sliding Friction in Ball Bearings. *ASME Trans*, 81:1–12, 1959.

[53] T. A. Harris. An Analytical Method to Predict Skidding in High Speed Roller Bearings. *A S L E Transactions*, 9(3):229–241, 1966.

[54] J.J. Kalker. The Influence of the Circulation of the Balls in an Unlubricated Angular Contact Thrust Ball Bearing. *Wear*, 13(4):293–300, 1969.

[55] J.J. Kalker. The Analysis of the Motion of the Balls in an Unlubricated Angular Contact Thrust Ball Bearing. *Wear*, 12:3–16, Jul 1968.

[56] D. A. Danielson. *Vectors and Tensors in Engineering and Physics*. Addison-Wesley, 1st edition, 1992.

[57] P. K. Gupta. ADORE, 2025. Accessed: 2025-03-26.

[58] P. K. Gupta. Transient Ball Motion and Skid in Ball Bearings. In *ASME-ASLE Joint Lubrication Conference*, Montreal, Canada, 1974. Paper no. 74-Lub-9.

[59] P. K. Gupta. Dynamics of Rolling Element Bearings. Part III: Ball Bearing Analysis. In *ASME-ASLE Joint Lubrication Conference*, Minneapolis, Minn., 1978. Paper no. 78-Lub-32.

[60] P. K. Gupta. Dynamics of Rolling Element Bearings. Part IV: Ball Bearing Results. In *ASME-ASLE Joint Lubrication Conference*, Minneapolis, Minn., 1978. Paper no. 78-Lub-33.

[61] J. Pirvics. Discussion: “Dynamics of Rolling-Element Bearings—Part I: Cylindrical Roller Bearing Analysis” (Gupta, P. K., 1979, ASME J. Lubr. Technol., 101, pp. 293–302). *Journal of lubrication technology*, 101(3):303–303, 1979.

[62] L. Chang, C. Cusano, and T. F. Conry. Analysis of High-Speed Cylindrical Roller Bearings Using a Full Elastohydrodynamic Lubrication Model. I. Formulation. II. Results. *ASLE Transactions (American Society of Lubrication Engineers); (USA)*, 33, 04 1990.

[63] W. Tu, Y. Shao, and C. K. Mechefske. An Analytical Model to Investigate Skidding in Rolling Element Bearings During Acceleration. *Journal of mechanical science and technology*, 26(8):2451–2458, 2012.

[64] Q. Han and F. Chu. Nonlinear Dynamic Model for Skidding Behavior of Angular Contact Ball Bearings. *Journal of Sound and Vibration*, 354:219–235, 2015.

[65] Y. Liu, Z. Chen, L. Tang, and W. Zhai. Skidding Dynamic Performance of Rolling Bearing with Cage Flexibility Under Accelerating Conditions. *Mechanical Systems and Signal Processing*, 150:107257, 2021.

[66] Y. Guo and J. Keller. Validation of Combined Analytical Methods to Predict Slip in Cylindrical Roller Bearings. *Tribology International*, 148:106347, 2020.

[67] S. Gao, S. Chatterton, L. Naldi, and P. Pennacchi. Ball Bearing Skidding and Over-Skidding in Large-Scale Angular Contact Ball Bearings: Nonlinear Dynamic Model with Thermal Effects and Experimental Results. *Mechanical Systems and Signal Processing*, 147:107120, 2021.

[68] Z. Shi and J. Liu. An Improved Planar Dynamic Model for Vibration Analysis of a Cylindrical Roller Bearing. *Mechanism and Machine Theory*, 153:103994, 2020.

[69] A. Loriemi, G. Jacobs, S. Reisch, D. Bosse, and T. Schröder. Experimental and Simulation-Based Analysis of Asymmetrical Spherical Roller Bearings as Main Bearings for Wind Turbines. *Forschung im Ingenieurwesen*, 85, 06 2021.

[70] J. Stirling, E. Hart, and A. Kazemi Amiri. Constructing Fast and Representative Analytical Models of Wind Turbine Main Bearings. *Wind Energy Science*, 6(1):15–31, 2021.

[71] D. Nelias, I. Bercea, and V. Paleu. Prediction of Roller Skewing in Tapered Roller Bearings. *Tribology Transactions*, 51(2):128–139, 2008.

[72] A. Shafiee, T. Russell, F. Sadeghi, and M. Wilmer. Analytical Investigation of Roller Skew and Tilt in a Spherical Roller Bearing. *Journal of Tribology*, 144:1–23, 12 2021.

[73] J. J. Kalker. A Fast Algorithm for the Simplified Theory of Rolling Contact. *Vehicle System Dynamics*, 11(1):1–13, 1982.

[74] J. J. Kalker. *User's Manual of the Fortran IV Program CONTACT*. Delft, The Netherlands, 1982.

[75] J. Santamaria P. A. Meehan J. Blanco-Lorenzo, S. Liu and E. G. Vadillo. Frictional contact Analysis in a Spherical Roller Bearing. *Journal of Computational Design and Engineering*, 10(1):139–159, 12 2022.

[76] D. J. Haines and E. Ollerton. Contact Stress Distributions on Elliptical Contact Surfaces Subjected to Radial and Tangential Forces. *Proceedings of the Institution of Mechanical Engineers*, 177(1):95–114, 1963.

[77] M. Eriten, A.A. Polycarpou, and L.A. Bergman. Physics-Based Modeling for Partial Slip Behavior of Spherical Contacts. *International Journal of Solids and Structures*, 47(18):2554–2567, 2010.

[78] A. Greco, S. Sheng, J. Keller, and A. Erdemir. Material Wear and Fatigue in Wind Turbine Systems. *Wear*, 302(1):1583–1591, 2013. Wear of Materials 2013.

[79] R. D. Mindlin and H. Deresiewicz. Elastic Spheres in Contact Under Varying Oblique Forces. *Journal of Applied Mechanics*, 20(3):327–344, 06 2021.

[80] J. J. Kalker. Transient Phenomena in Two Elastic Cylinders Rolling Over Each Other With Dry Friction. *Journal of Applied Mechanics*, 37(3):677–688, 1970.

[81] J. J. Kalker. Transient Rolling Contact Phenomena. *ASLE Transactions*, 14(3):177–184, 1971.

[82] On the Transient Dynamic Antiplane Contact Problem in the Presence of Dry Friction and Slip,.

[83] B. Gurrutxaga-Lerma. On the Transient Planar Contact Problem in the Presence of Dry Friction and Slip. *International Journal of Solids and Structures*, 193–194:314–327, 2020.

[84] E. Kausel. *Fundamental Solutions in Elastodynamics: A Compendium*. Cambridge University Press, 2006.

[85] E. Kausel. Lamb's Problem at its Simplest. *Proc R Soc Lon Ser A*, 469:462–499, 2012.

[86] E. de Mello, G. Kampolis, E. Hart, D. Hickey, I. Dinwoodie, J. Carroll, R. Dwyer-Joyce, and A. Boateng. Data Driven Case Study of a Wind Turbine Main-Bearing Failure. *Journal of Physics: Conference Series*, 2018(1):012011, sep 2021.

[87] M. D. Machado de Azevedo, A. M. Araújo, and N. Bouchonneau. Renewable and Sustainable Energy Reviews. *Renewable and Sustainable Energy Reviews*, 56:368–379, 2016.

[88] A. Stetco, F. Dinmohammadi, and X. Zhao and. Machine Learning Methods for Wind Turbine Condition Monitoring: A Review. *Renew. Energy*, 133:620–635, 2019.

[89] R. Moeini, M. Entezami, and M. Ratkovac and. Perspectives on Condition Monitoring Techniques of Wind Turbines. *Wind Engineering*, 43(5):539–555, 2019.

[90] A. Zaher, S. D. J. McArthur, D. G. Infield, and Y. Patel. Online Wind Turbine Fault Detection Through Automated SCADA Data Analysis. *Wind Energy*, 12(6):574–593, 2009.

[91] J. Carroll, S. Koukoura, and A. McDonald. Wind Turbine Gearbox Failure and Remaining Useful Life Prediction Using Machine Learning Techniques. *Wind Energy*, 22:360–375, 2019.

[92] Y. Qu, C. Chen, and B. Zhou. Study on Fault Diagnosis of Wind Turbine Main Bearing Based on Finite Element Analysis and Wavelet Analysis. *Advanced Materials Research*, 308-310:1264–1268, 2011.

[93] M. Ghane, A. R. Nejad, M. Blanke, Z. Gao, and T. Moan. Statistical Fault Diagnosis of Wind Turbine Drivetrain Applied to a 5MW Floating Wind Turbine. *J. Phys. Conf. Ser.*, 753:052017, 2016.

[94] M. Hamadache and D. Lee. 16th International Conference on Control, Automation and Systems (ICCAS). In *ICCAS*, pages 1579–1584, 2016.

[95] J. Wang, Y. Peng, W. Qiao, and J. Hudgins. Bearing Fault Diagnosis of Direct-Drive Wind Turbines Using Multiscale Filtering Spectrum. *IEEE Transactions on Industry Applications*, 53(3):3029–3038, 2017.

[96] R. Zimroz, W. Bartelmus, T. Barszcz, and J. Urbanek. Wind Turbine Main Bearing Diagnosis - A Proposal of Data Processing and Decision Making Procedure under Non Stationary Load Condition. *Key Engineering Materials*, 518:437–444, 2012.

[97] Z. Zhang. Automatic Fault Prediction of Wind Turbine Main Bearing Based on SCADA Data and Artificial Neural Network. *Open Journal of Applied Sciences*, 8:211–225, 2018.

[98] Z. Y. Zhang and K. S. Wang. Wind Turbine Fault Detection Based on SCADA Data Analysis Using ANN. *Adv. Manuf.*, 2:70–78, 2014.

[99] Natural Power. SCADA Data Acquisition, 2021. Personal communication.

[100] A. Kusiak and A. Verma. Analyzing Bearing Faults in Wind Turbines: A Data-Mining Approach. *Renewable Energy*, 48:110–116, 2012.

[101] Y. Zhao, D. Li, A. Dong, D. Kang, Q. Lv, and L. Shang. Fault Prediction and Diagnosis of Wind Turbine Generators Using SCADA Data. *Energies*, 10(8):1210, 2017.

[102] R. Bergua Archeli, J. Keller, O. Bankestrom, M. Dunn, Y. Guo, A. Key, and E. Young. Up-Tower Investigation of Main Bearing Cage Slip and Loads. Technical Report NREL/TP-5000-81240, National Renewable Energy Laboratory (NREL), Golden, CO, United States, 2021.

[103] Stephen P. Timoshenko and J. N. Goodier. Theory of Elasticity. *Journal of Applied Mechanics*, 42:911–911, 1975.

[104] J. R. Barber. *Contact Mechanics*. Solid Mechanics and Its Applications. Springer International Publishing, 2018.

[105] K. L. Johnson. *Contact Mechanics*. Cambridge University Press, 1985.

[106] E. W. Cheney and D. R. Kincaid. *Numerical Mathematics and Computing*. Cengage Learning, 7th edition, 2012.

[107] J. F. Antoine, C. Visa, C. Sauvey, and G. Abba. Approximate Analytical Model for Hertzian Elliptical Contact Problems. *Journal of Tribology*, 128(3):660–664, March 2006.

[108] A. Rao. *Dynamics of Particles and Rigid Bodies: a Systematic Approach*. Cambridge University Press, 2006.

[109] G. Wanner and E. Hairer. *Solving Ordinary Differential Equations II*, volume 375. Springer Berlin Heidelberg, 1996.

[110] A. W. Crook. The Lubrication of Rollers III. A Theoretical Discussion of Friction and the Temperatures in the Oil Film. *Philosophical Transactions of the Royal Society of London. Series A, Mathematical and Physical Sciences*, 254(1040):237–258, 1961.

[111] M. Masjedi and M. M. Khonsari. Film Thickness and Asperity Load Formulas for Line-Contact Elastohydrodynamic Lubrication with Provision for Surface Roughness. *Journal of tribology*, 134(1), 2012.

[112] L. D. Landau and E. M. Lifshitz. *Mechanics*, volume 3 of *Course of Theoretical Physics*. Butterworth-Heinemann, Oxford, UK, 3rd edition, 1976.

[113] A. Celletti. Perturbation Theory in Celestial Mechanics. In R. Meyers, editor, *Mathematics of Complexity and Dynamical Systems*. Springer, New York, NY, 2012.

[114] J. Slane and S. Tragesser. Analysis of Periodic Nonautonomous Inhomogeneous Systems. *Nonlinear Dynamics and Systems Theory*, 2, Jan 2011.

[115] H. Goldstein, C. Poole, and J. Safko. *Classical Mechanics*. Addison Wesley, 3rd edition, 2002.

[116] D. Halliday, R. Resnick, and J. Walker. *Fundamentals of Physics*. John Wiley & Sons, Hoboken, NJ, 10th edition, 2013.

[117] H. Eckardt. The Gyroscope Fully Understood: Complete Gyroscopic Motion with External Torque. 2018.

[118] V. Tanrıverdi. Revisiting Dissipative Motion of a Spinning Heavy Symmetric Top and the Rise of the Top by Friction, 2022.

[119] F. Hoppensteadt. *Analysis and Simulation of Chaotic Systems*. Springer, 2nd edition, 1993.

[120] H. Sheheitli and J. R. Touma. On the Dynamics of a Spinning Top Under the Influence of Rotation: Resonant Relative Equilibrium States. *Commun. Nonlinear Sci. Numer. Simul.*, 59:424–436, 2018.

[121] V. I. Arnold. *Mathematical Methods of Classical Mechanics*, volume 60 of *Graduate Texts in Mathematics*. Springer-Verlag New York, 2nd edition, 1989. Part of the Springer Book Archive. Series ISSN: 0072-5285, Series E-ISSN: 2197-5612.

[122] E Minguzzi. Rayleigh's Dissipation Function at Work. *European Journal of Physics*, 36(3):035014, mar 2015.

[123] A. M. Bersani and P. Caressa. Lagrangian Descriptions of Dissipative Systems: A Review. *Mathematics and Mechanics of Solids*, 26(6):785–803, 2021.

[124] O. Paulsson. The Rayleigh Dissipation Function: Theory and Application, December 2014. Analytical Mechanics Final Project.

[125] U. Felderhof, V. Sokolov, and P. Éminov. Hamiltonian Field Theory of Ferrohydrodynamics. *The Journal of chemical physics*, 135:144901, 10 2011.

[126] A. López-Gordón. The Geometry of Rayleigh Dissipation. Master's thesis, Institution Name, 2021.

[127] S. Montgomery-Smith. Hamiltonians Representing Equations of Motion with Damping Due to Friction, 2014.

[128] C. R. Galley. Classical Mechanics of Non-Conservative Systems. *Physical Review Letters*, 110(17), April 2013.

[129] W. Paulsen. *Asymptotic Analysis and Perturbation Theory.* CRC Press, Boca Raton, FL, 2013.

[130] T. A. Harris and M. N. Kotzalas. *Rolling Bearing Analysis.* CRC/Taylor & Francis, Boca Raton, FL, 2007.

[131] S. L. Brunton and J. N. Kutz. *Data-Driven Science and Engineering: Machine Learning, Dynamical Systems, and Control.* Cambridge University Press, 2019.

[132] P. Antsaklis and A. Michel. *A Linear Systems Primer.* Birkhäuser Boston, 1 edition, 2007. XVI, 517 pages.

[133] J. D. Lambert. *Numerical Methods for Ordinary Differential Systems.* John Wiley & Sons, 1992.

[134] R. L. Burden and J. D. Faires. *Numerical Analysis.* Brooks/Cole, Cengage Learning, Boston, MA, USA, 9th edition, 2010.

[135] D. Goldberg. What Every Computer Scientist Should Know About Floating-Point Arithmetic. *ACM Comput. Surv.*, 23(1):5—-48, March 1991.

[136] G. Boffetta, A. Crisanti, F. Paparella, A. Provenzale, and A. Vulpiani. Slow and Fast Dynamics in Coupled Systems: A Time Series Analysis View. *Physica D: Nonlinear Phenomena*, 116(3):301–312, 1998.

[137] J. S. Bay. *Fundamentals of Linear State Space Systems.* McGraw-Hill, 1999.

[138] T. Kailath. *Linear Systems.* Prentice-Hall, Englewood Cliffs, NJ, 1980.

[139] A. Taheri. Ee 5143: Linear systems - module 4. `https://ceid.utsa.edu/ataha/wp-content/uploads/sites/38/2017/07/EE5143_Module4.pdf`, 2017. Accessed: 2025-02-05.

[140] F. W. J. Olver. *Asymptotics and Special Functions.* Academic Press, San Diego, CA, 1st edition, 1974.

[141] J. Baudrillard. *Simulacra and Simulation.* University of Michigan Press, Ann Arbor, 1994.

[142] D. Vaes, Y. Guo, P. Tesini, and J. A. Keller. Investigation of Roller Sliding in Wind Turbine Gearbox High-Speed-Shaft Bearings.

[143] F. W. Carter and A. E. H. Love. On The Action of a Locomotive Driving Wheel. *Proceedings of the Royal Society of London. Series A, Containing Papers of a Mathematical and Physical Character*, 112(760):151–157, 1926.

[144] P. Silva, A. Giuffrida, N. Fergnani, E. Macchi, M. Cantù, R. Suffredini, M. Schiavetti, and G. Gigliucci. Performance Prediction of a Multi-MW Wind Turbine Adopting an Advanced Hydrostatic Transmission. *Energy*, 64:450–461, 2014.

[145] E. Hau. *Wind Turbines: Fundamentals, Technologies, Application, Economics.* 01 2006.

[146] S. E. Prameela, C. C. Walker, C. S. DiMarco, D. D. Mallick, X. Sun, S. Hernandez, T. Sasaki, J. W. Wilkerson, K. T. Ramesh, G. M. Pharr, and T. P. Weihs. Rapid Quantification of Dynamic and Spall Strength of Metals Across Strain Rates, 2023.

[147] R. L. Mott. *Machine Elements in Mechanical Design.* Pearson Prentice Hall, Upper Saddle River, N.J., 4th edition, 2004.

[148] J. Polák, R. Petráš, and V. Mazanova. Basic Mechanisms Leading to Fatigue Failure of Structural Materials. *Transactions of the Indian Institute of Metals*, 69, 12 2015.

[149] Kenneth Scott and David Infield and Nigel Barltrop and John Coultate and Anabel Shahaj. *Effects of Extreme and Transient Loads on Wind Turbine Drive Trains.*

[150] Paul Dvorak. How Turbulent Winds Abuse Wind Turbine Drivetrains. `https://www.windpowerengineering.com/how-turbulent-wind-abuse-wind-turbine-drivetrains/`, 2015. Accessed: 2026-02-13.

[151] Kenneth Scott. *Effects of Transient Loading on Wind Turbine Drivetrains.* PhD thesis, University of Strathclyde, 2014. Accessed: 2024-06-21.

[152] G. F. Miller, H. Pursey, and E. C. Bullard. The Field and Radiation Impedance of Mechanical Radiators on the Free Surface of a Semi-Infinite Isotropic Solid. *Proceedings of the Royal Society of London. Series A. Mathematical and Physical Sciences*, 223(1155):521–541, 1954.

[153] A. Cemal Eringen and Erdoğan S. Şuhubi. *Elastodynamics: Volume 2.* Academic Press Inc., 1975.

[154] J. J. Kalker. A Minimum Principle for the Law of Dry Friction, With Application to Elastic Cylinders in Rolling Contact—Part 1: Fundamentals—Application to Steady Rolling. *Journal of Applied Mechanics*, 38(4):875–880, 1971.

[155] J. J. Kalker. A Minimum Principle for the Law of Dry Friction—Part 2: Application to Nonsteadily Rolling Elastic Cylinders. *Journal of Applied Mechanics*, 38(4):881–887, 1971.

[156] F. Böhm R. Wille and A. Duda. Calculation of the Rolling Contact Between a Tyre and Deformable Ground. *Vehicle System Dynamics*, 43(sup1):483–492, 2005.

[157] R. Rahmani R. Turnbull and H. Rahnejat. The Effect of Outer Ring Elastodynamics on Vibration and Power Loss of Radial Ball Bearings. *Proceedings of the Institution of Mechanical Engineers, Part K*, 234(4):707–722, 2020.

[158] R. de la Presilla, S. Wandel, M. Stammler, M. Grebe, G. Poll, and S. Glavatskih. Oscillating Rolling Element Bearings: A Review of Tribotesting and Analysis Approaches. *Tribology International*, 188:108805, 2023.

[159] K. Thorne and R. Blandford. *Elasticity and Fluid Dynamics.* Princeton University Press, 2021.

[160] S. P. Timoshenko and S. Woinowsky-Krieger. *Theory of Plates and Shells.* 1959.

[161] J. D. Achenbach. *Wave Propagation in Elastic Solids.* Applied Mathematics and Mechanics Series. North-Holland Publishing Company, 1973.

[162] H. Lamb. On The Propagation of Tremors Over the Surface of an Elastic Solid. *Philos Trans R Soc Lon*, 203:1–42, 1904.

[163] H. R. Aggarwal and C. M. Ablow. On the Rayleigh Equation for Elastic Surface Waves. *The Journal of the Acoustical Society of America*, 47(5B):1461–1461, May 1970.

[164] M. Emami and M. Eskandari-Ghadi. Lamb's Problem: A Brief History. *Mathematics and Mechanics of Solids*, 25(3):501–514.

[165] P. G. Richards. Elementary Solutions to Lamb's Problem For a Point Source and Their Relevance to Three-dimensional Studies of Spontaneous Crack Propagation. *Bull Seismol Soc Am*, 69:947–956, 1979.

[166] C. L. Pekeris. The Seismic Surface Pulse. *Proc Natl Acad Sci*, 41:469–48, 1955.

[167] G. Xiang, Y. Han, J. Wang, J. Wang, and X. Ni. Coupling Transient Mixed Lubrication and Wear for Journal Bearing Modeling. *Tribology International*, 138:1–15, 2019.

[168] J. P. Vichard. Transient Effects in the Lubrication of Hertzian Contacts. *Journal of Mechanical Engineering Science*, 13(3):173–189, 1971.

[169] R. J. Kleckner and J. Pirvics. Spherical Roller Bearing Analysis. *Journal of Lubrication Technology*, 104(1):99–108, 01 1982.

[170] L. Houpert. TRIBOLOGY: Numerical and Analytical Calculations in Ball Bearings. Sep 1999.

[171] L. Houpert. Ball Bearing and Tapered Roller Bearing Torque: Analytical, Numerical and Experimental Results. *Tribology Transactions*, 45(3):345–353, 2002.

[172] A. Qu and D. L. James. On the Impact of Ground Sound. *ArXiv*, abs/1909.09235, 2019.

[173] W. Zhang and Y. Zhou. Chapter 2 - Level-set Functions and Parametric Functions. In *The Feature-Driven Method for Structural Optimization*, pages 9–46. Elsevier, 2021.

[174] L. I. Slepyan and M. Brun. Driving Forces in Moving-Contact Problems of Dynamic Elasticity: Indentation, Wedging and Free Sliding. *Journal of the Mechanics and Physics of Solids*, 60(11):1883–1906, 2012.

[175] P. M. Thompson. Snap, Crackle, and Pop. In *Proc of AIAA Southern California Aerospace Systems and Technology Conference*, page 1, March 2011.

[176] R. J. Brind and G. R. Wickham. Near-field Behaviour of the Fundamental Elastodynamic Solutions for a Semi-Infinite Homogeneous Isotropic Elastic Solid. *Proceedings of the Royal Society of London. Series A: Mathematical and Physical Sciences*, 433(1887):101–120, 1991.

[177] Heraclitus. *Fragments*. University of Toronto Press, 1987.

[178] van Dam, Jeroen and Santos, Rick. Mechanical Loads Test Report for the U.S. Department of Energy 1.5-Megawatt Wind Turbine. Technical Report NREL/TP-5000-63679, National Renewable Energy Laboratory, 2015.

[179] Sabine Haas, Birgit Schachler, Uwe Krien, and Stephen Bosch. windpowerlib: A Python Library to Model Wind Power Plants (v0.1.0), January 2019.

[180] Nicholas Hamilton. NREL - GE 1.5MW SLE Wind Turbine / Reviewed Data.

[181] Aris, Capell. Wind Power Reassessed: A review of the UK wind resource for electricity generation. Technical report, Institute for Energy Systems, Innovation and Sustainability (IESIS); Scientific Alliance and Adam Smith Institute, July 2017. Accessed 2025-12-25.

[182] Chen Wen-Hwa and Tsai Pwu. Finite Element Analysis of Elastodynamic Sliding Contact Problems with Friction. *Computers & Structures*, 22(6):925–938, 1986.

[183] F Ursell. The Local Expansion of a Source of Oblique Water Waves in the Free Surface. *Wave Motion*, 33(1):109–116, 2001.

[184] C. Song, R. Zhang, Y. Zhou, J. Tan, and C. Zhu. Transient Analysis of Non-Uniform Tilting-Pad Journal Bearing for Wind Turbine Main Shaft Under Dynamical Loading. *Mechanism and Machine Theory*, 203:105792, 2024.

[185] J. Wang, Y. Cao, W. Sun, R. Chen, Q. Jia, and Y. Cui. Research on the Lubrication Performance of Circular Tilting Pad Thrust Bearings for Large Wind Turbines. *Lubrication Science*, 36(6):421–430, 2024.

[186] R. Zhang, C. Song, Y. Zhou, J. Tan, and Z. Zeng. Tribodynamic Behavior of a Novel Double Bearing Layout for the Main Shaft System of Wind Turbines. *Tribology International*, 204:110496, 2025.

[187] Wikipedia contributors. King Ludd Image. `https://en.wikipedia.org/wiki/Luddite`, 2025. Accessed: 26 March 2025.

[188] K. Torokoff. Methods of Mathematical Physics - Lecture 4, 2019. Accessed: 2025-02-18.

[189] H. Nyquist. Certain Topics in Telegraph Transmission Theory. *Transactions of the American Institute of Electrical Engineers*, 47(2):617–644, 1928.

[190] C.E. Shannon. Communication in the Presence of Noise. *Proceedings of the IRE*, 37(1):10–21, 1949.

[191] R. Herman. *Introduction to Partial Differential Equations: Complex Representations of Functions*. LibreTexts, 2024. Accessed: February 2024.

[192] R. Courant, K. Friedrichs, and H. Lewy. On the Partial Difference Equations of Mathematical Physics. *IBM Journal of Research and Development*, 11(2):215–234, 1967.

[193] M. J. Ringel, J. S. Heiselman, W. L. Richey, I. M. Meszoely, W. Jarnagin, and M. I. Miga. Comparing Regularized Kelvinlet Functions and the Finite Element Method for Registration of Medical Images to Sparse Organ Data. *Medical image analysis*, 96:103221–103221, 2023.

[194] H. N. Nguyen and R. Cortez. Reduction of the Regularization Error of the Method of Regularized Stokeslets for a Rigid Object Immersed in a Three-Dimensional Stokes Flow. *Communications in Computational Physics*, 15:126–152, 01 2014.

[195] N. G. Chisholm and S. D. Olson. A Framework for Generating Radial and Surface-Oriented Regularized Stokeslets. *Fluids*, 7(11), 2022.

[196] B. Zhao, E. Lauga, and L. Koens. Method of Regularized Stokeslets: Flow Analysis and Improvement of Convergence. *Phys. Rev. Fluids*, 4:084104, Aug 2019.

[197] J. M. McNamee and V. Pan. *Numerical Methods for Roots of Polynomials Part II*. Newnes, 2013.

[198] O. Menck. The Finite Segment Method—A Numerical Rolling Contact Fatigue Life Model for Bearings Subjected to Stochastic Operating Conditions. *Journal of Tribology*, 145(3):031201, 11 2022.

[199] Nikesh Patel, Benyam Dejen, Stephen Church, Philip Dolan, and Patrick Parkinson. Nitrogen-Vacancy Color Centers in Nanodiamonds as Reference Single-Photon Emitters. *Opt. Express*, 33(12):25159–25169, Jun 2025.

[200] A. Frangoul. A "Quantum Leap": Monster Wind Turbines are Going to Get Even Bigger, April 2021. [Accessed 1 September 2021].

[201] M. Beretta, A. Julian, J. Sepulveda, J. Cusidó, and O. Porro. An Ensemble Learning Solution for Predictive Maintenance of Wind Turbines Main Bearing. *Sensors*, 21(4):1512, 2021.

[202] J. I. Taylor. *The Vibration Analysis Handbook*. Vibration Consultants, 2003.

[203] W. Teng, R. Jiang, X. Ding, Y. Liu, and Z. Ma. . *Shock and Vibration*, 2378435, 2016.

[204] Y. Ishida. Nonlinear Vibrations and Chaos in Rotordynamics. *JSME international journal. Ser. C, Dynamics, control, robotics, design and manufacturing*, 37(2):237–245, 1994.

[205] H. Sheheitli. On the dynamics of a spinning top under high-frequency excitation: Part i—pivot point under vertical harmonic vibration. *Nonlinear Dynamics*, 90(2):765–779, October 2017. Publisher Copyright: © 2017, Springer Science+Business Media B.V.

[206] H. Sheheitli. On the dynamics of a spinning top under high-frequency excitation. part ii: Pivot point under horizontal harmonic vibration. *Nonlinear Dynamics*, 90(4):2269–2276, December 2017. Publisher Copyright: © 2017, Springer Science+Business Media B.V.

[207] A. Encalada-Dávila, B. Puruncajas, C. Tutivén, and Y. Vidal. Wind Turbine Main Bearing Fault Prognosis Based Solely on SCADA Data. *Sensors*, 21(6):2228, 2021.

[208] R. B. Randall and J. Antoni. Rolling Element Bearing Diagnostics—A Tutorial. *Mechanical Systems and Signal Processing*, 25(2):485–520, 2011.

[209] D. S. Chandra and Y. S. Rao. Fault Diagnosis of a Double-Row Spherical Roller Bearing for Induction Motor Using Vibration Monitoring Technique. *J Fail. Anal. and Preven.*, 19:1144—-1152, 2019.

[210] A. P. Bradley. The Use of the Area Uder the ROC Curve in the Evaluation of Machine Learning Algorithms. *Pattern Recognition*, 30(7):1145–1159, 1997.

[211] D. J. Hand and R. J. Till. A Simple Generalisation of the Area Under the ROC Curve for Multiple Class Classification Problems. *Machine Learning*, 45:171–186, 2001.

[212] T. Fawcett. An Introduction to ROC Analysis. *Pattern Recognition Letters*, 27(8):861–874, 2006.

[213] A. R. Nejad, J. Keller, Y. Guo, S. Sheng, H. Polinder, S. Watson, J. Dong, Z. Qin, A. Ebrahimi, R. Schelenz, et al. Wind Turbine Drivetrains: State-of-the-art Technologies and Future Development Trends. *Wind Energy Science*, 7(1):387–411, 2022.

[214] Y. Guo, A. Thomson, R. Bergua, O. Bankestrom, J. Erskine, and J. Keller. Acoustic Emission Measurement of a Wind Turbine Main Bearing. Technical report, National Renewable Energy Lab.(NREL), Golden, CO (United States), 2022.

[215] Y. Guo, S. Sheng, C. Phillips, J. Keller, P. Veers, and L. Williams. A Methodology for Reliability Assessment and Prognosis of Bearing Axial Cracking in Wind Turbine Gearboxes. *Renewable and Sustainable Energy Reviews*, 127:109888, 2020.